2D modeling approach for propeller-wing-flap interaction

Pieter van Zelst

student nr. 4367251

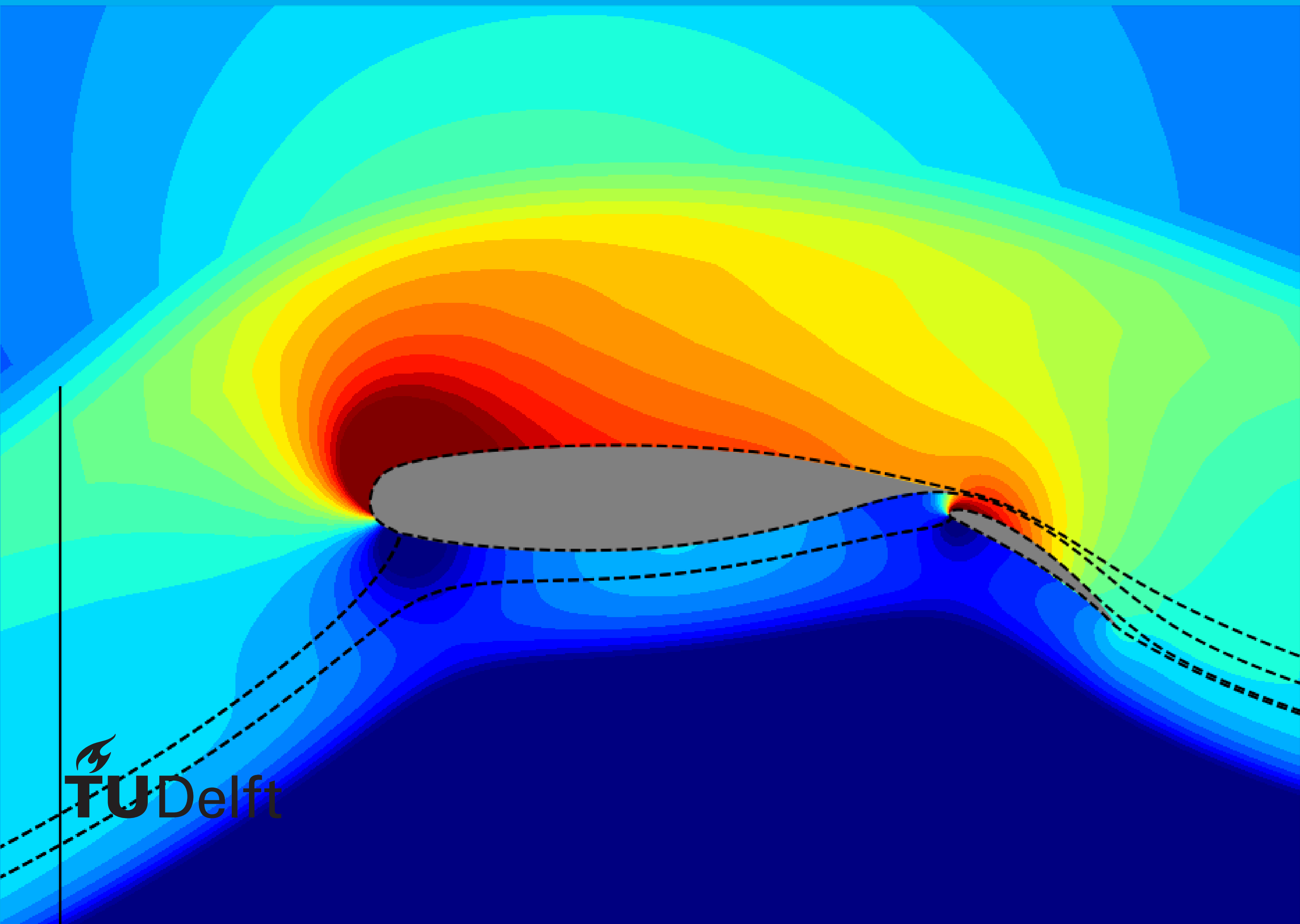

TUDelft

2D modeling approach for propeller-wing-flap interaction

by

Pieter van Zelst

to obtain the degree of Master of Science
at the Delft University of Technology,
to be defended publicly on Tuesday March 9, 2021 at 9:00 AM.

Student number:	4367251	
Project duration:	March, 2020 – February, 2021	
Thesis committee:	Prof. dr. ir. L. L. M. Veldhuis,	TU Delft, chair & supervisor
	Dr. ir. T. Sinnige,	TU Delft, daily supervisor
	ir. W. A. Timmer,	TU Delft, examiner

An electronic version of this thesis is available at `http://repository.tudelft.nl/`.

TU Delft

Preface

This report deals with 2D characteristics of multi-element airfoils in propeller slipstreams. A really interesting topic with the new configurations under consideration, such as distributed electric propulsion, which first caught my attention during my design synthesis exercise. Propeller-wing aerodynamics is a really interesting and broad topic, and I trust that this MSc. thesis made a useful contribution to the body of knowledge.

I would like to thank Prof. Leo Veldhuis and Dr. Tomas Sinnige for the opportunity to delve into this interesting topic. I enjoyed the constructive meetings where I would share my screen and discuss, the feedback really helped me to get this thesis to a higher level.

When selecting a thesis topic I could never have imagined that I would graduate at home from behind my computer in times of a pandemic. This required great resilience but luckily I enjoyed support of those around me. Special thanks to the fellow students of the self-proclaimed "Master support group" for their weekly support towards the end of this project. Thanks to my parents who supported me through my entire studies. They will remember me building airplanes out of lego, and I am grateful that I may now pursue a career in aerospace, and contribute to more sustainable aviation. I would also like to thank my roommates for making my days in Delft more fun and not making too much noise during these long days at home :). Finally, I would like to thank my girlfriend for all her encouragement and support.

Pieter van Zelst
Delft, February 2021

Summary

There is renewed interest in propeller-driven aircraft from the point of fuel economy, with new opportunities such as distributed electric propulsion (DEP). To this end, new wing/propeller combinations are investigated which require an improved understanding of the propeller-wing-flap interaction effects. This flow-field is particularly challenging as flaps are particularly non-planar, and contrary to a wing in cruise, this would require different methods of modeling. It should also be considered that most propeller installations are mainly optimized for cruise and not so-much for high-lift conditions. This requires new computational models and simulation methods that are fast, in order to quickly survey the design space. Semi-empirical methods are limited to the data-sets they were derived with, and apply limited possibilities for optimizing flap geometry. Lower order methods such as VLM, panel methods, viscous-inviscid simulations or a combination are some of the methods that could deliver a fast model with improved design insight and more flexibility, potentially at higher accuracy than semi-empirical methods, whilst still being much faster than RANS CFD.

One such category of new models may require "tuning" of an inviscid computation, which may have been obtained with planar or non-planar VLM. This has been performed before with lifting line methods: A 2D viscous-inviscid solver may provide a good insight in airfoil performance at any operating condition, and possibly even in stalled condition. It is hypothesized that a 2D viscous-inviscid solver may be modified to consider the effect of a slipstream combined with high lift devices, which will be the focus of this thesis. MSES has proven reliable for analyzing multi-element airfoils and it is hypothesized that it can also be reliably modified to deal with non-uniform inflow/blowing. The goal of this thesis is to demonstrate that this may be implemented and can be used to optimize designs, whilst also establishing the limitations of the method.

It is demonstrated that the formulation of MSES is suitable for considering a slipstream of limited height: A total pressure jump upward or downward from either side of the airfoil (which is very crude) was already an option on some later MSES versions. This feature is considerably extended: MSES is modified to allow a total pressure increase at a disk on any location in the domain. The MSES source code in Fortran was modified and wrapped by Python to model a velocity increase and display the results. Any desirable velocity profile may now be modeled. There is a choice between adding the velocity increase already at the inlet, leading to a fully developed slipstream, or closer to the airfoil, leading to an actuator disk with gradual contraction and velocity increase. The option of adding refinement near the edges of the slipstream, where a large velocity gradient may exist, is also added. With the correct refinement, both convergence rate and accuracy are significantly improved. This is found to require some knowledge of the path of the streamlines. Hence, for high-lift cases, this requires an iteration with a low and high detail solution. This is however not reliable for the free-contraction case as the curvature of the dividing streamlines is complex with the contraction and slipstream blowing effects.

The implementation is tested for a single airfoil and showed a good match with inviscid CFD simulations provided that the slipstream was pre-contracted at the inlet. Small slipstream heights/diameters generally lead to lower lift augmentation: the full lift augmentation expected from the dynamic pressure increase are encountered for slipstream height ratios of $h/c = 4$ or higher. There is also some sensitivity to the deflection of the slipstream due to upwash. Upper surface blowing may increase the airfoil lift due to higher suction. This may result in an 's'-shaped curve for the lift with vertical slipstream position as also found in the 3D APROPOS experiments. Contraction can be modeled but only during low-lift situations due to the aforementioned limitations. The results appear to follow the 3D model of Smelt and Davies. The results with contraction are lower than inviscid CFD simulations; whether the CFD simulations or MSES are more realistic is up for debate as the lift augmentation found by Patterson was higher than theoretically anticipated.

The behavior of the Boundary Layer (BL) model of MSES is evaluated with a realistic slipstream profile approaching a single element airfoil. The comparison of a non-lifting NACA0012 airfoil with upper surface blowing and a "regular" lifting condition yields some interesting insights: during upper surface blowing the stagnation point moves upward, and the pressure suction peak moves aft, contrary to the lifting case. This seems to have a favorable effect on the boundary layer development: the boundary layer growth for the upper surface blown case lies in-between that of the unblown airfoil at 0 lift and the case under angle of attack. One can actually split the contributions of the boundary layer model: the term depending on velocity gradient and BL history is shown to be dominant over that of the skin friction drag. It should be noted that viscous effects within the slipstream beyond the airfoil boundary layer are not considered. This is especially relevant with high velocity gradients near the boundaries of a slipstream, hence, results may be more smooth in reality. The same holds for the turbulence induced by propellers, the effect of which may not be approximated correctly.

For tests on a flapped airfoil, the NLR7301 is selected: it has been used before in other graduation projects at TU-Delft and other research. It is also validated with wind-tunnel tests including some boundary layer measurements, is considered suitable for validation of CFD codes. It seems that MSES can closely approximate the lift curve up to $C_{l,max}$ with $n_{crit} = 3$ but the wake bursting occurs less sudden than on the wind-tunnel model. It is also shown that grids may be sensitive to bubble movement near $C_{l,max}$. This flap configuration is used to asses the impact of slipstream positioning in lift.

It is found that the slipstream position drastically influences the lifting behavior and may suppress or aggravate wake-growth and bursting over the flap, leading to a relatively high variation in flap lifting contribution, depending on the slipstream location. If the main element and flap are in a high-velocity part of the slipstream this has a favorable impact on the development of the boundary layer: the adverse pressure gradient can more easily be overcome. On the contrary, incorrect positioning where almost the entire slipstream passes above the airfoil may lead to a wake-burst. The main element boundary layer and flap element receive less momentum which is detrimental for the BL development and the mutual interaction with the flap (i.e. the "dumping effect" and "off-the surface pressure recovery".) The main element wake above the flap grows significantly leading to flow retardation, causing loss of lift. Concerning measurements of this wake-burst behavior, is shown that the criterion of Gartshore may not be able to predict the severity of a wake-burst, and that the criterion for wake growth (from the research of Driver and Mateer) or simply the shape factor, may be more reliable indicators.

Finally, a parameter study into the optimal gap, overlap, and slipstream position is undertaken to establish the effect on the lift with various flap settings on the flapped NLR7301. Blowing suppresses the viscous-decambering and the wake-bursting phenomenon. The optimal designs seem identical between the blown and unblown situation. The optimal gap depends on the flap setting; this should be interpreted with care as the preference towards small gaps at high lift may fail to properly consider wake confluence. Wake bursting may be effectively delayed by shrinking the overlap to allow for the favorable effect of the LE suction of the flap on the wake coming of the main element. This study also proves that the modifications to MSES allow it to be used effectively for 2D design studies with blown flaps.

Contents

Nomenclature

Table 1: List of symbols

Symbol	Description	Unit
C_l	section lift coefficient	[-]
C_d	section drag coefficient	[-]
C_L	wing lift coefficient	[-]
C_D	wing drag coefficient	[-]
C_p	pressure coefficient	[-]
C_T	thrust coefficient	[-]
$C_{T,W}$	thrust coefficient normalized with wing	[-]
C_μ	blowing coefficient	[-]
C_J	jet momentum coefficient	[-]
D	propeller diameter	$[m]$
E_k	kinetic rotational energy	$[J]$
I	quasi-normal line index	[-]
I_{in}	number of quasi-normal lines on the inlet	[-]
J	streamline index	[-]
J_{max}	total number of streamlines	[-]
K_l	lift factor	[-]
M	Mach number	[-]
N	number of propellers	[-]
Re	Reynolds number	[-]
S	wing (reference) area	$[m^2]$
V_∞	reference (freestream) velocity	$[ms^{-1}]$
a	axial induction factor	[-]
c	chord	$[m]$
h	slipstream height	$[m]$
P_a	power available	$[hp]$
q	dynamic pressure	$[Nm^{-2}]$
s	streamwise coordinate	$[m]$
u_∞	reference (freestream) velocity	$[ms^{-1}]$
x_p	horizontal propeller offset	$[m]$
y_p	vertical propeller offset	$[m]$
z_p	vertical propeller offset	$[m]$
α	angle of attack	[°]
β	induced velocity multiplier	[-]
δ	flap deflection angle	[°]
η	viscous loss parameter	[-]
θ	slipstream turning angle	[°]
μ	dynamic viscosity of air	$[kgm^{-1}s^{-1}]$
ν	kinematic viscosity of air	$[m^2s^{-1}]$
ω	induced velocity at propeller plane	$[ms^{-1}]$

Table 2: List of boundary layer symbols

C_Δ	dissipation coefficient	$[-]$
C_f	skin-friction coefficient	$[-]$
H	shape parameter	$[-]$
H^*	kinetic energy shape parameter	$[-]$
H^{**}	density shape parameter	$[-]$
M_e	boundary layer edge Mach number	$[-]$
u_0	velocity at start of pressure rise (peak velocity)	$[ms^{-1}]$
u_e	boundary layer edge velocity	$[ms^{-1}]$
δ^*	displacement thickness	$[m]$
δ^{**}	density thickness	$[m]$
θ	displacement thickness	$[m]$
θ^*	kinetic energy thickness	$[m]$
ξ	shear layer coordinate (streamwise)	$[m]$

Table 3: List of abbreviations

Abbreviation	**Description**
A/C	Aircraft
AD	Actuator Disk
AR	Aspect Ratio
BNF	BürgerNahe Flugzeug
BEM	Blade Element Momentum
BL(C)(M)	Boundary Layer (Control)(Model)
CFD	Computational Fluid Dynamics
FPS	Foot-Pound-Second
GA	General Aviation (small/private aircraft)
LE/TE	Leading/Trailing Edge
LFC	Laminar Flow Control
LL	Lifting Line
MIL	Minimum Induced Loss
NS	Navier-Stokes
PG	Prandtl-Glauert
SRF	Swirl Recovery Factor
STOL	Short TakeOff and Landing
TO	TakeOff
UAM	Urban Air Mobility
(U)RANS	(Unsteady) Reynolds Averaged Navier-Stokes
VLM	Vortex Lattice Method
VTOL	Vertical TakeOff and Landing

1 Introduction

1.1. Historical & current interest in propeller-driven STOL

This research deals with the interaction between propellers and high-lift systems such as flaps. Multiple projects are currently investigating lift augmentation by means of propellers in tractor configuration. Some of these designs have the potential to vastly increase the lift coefficient, as the high lift system receives higher dynamic pressures. This technology could dramatically improve the field performance, leading to Short Take-Off and Landing capability (STOL). Fixed-wing STOL technology has had the interest of the military since the second world war. Difficulties in controllability and airspace management made these technologies difficult to implement for commercial use. Since the beginning of this century, STOL technology has regained interest for use in the civilian market, as large airports become more congested, and steeper flight paths could lead to less noise, as investigated by NASA (Hange [1]) and the "citizen friendly aircraft" (das Bürgernahe Flugzeug, BNF) project of the TU Braunschweig/DLR [2]. Flaps blown by propellers in a tractor configuration may be a very efficient method to create high lift: under the right conditions, lower power input is needed than when mounting the propellers vertically for comparable lifting force as noted by Drela [3]. The topic will be introduced with two design examples leading to tangible performance metrics: a more conventional design, and the ongoing research into Distributed Electric Propulsion (DEP). One may refer to the literature study for an overview of other technologies, experiments and aircraft flown (van Zelst [4]).

The Brequet 941(s): conventional (super)STOL Looking at (commercial) transport aircraft, the most profound use of the propeller lift augmentation by means of flaps is the Brequet 941(s). Harris [5] includes the specifications of the production model (the 941S), it combined a stall speed of 46 kts at gross weight of 44,100 lbs at high landing power, a takeoff run of 1,050 ft (320 m) over a 50 feet obstacle, and a landing distance of just 820 ft (250m) over a 50 feet obstacle, combined with a range of 1650 nm. Although a commercial failure, the aircraft was a technological success: The aircraft layout represents a conventional transport. The flap system is fairly conventional. Almost all of the wing is submerged in the slipstream of the four large propellers, utilizing the deflected slipstream approach. Many safety concerns were overcome by linking the four engines by a common shaft. A clever differential pitching scheme for the propellers was used to increase drag upon landing; inboard propellers were pitched for higher thrust and the outer ones set to neutral. This allowed to have effectively lower aspect ratio with lift concentrated on the inboard section, whilst also maintaining high engine power, enabling quick stopping with reverse pitch. This system did lead to higher maintenance costs, but as the wing and engines do not pivot, the weight increase over a regular transport aircraft was limited.

Another positive side-effect of this deflected slipstream approach was that there is a very flat lift curve at stall, so no clear stall speed or angle could be defined, as confirmed by NASA's tests on the Brequet 941 in the early 1960's. (Holzhauzer [6]) Some data on the flap construction and deflections is shown in fig. 1.1 & fig. 1.2. The flap was divided into four sections on each wing, the flaps are double slotted with a vaned second element. The inner two sections deflect up to 98°(!), the trailing flap on the outer section also acts as an aileron. These are very extreme deflections without circulation or boundary layer control. It would be very interesting to see if flow is still attached, and how this is achieved, as these kind of deflection angles are hard to attain for double slotted flaps, which could function up to around 75° as established by Kuhn [7].

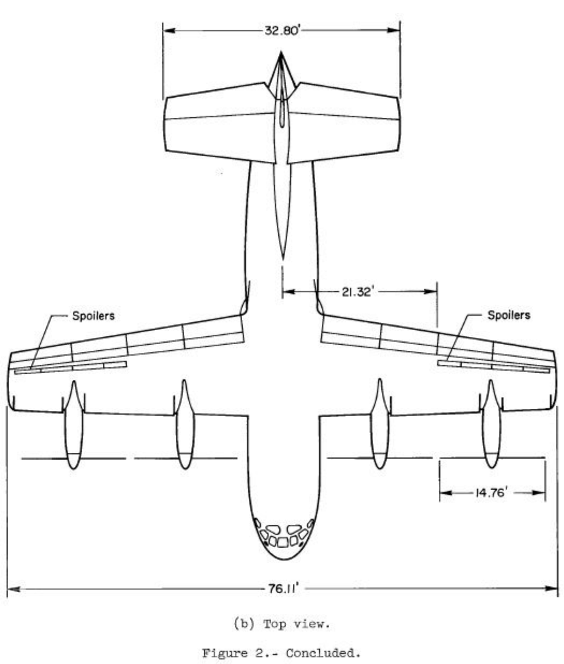

Figure 1.1: The planform of the Bréguet 941. (Holzhauser [6])

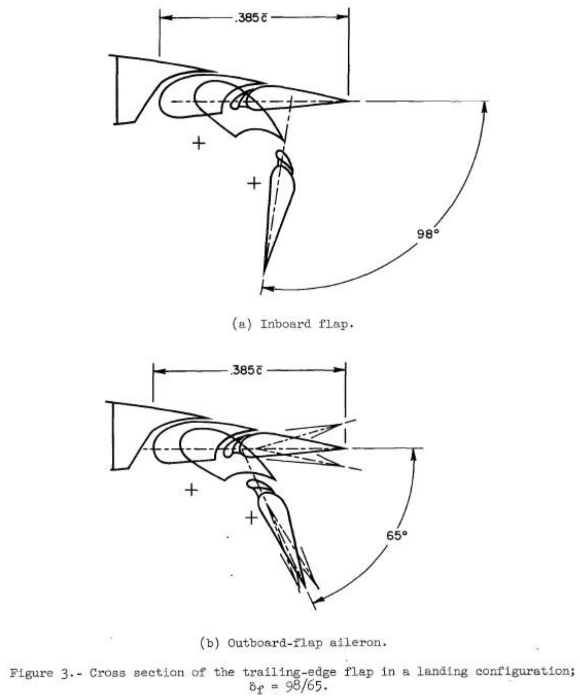

Figure 1.2: Bréguet 941 flaps at landing. (Holzhauser [6])

Figure 1.3: The X-57 Maxwell DEP aircraft. (Viken et al. [8])

Distributed Electric Propulsion (DEP) It is advantageous to blow a large portion of the wing, leading to large propellers as seen on the Bréguet 941(s). Propeller and jet aircraft are usually equipped with 2 or 4 engines to keep high efficiency and low maintenance costs.This may change in the future: Electric engines are better scalable and pose fewer maintenance issues, opening up new design possibilities such as DEP.

The application of a large count of smaller propellers has the potential to create high lift augmentation due to concentrating momentum near the wing. A doubling of lift coefficient was demonstrated on the LEAPTECH wing, reaching $C_{L,max}$ values of 5.5~6 (Murray [9].) Doubling the takeoff C_L would imply halving V^2, and thus, at constant acceleration, cut the ground run distance in half (see, for instance Ruijgrok [10]). Improved lifting capability allows for higher wing loading, in turn leading to improved cruise efficiency, as to be demonstrated by the NASA X-57 Maxwell project[11]. The aircraft is shown in fig. 1.3, Viken et al. [8] showed that such high lift augmentation may be reached on a simple general aviation airfoil with a single slotted Fowler flap. Besides, these propellers can be controlled independently for improved control and tweaking of the lift distribution. The high-lift propellers are intended to fold away during cruise, with the high-efficiency tip-mounted propellers providing cruise power. The aircraft is expected to fly in DEP configuration in the not-too-distant future. DEP technology is also being considered for Urban Air Mobility (UAM) by MIT.[12] Contributing to the improved modeling of DEP aircraft is seen as a key opportunity for this thesis.

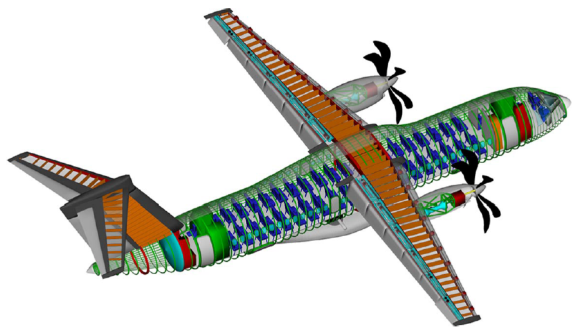

Figure 1.4: "SFB 880 aircraft design, 100 passengers, range 2000 km, $M = 0.74$, in landing configuration."(Diekman [13])

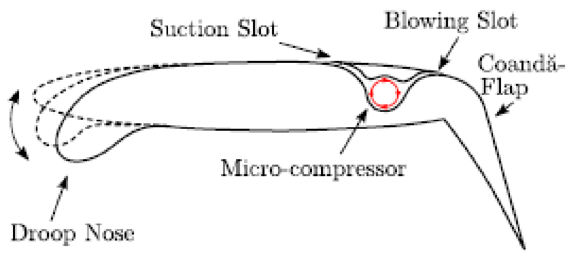

Figure 1.5: "Schematic diagram of the SFB 880 wing profile and the active high-lift system integration."(Diekman [13])

Boundary Layer Control (BLC) and Coanda effect Boundary layer suction removes the low-velocity region of the boundary layer before any back-flow occurs, thus delaying separation. In practice, although assumed highly dependent on the configuration, increases of 0.9 to over 2.0 $C_{L,max}$ are possible according to McCormick.[14]

It seems that wing blowing (or flap blowing for that matter) was a more common strategy, although no longer used on airliners. This technique adds momentum to the boundary layer by blowing high-pressure air in the flow direction by slots or nozzles on the wing surface. This technique is best applied between 25% and 60% chord of the main wing, but can also be applied on the flap. Examples of aircraft using this technique are: (early) carrier based F4 phantoms, the Blackburn Buccaneer, the F-104 Starfighter, and PS-1 flying boat.

Another form of flap blowing is to make use of the Coanda effect, the Coanda effect describes how a jet of high-energy air will tend to follow a surface for an extended time before separating: additional air is entrained which aids the lifting effect, see for example Norton [15] or Harris [5]. For propeller aircraft with bleed air, a good example under investigation is the BNF project layout: the 25% chord plain flap element has a rounded nose and a flat contour elsewhere, this resulted in a flap deflection of up to 65° with an attached boundary layer as shown by Radespiel et al. [16] Whether any wake bursting took place is uncertain, but total lift coefficients of 4.2 were observed at low angle of attack. The stalling behaviour seems fairly gradual especially for lower amounts of blowing.

A combination of the two systems is also possible: In a more complex concept reported by Diekman [13]), which also included a morphing droop nose (see fig. 1.4 and fig. 1.5) suction and blowing were combined to enable the Coanda effect on a flapped wing. Using 2D RANS simulations.[17] it was confirmed that momentum in the BL is increased by these measures, and hence the displacement thickness is decreased. Another interesting effect is that velocities around the airfoil are increased, leading to higher C_p's. Whether this is due to removing air volume, or decreasing de-cambering effect of the BL is not clear from the report. The effect of suction is similar to that of blowing, so less blowing may be required.

BL suction and wing blowing systems are fairly complex and are not applied to commercial (transport) aircraft. These concepts will not be explored in this thesis: For boundary layer suction, one may refer to an earlier thesis by Van Craenenbroeck [18].

A note on system complexity Looking at trailing edge (TE) flaps, there is a tendency to designing systems with lower complexity by using only single slotted flaps. However, as multi-element flaps are the most efficient in creating high lift augmentation, they should definitely be possible to model by the method presented in this thesis. Slats can significantly contribute to increased performance at high AoA, which is required for flying steep approaches as proven by the Ryan VZ-3 (described by Turner [19]). However, looking at information on Jane's [20][21], reference propeller aircraft such as the ATR42-600S (STOL), DHC-7, C-27 Spartan, and the Fokker 50 employ leading edge (LE) de-icing boots, and thus no leading edge devices such as slats. It is decided that due to the complexity of flow around LE devices such as slats, they are omitted in this research, but slats or a drooped nose shape may be modeled by the method anyway.

1.2. Research scope

In order to properly conduct the research and reach conclusions, it is important to set the scope by means of the following research questions and research objective. The research questions are justified, and the scope in terms of technical parameters is also defined.

1.2.1. Research Questions & Objective

The research questions to be answered in this thesis are:

1. How can you effectively predict 2D airfoil lifting behavior under the influence of a propeller/slipstream with a coupled viscous-inviscid solver?
2. What are the limitations of this low-fidelity approach for predicting this flow case?
3. How does a slipstream influence limitations on maximum lift?

Justification and elaboration of each research question

1) The research projects mentioned in the introduction were used as input to determine the need and scientific lack of knowledge to be filled by this research. It became clear that there exists a gap in analyzing capability between, on the low end, semi-empirical techniques and, on the upper end, Computational Fluid Dynamics (CFD). The same holds for computational time, which is far too high for RANS CFD on a normal PC A low-fidelity model is desired that can run in a couple of minutes on a simple PC. This would enable analysis and automated optimization within a reasonable time frame to aid in conceptual design. Previous methods for wings with flap deflections have used 2D data to “tune” inviscid methods such as lifting line, VLM, or the Weissinger method. No 2D tool that considers the effect of propeller installation exists yet and 2D data may be a good starting point for better understanding the issue at hand.

2) As with all models, the approach to be developed will of course have its limitations in applicability and accuracy. The consequences of simplifying assumptions should become clear, one major one being that 2D flow is considered rather than 3D, which is even more troubling with flaps and propellers than for regular wings. On an implementation level, the goal is to have similar accuracy and utility as a more proven method (in this case the unmodified version of MSES).

3) This analysis may already prove the model worth-wile: it may lead to new insights in flap design tailored specifically for high lift in combination with a propeller (“power-on” conditions.) This method may be a useful addition to analytical, empirical, and CFD tools. This model will only answer the question of maximum lift in 2D under a number of assumptions, whereas practical configurations also exhibit strong 3-dimensional effects. Besides, real-world applications will also have requirements on excess thrust to enable reasonable climb and approach angles.

The main research objective of this thesis is:

> "To evaluate the lifting performance of a multi-element airfoil in a 2D slipstream by means of a low-fidelity method."

Elaboration on the research objective

The airfoil performance indicator of interest in this thesis is lift coefficient (C_l). It can be expected that moment coefficients may also be predicted by a reasonable extent: Moment coefficients are mainly driven by lift, as drag forces are relatively small and have a smaller arm. Thus, provided that the chordwise lift/pressure distribution is accurate, the moment coefficients can be determined with reasonable accuracy. For an integral expression, refer to Anderson.[22] Drag prediction and thrust bookkeeping are notoriously difficult and considered beyond the scope of this research, although the aim is to include viscous effects.

The low-fidelity method may fall in the same category as the methods mentioned in section 3.3.1. A desirable property in terms of computation time is that the simulation should be completed in the order of a few minutes or less. There is a need for faster methods as CFD simulations take too long for elaborate design space exploration.: According to Duensing et al. CFD simulations can still take around 1 day on mainframe computers in the order of 1000 cores.[23]

1.2.2. Parameters of interest

The ongoing research projects in the field of DEP allow to define the appropriate range of parameters that the model should be able to handle. These will be used in this thesis, unless indicated otherwise.

Mach numbers A representative freestream Mach number for blown flaps may be determined from DEP experiments or existing transport aircraft. The SCEPTOR program targets a freestream velocity of $M = 0.083/55kts$ (on a small GA aicraft) whereas classical high-lift conditions for transport aircraft occur at far higher Mach. The NLR considered a Mach number of 0.185 for their experiments on the NLR7301 airfoil, which will be used as a reference flap design. MSES does not accept viscous cases with separation below $M = 0.10$, where MSIS should be used instead.[24] However, the subcritical formulation of MSIS may not be appropriate as transonic effects are not ruled out in the slipstream: A maximum Mach number of around $M = 0.80$ is reached for the high-lift cases considered in section 9.2, so critical conditions during the solution process are not unthinkable. On the other hand, compressibility should not influence the solution very significantly, the slipstream reaches $M = 0.25$, which should increase the lift by no more than 3.3% according to the PG correction. All things considered, the case of $M = 0.15$, or 100 kts, is deemed an appropriate test case.

Dynamic pressure increase According to Borer et al. [25], dynamic pressure ratios in the order of 2-4 are desirable for distributed propulsion concepts. This led to Patterson [26][27] and Nederlof [28] focussing on ratios up to V_s/V_∞ =2.0. This will be the maximum for the uniform flow cases in this thesis. The wake surveyed in the DEP experiments of Drela et al. peaked at a velocity ratio of about 3.2, with the flap included.[3]

Relative sizing A propeller diameter of $D/c = 1.0$ is selected, as is appropriate for DEP applications. Horizontal offset, however, is a trade-off that is dealt with differently in various designs. Folding propellers are sometimes desired, leading to the lower bound of one radius ahead ($x_p/D = -0.5$) as assumed in the SCEPTOR project, described by Patterson [27]. Other investigations, such as the BNF project, which has a relatively (much) larger propeller, opts for an offset of about $x_p/D = -1.0$, as can be seen in the setup in the report of Radespiel et al. [16]. For the current investigation a close position is desirable from the point of view of convergence. However, a larger horizontal offset would be would be more representative for a fully contracted propeller slipstream. Therefore, an offset of $x_p/c = x_p/D = -1.0$ is selected, apart from the free-contraction cases and the parameter study, the latter requiring a more rigid constraint at $x_p/D = -0.5$. The reference chord for all simulations in this report is 1.0.

Propeller positioning: Two propeller positioning frames are used in this report: one frame for the low lift cases (Part II) and high lift cases (Part III). The low lift frame is shown in fig. 1.6. The airfoil rotates without moving the actuator disk/slipstream: this is consistent with the comparison and validation material. On the other hand, the high-lift frame is centered around the airfoil as shown in fig. 1.7 as used by MSES. This is basically a simplified version of the propeller positioning used in ESDU88031 [29] with the propeller shaft aligned with the airfoil. This is also deemed more convenient for airfoil design. Within MSES, it is customary to rotate the entire outer domain around the airfoil. The coordinate Z will be used for vertical positioning throughout this thesis. MSES uses the notation of Y in the context of the outer domain boundaries but returns the coordinates in an airfoil centered frame. The Z and Y axis may be aligned if $\alpha = 0$. The y axis is usually reserved for denoting a span-wise coordinate on wing system coordinates and will be avoided if possible. AD incidence angle is not indicated. A slightly negative propeller incidence angle is common to align the slipstream more with the local flowfield/upwash. Although incidence angle is not implemented in this thesis the impact will be relatively small as the velocity increase is added in the direction of the streamlines. The methodology chapter also briefly addresses this topic.

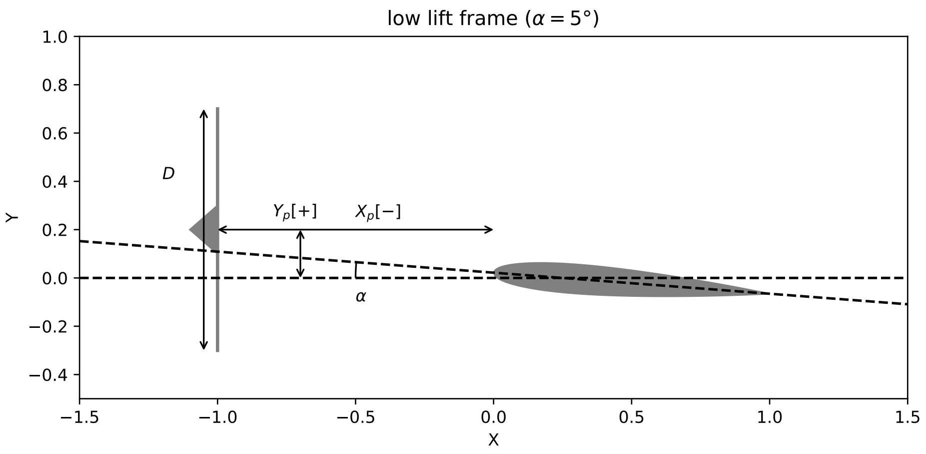

Figure 1.6: Freestream centered positioning frame.

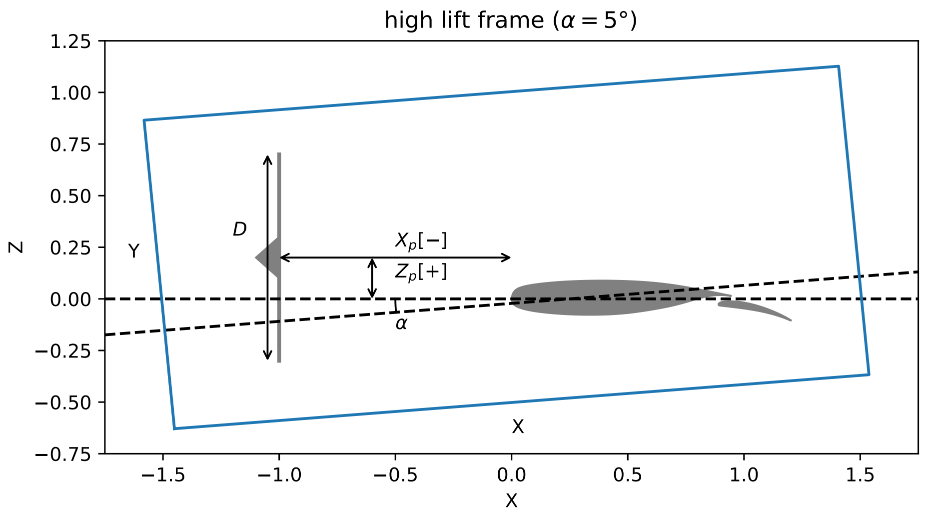

Figure 1.7: Airfoil centered positioning frame with the freestream centered frame indicated in blue.

2

Flow phenomena in flaps

This chapter deals with the main flow phenomena associated with flaps. One may also refer to the literature study which also discusses propeller effects. [4]

2.1. 2D phenomena

The 5 main effects associated with using multiple airfoil sections in conjunction (i.e. flaps) are originally outlined by Smith [30]. These are 2D effects and are important to interpret the results of this thesis.

The five main effects are [30], as rephrased by Veldhuis[31]:

1. "**Slat effect.** The circulation on a forward element (e.g. a slat) induces velocities on the downstream element which reduce negative pressure peaks (high velocities) on its nose."
2. "**Circulation effect.** In turn, the circulation on the downstream element induces velocities on the upstream element which increase its circulation. The effect is similar to deflecting a small plain flap; higher velocities on the upper surface - in particular near the trailing edge - and lower velocities on the lower surface."
3. "**Dumping effect.** The increased velocity at the trailing edge of the forward element relieves the upper surface pressure recovery impressed on the boundary layer, so alleviating separation problems."
4. "**Off-the-surface Pressure Recovery.** The boundary layer from forward elements is dumped at velocities appreciably higher than free stream. The final deceleration to free stream velocity is done in an efficient way; without this effect the boundary layer would be unable to overcome the entire pressure rise. The deceleration of the wakes occur out of contact with a wall; this is usually more effective than the best possible deceleration in contact with a wall."
5. "**Fresh-Boundary-Layer Effect.** Each new element starts out with a fresh boundary layer at its leading edge. Thin boundary layers can withstand stronger adverse pressure gradients than thick ones. Hence, breaking up a boundary layer into several thinner boundary layers is favorable to the delay of separation."

These phenomena pose requirements on the computational codes/models. I.e. the best results are obtained if the code considers multiple elements (thus with gaps). Effects number 4 and 5 are viscous phenomena which need to be sufficiently modeled to prevent an over-estimation of lift. Viscous boundary layer growth can lead to **de-cambering** as shown in fig. 2.1 or even earlier separation. A de-cambered airfoil produces lower lift and can be considered as having a lower effective flap deflection.

Poorly designed slotted flap systems will be limited in lift by **wake confluence**. For sufficiently large gap sizes, the wake of the preceding element and the boundary layer of the next one are separated by a potential flow layer, i.e., they are not merged. Wake confluence occurs when they do merge and become one, thicker boundary layer, as explained by Smith [30]. As noted by Drela [32] confluence also reduces the resistance of a wake to adverse pressures: over-estimation of lift of the example airfoil system in Drela's paper is attributed to absence of confluence effects in the calculation.

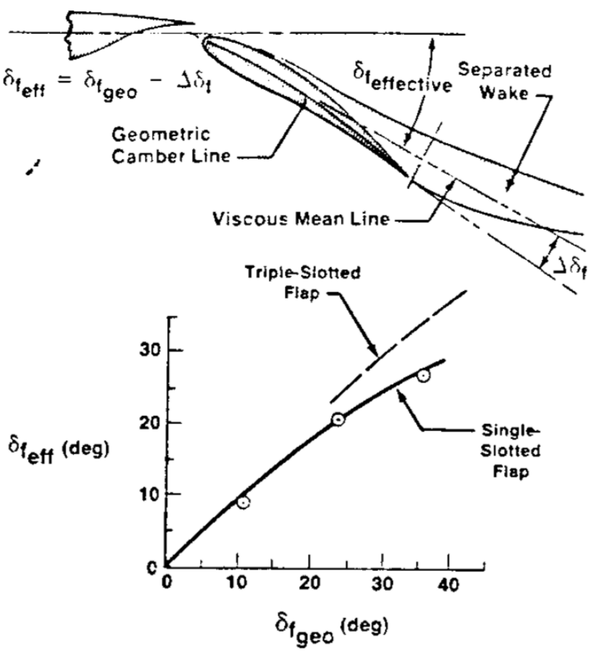

Figure 2.1: Effectively lowered camber of a flapped airfoil, and effective deflection angles. (Murillo & McMasters [33])

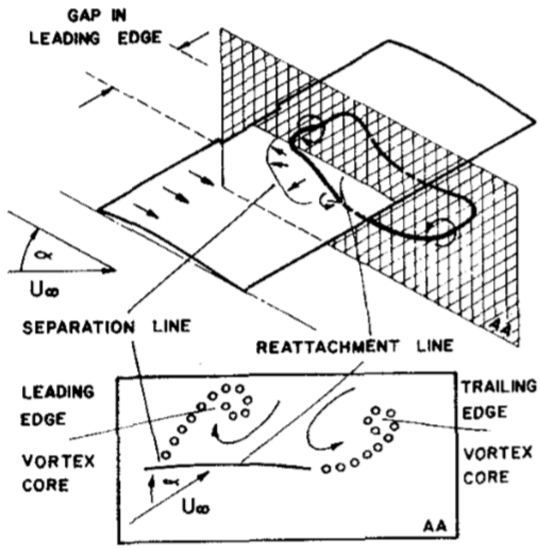

Figure 2.2: Vortex model of separation (a single cell) (Katz & Plotkin [34])

2.2. 3D phenomena

Cross-flow/discontinuities Important 3-Dimensional flow characteristics with an impact on lifting performance arise from discontinuities in propeller blowing, span-wise loading, sweep, cutouts, flap ends, and interference with other bodies such as the fuselage or nacelles. Swift changes in span-wise lift distribution due to the finite extent of flaps may lead to effectively lower lift-curve slope on the flap; the trailing vortices of the flap ends incur a downwash, lowering their efficacy. The same holds for cut-outs or flaps not properly sealed against a rearward extending nacelle, which would else partly carry-over the lift (see ESDU88031e [29]). Engine nacelles or other bodies could also incur separation. Sweep also lowers flap efficacy. The scope of this research is limited mainly to 2D and sectional characteristics. Limitations concerning the loss of lift due to finite width of the slipstream are addressed in chapter 3.

Separation rings An interesting phenomenon occurring on flapped wings under separation is the formation of separation rings as described by Katz and Plotkin [35]: along the span the separation actually takes place in pockets, the number of which scales quite nicely with aspect ratio, 1, 2 and 3 cells for aspect ratio's of 3, 6 and 9, respectively, and 5 narrower cells for an aspect ratio 12 wing. What is remarkable is that these pockets exist in a fairly predictable fashion on large-aspect ratio wings, the pockets have an aspect ratio of approximately 1:5. These can be modeled using an unsteady VLM formulation in conjunction with the usual, 2D modeling of separation using Karman sheet vortex shedding, as demonstrated in the 1980's by Katz[34]. An example of the model is shown in fig. 2.2. Other models may also work.

2.3. Boundary layer & wake growth

As boundary layer and wake growth can lead to viscous de-cambering and separation, its development and the impact on lift should be established. Several measures and the phenomenom of wake bursting are discussed in this section.

2.3.1. Key measures

The displacement thickness δ^* is the equivalent displacement of streamlines directly outside the boundary layer to compensate for the loss in mass flow. This is defined by eq. (2.1a) as written by Anderson [22]. This can also be seen as the shape of an equivalent body seen by the streamlines far away. This is actually how the inviscid calculation of MSES works as explained by Drela [32].

The momentum thickness is the equivalent displacement to compensate for the momentum that is missing in the boundary layer, at the same conditions as the external stream as also explained by Anderson [22]. The equation is shown in eq. (2.1b). Integrating this value will yield the skin friction drag from the leading edge up to that station.

$$\delta^* \equiv \int_0^{y_1} \left(1 - \frac{\rho u}{\rho_e u_e}\right) dy \quad \delta \leq y_1 \to \infty \tag{2.1a}$$

$$\theta = \int_0^{y} \frac{\rho u}{\rho_e u_e} \left(1 - \frac{u}{u_e}\right) dy \tag{2.1b}$$

The shape factor is another metric that is used to describe the velocity profile of the boundary layer as defined in eq. (2.2a) where θ is the momentum (loss) thickness, if written as $\bar{H}$ it is time-averaged. The shape factor can give clues about the development and resilience of the boundary layer to overcome adverse pressures and separation. However, the comparisons do not allow for exact conclusions as the turbulence levels, flow conditions, and other measurements of the boundary layers vary. Though in general, lower shape factors are better when it comes to the onset of separation downstream. Turbulent separation is likely with a H above 2.2 to 2.4 as noted by Veldhuis [31]. $H = 4$ is indicative of separation as noted by Katz and Plotkin [35], though this largely agrees with the MSES data, the negative C_f criterion is deemed more reliable as an indication of separation, and was sometimes reached one point sooner than $H = 4.0$.

The growth of the momentum thickness may provide some insight into the development of the boundary layer. The integral momentum equation (see also section 4.3) is not very insightful as the pressure gradient term is lost in the derivation of this formula, as it is cast into the displacement and momentum thickness. However, the dependence on the velocity gradient is present. With the simple definition of H, one could rearrange it to eq. (2.2b) which shows that in the growth of the momentum thickness there are two terms. The first one is due to the skin friction coefficient, and the second due to both the values of the BL displacement and momentum thickness, which depend on the history of the boundary layer but also on the gradient of the external velocity. This may be interesting when considering the impact of a near-by slipstream as this changes the circulatory effects and hence $du_e/d\xi$ but also the history of the other values. The the BL displacement growth can also be determined through the local H value.

$$H = \frac{\delta^*}{\theta} \tag{2.2a}$$

$$\frac{d\theta}{d\xi} = \frac{C_f}{2} - \frac{2\theta + \delta^*}{u_e} \frac{du_e}{d\xi} \tag{2.2b}$$

Canonical pressure distributions: As the pressure recovery plays a crucial role in determining boundary layer growth and separation, it is important to be able to compare pressure distributions between elements, and, in the case of this thesis, also between blowing conditions. Smith [30] elaborately describes how the so-called canonical pressure distribution $\bar{C}_p$ may be used towards this purpose, making two flows identical by proper scaling in the x and C_p directions, apart from Reynolds number effects. Note that Reynolds numbers are not changed between blowing conditions in this thesis. The canonical pressure is defined in eq. (2.3), it can be expressed using the ratio between local speed at the BL edge U_e, and the maximum speed before de-deceleration U_0. Note that $\bar{C}_p$ always lies between 0 and 1.

$$\bar{C}_p = 1 - \left(\frac{U_e}{U_0}\right)^2 \tag{2.3}$$

The velocity U_e (scaled with U_∞) is available in MSES, and U_0 can simply be determined from the maximum on the main surface.

2.3.2. Wake burst

Off-the-surface pressure recovery has its limits. Smith [30] showed using Bernoulli that a velocity deficit should always worsen when an adverse pressure is encountered. This is, however, opposed by the effect of viscosity.

This may lead to the phenomenon of "wake bursting", in which the wake of a preceding element "bursts" leading to a loss of lift. As summarized by Pomeroy et al. [36], a wake burst has the following properties:

- Rapid wake thickening and flow deceleration with, potentially, flow reversal
- Increased turbulence, higher drag and lower maximum lift
- Effective de-cambering of the airfoil system

The phenomenon is illustrated by fig. 2.3. Note thow the main element wake burst on the right figure.

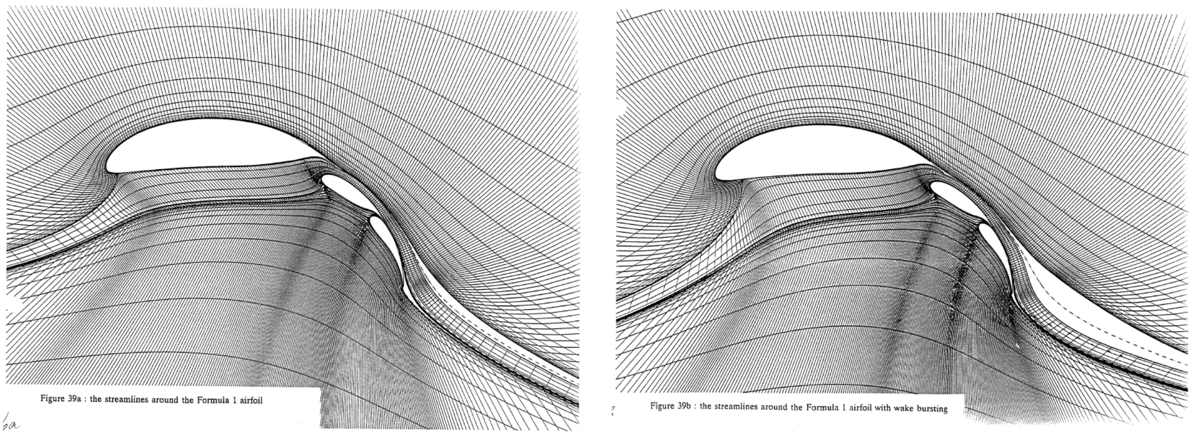

Figure 2.3: "The streamlines around a Formula One Racing Car airfoil (a). In (b) the main element wake bursts"(Veldhuis [31])

2.3.3. Detecting wake burst

Gartshore [37] derived an approximate relation to tell whether a wake grows or decays. The criterion is shown in eq. (2.4): if the left hand side exceeds the right hand side, the wake grows, this could be an indication of an imminent wake-burst. It is required that boundary layers and wakes are not merged. MPLOT is modified to also output the wake coordinates in the BL dump file. Conveniently, as shown by Smith [30], one may use either C_p or $\bar{C}_p$ in eq. (2.4).

$$\frac{1}{1-C_p}\cdot\frac{dC_p}{dx}=\frac{1}{1-\bar{C}_p}\cdot\frac{d\bar{C}_p}{dx}>\frac{0.007}{\delta^*} \tag{2.4}$$

It can be proven mathematically that the LHS is actually a scaling of the velocity dependent term in the momentum growth equation eq. (2.2b):

$$\frac{1}{1-\bar{C}_p}=\frac{1}{1-\left(1-\left(\frac{u_e}{u_0}\right)^2\right)}=\left(\frac{u_0}{u_e}\right)^2 \tag{2.5a}$$

$$\frac{\bar{C}_p}{dx}=-\frac{1}{u_0^2}\frac{d(u_e^2)}{dx}=-\frac{2u_e}{u_0^2}\frac{du_e}{dx} \tag{2.5b}$$

Hence:

$$\frac{1}{1-\bar{C}_p}\cdot\frac{d\bar{C}_p}{dx}=-\frac{2}{u_e}\frac{du_e}{dx} \tag{2.6}$$

Which, considering that x is usually roughly equivalent to ξ, is thus a scaling of the last term in eq. (2.2b). Hence, the left term of the criterion (eq. (2.4)) purely considers the adversity of the pressure, and the right hand side accounts for the time history by means of the displacement thickness, and a constant. Note that the validity may depend on the type of boundary layer profile. Van Craenenbroeck [18] considered the Gartshore Criterion for the flapped NLR7301 to be considered in this thesis. His conclusion was that the Gartshore may be used to indicate the presence of wake growth, but not the severity of it.

Driver and Mateer: Van Craenenbroeck [18] concluded that the onset of wake burst could reliably be determined for the NLR7301 by considering the gradient of the displacement thickness. The range was established by Craenenbroeck by looking at experiments from Driver and Mateer [38] who looked at wake flows in adverse pressures by means of considering a diverging wind tunnel. The results in terms of displacement thickness development are shown in fig. 2.4. Van Craenenbroeck established the range by considering the slope for "Small" and "Massive" flow reversal. This range is indicated by eq. (2.7).

$$0.23 < \frac{d\delta^*}{d\xi} < 0.44 \tag{2.7}$$

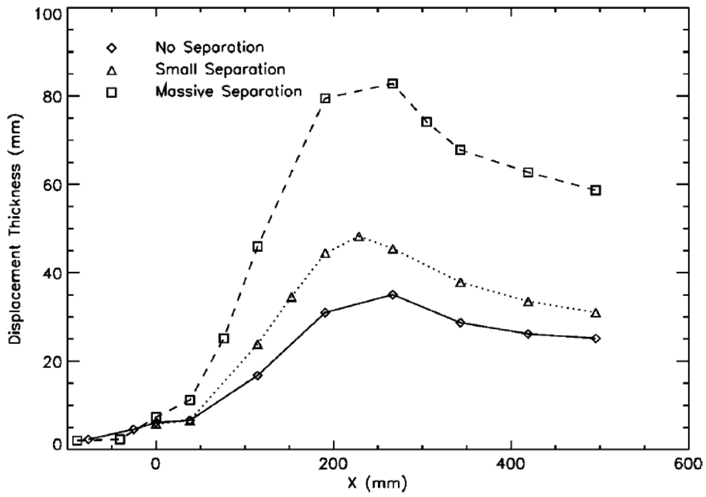

Figure 2.4: "Displacement thickness distribution"(Driver and Mateer [38])

3

Slipstream interaction & modeling

This chapter focuses on the modeling of flapped wings and effects of propeller installation but not propellers in isolation. Some subjects are discussed more elaborately in the literature study [4].

3.1. Introduction to some mutual interference effects

This section refers to flow phenomena that occur due to the installation of a propeller and the associated 3-dimensional variation in flow properties.

A body directly behind the propeller (in this case, the nacelle) slows down the flow at the propeller disk, which, in turn, rotates at a lower advance ratio (J). For somewhat round nacelles (not grossly non-axisymmetric), the interference effects can generally be regarded as symmetric as per ESDU85015 [39], the lack of pylons also limits complexity.

Interference from the wing on the propeller is not symmetric. This causes periodic interference, leading to different angles of attack for the blades at different times. Three major sources are identified: Firstly: “the helicoidal wakes from each blade passing across the wing will cause periodic perturbations in the induced loss” (this effect doesn’t directly seem interesting for the lifting capability, which is the prime interest of this thesis.) Secondly, the wing has a blockage effect similar to the nacelle, slightly decreasing the axial velocity through the propeller. Thirdly, the upwash of the wing, which is also not constant across the disc, will introduce a normal force (i.e. lift!) and moment on the propeller. The wing upwash is strongest during high-lift conditions, especially landing, and the propeller is more sensitive to inflow perturbations at low thrust setting than at high thrust setting. These effects are of key interest for STOL applications.

Interference from the propeller on the wing can be divided into roughly two main effects: the axial slipstream component and the tangential component (swirl). The axial slipstream increases the velocity, and, closely behind the tractor propeller, increases the static pressure. Behind the propeller, the static pressure is increased beyond the freestream static pressure, which returns to freestream values as the velocity increases further down the slipstream. These axial effects increase the lift and drag. The second main effect of swirl, causes the wing-section behind the up-going blade to experience higher local α, and that behind the down-going blade lower α. Again, the amount of swirl is greater at low speeds at takeoff [39] (or STOL for that matter). Veldhuis [40] found that a Swirl Recovery Factor (SRF) has to be applied or else the influence of propeller swirl is grossly overestimated, he determined that a factor of 0.5 is approximately correct. The SRF depends on geometry of the propeller, wing, and their relative position. Again, the amount of swirl is greater at low speeds at takeoff [39] (or STOL for that matter). Other interference effects due to intakes/exhausts or other bodies are beyond the scope of this research. The fuselage is not listed separately by ESDU.[39]

Turbulence and transition behind propellers Turbulence behind propellers is a complicated, 3-dimensional phenomenon that depends on flow conditions, propeller/wing design, and operating conditions. The passing wakes of blades and their tip vortices introduce unsteady effects and can thus alter transition as investigated by Catalano [41]. His findings were that the turbulence introduced by propellers promotes early transition, and that a higher propeller blade count increases turbulence intensity. Catalano conducted wind tunnel experiments into this subject at a Reynolds number of 350,000. With this configuration, the transition location shift due to adding a tractor propeller is very clear as illustrated by fig. 3.1. As the Reynolds number is much lower than expected for full-scale propeller aircraft natural transition can be expected much closer to the nose, leading to a much smaller shift when adding a propeller. It is worth noting that most projects focus on drag whereas this project focuses on mainly on lift increase. Alba [42] (somewhat arbitrarily) suggested to expedite transition by using $n_{crit} = 3$ in the e^n transition model.

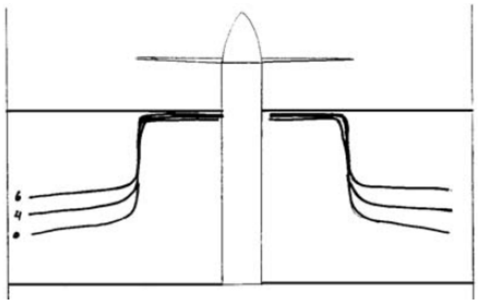

Figure 3.1: "Location of the transition front determined by flow visualization" (Catalano [41])

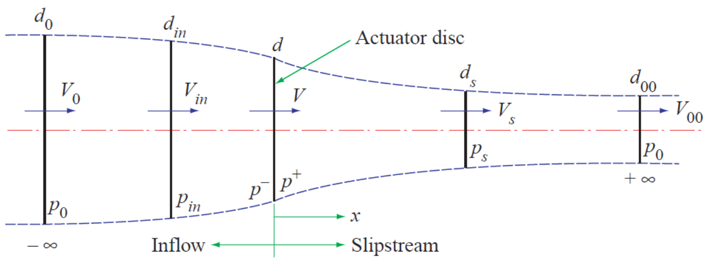

Figure 3.2: Wake contraction (ESDU85015b [39])

Wake contraction Due to obtaining a velocity increase, the streamtube containing the propeller will contract to satisfy the continuity equation. This is illustrated by fig. 3.2. It would be interesting to compare the observed contraction to that of existing models. ESDU85015b [39] presents an analytical model that was first derived by Smelt & Davies [43]. Note that we are assuming incompressible, inviscid, irrotational flow. a is defined as the ratio of velocity increase at the disk [39], generally referred to as the axial induction factor (Burton [44]). The total velocity increase is $V_\infty * 2a$. Thus, for $V_s/V_\infty = 2.0$, $a = 0.5$. s is defined as the velocity increase anywhere in the streamtube containing the AD. Thus, the maximum value of s is $2a$. The following set of equations 3.1 describe the slipstream diameter variation behind a uniform AD.

$$\frac{V_s}{V_0} = 1 + s \quad (3.1a) \qquad s = a\left[1 + \frac{x}{(x^2 + d^2/4)^{1/2}}\right] \quad (3.1b) \qquad \frac{d_s}{d} = \left[\frac{1+a}{1+s}\right]^{1/2} \quad (3.1c)$$

This model is derived for 3D, but more contraction is needed for continuity in 2D than in 3D, as we are comparing the height of the slipstream to the diameter of a disk. For continuity in 3D, the *area* should be inversely proportional to the change in velocity. Hence, for continuity in 2D, the *height* should be inversely proportional to the change in velocity. Hence, for a velocity ratio of 2.0, the inlet diameter (or height) is 1.5, at the disk 1.0, and fully contracted it is 0.75. However, for 3D, the *area* should equal the aforementioned numbers. Hence, the variation in diameter is smaller, resulting in a diameter of 1.22, 1.0, and 0.866, respectively.

A 2D derivation is required. Jameson derived equations for rectangular jets.[45] One may argue that the 2D case is equivalent to an infinitely wide rectangular jet, where virtually all contraction must be due to a decrease in height.[45] This reduces equation $A6$ from Jameson [45] to that seen in eq. (3.2) with $\mu = v_\infty/v_j$. Note that we are still assuming incompressible, inviscid, irrotational flow.

$$\frac{h(x)}{D} = \frac{1}{1 + \frac{1-\mu}{1+\mu}\frac{2}{\pi}tan^{-1}\left(\frac{2x}{D}\right)} \tag{3.2}$$

According to Jameson [45], the velocity is nearly uniform throughout the slipstream. Hence, one may also analytically derive the expected velocity development of the slipstream. From continuity ($hV = constant$), and the fact that half the velocity increase should obtained at the AD, one can derive eq. (3.3):

$$V(x) = V_p\frac{D}{h(x)} = \frac{V_\infty(1+a)}{\frac{h(x)}{D}} \tag{3.3}$$

3.2. Semi-empirical theories

The designation semi-empirical means that physical phenomena are partly captured analytically and corrected using experimental (empirical) data or surrogate models. These methods may have limited accuracy or applicability, but may provide useful for providing insight or providing a quick evaluation. The current work may be especially useful to quickly establish the β value used by Patterson [26] including the effects of introducing a non-uniform slipstream and high-lift devices in 2D.

3.2.1. Early observations & methods

Linearized theory An early theory by Smelt & Davies [43] provides some insight into the effect of propeller dimension. This method is based on considering the dynamic pressure increase behind the propeller between two limiting cases: a narrow slipstream with constant circulation along the wing, and a wide slipstream with negligible induced effects. As a result, the lift can simply be approximated by the following equation 3.4 as reformulated by McCormick [14]:

$$\Delta C_L = C_l \frac{D_1 c}{S} \frac{w_1}{V} \lambda \tag{3.4}$$

Where w_1 is the induced velocity at the wing, w_1/V^2 is assumed negligible, corresponding to low propeller loading. λ is determined empirically as a function of the AR of the wing section behind the slipstream, see fig. 3.3.

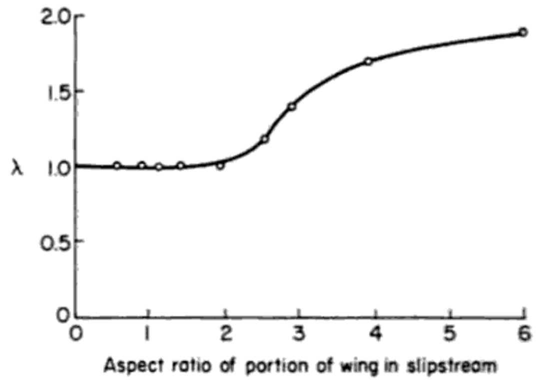

Figure 3.3: "Smelt and Davies lift factor" (McCormick [14])

Jet flap and deflected momentum McCormick [14] clearly summarizes important effects of a flapped wing in the slipstream of a propeller. The main contributions considered are the clean wing, the jet-flap effect, and the deflected momentum. These 3 contributions are visible in the simplified equation 3.5[14]:

$$C_L = C_{L_{T=0}} + C_{L_\Gamma} + C_\mu \frac{sin\alpha_p}{sin\alpha_s} sin(\alpha_s + \theta) \tag{3.5}$$

The first term, $C_{L_{T=0}}$, is the unaltered lift of the wing at 0 thrust. It should be noted here that this lift term could change under influence of the propeller: as the blowing may provide some form of BLC.

The second term, C_{L_Γ}, is the **jet-flap effect.** It may easily be overlooked, but is an especially important effect for relatively small propellers which enable highly effective flap deflections. As the high momentum wake is deflected upwards by the free-stream, the force it exerts on the surrounding air can be modeled as a vortex behind the airfoil, equivalent to a virtual flap. This effect was studied extensively by Spence et al. [46][47]. Using Spence's developments [46], omitting jet reaction force and α for $C_\mu = 0$, McCormick arrives at formula's 3.6 through 3.8.[14] When using eq. (3.6), δ should be replaced with the effective deflection angle θ in case of propellers rather than using the larger deflection δ associated with pure jet-flaps. Limited AR should be compensated for to arrive at C_{L_Γ}.

$$C_{l_\Gamma} = C_{l_\alpha}\alpha + C_{l_\delta}\delta \tag{3.6}$$

$$C_{l_\alpha} = 1.152\sqrt{C_\mu} + 0.106 C_\mu + 0.051 C_\mu^{3/2} \tag{3.7}$$

$$C_{l_\delta} = 3.54\sqrt{C_\mu} - 0.675 C_\mu + 0.156 C_\mu^{3/2} \tag{3.8}$$

Where the blowing coefficient may be described by eq. (3.9a) & eq. (3.9b), which are equivalent:

$$C_\mu = \frac{NT}{qS} \tag{3.9a}$$

$$C_\mu = \frac{m_j v_j}{qS} \tag{3.9b}$$

Within the MIT project, Courtin et al. [48] used this original formulation for the attached cases. The question of how the jet-height relates to the effectiveness of this flap type is perhaps more clearly addressed in the wind-tunnel test report by Drela et al.[3] The resulting lift coefficient depends once again on the contribution of the bound vorticity and the lift due to turning the wake momentum excess.

The third term in eq. (3.5), $C_\mu \frac{sin\alpha_p}{sin\alpha_s} sin(\alpha_s+\theta)$, represents the **deflected slipstream momentum**. Note that with $v_j = 2w$, this term is identical to $mV_R sin(\alpha_s+\theta)$. Again this is approach is simplified: One should also account for the vertical component of the drag of the blown wing (included in McCormick [14]), also, normal force on the propeller under α is neglected here. The deflection angle can be determined using the flap turning effectiveness θ/δ. This depends on the relative flap chord c_f/D. This may be determined from the work of Kuhn [7] and is also included in ESDU88031 [29], described later. Kuhn also plotted maximum deflection: advanced double slotted flaps with large chords may reach a θ of around 75°. Note that these are flaps from the 1950's, leaving room for improvement.

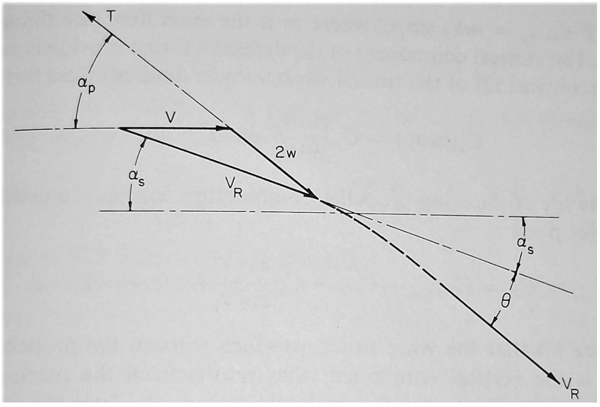

Figure 3.4: Slipstream deflection velocity diagram. (McCormick [14])

Finally, it should be noted that these 3 contributions may not always be physically discernible, and care should be taken not to take double contributions. For instance, both the slipstream momentum and jet flap may be incorporated in a vortex sheet representation. The ESDU method does not use a jet-flap contribution, and in this sense, certain representations may be more applicable to one experiment than to another.

3.2.2. Contemporary engineering methods

Roskam Roskam briefly discusses the effect of increased dynamic pressure behind propellers [49], the increase in wing lift due to propeller slipstream may be estimated from equation 3.10. The equation should be used with FPS units, adding this contribution for each propeller. Note that this is a very simplified approach; for a more detailed consideration, Roskam refers to the DATCOM guideline from the 1970's.

$$\Delta C_{L_W} = \frac{S_p}{S} C_{L_W} \frac{2200 P_a}{q V \pi D_p^2} \tag{3.10}$$

Taking into account that power and thrust can be written in terms of induced velocity, one will find that eq. (3.10) is equivalent to the linearized theory described by eq. (3.4); they both reduce to factors of the ratio of induced velocity to airspeed.

ESDU method The ESDU guideline 88031 [29] offers a semi-empirical procedure to estimate the lift and longitudinal forces on propeller/nacelle/wing/flap systems, provided with an online software package. The method is based on experimental data and methods from NACA/NASA from 1954 to 1968, and some unpublished wind-tunnel data from companies. Regularly appearing authors are R.E. Kuhn, K.P. Spreemann, Fink, Mitchell and White. The method is built on the application of simple momentum theory, with an extensive amount of corrections determined by experiments, for a wide range of flaps. It is in essence an improved version of the method of Kuhn [7]. Two circular streamtubes are defined: one around the wing, and a cutout for all flow passing through the propeller. The main corrections to account for viscosity are the slipstream deflection angle θ and slipstream viscous loss parameter k_s, determining these values is at the heart of this method. This method accounts for planform characteristics, flap dimensions and type, propeller dimensions and both propeller shaft tilting and translation. There are also corrections for flap cut-outs (limited amount of data), nacelle size (large lack of data), and even propeller overlap (again only limited cases).

The method is meant for wings with straight taper, constant thickness, and no twist, however, "in practice, the effects of such asymmetries along the slipstream width are insignificant" [29] and the method will work for low amounts of sweep. It is meant for landing or takeoff flap settings with fully attached flow, and does not account for ground effects. The three main restrictions are: constant flaps along the slipstream, circular nacelles no larger than the spinner, and non-overlapping propellers. Ranges for the covered geometric values are listed in table 3.1.[29] What is striking about table 3.1, is the maximum total flap deflection δ of 80°, provided that the flow is fully attached, of course. The moment coefficients and subdivision in forces between flap elements are not computed. Due to the nature of the experiments, the method may be less suitable for modern propellers with a large amount of swept blades (such as on the Airbus A400m). However, the number of blades on current DEP concepts is limited, and size and loading may fall in the appropriate range. As the flap designs were hardly optimized, the better boundary of the experimental data is taken as reference. Remarkably, the Reynolds number had no significant impact, as long as the flow was attached, in the range of 0.5e6 to 3e6 in the slipstream.

In general, if all requirements are met (i.e. attached flow), the program is accurate to within 10% for the lift, and 15% for the longitudinal force. Overall, this method may very well be fast and accurate enough to quickly validate parts of other methods, or provide a starting point for iterative schemes.

Table 3.1: Applicability of the ESDU method [29]

A	λ	b/D	c/D	c_{teff}/D
4 to 12	0.3 to 1	2.5 to 11	0.5 to 1.5	0.05 to 0.5
δ	N	i_w	x_p/D	z_p/D
0 to 80°	2, 4	0 to ±5°	0.2 to 0.7	0 to ±0.3

Patterson For DEP applications Patterson and German [26] developed a quasi-2D method based on vector addition of the free-stream and propeller velocities (see fig. 3.5). This may be used to compute the lift increase for a blown section with regards to propeller inclination and local twist/angle of attack using eq. (3.11). The method also compensates for the limited slipstream height by means of the induced velocity multiplier β, which is further elaborated upon in eq. (6.1). Finally, the lift may be obtained by adding the contributions of blown sections by weighing against their respective span as in eq. (3.12a). This method is limited by not considering local chord, nor propeller swirl or other 3D effects such as the span-wise lift variation.

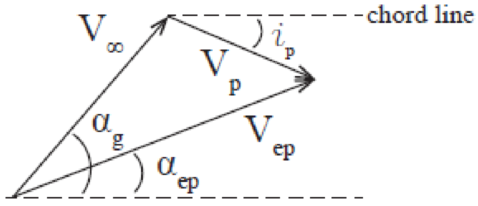

Figure 3.5: Velocity triangle used by Patterson and German [26]

$$\frac{\Delta L'}{L'_\infty} = \left(1 - \frac{\beta V_p \sin i_p}{V_\infty \sin \alpha_g}\right) \frac{\sqrt{V_\infty^2 + 2V_\infty \beta V_p \cos(\alpha_g + i_p) + (\beta V_p)^2}}{V_\infty} - 1 \tag{3.11}$$

Both Drela et al.[3] and Patterson and German[26] argue that the effective height of the slipstream may be approximated by using the conservation of mass to describe the disk as an equivalent rectangle. This equation is shown in eq. (3.12b). Patterson suggests the full height be taken to mitigate the negative effects of other assumptions. This theory is however not proven and may be too crude: Propellers with overlap may more closely approximate this assumption. Pattersons method appears to work reasonably well, but underpredicts the lift in cases with large flap deflections.

$$\frac{\Delta C_L}{C_{L_\infty}} = \sum_{i=1}^{N} \left(\frac{\Delta L'}{L'_\infty}\right)_i \left(\frac{b_{blown}}{b}\right)_i \tag{3.12a}$$

$$\frac{h_d}{c} = \frac{\pi(R^2 - r_h^2) n_p}{bc} \tag{3.12b}$$

Patterson and German [26] draw some interesting conclusions on flaps as high lift devices:

- Installing propellers inclined upwards (nose up) yields more airfoil drag as the lift vector is tilted backwards due to decreasing effective α. This is a dangerous installation concerning engine failure: although the lift loss is limited, the effective α increase can cause the wing section to stall.

- The propeller inclination aligned with the freestream poses no risk or benefit in these areas: the effective airfoil α and circulation remain virtually constant.

- Installing propellers inclined downwards (nose down) will yield more lift but a large loss of lift upon engine failure, due to the combined effect of losing blowing and a decrease in effective α. The airfoil starts producing thrust as the lift vector is tilted forward.

Jameson Jameson [45] developed analytical models for elliptical and rectangular slipstreams. An exact solution for use in the lifting line equations is available for an elliptical slipstream with the foci located at the wing tips, and some approximated solutions are available for rectangular slipstreams. This may later be compensated for by semi-empirical factors for flap turning effectiveness. Patterson found that Jameson's theory only worked well in some situations and was not applicable to only a single propeller: A large over-prediction was noted with a highly loaded propeller.

3.3. Numerical methods

This section explores numerical methods and results for simulating flapped wings and slipstreams.

3.3.1. 2D lower-fidelity methods

Airfoil and flap simulations Different viscous-inviscid interaction schemes exist for the simulation of airfoils, as explored in detail by Wiliams [50]. In terms of inviscid computation, there is the choice between using a streamline dicretized model or a panel method with vortices (or sources/doublets). Either way, the viscous boundary layer displacement can be modeled by a wall transpiration model or by an enlarged equivalent body. As the inviscid solution influences the boundary layer development, these need to be coupled. Large separated regions are difficult to resolve: inverse methods may overcome difficulties of ill-posed problems. Using inverse methods may not be required though: solving the viscous and inviscid problems simultaneously may lead to faster convergence, but if the displacement thickness is updated iteratively this may lead to convergence errors. In terms of solving the BL momentum equation there is choice between an integral formulation and a numerical approach. More advanced features such as normal pressure gradients and Reynolds normal stresses could be imposed, bringing the solution closer to Navier-Stokes (NS) solutions.

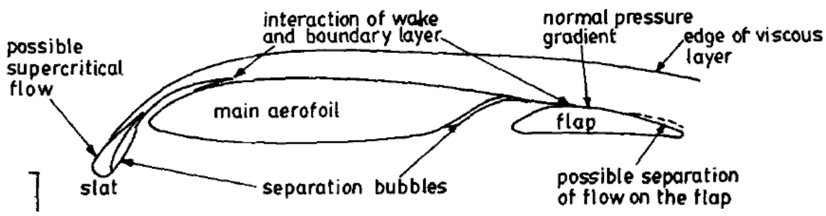

Figure 3.6: Flow attributes that may exist around a multi-element airfoil. (Wiliams [50])

For flaps it is also important that the wake thickness and curvature is modeled correctly, as a trailing element is influenced by the wake of preceding elements. Consider, for example, fig. 3.6. Despite the low flight Mach numbers, transonic conditions may be reached around the flap gap region under certain high lift conditions as noted by Obert [51], or on the nose region as shown in fig. 3.6. For single-element airfoils, popular programs are the Viscous Garabedian and Kom (VGK) code, and XFoil. JavaFoil is popular for inviscid computations: this would severely over-estimate lift due to the lack of a boundary layer model.

As summarized by van Dam [52], an example of an earlier, incompressible method is that of Le Balleur and Néron [53] called VIS18. This uses a panel method with an inverse method where flow is separated. This may be better and handling (deep) separation but the code is not available, nor is a full English translation of the paper. An example of the streamline-based software is the MSES code by Drela [32], this uses a coupled method with a multi-equation integral boundary layer model (see also chapter 4).

MSES is perhaps one of the most successful methods as endorsed by Van Dam.[52] It has seen wide-spread use for modeling high-lift airfoils without propellers with good results, see also section 4.1. Conveniently, the source code is available, and the streamline discretization is promising for adding a slipstream, including compressibility effects. Nowadays, this code takes only seconds to converge.

Modeling a slipstream with mirrored images Nederlof [28] dedicated part of his MSc. thesis to mirrored images, as developed by Ting.[54] In summary: a velocity discontinuity may be represented by adding an extra vortex to that representing the airfoil, on the opposite side of the velocity discontinuity. This is often applied to model either the presence of a wind-tunnel wall or ground effect, where the image is opposite in sign but has equal strength. Similarly, a free-jet wind tunnel can be represented with a mirror vortex of equal sign and equal strength. The boundary conditions are 0 velocity at the wall, and 0 pressure for the free jet case. One may refer to AG-336 section 2 for more information [55].

In case the outer domain still has some velocity, the strengths need to be weighed, as illustrated by Prabhu [56] in fig. 3.7. The airfoil flowfield is influenced by both vortices, whilst the outer domain only by that of the airfoil vortex. A similar system is set up extending on either side of the slipstream. The reflections themselves also require reflections, with an expanding pattern, but their influence decays with increasing distance.

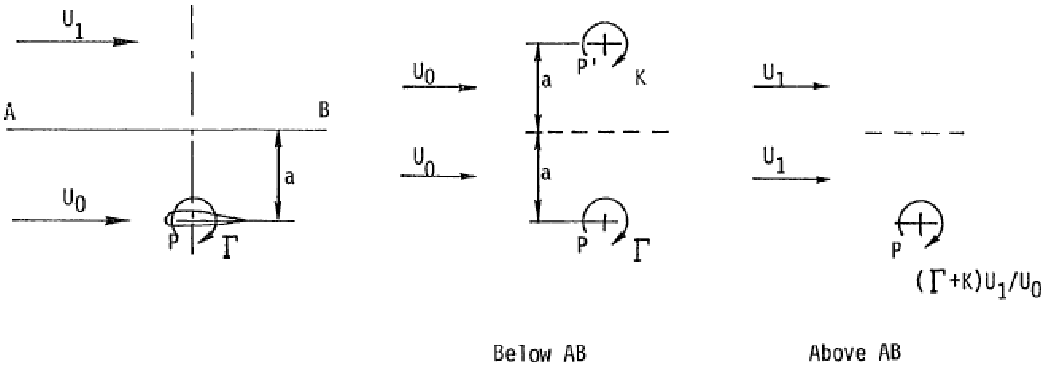

Figure 3.7: "Image system for an airfoil near a surface of velocity discontinuity" (Prabhu [56])

There are some limitations: The slipstream boundaries are modeled to be straight lines. This may be very unrepresentative for high-lift conditions: the images may be incorrectly positioned. Another drawback is that an off-center position of the airfoil will always lead to lower lift: this results is symmetric, caused by the larger downwash of either vortex if the airfoil moves closer. This is a different result than CFD simulations, by Nederlof [28] or Patterson [27], which indicate that there is potential for upper-surface blowing, where the airfoil would get extra lift augmentation. These effects will probably also yield highly inaccurate solutions for flaps, which may protrude through the domain boundaries.

3.3.2. 3D lower-fidelity methods

Generalized vortex-lattice method Yahyaoui [57] presents a generalized VLM for wings with flap and aileron deflections. It differs from early, classical VLM in the sense that vertical displacement is not neglected, and that the horseshoe vortices are split up into multiple trailing elements following both the camber line and the flaps, and also deflect back up some distance behind the flap (or aileron for that matter). The method can be adopted to include geometric features such as sweep and dihedral. For a clean wing, there was good agreement up to at least $\alpha = 12°$. Flap effectiveness measured with the derivative of $C_{L_{\delta_f}}$ was within 4% of semi-empirical methods. Some more validation may be necessary, and viscous effects are not covered. A (somewhat questionable) conclusion was that the lift was largely independent of the deflection of the wake upon leaving the trailing edge, whether it was aligned with the free stream or leaving the flap tangentially, with an error in the order of 1%. (the exact conditions and flap deflection are not reported, but it seems the flap spanned the entire wing.) Although this method seems promising, it does not seem very useful for directly computing the lifting capabilities of slotted flap systems or large deflections exceeding 30°. On the other hand, a similar method may be employed to estimate the deflection of propeller wake, as demonstrated by Bohari et al. [58], as shown in the last paragraph.

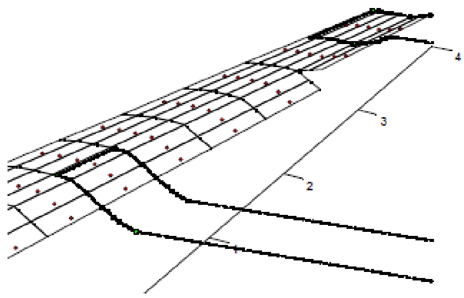

Figure 3.8: VLM grid on a wing with a flap and aileron deployed. (Yahyaoui [57])

VLM and slotted flaps Modeling slotted flaps with VLM without the use of BL models does not appear to be a common technique. Moerland in his Master's thesis [59] argues that slot flow mainly contributes to viscous effects and that, as VLM is based on potential flow theory, slots may be allowed to be filled. His conclusions were that filling slots rather than modeling flaps yields far better results. However, the scientific basis for this is fairly slim, he refers to the original paper on this idea by Rajeswari[60], who only published results for the rather low flap deflection of 10°. The paper is valuable in the way it describes the dealing with flap edges. Moerland used this filling method for (aeroelastic) load calculations on a Fokker 100. It appears that he modeled double-slotted flaps with a single element, at large deflections up to 42° and compensated for de-cambering. This was done using a chart with pre-determined effective flap flow deflection angle for the

Fokker 100, similar to figure 2.1 which may not be generalized for other flap types. Using a modified version of AVL, the control points were deflected but the vortex points were not, the process does not become entirely clear from the report. Overall, the lift polars were very accurate, but the lift distribution less so. This results is considered insufficiently proven to be accurate, along with the lack of an actual de-cambering model.

Singh in his Master's thesis [61] studied maximum lift with both a 2D and a 3D AVL/VLM method. He actually got very close to the polar with the closed gap method, combined with Torenbeek's correction for multi-element lift curve slope, and (apparently) the decambering reduction model of Murillo & McMaster's. For 40° flap angle there was approximately 10% over-prediction at α=3°. This method is still deemed too uncertain for higher flap deflections.

Van Dam/Modified Weissinger method In 2001, Van Dam et al. [62] published a methodology for computing high-lift performance of GA and transport aircraft. It couples 2D data to a 3D-Weissinger method, which is a lifting line method (seemingly equivalent to 1-panel VLM method) extended to include sweep and dihedral effects, introduced in 1947.[63] In essence, the model is a lifting line model with sectional characteristics provided by 2D data of choice to provide a lift polar, including (past)-stall. The effective angle of attack and zero-lift angle are compensated for the viscous 2-D data to improve the model. This is done by moving the control point location, the 2D data are computed using 2D CFD software (INS2D). This is also called a non-linear lifting line model, as it incorporates non-linear lifting behaviors of airfoils. The method proved effective for both clean and flapped conditions, but care should be taken in providing the 2-D data. A flat-wake assumption, which worked well for the clean, and fully flapped wings, proved inaccurate for flap cutouts, introducing premature stall by overloading adjacent sections, this was solved by introducing a non-planar wake method. Phillips and Snyder [64] describe the implementation of the nonlinear/modified Weissinger method more elaborately.

VLM with propellers

There have been multiple attempts at modeling the propeller-wing interaction at cruise conditions. Many were reasonably successful and dealt with a VLM approach:

Veldhuis [40] extensively studied propeller-wing interactions on a Fokker50 model. Numerical simulations were performed in the form of VLM, panel methods, and Navier-Stokes calculations. The research was supported by the experiments APROPOS and PROWIM. An important finding was that a swirl-recovery factor of around 0.5 should be used when accounting for the angle of attack induced by the propeller swirl. Overall, the results for the VLM calculations were reasonable, and also worked for a limited flap deflection of 26.5°. Some limitations were the lack of viscous de-cambering.

Alba in his masters thesis [42] successfully applied a VLM method, again for the cruise wing. Here, the swirl recovery was determined with an iteration by looking at the actual rotational kinetic energy of the flow. The VLM is expended to allow for the propeller bound vortices, the propeller slipstream was allowed to deflect as a kink around the quarter-chord. Alba concluded that only the propeller normal velocity component should be added in the Kutta Joukowki equation for determining the lift (and thus not the axial component), as the propeller effects are already accounted for by the local inflow angle. The results were reasonably accurate.

Over-estimates with propellers

Unfortunately, the application of increased velocity directly to a LL code of VLM code proves to (often) yield an over-estimate of lift:

Fischer in his Masters thesis [65] attempted to model propellers with a LL code and validated this with URANS CFD and body-force simulations. Where was a gross over-estimate of wing lift of 50-71%.

Epema in his Masters thesis [66], tested both the VLM method of Alba and a LL method. The standard LL method is modified by adding the induced angle of attack by the propeller. Not including the additional axial velocity was indeed better for the VLM results. Unfortunately, the LL proved to be too inaccurate, the VLM proved to be accurate only outside the slipstream: the lift inside the slipstream was slightly over-estimated.

Nederlof in his Masters thesis [28] showed that small slipstream heights can substantially reduce lift, as also tested against in this thesis. Correcting for height in 2D in the LL method or in 3D in a 1-panel VLM method still yields an over-prediction of lift inside the slipstream, see fig. 3.9.

3D image method Based on the work of Rethorst [67], Nederlof [28] successfully employed images in 3 dimensions. There are some similarities with section 3.3.1 in that there is both a potential function for the flow inside the jet and that outside of it. The bound vortices on the wing inside of the slipstream are divided into an odd and even system of vortices. This is introduced in a 1-panel VLM system. The system is solved based on the boundary condition of equal pressure and equal slope along the jet boundary. A single circular slipstream with a uniform velocity profile was assumed. The method showed to work well for a centered propeller position and one at half the semi-span, though the initial assumptions were violated for the latter case.

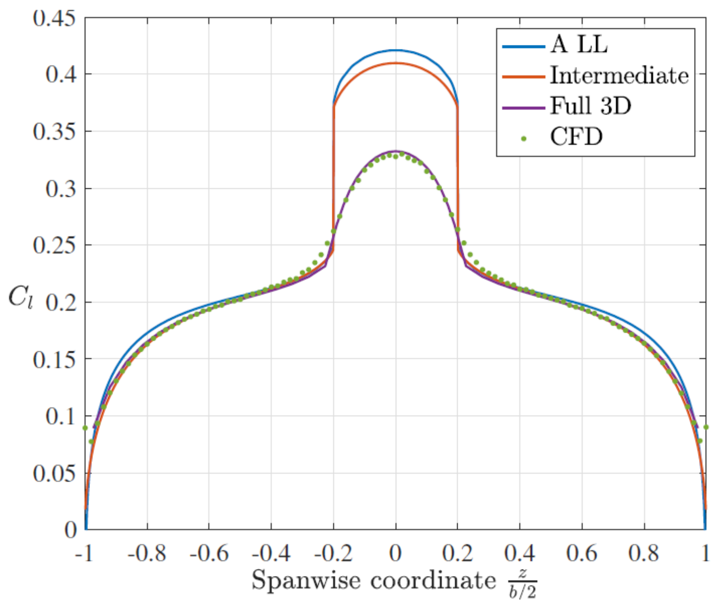

Figure 3.9: Comparison of different potential flow methods (Nederlof [28])

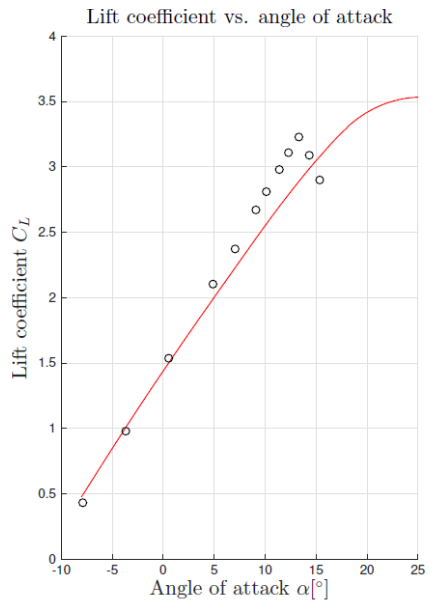

Figure 3.10: Lift polar with propellers on and $\delta_f = 40°$. (Bohari [58])

Bohari et al. used an established method for high-lift: a one-panel VLM method of Van Dam [62], also referred to as an alpha-method: it allows to compensate for viscous-de-cambering obtained by 2D polar data, to change the panel angle and collocation point. This improved on the method of Weissinger [63], by allowing for the deflection of the wake by the flap. It added the separately computed propeller contribution to a velocity triangle, also including the z-component (i.e. swirl). As this appears to be a single-interaction model, the flow distortion on the propeller may not be modeled, causing some inaccuracies. Maximum lift gets over-predicted in terms of both α and C_L as shown in fig. 3.10, this is attributed to XFoil/MSES, cross-flow phenomena, and interpolation: maximum lift was weighted between spanwise points. The discrepancy towards the experimental $C_{L,max}$ was inexistent on the clean wing, and increasing with the addition of flaps, and aggravated by the propeller.

The method of Bohari may benefit from airfoil data that actually contains the influence of a slipstream of limited height (though this would decrease lift) and that of separation suppression (which could increase lift) and propeller vertical positioning. This is where 2D data as modeled in this thesis can be valuable, the use of MSES would also allow for direct comparison with the results.

3.3.3. CFD

SFB880/BNF project For the BNF project several CFD campaigns were run with different goals, including propeller design and flight dynamics. The most relevant paper by Radespiel et al. [68] considers propeller installation on an infinite wing span. This is highly interesting as span-wise distribution of lift, drag and moment are included, as is the pressure distribution behind the actuator disk. A striking observation is that, even for the high propeller offset of the BNF concept, the propeller experiences between 5 and 10° angle of attack during high lift operations. This occurs due to the strong circulation of the wing at high lift coefficients, and may cause normal force and a moment on the propeller due to asymmetric loading.

LEAPTECH/NASA X-57 An extensive paper by Viken et al. was published by NASA on the design of the airfoil for the X-57 in cruise and flapped configuration.[8] They required a design C_l of 0.90, a flapped, unblown $C_{l,max}$ of 2.5 or greater to achieve a $C_{L,max}$ of 4.0 or greater. They modified an airfoil with slotted flap design based on the GAW series. They also ran tests on a GAW-1 airfoil with DEP using MSES and USM3D (RANS CFD), but these were not directly compared. Deviations of 10% between CFD turbulence models was common, they tested SA, SAQCR, and SST, in descending order of predicted lift value. The influence of wing chord to propeller diameter (retaining propeller and nacelle size) was investigated using FUN3D under fully turbulent conditions with 0.5, 1.0 and 2.0 relative chord length. Drag and pitching moments are also investigated.

Deere et al.[69] conducted a RANS CFD study into the LEAPTECH wing. Lift, moment and drag are reported. An extensive study in the effect of switching off certain propellers or groups was conducted, as was the effect of using co- or contra-rotating propellers. The wing was also tested on a driving truck, but the experiment suffered from various issues leading to rather inaccurate results.

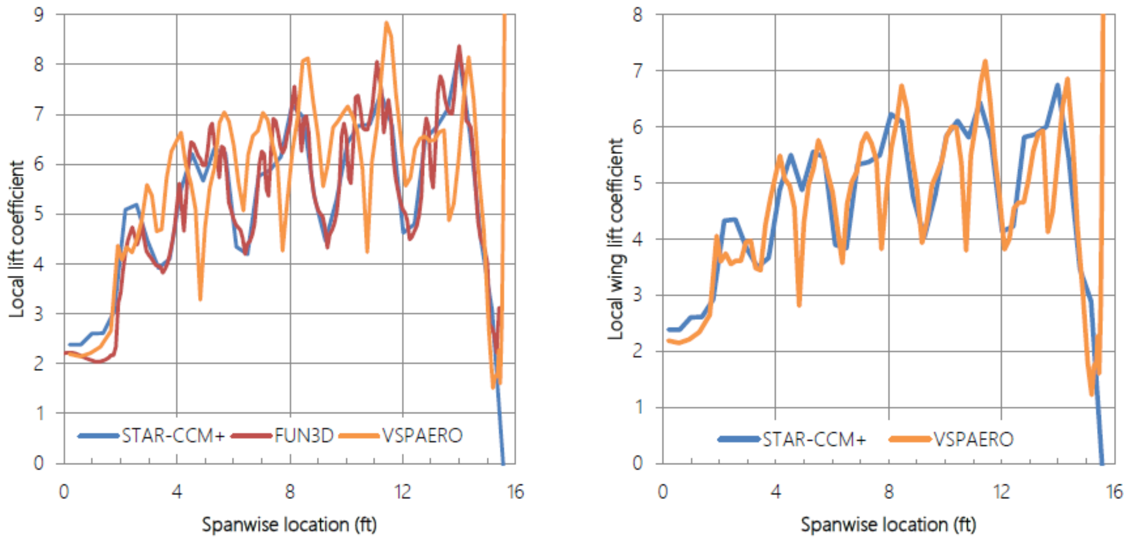

(c) Comparison of computational spanwise lift coefficient distribution at $\alpha = 6°$. The STAR-CCM+ data is smoother because it is calculated by summing the forces in spanwise bins, while the FUN3D and VSPAERO data shows lift coefficients at a series of spanwise sections.

(d) Comparison of STAR-CCM+ and VSPAERO spanwise lift coefficient distribution from the wing only (excluding the flap) at $\alpha = 6°$.

Figure 3.11: Leaptech wing sectional lift predicted by RANS CFD (STAR-CMM+, FUN3D) and VLM (VSPAERO) (Stoll [70])

Two years earlier, a numerical investigation into this wing was conducted by Stoll.[70] As seen in fig. 3.11, the propeller slipstreams can hardly be considered merged. What makes this paper interesting is the brief comparison not only between CFD results but also with a VLM result using a program called VSPAERO. The results were briefly summarized: There was disagreement between CFD and VLM (VSPAERO) for the flap deflected case, but reasonable agreement between the STAR-CCM+ (RANS) simulation and the VLM model for the wing with flap lift force removed, as can be seen from the left and right plot in figure 3.11, respectively. According to the (brief) report discussion this is due to the inability of the VLM model to capture stalled flap sections. Presumably due to the same effect, the $C_L - \alpha$ curve is steeper for VSPAERO and lift becomes significantly higher than CFD for increasing angle of attack. At $\alpha = 6°$, C_L is in the order of 5.5 instead of 5.2.

It is worth reiterating that the CFD takes a long time to execute: according to Duensing et al. CFD simulations on the X-57 can still take around 1 day on mainframe computers in the order of 1000 cores.[23]

I

Methodology

4

Background information on MSES

In this chapter, both a general introduction on MSES is given, along with more details on how it operates, which is useful for considering the implementation of a slipstream.

4.1. History, accuracy & features

History MSES is described in the 1990 AIAA conference proceedings by Mark Drela [32]: It is basically a modification of the single-element ISES code which is explained and demonstrated in a 1987 AIAA paper by Drela and Giles [71]. It was actually the Ph.D. thesis subject of Drela, which one could also consult for more details [72]. For the MSES code the discretization, Newton solver, and boundary layer models of the ISES code were modified to handle multiple-elements and wakes with a multi-layer formulation, but their basis remains the same.

It is also worth noting that the ISES code was modified into the open-source XFoil code. XFoil (described by Drela [73]) is faster and still accurate for low-Reynolds number flows, but only applies to single element airfoils and subsonic conditions. Instead of the Newton scheme it uses a vorticity panel method with a Karman-Tsien compressibility correction. All 3 programs are written in Fortran, following the Fortran77 standard. XFoil has been translated to more modern languages including MATLAB.

Accuracy As mentioned in the literature study (van Zelst [4]), Florjancic [74] made extensive use of MSES in his Master's thesis. His validation effort (for slotted flaps) showed fairly large deviations in the linear range of C_l between 0 and 0.22 but very small deviations in $C_{l,max}$ of 0.1. (which is just 3% on a $C_{l,max}$ of 3...) It turns out that gap modeling and transition location is critical: the early transition behind propellers may even increase accuracy for the coming project. Actually, these figures are not bad, considering that a recent (meta)study into CFD (2015) results concluded a scatter on the C_L of 0.2 at low α and 0.3-0.6 for higher $\alpha's$, albeit 3D with flap tracks etc. installed.[75] It will be important to identify corrects grid settings and validate MSES for geometries and flow conditions to be considered.

Orlita [76] was quite skeptical of using MSES for slotted flaps: Orlita encountered difficulties where MSES would fail to converge, even though the geometry posed no obvious problematic areas: The cove area was smoothed (and a remaining one is usually filled in as a solid body by MSES.) Failure to converge also yields difficulty in obtaining the exact maximum lift coefficient, the cases were not validated for slotted flaps.

Kounenis [77] concluded that MSES was accurate for predicting the linear regime of multi-element airfoils. In the post-stall regime, MSES turned out to be inaccurate and would often fail to converge. Failure to converge would result in "wrinkly" pressure distributions.

Features For an overview of the features, one may refer to the MSES paper (Drela [32]), the manual (Drela [24]), or simply the software suite itself. MSES can calculate flows around multi-element airfoils, i.e. with flaps and slats. Its range of applicability extends from the low subsonic regime (using ISES with $M < 0.10$) up to the transonic regime: it can also reliably model shock waves and transitional separation bubbles. It can also automatically or manually model large areas of separation behind slats, in flap slots, and those near maximum lift. In terms of drag, MSES can compute the viscous drag for each element and the total wave drag to arrive at the total drag of the combination. Pressure distributions, moment coefficient, and the boundary layer variables of each element are available, but not the direct boundary layer profiles used by the BLM. The total field variables can also be saved. Polars can also be generated using MPOLAR: this saves a lot of work, especially when it comes to “skipping” non-converged points. Inverse design methods can be used for improving airfoils and there is also a geometry optimizer (in terms of translation/rotation). The roadmap of the software suite, also indicating modifications and Python interaction (to be explained later), can be found in appendix A.

4.2. Inviscid Euler formulation & Newton procedure

The solution process is not only described by the original papers [71][32] but also conveniently summarized by Veldhuis [31] and the MSc. thesis of Van Craenenbroeck [18].

The inviscid formulation uses the steady state Euler equations. These are the conservation of *mass, momentum, and energy*, shown in eq. (4.1) through eq. (4.3), where $\mathbf{V},\mathbf{n}$ denote the velocity and normal vector and h_t is the total (stagnation) enthalpy.

$$\oint \rho\mathbf{V}\cdot\mathbf{n}ds = 0 \tag{4.1}$$

$$\oint (\rho(\mathbf{V}\cdot\mathbf{n})\mathbf{V} + p\mathbf{n})ds = 0 \tag{4.2}$$

$$\oint \rho\mathbf{V}\cdot\mathbf{n}h_t ds = 0 \tag{4.3}$$

Conveniently, due to the way the grid is discretized along the streamlines, the following forms of the conservation of **mass and energy** hold along each streamtube:

$$\dot{m} = \rho V A = constant \tag{4.4}$$

$$h_t = \frac{\gamma}{\gamma-1}\frac{p}{\rho} + \frac{V^2}{2} = constant \tag{4.5}$$

Instead of eq. (4.5), it is advisable to use the *isentropic condition* eq. (4.6) away from shockwaves. Recall that at high-lift conditions shockwaves may occur on the nose or in the flap region despite the low flight Mach number. The implementation of the momentum and entropy conditions throughout the domain can be changed through the ISMOM option. Both the conservation of energy and the isentropic condition allow manipulation of the total energy by adding a total pressure increase. This property is utilized in this thesis to arrive at a desired velocity increase as further explained in section 5.1.

$$\rho_0 = p\left[1 - \frac{V^2}{(\gamma-1)h_0}\right]^{\frac{-1}{\gamma-1}} = constant \tag{4.6}$$

This pair of equations reduces the number of variables (i.e. ρ, p, V, A) from 4 to 2. The remaining two variables are the change in normal displacement of each node (δn) and the change in density of each cell ($\delta\rho$), as illustrated by fig. 4.1.

Boundary conditions and constraints The far-field nodes are usually determined by a circulation term, a source, and two doublets using the Infinite Farfield Flow Boundary Condition (IFFBC). The velocity potential obtained with the singularities is used to determine both the farfield velocity and pressure. This pressure is used to set a pressure boundary condition on the top and bottom streamlines. The inlet streamlines are constrained to be parallel to the freestream α. The farfield circulation and mass fractions in-between elements are solved by a Kutta condition on each element. Also, the stagnation point location, which may move during the process, is constrained by specifying equal pressures on either side, once for each element.(Drela [24]) Other variables and constraints may be specified by the user, for instance with the presence of a wind tunnel wall, or a free-jet wind tunnel.

Newton procedure The Euler equations, boundary layer equations, and other constraints are all added to a system of equations **F** with the variables in the vector(s) **U**. The goal is to minimize the residuals of eq. (4.7). This is similar to a root finding process illustrated by fig. 4.2. The maximum Newton residuals for each variable are actually printed out in the MSES console during the solution process.

$$F(U^{n+1}) \equiv F(U^n + \delta U^n) = 0 \tag{4.7}$$

To this end, the sensitivity of the solution determines the next step in U as written in eq. (4.8):

$$\delta U^n = -\left(\left[\frac{\delta F}{\delta U}\right]^n\right)^{-1} F(U^n) \tag{4.8}$$

Large discontinuities in the solution, i.e. from the shifting of a propeller slipstream, should be avoided, else the Newton procedure may diverge or oscillate.

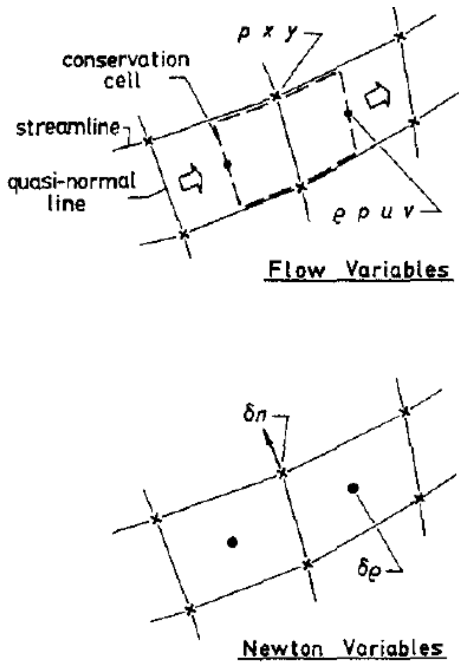

Figure 4.1: ''Euler grid node and variable locations'' (Drela [32])

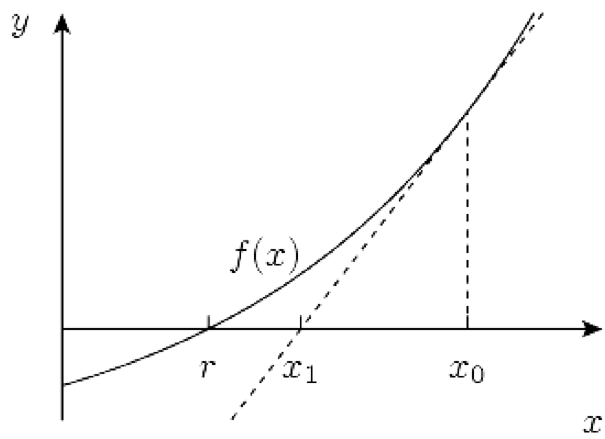

Figure 4.2: "Illustration of Newton's method" (Johansson [78])

4.3. Boundary layer model formulation

ISES uses a two-equation boundary layer model with different equations towards closure of the dissipation in the relations. The use of a two equation model allows to also model separated flows by differentiating between a wall layer and a wake layer. These employ different methods based on whether the flow is laminar, turbulent, or in transition with certain assumed boundary layer velocity profiles as explained later.

Main equations and variables Let us first consider the basic two equations used which are the dimensionless (compressible) von Karman *integral momentum* equation and the *kinetic energy thickness* equation eq. (4.9). Note that the dissipation coefficient recieves the C_Δ symbol in this thesis instead of C_D, to avoid confusion.

$$(i) \quad \frac{d\theta}{d\xi} + (2 + H - M_e^2)\frac{\theta}{du_e}\frac{u_e}{d\xi} = \frac{C_f}{2} \tag{4.9a}$$

$$\frac{d\theta^*}{d\xi} + \left(\frac{\delta^{**}}{\theta^*} + 3 - M_e^2\right)\frac{\theta^*}{u_e}\frac{du_e}{d\xi} = 2C_D \tag{4.9b}$$

The latter is rewritten using the integral momentum equation to arrive at the second equation (ii) to be solved alongside equation (i):

$$(ii) \quad \theta \frac{dH^*}{d\xi} + [2H^{**} + H^*(1-H)] \frac{\theta}{u_e} \frac{du_e}{d\xi} = 2C_D - H^* \frac{C_f}{2} \tag{4.10}$$

Simplification Now, before proceeding to the solution (closure) process, it is worth noting that these equations can be simplified with two assumptions pertaining to compressibility. Firstly, it may be assumed that at low speed and low lift conditions the BL edge Mach number is low, and the M_e^2 terms may be neglected. Secondly, it may be assumed that the density throughout the boundary layer is constant, leading to the density thickness and density shape parameter being 0: $\delta^{**} = 0; H^{**} = \delta^{**}/\theta = 0$. The equations now simplify to:

$$\frac{d\theta}{d\xi} + (2+H) \frac{\theta}{u_e} \frac{du_e}{d\xi} = \frac{C_f}{2} \tag{4.11a}$$

$$\frac{d\theta^*}{d\xi} + 3 \frac{\theta^*}{u_e} \frac{du_e}{d\xi} = 2C_\Delta \tag{4.11b}$$

$$\theta \frac{dH^*}{d\xi} + H^*(1-H) \frac{\theta}{u_e} \frac{du_e}{d\xi} = 2C_\Delta - H^* \frac{C_f}{2} \tag{4.12}$$

Which are equivalent to the equations in Katz and Plotkin [35], chapter 14.

Turbulent closure relations The relations are also described by Drela and Giles [71]. There are 4 functional dependencies to be solved:

$$H^*(H_k, M_e, Re_\theta), \quad H^{**}(H_k, M_e), \quad C_f(H_k, M_e, Re_\theta), \quad C_\Delta(H_k, M_e, Re_\theta) \tag{4.13}$$

The kinematic shape parameter H_k is derived by Whitfield, and simply equals H for very low Mach numbers. All 4 equations use velocity profiles and not density profiles: for the turbulent case (which is most interesting for this report) the closure relations are solved using the skin-friction and velocity profile formulas of Swafford.

Swafford's formulas allow to determine the skin friction C_f. These are also used to derive equations for H^*. The dissipation coefficient C_Δ is determined from splitting the boundary layer in two parts with a wall layer part with C_f and wake layer part with C_τ. A rate equation may slow the development of C_τ under quickly changing boundary layer conditions. It is also interesting to note that the model holds in the wake by stacking the two opposing wakes and simply setting $C_f = 0$. For more details, refer to the original paper from Drela and Giles [71].

Main variables The main variables of the system are θ, δ^* and $C_\tau^{1/2}$ in case of a turbulent flow. These may be used to determine any other boundary layer variable encountered (but this does not seem very straightforward). In fig. 4.3 the position of boundary layer variables on the surface is shown with the inviscid grid above it.

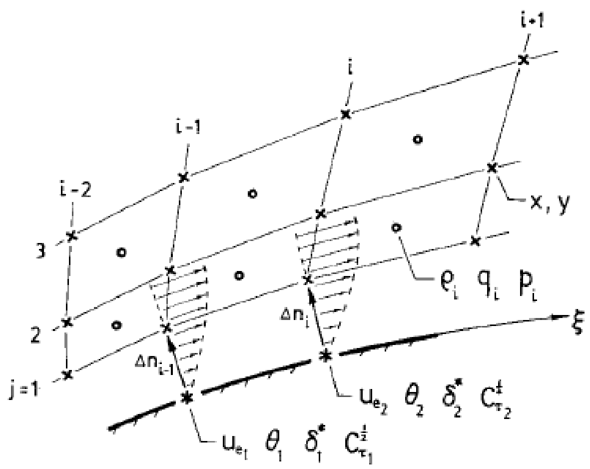

Figure 4.3: "Boundary-layer variable locations" (Drela and Giles [71])

4.4. Multi-element formulation

The present formulation of MSES (without boundary layer confluence) uses a "multi-layer" representation. The closure dependencies are of the same form as the ISES model, however, they are solved differently. In the wake, different velocity profiles are used: each wake consists of two half-sine wave profiles of Coles stacked on top of eachother as shown in fig. 4.4.

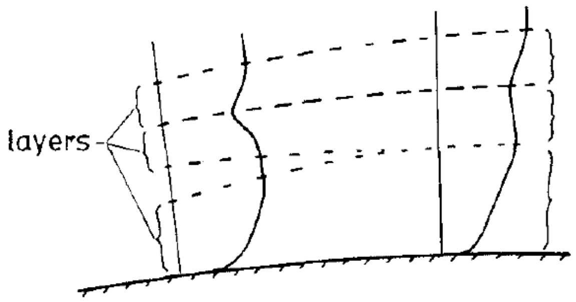

Figure 4.4: "Multi-layer velocity profile representation" (Drela [32])

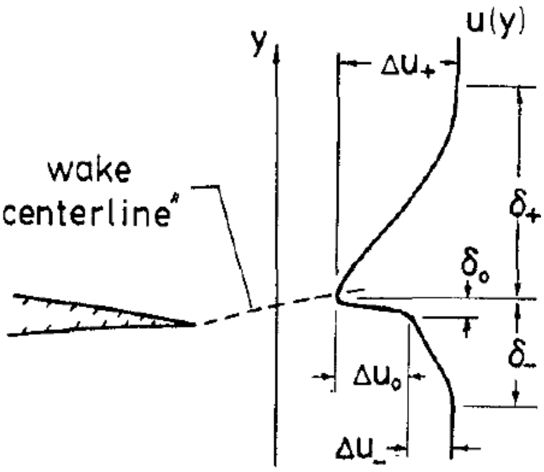

Figure 4.5: "Steep shear layer downstream of trailing edge" (Drela [32])

The wake centerline lies at the velocity minimum, as illustrated in fig. 4.5. No shear is (explicitly) assumed and the shear layer between the wakes is modeled as a simple velocity discontinuity, apparently contrary to the figure. Both these assumptions are deemed acceptable: the discontinuity quickly decays in the model, as in real-life. This is probably due to the Clauser eddy viscocity is used in the wake containing the velocity minimum with a larger Clauser constant. The paper of Drela [32] also includes the formulation needed for wake confluence, which never seems to have been implemented.

5

Extension of MSES to include effects of finite slipstreams

This chapter describes modifications done to MSES in order to model the effect of a finite slipstream on (flapped) airfoils. Special attention is paid to correct implementation and the correct use of grid and domain size. A non-uniform velocity field is also included. Files changed and the new inputs are summarized in appendix A, including interaction with the Python wrapper constructed for this project.

5.1. Addition of a uniform actuator disk

The basic MSES 3.11 software (and some earlier versions) include a very crude option to model a fan as an Actuator Disk (AD) (Drela [24]): A single jump in total pressure could be specified on one side of a blade, extending to the upper of lower edge of the computational domain (or another airfoil, as discussed and tested later). It seems that this could be used to model, for instance, a turbofan inlet cowl/lip. The limit of the code is that a free AD and slipstream of limited height could not be modeled. An x/c position other than on the airfoil chord could not be specified, except for a value of exactly 0 would cause the AD to be placed on the inlet, again attached to a stagnation streamline, extending either up or down. The AD feature, however, is a good starting point, as the physics of an enthalpy jump are already included.

The first step was to add two parameters to the source code: $ztop$ and $zbot$, which may be determined from a desired propeller slipstream height h and offset z_p. This should be constrained setting $ISDELH = 0$. Alternatively, a slipstream can be attached to the top or bottom of a dividing streamline with higher numbers (side index $ISDELH = 1, 2...$ labeled top to bottom), retaining the intended actuator disk height $ztop - zbot$. The J values of the affected streamlines are printed as standard: These are assigned being closest to the AD edge. The local y-values of the boundary are now also printed. Furthermore, the code was modified to effectively handle negative x/c positions, i.e. ahead of the airfoil.

It may be desirable to constrain the AD in a different location than actually adding the velocity increase (such as at the inlet, leading to a fully developed slipstream). To this end, both the X-position of the AD and of the constraint location can now be specified. If these coincide, a message is printed and the AD is constrained on the nearest quasi-normal line. Else, the velocity jump is constrained by projecting it onto a straight line at the desired constraint location.

Compressible pressure equations: Care should be taken when defining the inputs for the MSES actuator disks: the total (or stagnation) pressure ratio π_{AD} is required as input to determine the jump in total enthalpy. One should keep in mind that stagnation pressure p_0 can only be defined using the dynamic pressure at in-compressible flow assumed at low Mach numbers, less than approximately $M = 0.3$. (See, for instance, Anderson [22].) Typical free-stream Mach numbers under consideration in this thesis are in the order of $M = 0.15$ (at 100 kts flight speed). At a velocity ratio of 2, the limit of the assumption is reached. The correct method of establishing total pressure increase that is used is shown in eq. (5.1)[22]. At 100 m/s, eq. (5.1) gives 2.4% higher total pressure than Bernoulli. Note that this is not the same as the 5% expected with Prandtl-Glauert scaling, but still relevant at higher velocities.

$$\frac{p_{0,1}}{p_1} = \left(1 + \frac{\gamma - 1}{2} M_1^2\right)^{\frac{\gamma}{\gamma-1}} \tag{5.1}$$

The total pressure ratio π_{AD} may be determined by eq. (5.2) from the MSES manual (Drela [24]):

$$\Delta C_{p_0} = \frac{p_{0_2} - p_{0_1}}{\frac{1}{2}\rho_\infty V_\infty^2} \tag{5.2a}$$

$$\pi_{AD} = 1 + \Delta C_{p_0} \frac{\gamma M_\infty^2}{2} \left[1 + \frac{\gamma - 1}{2} M_\infty^2\right]^{\frac{-\gamma}{\gamma-1}} \tag{5.2b}$$

As the quasi-horizontal gridlines are actually the streamlines, the grid changes throughout the solution process, which means that the initial determination of affected streamlines will often be invalidated. Therefore, the enthalpy jump is now assigned for every Newton iteration, and the AD data is plotted continuously.

Solution process with Python wrapper Along with adding features to MSES, a Python wrapper is produced to automate the generation of input files, running the MSES suite, and plotting the results (see also appendix A). To aid in visual representation, the i and j-values of the AD, as printed by MSES, are read to plot the geometry of the AD, airfoil, and streamlines. Axial velocity profiles and pressure distributions can also be viewed, as can the pressure coefficients, field values, and boundary layer history. An example grid with an actuator disk included is shown in fig. 5.1. Note that the quasi-horizontal grid-lines are the streamlines, and the slipstream is marked in red.

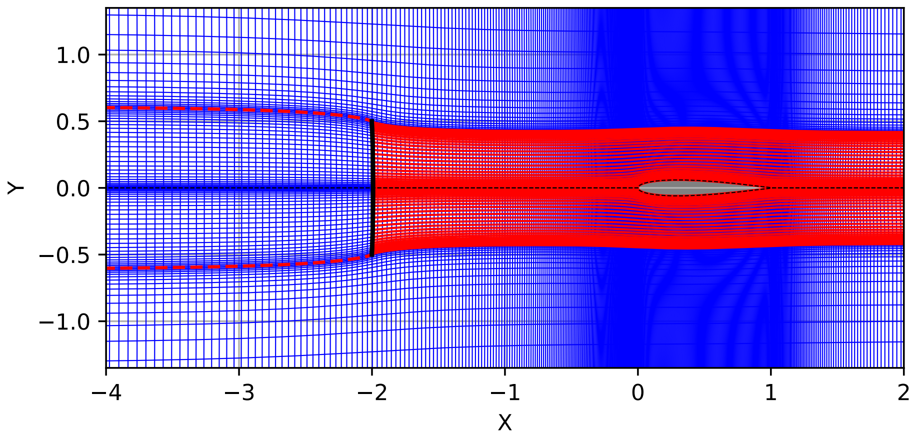

Figure 5.1: An actuator disk of diameter $D/c = 1.0$ placed ahead of a NACA0012 airfoil, at a slipstream velocity ratio of $V_s/V_\infty = 1.5$

It is worth mentioning that inclination of the AD has no significant effect of the flowfield: the slipstream is not deflected upward or downward by tilting the AD. This would require the addition of new potential flow components to the MSES simulation.

5.2. Addition of a non-uniform propeller slipstream

This section aims to introduce a realistic propeller slipstream and establish the appropriate parameters and constraints for the following blown airfoil and flap experiments.

A uniform axial velocity profile is usually not an accurate representation of a propeller slipstream. Common propeller designs are loaded more heavily near the tip and display a velocity field that peaks at around 70-80% radius. Propellers are loaded differently across the wing span and may not be symmetrical, hence MSES needs to be modified to accept any axial velocity profile. This discretization should be able to model a non-uniform profile with asymmetry, freestream velocity at the edges, and a possible dip near the center (hub). Taylor series expansions and Fourier transform are deemed unsuitable as they would be limited in accuracy near the edges, or unable to properly capture the asymmetry, respectively. Bezier curves may be used, but using polynomial(s) is deemed convenient and sufficiently accurate.

It is decided to discretize the pressure increase across the actuator disk using a separate 5th order polynomial spline for the top and bottom domain. This also allows to create asymmetry in the flowfield, and model a discontinuity introduced by a propeller hub. MSES enforces a minimum velocity ratio of 1.0.

A reference propeller/slipstream design needs to be selected. Patterson [27] sought to modify an existing propeller design to produce a more uniform slipstream. It appeared that non-uniformity decreased the lift-augmentation performance and more uniformly loaded propellers should be used for maximum lift. However, as most propellers are designed for propulsive efficiency, the Minimum Induced Loss (MIL) propeller as designed by Patterson is chosen for the current discussion. This MIL propeller is more representative of mainstream designs and can be used to clearly illustrate the differences with a uniform velocity profile. As the dissertation of Patterson was a study for the DEP NASA SCEPTOR demonstrator, the relative sizing and velocities can be used as a typical study of a high-lift configuration.

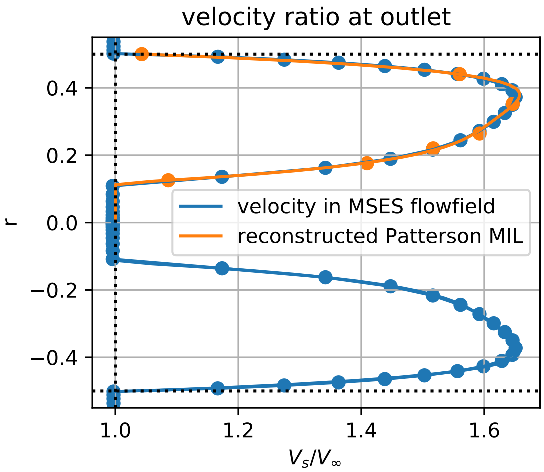

Figure 5.2: MIL propeller axial velocity profile reconstructed from Patterson [27]

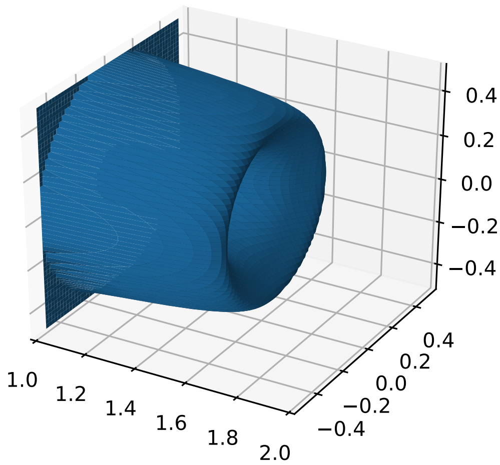

Figure 5.3: 3D representation of the axial sliptream velocity profile under consideration.

The reconstructed MIL propeller velocity profile from Patterson is shown in fig. 5.2, note that the values represent the total velocity ratio downstream and contraction is neglected here. Together with refinements near the AD edges this provided excellent results as seen in the figure. Omitting all but the first polynomial coefficient will result in a uniform AD. The effect of upwash on the development of the velocity profile is considered in section 5.3. The 3D representation of the “sliced doughnut” velocity profile is shown in fig. 5.3. It should be noted that the influence of the relatively large propeller hub (or nacelle, for that matter) is neglected in this thesis. It is assumed that the free-stream velocity component is uniform across the disk as if the hub is not present.

Of course, the axial velocity profile will look different at different locations along the blown wing-span. This can be easily reconstructed assuming that the propeller is operating with purely axial inflow, thus neglecting the effect of angle of attack, or the wing. This is illustrated by fig. 5.4. On the left, the relative positions on the propeller disk plane are indicated, on the right, the local axial velocity profiles are drawn. The outboard position has a slipstream height of $h = \sin 60 = 0.866$. Note that the more outboard position caries more momentum as the velocity dip at the hub is replaced by the loading at the center of the blade as it passes the wing. The effect of the hub on flow displacement around it may not be properly captured by this model. The outboard velocity profile will be considered extensively, the results under blowing by the centerline profile with its two distinct peaks are presented in section 9.5.

Table 5.1: Velocity and dynamic pressure increase, averaged over h/c=1.0

	average V_s/V_∞	average q_s/q_∞
center location	1.37	1.96
$y = 0.5r$	1.49	2.27

The induced velocities cause an average increase in velocity and dynamic pressure. If this is averaged over the total height of the disk (1.0), the values in table 5.1 are obtained. Although the slipstream at the $y = 0.5$ station has lower height than the center station, both a higher average induced velocity and average induced dynamic pressure are obtained due to the increased momentum. The averages cannot be directly related to effective lift increase but this will again be considered in section 9.5.

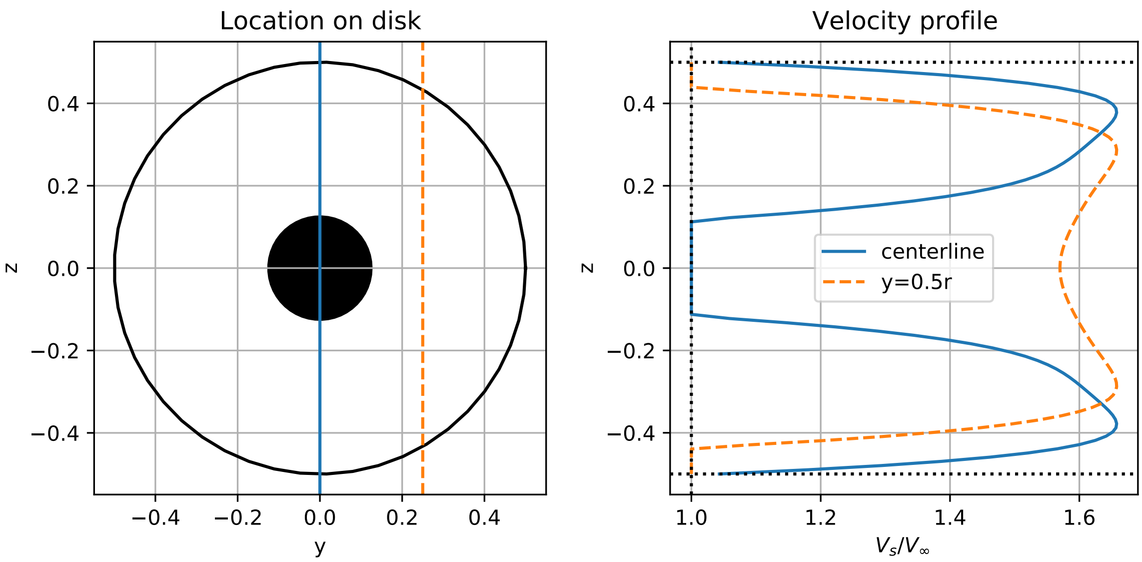

Figure 5.4: Velocity profiles at indicated locations on the disk.

5.3. Constraining a developed slipstream

Slipstream/disk constraint: It may be desirable under some cases to not include the effect of slipstream contraction in the simulation. However, constraining the vertical position of a slipstream at the inlet may yield some inaccuracies. As the inlet is multiple chord lengths away from the airfoil the slipstream is allowed to displace significantly away from the location of a propeller. Therefore, an effective constraint is desired. A good overview is shown in fig. 5.6.

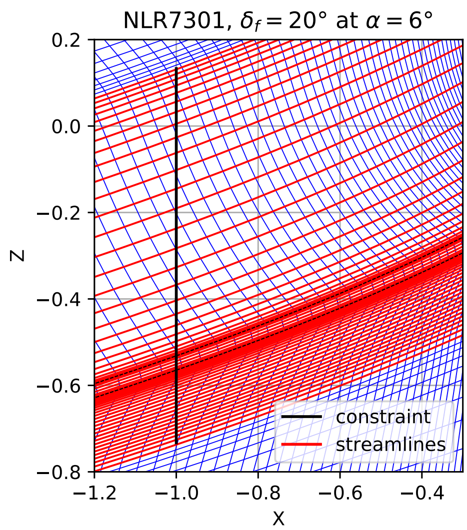

Figure 5.5: Close-up of the slipstream constraint

A closeup of the new constraint is shown in fig. 5.5. The reason a straight disk is now used rather than selecting a quasi-normal line is that the v-shape of these lines would cause high inaccuracies with determining the Z-coordinate, leading to a heavily skewed velocity profile. This is caused by the combined effect of the significant upwash and angle of attack associated with these high-lift cases. In order to reach this determination of Z, the crossing streamline grid segments are interpolated based on X-location to determine the proper Z. This yields a smoother velocity distribution across the streamlines.

To ensure the interpolation and assignment is correct, the solution may first be verified using a symmetric case, in this case the NACA0012 with $h/c = 0.866$ as shown in fig. 5.6. This solution shows a near-perfect match in fig. 5.7 and fig. 5.8, with no vertical shift. Hence, the discretization seems accurate. Note that Y is aligned with the inlet face, and is equal to Z in this symmetric case.

A high-lift case with large asymmetry is also tested, as shown in fig. 5.9. As can be seen in fig. 5.10, the prescribed flow-field matches reasonably well. (Note that Y is no longer in the direction of Z in this case.) The apparent shrinkage observed at the inlet plane is explained by the difference in relative angle between the constraining disk, and the inlet plane. The inlet plane is (almost) normal to the streamlines, whereas the constraining disk experiences a high angle of attack of about 19°. As $cos(19°) = 0.95$, this explains 5% slipstream shrinkage, which is deemed acceptable. The velocity increase follows the local streamlines, hence does not decrease the local angle of attack in this case.

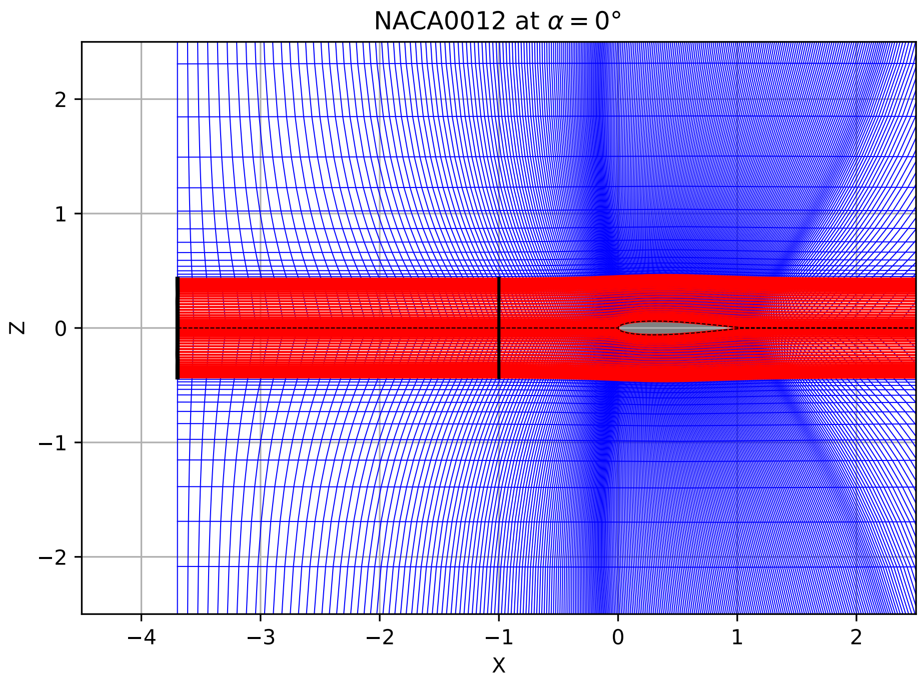

Figure 5.6: NACA0012. Propeller constrained $x/c = -1.0, h/c = 0.866$. $M = 0.15, Re = 2.51e6, n_{crit} = 9.0, \alpha = 0°$

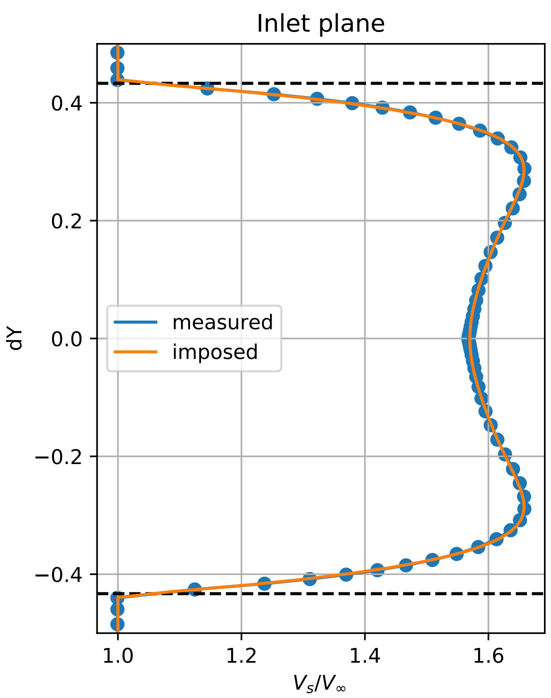

Figure 5.7: Inlet plane velocity ratios, NACA0012. $M = 0.15, Re = 2.51e6, n_{crit} = 3.0, \alpha = 0°$

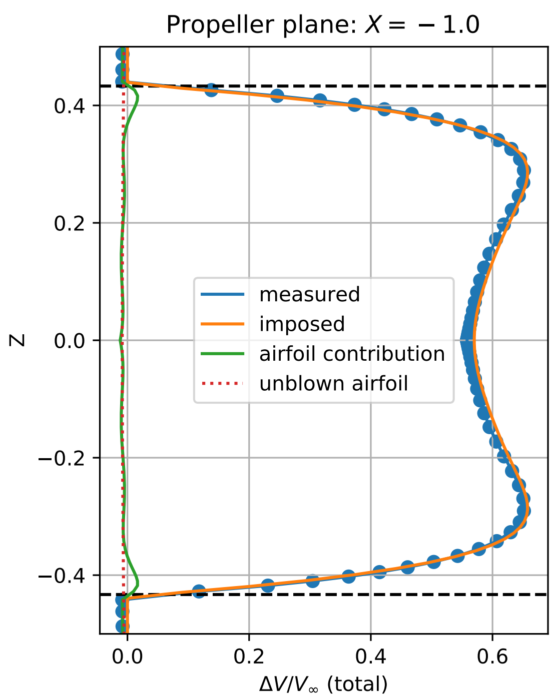

Figure 5.8: Propeller constraint plane velocity ratios, NACA0012. $M = 0.15, Re = 2.51e6, n_{crit} = 3.0, \alpha = 0°$

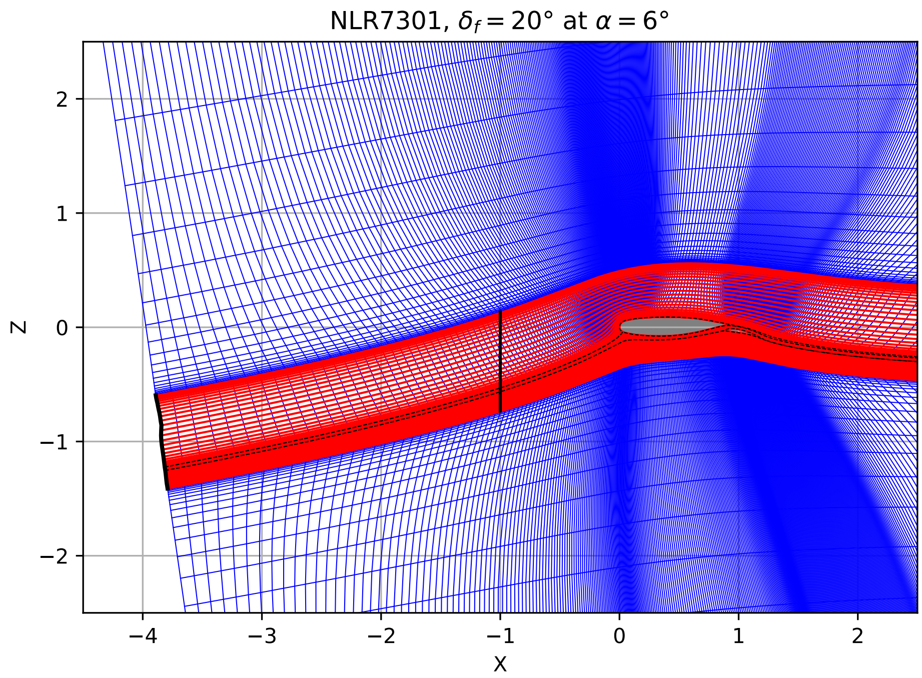

Figure 5.9: NLR7301 with $\delta_f = 20°$. Propeller constrained $x/c = -1.0, h/c = 0.866$. $M = 0.185, Re = 2.51e6, n_{crit} = 9.0, \alpha = 6.0°$

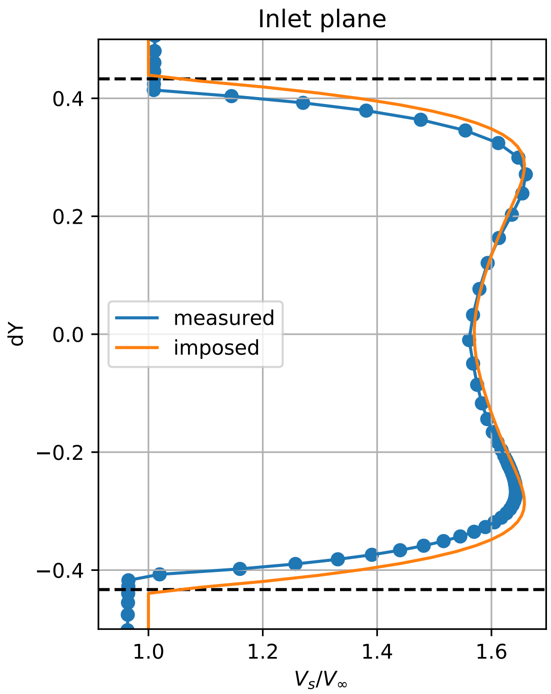

Figure 5.10: Inlet plane velocity ratios, NLR7301 with $\delta_f = 20°$. $M = 0.185, Re = 2.51e6, n_{crit} = 3.0, \alpha = 6.0°$

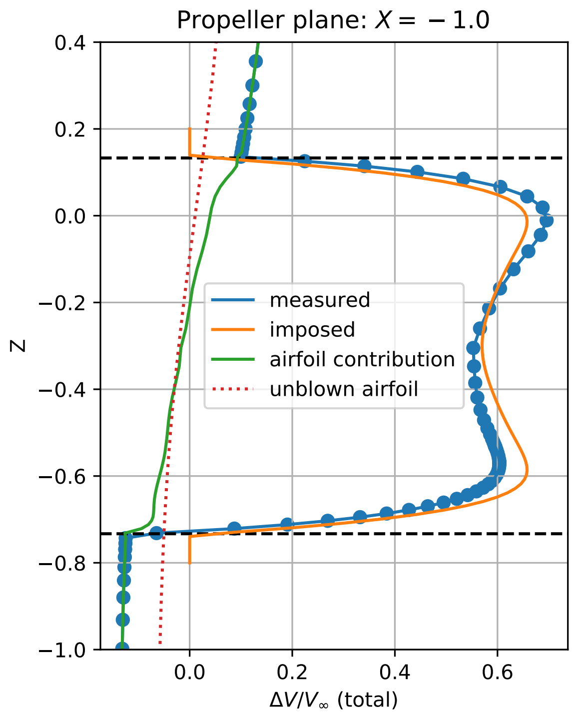

Figure 5.11: Propeller constraint plane velocity ratios, NLR7301 with $\delta_f = 20°$. $M = 0.185, Re = 2.51e6, n_{crit} = 3.0, \alpha = 6.0°$

Insight into the superposition of propeller velocity and the wing-induced flowfield is obtained from fig. 5.11. The propeller is close to the wing and the wing influence on the local flowfield can not be ignored. However, keep in mind that the velocity profile prescribed does not change by the wing upwash, i.e. we are dealing with a single interaction model (SIM). The expected effect of adding a propeller is the following: the wing-induced velocity field changes, and the total flowfield becomes a combination of the wing-induced flowfield and the propeller velocity profile. Wing-induced velocity is determined by the wing circulation (and, to a limited extent, blockage). As we are dealing with potential flow, the resulting measured velocity (blue) should be an addition of the propeller and wing-induced velocities. This may be reversed to obtain the wing-induced velocity (green). Note that this is to some extent scaled up from the unblown wing-induced velocities (red dotted lines), as the flowfield changed considerably the "correct" airfoil contribution is less predictable. As we are dealing with different velocities, lift may no longer be related directly to circulation through the free-stream velocity. The C_l is increased from 2.46 to 5.50 which is a factor 2.24. This would be equivalent to a free-stream velocity increase of a factor $\sqrt{2.24} = 1.50$. This happens to be roughly the same as the velocity increase averaged over $h/c = 1.0$ for this particular set-up.

This new constraint is automatically disabled if both the AD and the constraint line cross the stagnation streamline within one cell apart. This makes the constraint follow a quasi-normal line and create a curved constraint, leading to a different determination of the Z coordinate which may only be accurate for low-lift conditions.

5.4. Gridding

This section deals with modifications to the grid that are required to accurately perform the MSES simulations with an actuator disk included. Refinements are necessary and the number of streamlines and quasi normal lines needs to be determined to handle the inclusion of an actuator disk and a slipstream.

Horizontal: MSES has extensive options for modifying the grid in horizontal direction. In the x-direction, the number of points in front of the foremost and behind the trailing airfoil can be specified. The main airfoil also receives a preset amount of side points, for the trailing airfoil the main airfoil number gets scaled with an exponential function, depending on its chord, and an exponent of choice. An important parameter if the AD is located on a single quasi-normal line, is the X-spacing parameter. As per the manual, this "controls how much the quasi-normal grid lines spread out away from the airfoil."(Drela [24]) A high factor leads to high orthogonality, and a more straightened AD, but this is not suitable for high-lift conditions, as it will cause an excessive concentration of quasi-normal lines near the LE and TE of the airfoil. Thus it is only used for the following low-moderate lift cases, with $C_l < 1$. A total of 480 quasi-normal lines (I_{max}) may be introduced.

Vertical: In terms of vertical spacing there exist few options: one can in principle only specify the amount of lines above and below the main airfoil, and specify the maximum number of streamlines between flap slots. The spacing follows an exponential pattern from the airfoil surface outward: changing cell aspect ratio was also found to have little effect and may negatively impact accuracy or convergence. The total maximum number of streamlines (J_{max}) is 70, but versions with $J_{max} = 100$ and 120 were compiled. The version with 120 showed trouble refining after coarsening, though this feature is not critical. Versions with more streamlines could be compiled: however, this still yields a fairly coarse grid near the edges of most actuator disks that have a diameter in the same order as the airfoil or larger, yielding inaccuracies in assigning streamlines at the actuator disk boundary. Therefore, a different approach to increasing accuracy is sought in the next section.

5.4.1. Grid modifications enabling slipstream refinement

There are multiple options for modifying the code to enable refinement near the disk outer edges, but first it is important to define the more challenging case: that is of the free actuator disk under contraction. This is more difficult to grid as the position of the streamlines on the edge of the disk move considerably during the solution process.

From this point one could either modify MSET during grid initialization, or modify MSES during the solution process. The option for dynamically modifying the grid in MSES could be achieved by means of splitting/merging streamtubes near the edges (a feature that is only proven to work on the entire computational domain). Alternatively one could modify the stream function or mass fractions directly. However, it is decided that the option of modifying MSET carries lesser risk of introducing bugs or numerical instabilities into the code. This does require a transfer to obtain the correct streamline distribution. MSET works in the following way as outlined by the MSES manual:

> Option 1 uses the specified angle of attack to generate a panel solution, which is then used to trace a pair of stagnation streamlines just above and below each element, as well as the upper

> and lower farfield streamlines. Iso-potentials emanating from all leading and trailing edges are also located. This divides up the domain into blocks, which are then automatically displayed in a plot. These blocks form the skeleton on which the grid is generated. (MSES manual, Drela [24])

Between the streamlines of the aforementioned skeleton, the streamlines are distributed by means of the stream function. Fortunately this is equivalent to the change in Y-coordinate, before angle-of-attack rotation. The fact that the stream function varies linearly with Y has to do with the fact that the stream function is defined in the Y-direction ($dx = 0$) assuming a uniform free-stream velocity ($u = c$) and incompressible flow. A definition of the incompressible stream function in 2D is shown in eq. (5.3b).

$$\psi \equiv \bar{\psi}/\rho \qquad (5.3a) \qquad\qquad d\psi = u\,dy - v\,dx \qquad (5.3b)$$

MSET uses two spacing functions: Both are exponential spacings, but one is bounded only on one side whilst the other is a distribution where exponential spacings are defined from two sides and blended in-between. The former is used from the (out-most) airfoil surface up to the top and bottom domain walls, whilst the blended function is used between multiple airfoil elements.

New refinement option: The desired effect of controllable refinement near the AD edge is obtained by applying a strategy similar to introducing another airfoil element: the double exponential distribution is now used between the airfoil and actuator disk edge, whilst the single exponential distribution is used outside the actuator disk slipstream. The refinement does not introduce other (airfoil) objects in the domain as this yields erroneous results. The vertical position of the refinement on the top and bottom domain is now specified in the grid parameters, together with the amount of streamlines above and below the slipstream, as well as the cell height at the slipstream edges. Positioning however does require an accurate initial guess of the slipstream boundary before contraction which is described next. The original spacing is still available if the refinement cell height input is set to 0. The result of the grid modification is shown in fig. 5.12. The top of the domain shows the modified grid whilst the lower half shows the original exponential spacing. The new spacing should yield more accurate assignment of streamline properties near the actuator disk edge. Note however that viscous effects are not included in this region.

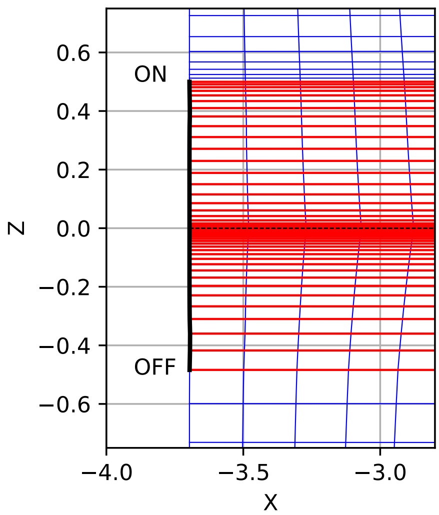

Figure 5.12: Effect of modified spacing

Low lift: Positioning the refinement using MSET and a fudge-factor: Transferring between MSET and MSES one has to consider not only the angle of attack but also the contraction that the grid will be subject to. This is only practical for a uniform-flow actuator disk, and different methods may be required for non-uniform flow. It is suggested that the average axial velocity increase at the AD be used to determine the grid shrinkage as the mass flow through through each streamtube remains constant, assuming incompressible flow. Any change in Z is assumed to be the same as change in Y as these axis are closely aligned up to moderate α, recall that Y is in the domain/free-stream frame and Z may be aligned with the airfoil for high-lift conditions. At $\alpha = 10°$ this may create an error of 1.5%, which is acceptable as the exact refinement location is not critical.

Another complicated factor is that the effective upwash changes which also has a significant impact on the solution. The corrections presented in eq. (5.4) and eq. (5.5) proved to capture these effects well for single-element airfoils under moderate angle of attack and under all contraction conditions . It should be noted that V_{AD} is equal to $1+2a$ for the pre-contracted case and $1+a$ for the case with free contraction. The correction in eq. (5.4) was based on the presumption that the ψ allocation would occur in the reference frame of the airfoil, as used in MSES, where the entire flow-field is tilted to satisfy the boundary conditions to arrive at the appropriate domain size. However, it later turned out that the ψ allocation occurred with reference to the

$YBOT$ and $YTOP$ specified. Hence, the correction in the last term of eq. (5.4) actually represents another effect: it compensates for the upwash.

$$y_{edge} = y_{des}\left(\frac{V_{AD}}{V_\infty}\right) + 2a \cdot sin(\alpha)(0.25 - x_p) \tag{5.4}$$

It was found that after this correction on y_{edge}, a small correction for the upwash was needed, suspected to be a discrepancy between the initial panel code estimate of MSET and the final MSES solution. The last factor in eq. (5.5) is a fudge factor which proved good results for all examined grids at velocity ratios of $V_s/V_\infty = 1.5$ and 2.0. Note that this factor depends only very mildly on the inverse of the velocity ratio.

$$\delta\psi_{edge} = y_{edge} - \psi_{div} \cdot 1.2^{V_\infty/V_s} \tag{5.5}$$

Applicability: Due to linearizing the upwash, and tuning with the fudge factor, these equations provide good grids only for moderate lifting conditions, which apply to the single-element airfoils considered, at low to moderate angle of attack. Without blowing, the new grid delivers exactly the same lift for the standard NACA 0012 test case.

High lift: Positioning the refinement using MSET tuned with 1 iteration: For high lift applications the grid refinement generation method is changed. Due to the complexity of the high-lift solution the panel method in MSET is not nearly accurate enough for use to determine the upwash with a small fudge-factor. Therefore, the correction is now determined with an iteration where the upwash is approximately determined using a run with the normal exponentially spaced grid. During the next iteration, the grid refinement is activated and positioned using the upwash determined with the aforementioned run. As MSET runs the initial panel code without actuator disk, the y-coordinate in MSET may simply be related to the desired z using the contraction ratio V/V_∞ as in eq. (5.6):

$$y_{edge} = y_{des}\left(\frac{V_{AD}}{V_\infty}\right) \tag{5.6}$$

However, to arrive at the correct stream-function spacing centered at the dividing streamline ψ_{div}, it is required to correct for the difference in ψ observed after the first MSET and MSES run, $\psi_{div,1}/\psi_{div,0}$. This also needs to be corrected for using the contraction ratio, leading to the relation shown in eq. (5.7). V_{AD} & V_{inlet} are both equal to $1+2a$ for the pre-contracted case.

$$\delta\psi_{edge} = y_{edge} - \psi_{div}\frac{\psi_{div,1}}{\psi_{div,0}}\left(\frac{V_{inlet}}{V_\infty}\right) \tag{5.7}$$

It can be beneficial to have a fully contracted slipstream which height is constrained closer to the airfoil. This feature is developed and incorporated by differentiating between the AD where the velocity is added at $XCDELH$ and the point called $XPROP$ where the propeller is constrained and the flow field variables per streamline are actually determined. To this end, a final correction should be made on y_{des} before applying eq. (5.6) as shown in eq. (5.8):

$$y_{des} = y_{des} - (y_{div,prop,1} - y_{div,AD,1}) \tag{5.8}$$

Applicability: The aforementioned method accurately produced the desired grid for high-lift configurations on the condition that the AD be placed at the inlet. Else, the transfer from the actuator disk coordinates to the intlet stream function could not be accurately described. The case where the slipstream is constrained away from the left domain work quite accurately, as shown in fig. 5.13. Non-uniformity in the slipstream velocity may lead to only minor deviations in high-lift cases. However, free-contraction where the AD was positioned away from the domain inlet could not provide accurate results. The upwash and curvature of the dividing streamline is too difficult to capture under high lift conditions.

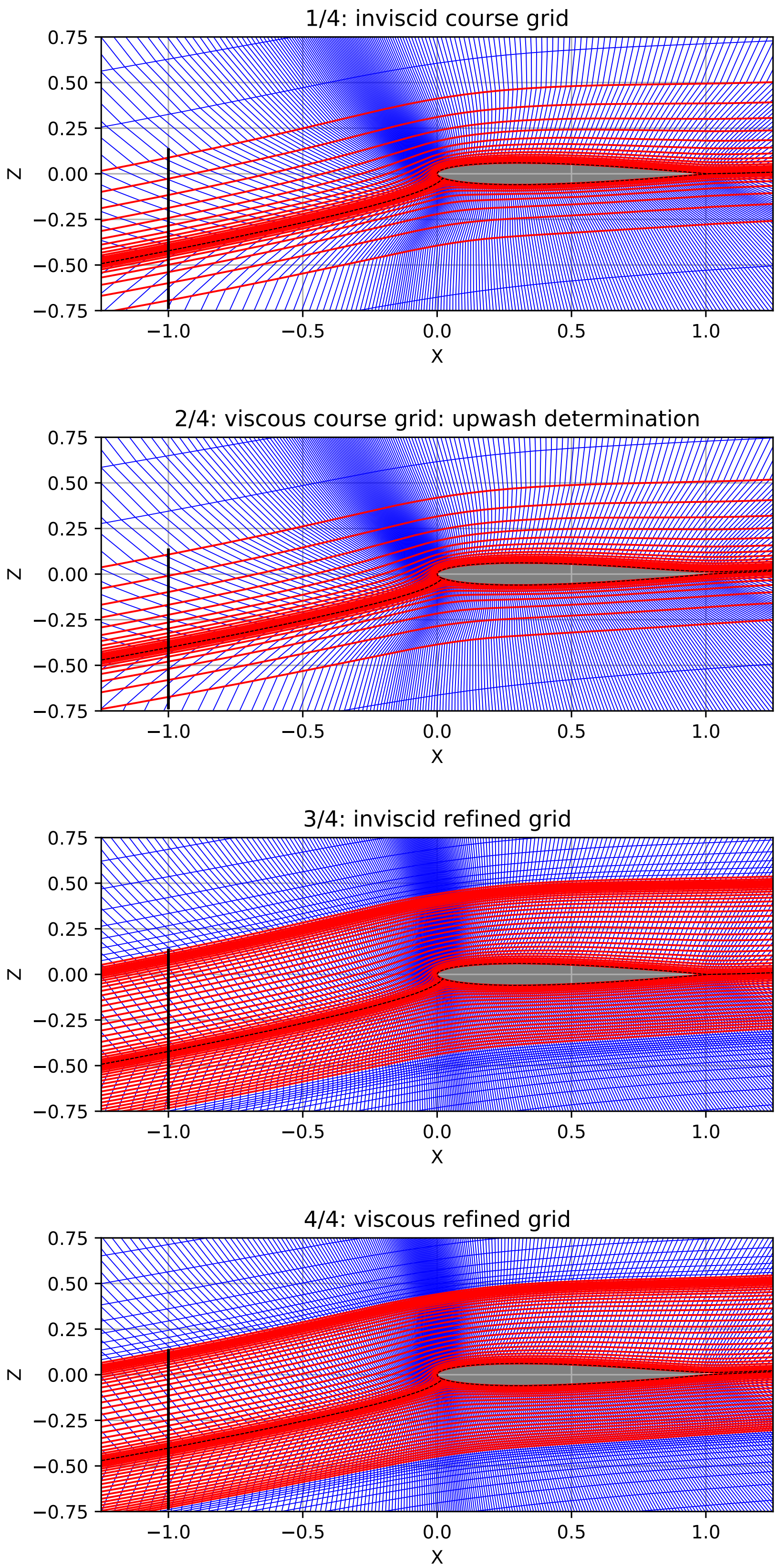

Figure 5.13: Example iterative solution process grids, blown NACA0012 at $\alpha = 10°.Re = 2.51e6$, $n_{crit} = 9.0$, $M_\infty = 0.15$.

Iterative gridding for viscous high-lift cases The set of grids in fig. 5.13 show how a viscous high-lift case is best approached. In the first two steps, an inviscid and then more challenging viscous solution is obtained on a coarse grid, to determine the upwash. The upwash is needed to determine the refinement location on the inlet plane. Subsequently, the following two steps are run to determine an inviscid and viscous solution of the case, with higher accuracy. Skipping the viscous coarse grid may be acceptable provided that there is not much lift decrease expected due to viscosity, as the exact refinement location is not critical. It may sometimes help to first run an inviscid computation to start a difficult viscous case.

5.4.2. Domain size & shrinkage

As outlined by Drela [24] the domain should be increased in size for higher lift coefficients and Mach. The exact values are not very important, as long as any shock-waves are captured. In high-lift conditions the domain size should be increased with $\sqrt{C_L}$. A square domain with an $r/c = 2.0$ where $r = \sqrt{A}/2$ is recommended according to the domain sensitivity study by Drela [79]. This implies a square with sides of length 4 for a unit-length airfoil. As will be shown shortly, the introduction of the AD shrinks the domain in the current version of MSES, thus, as a precautionary measure, the grid size is increased from the recommended $[xmin, xmax, ybot, ytop] = [-1.75, 2.75, -2.0, 2.5]$ to at least $[xmin, xmax, ybot, ytop] = [-2.0, 3.0, -3.0, 3.5]$ to ensure that the slipstream is always fully captured. The airfoil suction side may require a slightly larger minimum domain than the pressure side.

The grid shrinkage is shown in fig. 5.14 and fig. 5.15: The side of the domain where the actuator disk is introduced shrinks considerably. This is due to the fact that the initial solution and spacing in MSET is set-up with mass flows defined by the (uniform) freestream velocity. Upon solving, all cells affected by the slipstream contract. The domain size is justified and indicated for each simulation.

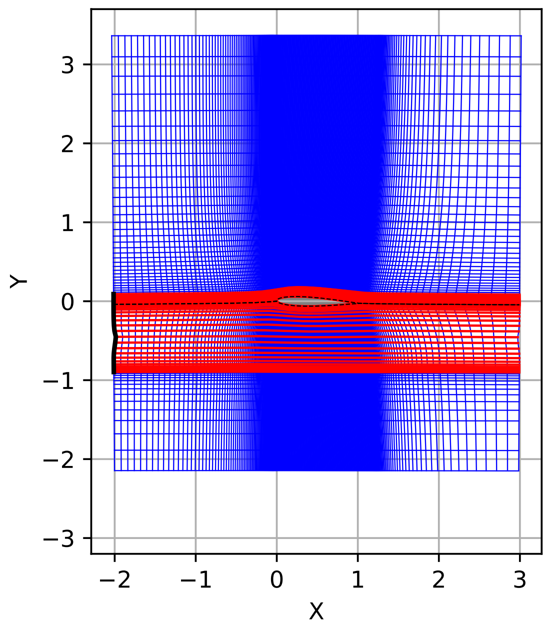

Figure 5.14: $y_p/c = -0.4$, NACA0012 $\alpha = 2°$, $M = 0.15$, $V_s/V_\infty = 2$.

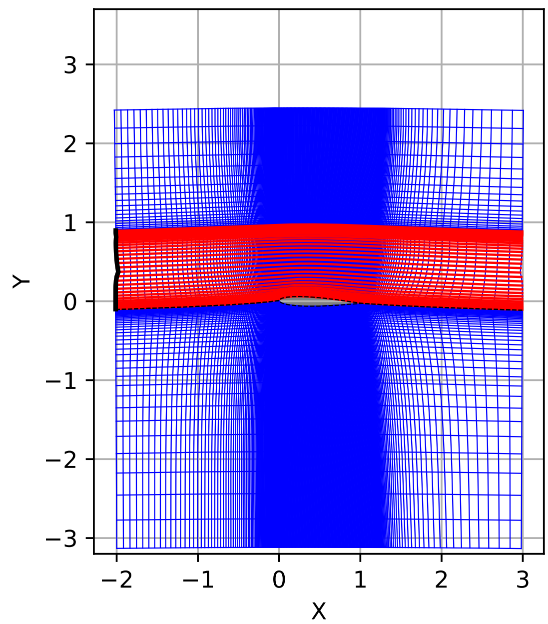

Figure 5.15: $y_p/c = 0.4$, NACA0012 $\alpha = 2°$, $M = 0.15$, $V_s/V_\infty = 2$.

5.4.3. Grid convergence study

A grid convergence study is undertaken to determine how many streamlines are required for satisfactory accuracy. For the free-contracting AD, the number of inlet points is also tested. For both cases, the NACA0012 is considered at $\alpha = 2°$.

AD at inlet The AD is first placed on the inlet, leading to a fully developed slipstream. The test are run at two slipstream heights: both small ($h/c = 0.5$) and large ($h/c = 1.0$), with both the usual single exponential spacing and the modified double exponential spacing. The domain is set to $[xmin, xmax, ybot, ytop] =$

$[-2.0, 3.0, -3.0, 3.5]$. The number of quasi normal lines on the inlet I_{in} is increased from 37 to 70.

As can be seen comparing the results for $h/c = 0.5$ between the usual spacing (fig. 5.16) and the double spacing (fig. 5.17) the latter shows much clearer convergence with higher accuracy. For a solution of around $C_l = 0.695$ the former shows around $+-0.015$ deviation whilst the spread of the latter is much smaller at around $5e-3$. For $h/c = 1.0$, the results are shown in fig. 5.18 and fig. 5.19, again the double exponential grid converges far quicker. Note that the slipstream boundaries are, in this case, further away from the airfoil which means that the resolution in the single exponential case is worse. Also, the impact of mis-assigning a streamline in the double exponential case becomes less as the slipstream boundary is further from the airfoil whilst maintaining accuracy. This leads to even better convergence.

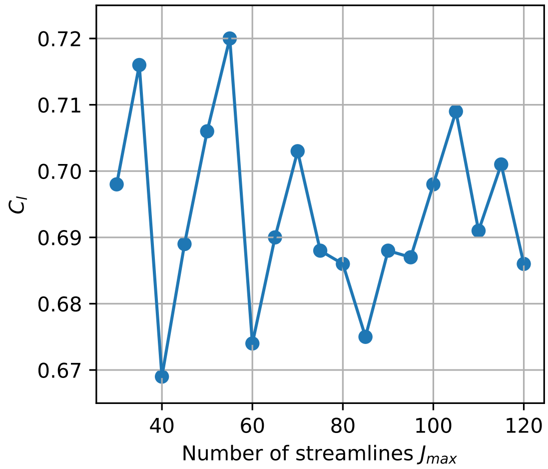

Figure 5.16: Effect of J_{max} on C_l. $\alpha = 2°$, $M = 0.15$, $V_s/V_\infty = 2.$, $h/c = 0.5$. Single exponential grid.

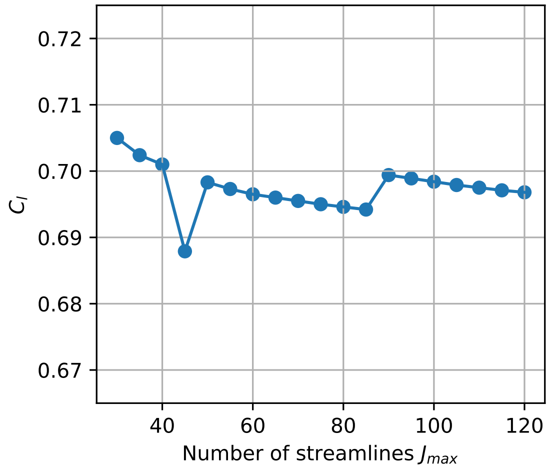

Figure 5.17: Effect of J_{max} on C_l. $\alpha = 2°$, $M = 0.15$, $V_s/V_\infty = 2.$, $h/c = 0.5$. Double exponential grid.

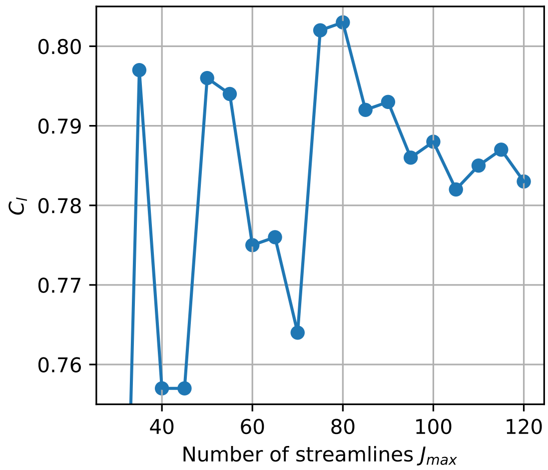

Figure 5.18: Effect of J_{max} on C_l. $\alpha = 2°$, $M = 0.15$, $V_s/V_\infty = 2.$, $h/c = 1.0$. Single exponential grid.

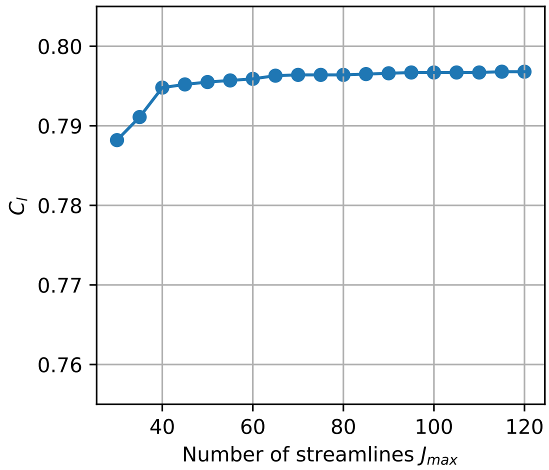

Figure 5.19: Effect of J_{max} on C_l. $\alpha = 2°$, $M = 0.15$, $V_s/V_\infty = 2.$, $h/c = 1.0$. Double exponential grid.

As these cases are run with a substantial uniform velocity increase of $V_s/V_\infty = 2$, assigning the streamline properties correctly is critical. The scheme to determine the blown cells is expected to be too conservative under coarse conditions. The current scheme uses the average coordinate between streamlines to determine the grid node coordinate. If this is not originally within the slipstream the streamtube would not have shrunk. If it was, it might actually be included in the streamtube leading to a larger streamtube with more momentum which may also impact lift. This may be an explanation for the (on average) lower results in fig. 5.18. This may occur for both the top and bottom streamlines around the slipstream. Round-off in dividing the number of streamlines between the top and bottom domain may also cause some discontinuities in the solutions.

As both results indicate that a number of 70 streamlines would yield very satisfactory results with a deviation of 1% or less, all following simulations are run with at least 70 streamlines.

Free-contracting AD For the free-contraction cases in section 6.4.2, the grids used are far larger to be able to capture the actuator disk with D/c up to 6. First off, the more or less standard case of $D/c = 1$ is tested. This has domain size $[xmin, xmax, ybot, ytop] = [-10.0, 5.0, -5.0, 5.0]$. Secondly there are the larger AD cases of $h/c = 2$ and $h/c = 6$ which are run on the domain $[xmin, xmax, ybot, ytop] = [-20.0, 18.0, -12.0, 12.0]$. Note that these are definitely appropriate for $V_s/V_\infty = 1.5$ as established in section 5.5 but may lead to a small overestimate in lift for $V_s/V_\infty = 2.0$ which has more contraction. The number of QN lines on the inlet I_{in} was also varied with $I_{in} = 100, 150 and 200$, with $0.5I_{in}$ outlet lines. A high I_{in} may be beneficial for a free-contracting AD.

It was found that setting the X-spacing parameter to 1.0 was beneficial for more consistent results. Nevertheless, lower accuracy than in the pre-contracted case could be obtained especially for the larger actuator disks. The results are summarized in table 5.2 and fig. 5.20 through fig. 5.22. The larger grids converge more poorly and the largest AD ($D/c = 6.0$) requires a lot if streamlines. Note that increasing the number of QN lines does not improve the accuracy in general.

For the free-contracting AD cases it is thus recommended to use 100 streamlines. Furthermore, for improved accuracy in horizontal positioning of the AD it is also sensible to set the number of inlet points to 200, but this is not required if the AD is placed at the inlet.

Table 5.2: Summary of anticipated error bound and suggested streamline count.

grid	h/c	rel. error	min. j_{max}
small	1	+/- 1%	70
intermediate	2	+/- 2%	70
large	6	+/- 2%	100

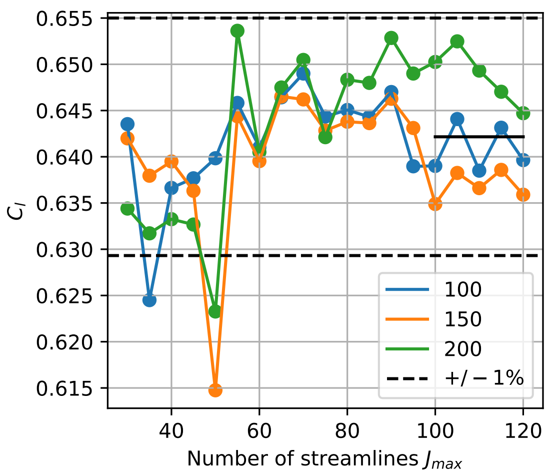

Figure 5.20: Effect of J_{max} on C_l. $\alpha = 2°$, $M = 0.15$, $V_s/V_\infty = 2.$, $h/c = 1.0$. Free disk. Double exponential grid

Oscillating solutions When considering cases with the slipstream near the lifting surface, oscillatory behavior can prevent or seriously slow convergence. For instance, a slipstream may lose contact with the upper surface, thus decreasing circulation. This decreased circulation may decrease upwash enough to lower the slipstream onto the surface again, etc.. A similar case (though opposite) can be observed with the slipstream below the airfoil. This becomes aggravated with the actuator disk further away from the airfoil. Similarly, the triggering of cells to be included in the slipstream can pose difficulties with the velocity discontinuity: if the slipstream is out of contact with the airfoil, the slipstream boundary closest to the airfoil does not receive additional refinement, though this is a case that would generally be avoided anyway.

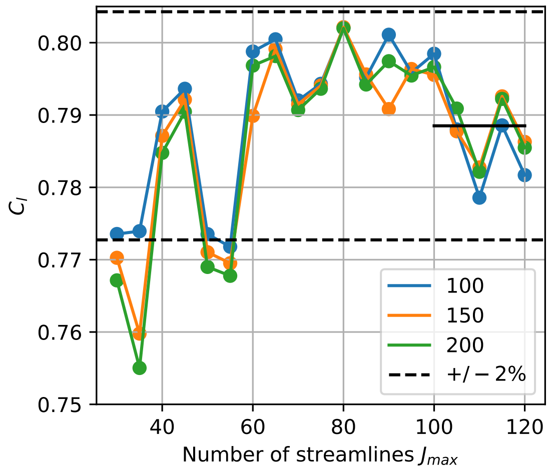

Figure 5.21: Effect of J_{max} on C_l. $\alpha = 2°$, $M = 0.15$, $V_s/V_\infty = 2.$, $h/c = 2.0$. Free disk. Double exponential grid

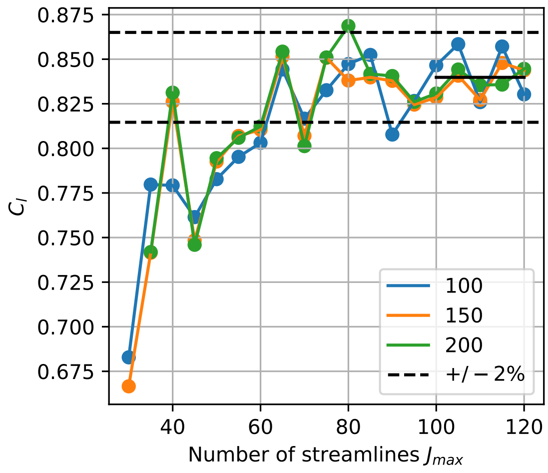

Figure 5.22: Effect of J_{max} on C_l. $\alpha = 2°$, $M = 0.15$, $V_s/V_\infty = 2.$, $h/c = 6.0$. Free disk. Double exponential grid

5.5. Domain sensitivity study

The boundary conditions of MSES allow a small grid to be used for airfoils, and this scales with lift coefficient and Mach number, as explained before. This should also hold for pre-contracted slipstreams. Contrary to this, a contracting slipstream needs space in the horizontal and vertical extent. In order to find the appropriate domain size for the free contraction actuator disk, it is decided to undertake a domain sensitivity study.

Boundary conditions As explained in section 4.2 the source terms and doublets are generally determined using the infinite farfield conditions. This determines the velocity and hence pressure condition on the top and bottom streamlines. The inlet streamlines are constrainted to be parralel to the freestream angle of attack. This has impact on all sides of the domain:

- The inlet should be large enough to capture contraction ahead of the actuator disk, else the contraction process will get hindered. If the left boundary is too close, one will observe that the velocity at the intake is already higher than the freestream. This leads to less contraction downstream, but the required speed increase is attained, hence, the slipstream will be higher and contain more momentum than intended. The reason for this behavior lies in the boundary condition: The infinite-flow farfield boundary condition requires the velocity vectors at the inlet to be aligned with the freestream angle of attack. This fails to properly portray the streamlines that would otherwise be inclined towards the slipstream center.

- The top and bottom streamlines should also be far enough as the pressure boundary condition is only based on the potential flow terms. This may fail to correctly respond to slipstream contraction: the contraction of the outer streamlines of the domain may cause the slipstream to contract too quickly as there is no external force applied.

- The outlet size is also of importance. In cases with a relatively small outlet, the doublet term in x-direction D_x would become excessive (up to 100x larger). This explains the observed retardation of the flow behind the airfoil. This exact cause for this issue remains unknown.

The impact of the grid boundaries is investigated throughout the rest of this section. Only the velocity development in non-lifting conditions is considered to limit the number of variables.

5.5.1. Free AD setup

For the following simulations, the NACA0012 airfoil is included in an inviscid calculation, the number of inlet points is set to 201 and the outlet to 100. One may obtain a first estimate of appropriate values knowing that actuator disk properties converge approximately 2 diameters downstream, and that the AD flow follows a symmetric pattern. This, together with the knowledge that the originally recommended frames are approximately square, helps determine appropriate domains. The domain sizes and actuator disk positions considered are shown in fig. 5.23 and fig. 5.24. The numerical values are included in appendix B. The smallest grid used for $D/c = 1$ is shown in fig. 5.25. Note that this is already larger than regular MSES airfoil runs.

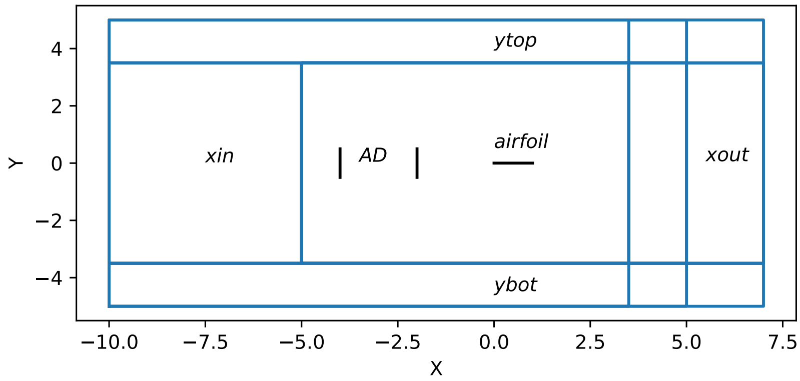

Figure 5.23: Domains for the smaller AD ($D/c = 1.0$).

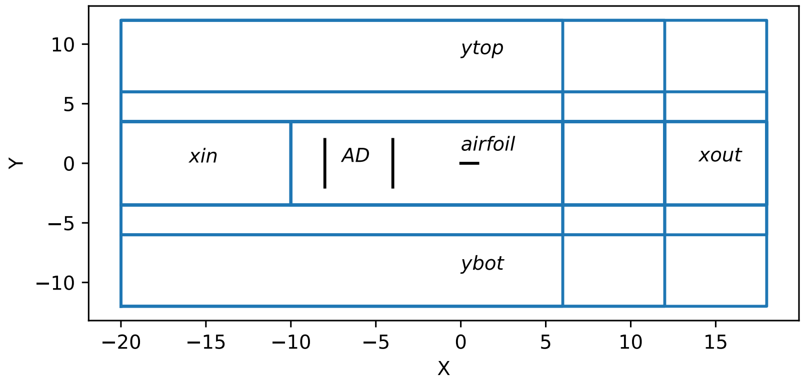

Figure 5.24: Domains for the large AD ($D/c = 4.0$).

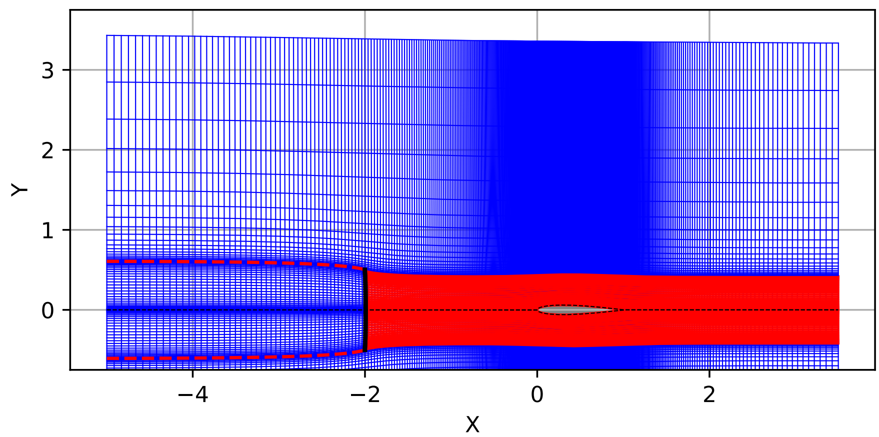

Figure 5.25: Grid with the smallest domain tested, smaller AD ($D/c = 1.0$), NACA0012 included, $V_s/V_\infty = 1.5$

5.5.2. Free AD results

The development of the velocity in the slipstream is of high importance to the lift augmentation and is related directly to the contraction of the actuator disk. The dynamic pressure due to axial velocity should reach desired values far upstream and downstream and is considered as the key indicator for this domain study, rather than airfoil lift. The domains with the resulting exit q are included in appendix B.

Effect of inlet boundary and AD location In fig. 5.26 results are plotted for the small AD with varying inlet location and AD position. It can be seen from the results that the inlet position definitely impacts the development of the velocity upto the actuator disk by starting at a higher velocity. This effect diminishes towards the airfoil. The effect of subsequently placing the AD closer to the airfoil is also tested: the results for the small and large inlet almost coincide now that the AD is not 1 but 3 diameters away from the inlet. Hence, for accurate contraction, it would be advisable to have the inlet at least 3 diameters ahead of the AD.

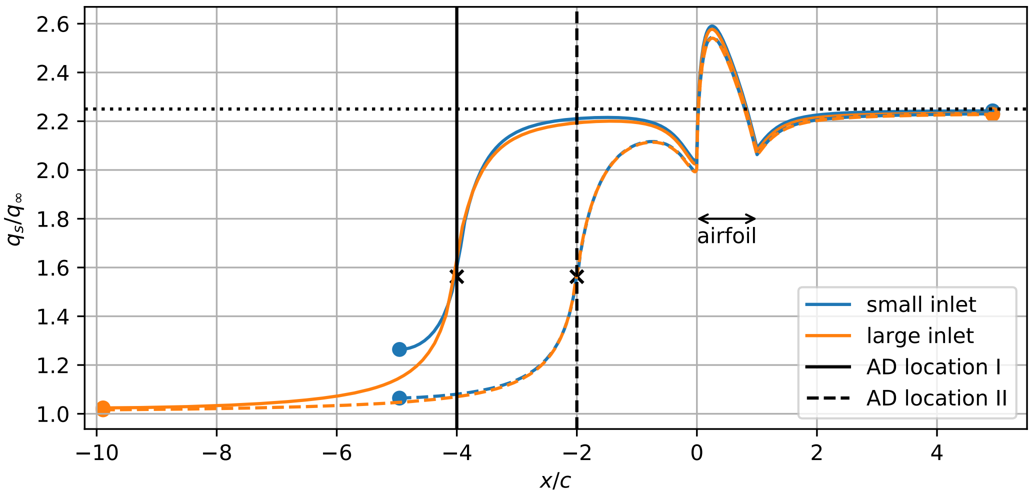

Figure 5.26: Effect of XIN and AD position. NACA0012 included. $D/c = 1.0$, $y = +-3.5$, $V_s/V_\infty = 1.5$

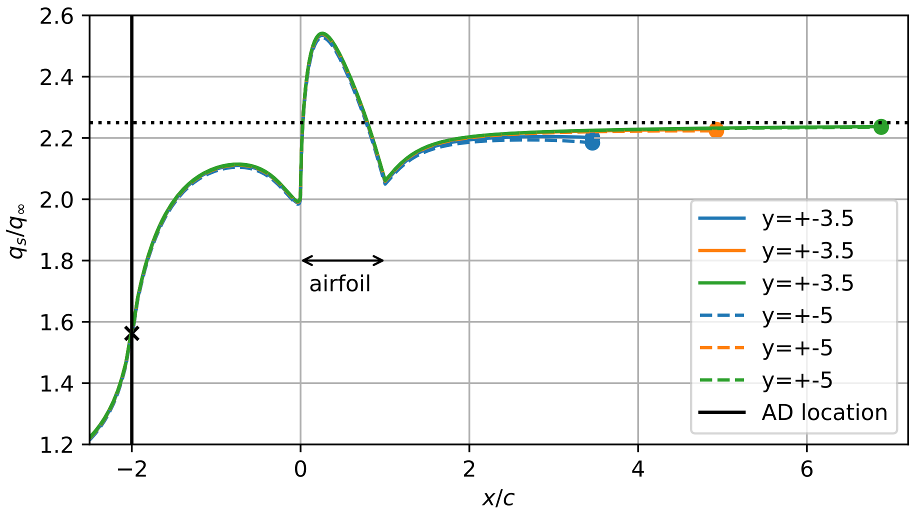

Figure 5.27: Effect of XOUT and Y limits. NACA0012 included. $D/c = 1.0$, $V_s/V_\infty = 1.5$

Effect of vertical boundaries and outlet boundary In fig. 5.27 the effect of the outlet size in relation to the domain height is tested. The smaller outlet leads to a lack of velocity recovery, which becomes aggravated by a larger vertical domain. However, the solution near the airfoil is barely impacted: Apparently, the vertical extent was sufficient, and the relationship between these and the length of the outlet plays an important role directly aft of the airfoil. It seems advisable that the outlet be equal to the total vertical extent of the domain to ensure maximum velocity recovery at the outlet, though less (in the order of $ytop$ or $ybot$) may be acceptable when considering the flow at the airfoil only.

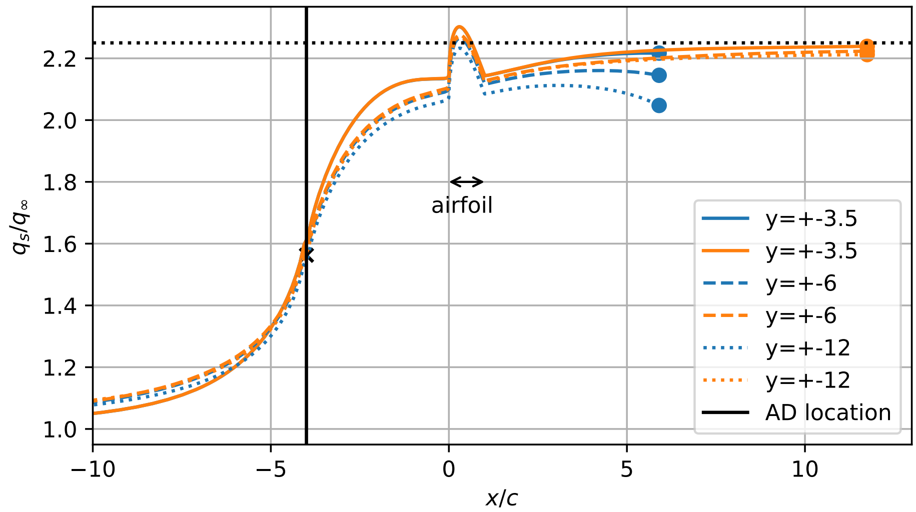

Figure 5.28: Effect of XOUT and Y limits with large AD. NACA0012 included. $D/c = 4.0, V_s/V_\infty = 1.5$

Effect of AD size In fig. 5.28 the AD is 4x taller, leading to the need for a much larger domain. Here, the value of the outlet length and vertical extent are varied once again. It can be seen that a vertical extent of at least $y = +-6$ (3x the radius) is required: for smaller vertical domains, the contraction occurs quicker. This indicates that the momentum of the streamlines outside of the smaller domains is not considered, including this slows the contraction process. A smaller exit decreases the amount of velocity recovered, especially for the larger vertical domain. It is recommended to apply at least $1.5ytop$ (or $1.5ybot$) spacing, but the exact relationship is not clear.

5.5.3. Pre-contracted slipstream

With the pre-contracted slipstream, the velocity increase is added at the inlet. This results in the slipstream being readily contracted, which should only require some extra vertical spacing of the domain to facilitate the higher amount of momentum in the slipstream (i.e. the grid shrinkage discussed in section 5.4.2). The inlet size has indirect impact on the lifting performance due to vertical displacement of the slipstream due to airfoil upwash. Fortunately, this effect can be isolated for smaller offsets by using to the constraint introduced in section 5.3. The effect of constraining the slipstream at various offsets will be tested in this section. The setup for two equivalent cases with the slipstream constrained at $X/c = -2$ are shown in fig. 5.29 and fig. 5.30.

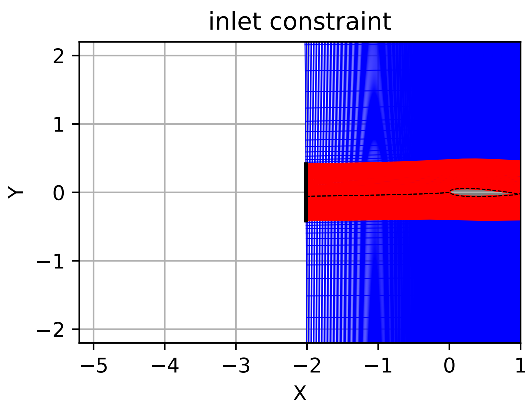

Figure 5.29: NACA0012 streamline grid constrained at inlet. $h/c = 0.833, \alpha = 2°, V_s/V_\infty = 1.5$, at $M_\infty = 0.15$

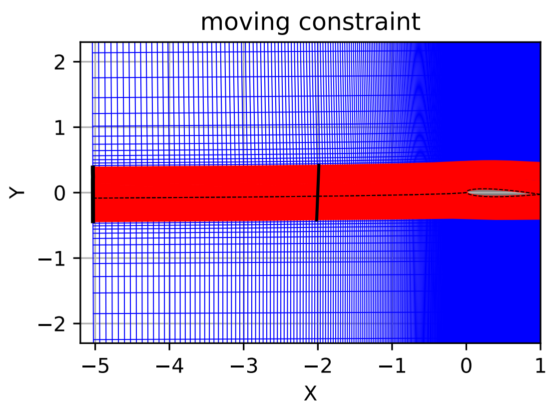

Figure 5.30: NACA0012 streamline grid constrained in the domain. $h/c = 0.833, \alpha = 2°, V_s/V_\infty = 1.5$, at $M_\infty = 0.15$

A smaller range of parameters than for the free-AD is investigated here. The lift is determined for the slipstream height of $h/c = 0.833$ and $\alpha = 2°$, note that this slipstream height is the contracted height for an AD of height 1 at $V_s/V_\infty = 1.5$. This is done for a small and large outer domain, and a range of inlets as shown in fig. 5.31. The "moving constraint" case will use the small and large domain, both with $xin = -5$. The results for both constraints should be similar but only the latter is suitable for constraint positions closer than 2 chords to the airfoil.

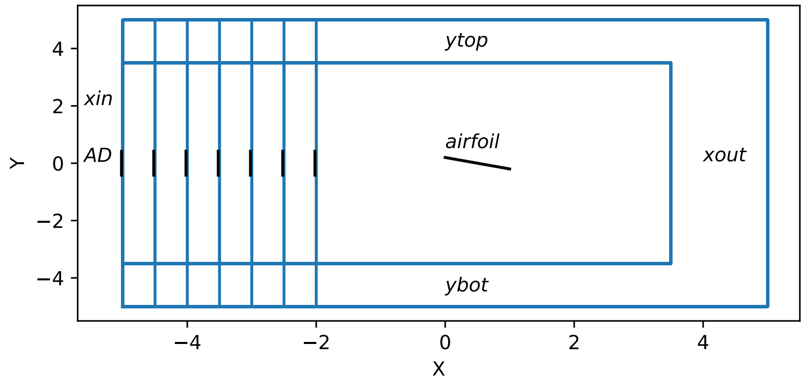

Figure 5.31: Domains tested with the pre-contracted AD ($h/c = 0.833$).

The results in terms of c_l are shown in fig. 5.32 and the data is again included in appendix B. Note that indeed the solutions are very close. The larger domains (in terms of $ybot, ytop, xout$) show slightly higher lift coefficient. The lift coefficient decreases upon getting closer to the airfoil, as there is less slipstream deflection and uppper surface blowing. Upon getting closer to the airfoil the influence of its circulation is stronger: integrating the circulation on positions closer to the airfoil results in a more rapid decrease in total vertical displacement of the slipstream from thereon. Blockage near the airfoil may also lead to a smaller slipstream as the streamlines are displaced away from the constraint, leading to a slipstream with effectively lower h/c. The lines may be expected to level off more towards the left part of the graph at high offset. Note that the effect is quite limited for this slipstream height and angle of attack. The marker indicates the result measured in section 6.4.1: knowing the unblown lift, this data may be converted to the lift factor K_l.

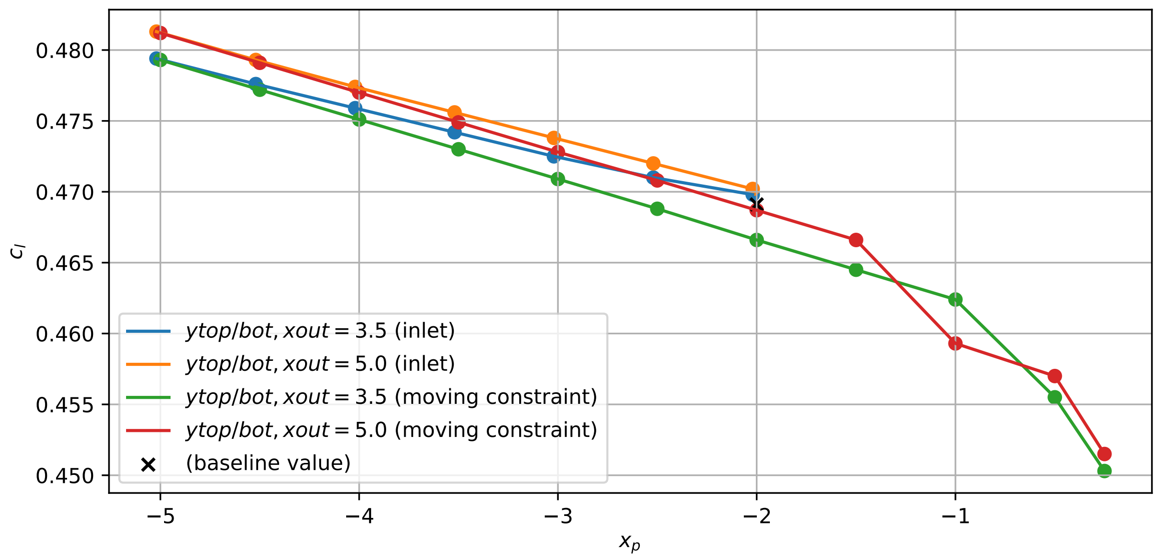

Figure 5.32: Results for the various domains with the developed slipstream. NACA0012 $h/c = 0.833, \alpha = 2°, V_s/V_\infty = 1.5$

II

Single-element airfoil

6

Inviscid results & validation under uniform slipstream

This chapter aims to explore and validate results for low-lift conditions with a single airfoil, the NACA0012. The lifting performance of this airfoil is compared to the CFD results of Nederlof [28] and Patterson [27]. 2D CFD results of slipstreams are quite rare as slipstream interaction problems are strongly governed by asymmetric, 3-Dimensional effects. The implication is that there is limited material for reference. The same holds for wind-tunnel experiments on airfoil sections approaching the 2D case.

Chandha [80] performed both 2D and 3D RANS CFD simulations on a symmetrical airfoil in a propeller slipstream at different thrust ratios and angles of attack. Unfortunately, for comparison with the current MSES set-up, the tests are not suitable: The actuator disk is rotated with the airfoil and changes the effective angle of attack perceived by the airfoil. These may be used at a later stage, in case angle of attack effects on the actuator disk are somehow simulated or modeled in MSES.

Prabhu [56] applied mirrored images as published in 1984, similar to the recent work of Nederlof [28]. The results were compared with results from a modified NASA Euler solver. The lift slope on a NACA0012 was determined for a uniform and a non-uniform flow profile, with the same conclusion that upwash may slightly change results of the Euler simulation w.r.t. the mirrored images. A pressure difference distribution is also included. This material is not used in this thesis as sufficient confidence is gained from the comparison with the CFD results of Nederlof.

6.1. Effect of finite slipstream height on lift

The finite nature of a slipstream limits the lifting capability of airfoils immersed in a slipstream, which may lead to the over-estimate of lift, if neglected. This section seeks to show the effects and validate it with the CFD results from Nederlof [28]. The role of domain size/angle of attack and compressibility is also investigated.

6.1.1. Validation with CFD results of Nederlof

Setup In order to compare the results with the CFD and mirrored image results of Nederlof [28], it was desired to have a fully developed, uniform slipstream to assess the influence of the slipstream height. To this end, the slipstream (i.e. the enthalpy jump) was defined at the inlet of the domain. If this were to be defined elsewhere, slipstream contraction would occur, as the mass-flow is determined at the inlet of the domain.

Care should be taken to define the location with respect to the freestream, i.e. translating the propeller, as the coordinate system of MSES is centered around the airfoil Leading Edge (LE). This is done by shifting the AD downward for positive angle of attack. The perturbation due to upwash however, is assumed small and is not accounted for during these low-lift conditions with the NACA0012 airfoil. The reason the Mach number is set to just 0.015 is to rule-out compressibility effects

Up to $h/c = 2.0$ the domain size is identical to the convergence study (section 5.4.3) at a domain size of $[xmin, xmax, ybot, ytop] = [-2.0, 3.0, -3.0, 3.5]$. For $h/c > 2.0$ the vertical domain extent is increased to

$[ybot, ytop] = [-7.0, 7.0]$ to account for the vertical grid shrinkage. Else, the lift would be underestimated, as was noticeable for $h/c = 6$. The other grid settings are the same to the convergence study with $J_{max} = 100$ streamlines.

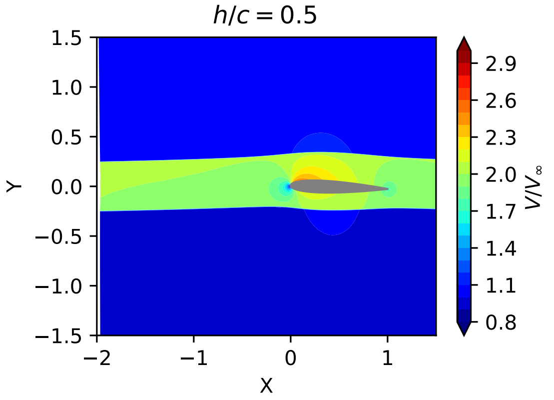

Figure 6.1: Smaller slipstream at $V_s/V_\infty = 2.0$. NACA0012 $\alpha = 2°, M_\infty = 0.015$

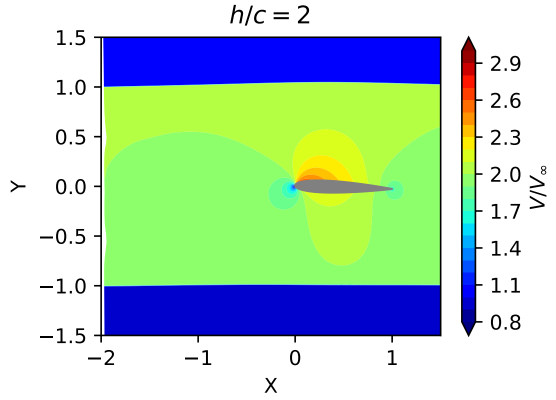

Figure 6.2: Larger slipstream at $V_s/V_\infty = 2.0$. NACA0012 $\alpha = 2°, M_\infty = 0.015$

Results The resulting velocity field is shown in fig. 6.1 and fig. 6.2. The lifting results are shown in fig. 6.3: The lift factor K_l is defined as the ratio of the sectional lift obtained with a slipstream compared to that obtained in the freestream as in eq. (6.1a). The baseline lift coefficient was established to be 0.24073. Note that the lift factor should lie between $K_l = 1.$, which means no increase in lift, and $K_l = [2.25, 4.0]$, which are the result of squaring the velocity ratio V_s/V_∞, which is the dynamic pressure ratio q_s/q_∞. These upper values are assumed to be reached at higher slipstream heights, equivalent to a slipstream of infinite height. The maximum K_l of 3.96 seems reasonably close to the expected maximum value of 4.0.

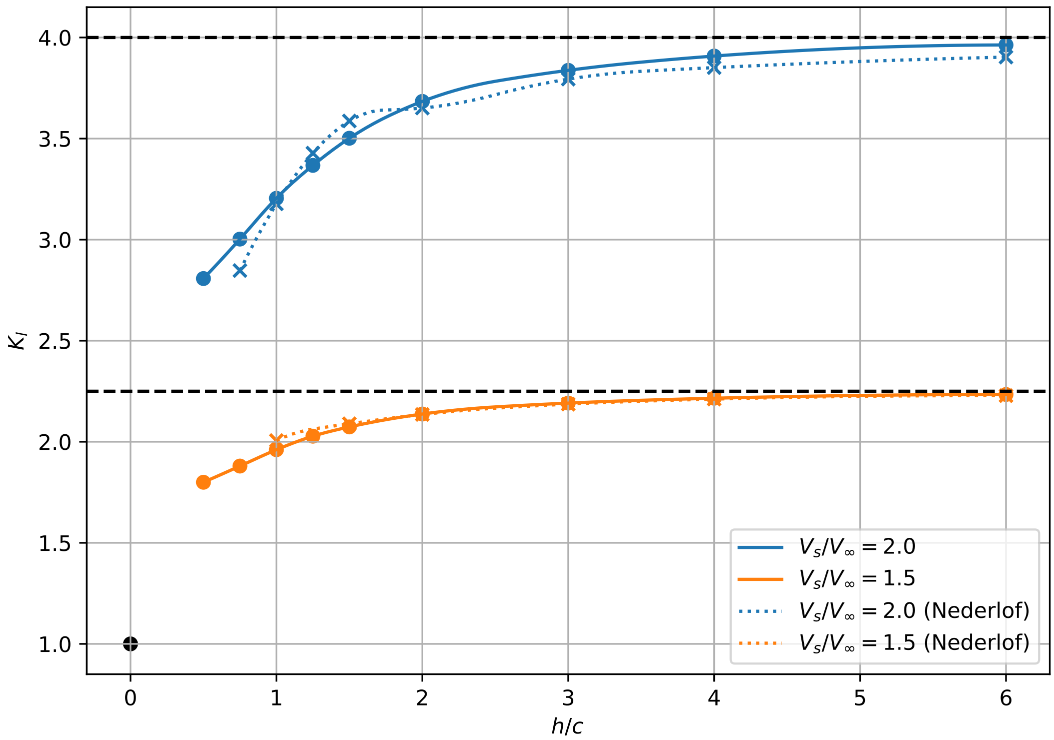

Figure 6.3: Effect of slipstream height on the lift factor. NACA0012 $\alpha = 2°, M_\infty = 0.015$ (virtually incompressible)

Nederlof [28] conducted 2D CFD simulations of an airfoil suspended in 2D, solving the incompressible Euler equations, hence assuming inviscid flow. Tests were performed on a NACA0012 airfoil at 2° angle of attack. These simulations are used as the benchmark for the single airfoil tests performed with MSES. The results are also shown in fig. 6.3. They show a good match at both velocity ratios with the MSES solution being smoother than that of the CFD campaign. Note that the double-exponential spacing was required for obtaining smooth results. It may be concluded that, for a low-lift setup, MSES can capture the effects of a uniform slipstream at inviscid, incompressible conditions to the same extent as CFD simulations.

One may expect the results to monotomically decrease towards 0 as the h/c is decreased further. This was also the result for the successive reflections tested by Nederlof as discussed in section 3.3.1. This is however not the case for small slipstream ratios due to the upper surface blowing effect: the slipstream is constrained at the inlet and is allowed to pass over the upper surface of the airfoil, boosting the wings lift. This explains why the MSES values for $h/c = 0.5$ are higher than otherwise expected. Lower lift values are obtained if the slipstream is constrained closer to the airfoil. In CFD simulations Nederlof also observed the upper surface blowing effects. For a small slipstream height of $h/c = 0.25$ he observed a lift increase close to the theoretical maximum for an infinitely large slipstream.

6.1.2. Sensitivity analysis

Alternatively, one may express the increase in lift by an effective velocity increase, as used extensively by Patterson [27]. Using this factor makes it easier to compare results across different velocity ratios. Patterson defines β as the induced velocity multiplier, hence, $\beta = 0$ would imply no effective velocity increase, and $\beta = 1$ would imply the full propeller velocity increase. Its effect on the effective lift increase is obtained by the ratio of the dynamic pressures, as illustrated by eq. (6.1a). Note that the velocity increase is noted as twice the induced velocity ω: $V_s - V_\infty = 2\omega$. One may obtain β from K_l as shown in eq. (6.1b)[27].

$$K_l = \frac{C_{l,blown}}{C_{l,unblown}} = \left[\frac{V_\infty + 2\omega\beta}{V_\infty}\right]^2 \tag{6.1a}$$

$$\beta = \frac{\sqrt{K_l} - 1}{V_s/V_\infty - 1} \tag{6.1b}$$

To bridge the gap between the preceding analysis and the comparison to Patterson [27], it is useful to consider the behavior of the induced velocity multiplier β and the impact of small changes of the setup for a pre-contracted slipstream. The set-up is identical to the aforementioned slipstream height experiments, meaning that for $h/c > 2.0$, the grid height is increased to $+/-7$. This time, a variation in one parameter is performed to assess the impact of compressibility, a larger grid and larger α. It is important to re-iterate that the slipstream is positioned with respect to the free-stream, and not the airfoil. Maximum theoretical limits to β due to compressibility may be expressed by eq. (6.3) which is obtained by using the Prandtl-Glauert (PG) correction shown in eq. (6.2) with the slipstream Mach number.

$$c_l = \frac{c_{l,0}}{\sqrt{1-M^2}} \tag{6.2}$$

$$\beta_{max} = \frac{\sqrt{K_{l,max} \cdot PG} - 1}{V_s/V_\infty - 1} = \frac{V_s/V_\infty (1-M^2)^{-1/4} - 1}{V_s/V_\infty - 1} \tag{6.3}$$

The results are shown in fig. 6.4, the impact of each change is explained below:

- **Larger velocity ratio:** Changing the velocity ratio V_s/V_∞ has little impact on the solution in terms of β. This makes β a good non-dimensional measure.
- **Higher Mach number:** There is a vertical shift compared to the low-Mach results. This is largely explained by the compressibility effect: the new limit determined with eq. (6.3) indeed holds for large slipstreams.
- **Larger domain:** For the smaller AD heights $[xmin, xmax, ybot, ytop] = [-12.0, 12.0, -6.0, 6.0]$ and for $h/c > 2.0$ $[ybot, ytop] = [-12.0, 12.0]$. This has a clear effect on lift for the small h/c values: flow can gain more upward deflection due to the AD being farther away. Numerically, the solution may be less accurate as noted in the convergence study section 5.4.3.
- **Larger α:** This was expected to increase lift due to increased upper surface blowing caused by upwash associated with this higher α. There is visible slipstream deflection, similar in magnitude to the "larger domain" case, but why this fails to result in a lift increase is not clear. Patterson also noted small variation in results with α except for very small h/c values. [27].

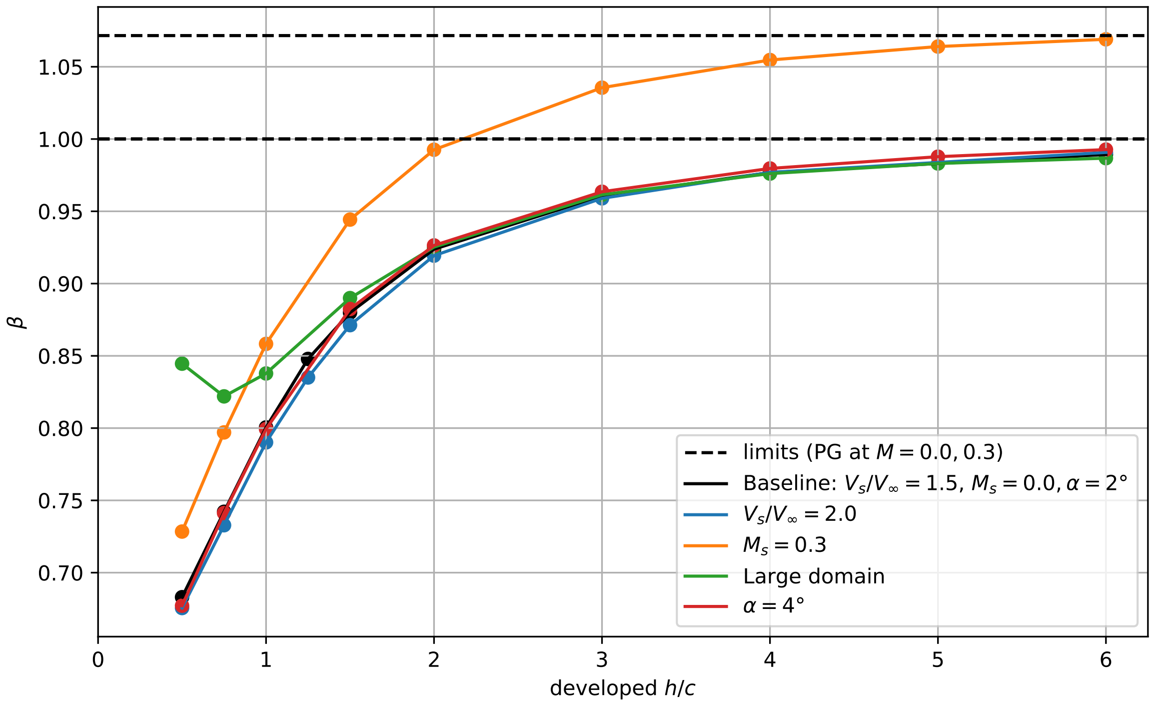

Figure 6.4: Impact of pre-contracted slipstream height on β. NACA0012

Finally, it should be noted that the result will also be shifted if contraction is accounted for. The transfer between developed slipstream height, and AD height is shown in eq. (6.4).

$$\frac{h}{D} = \frac{1+a}{1+2a} \tag{6.4}$$

6.2. Effect of vertical offset on lift & pressure distributions

In this section, a sweep of vertical slipstream positions is investigated. The viscous results are included for comparison but are considered in much more detail in chapter 7.

6.2.1. Lift & comparison to APROPOS

For this experiment, the NACA 0012 airfoil is submerged to a fully developed slipstream, 2 chord lengths ahead, similarly to the previous experiment on the effect of slipstream height, with $V_s/V_\infty = 2$. The vertical extent of the grid is set to $[ybot, ytop] = [-3.5, 3.5]$ The extreme positions are shown in fig. 5.14 and fig. 5.15.

The converged results for the slipstream are shown in fig. 6.5 and fig. 6.7. For certain raised propeller positions (as seen for $z_p/c = 0.3$ and $z_p/c = 0.4$), the increased suction on the top surface increases the lift factor K_l to values above the theoretical maximum of 4, this effect drops off as the propeller slipstream is raised more and loses contact with the airfoil upper surface. The higher lifting effect of increased suction was also noticed by Nederlof [28] and by Patterson [27]. Also note how blowing may decrease the lift of the airfoil at lower angles of attack.

As reported by Veldhuis [40], the APROPOS experiments also tested the effect of vertical offset for changing alpha as shown in fig. 6.6. Note that the results for lift also clearly indicate the same S-shape curve of decreasing and increasing lift moving the propeller upward. Also note that the peak shifted slightly leftward, as with the MSES result, though for the MSES results at $\alpha = 4°$, the lift decrease is smaller.

Viscosity The dashed lines indicate results with the viscous boundary layer enabled, triggered at the LE. Note that this always leads to lower lift, seen in fig. 6.5. However, the lift increase relative to the unblown case can be improved if the airfoil is fully submerged in the slipstream, as is the case for some values in fig. 6.7. Note that not all cases converged, especially for the the $\alpha = 6.0$ line.

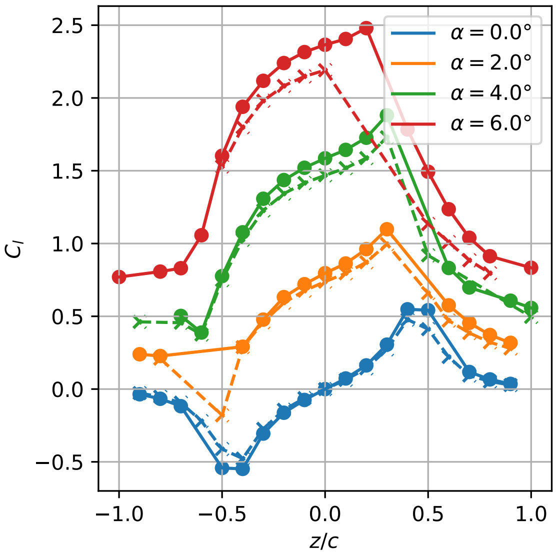

Figure 6.5: Effect of vertical propeller offset on the lift coefficient. NACA0012 $M_\infty = 0.15, V_s/V_\infty = 2$. dashed lines: $Re = 2.51e6, n_{crit} = 3.0$

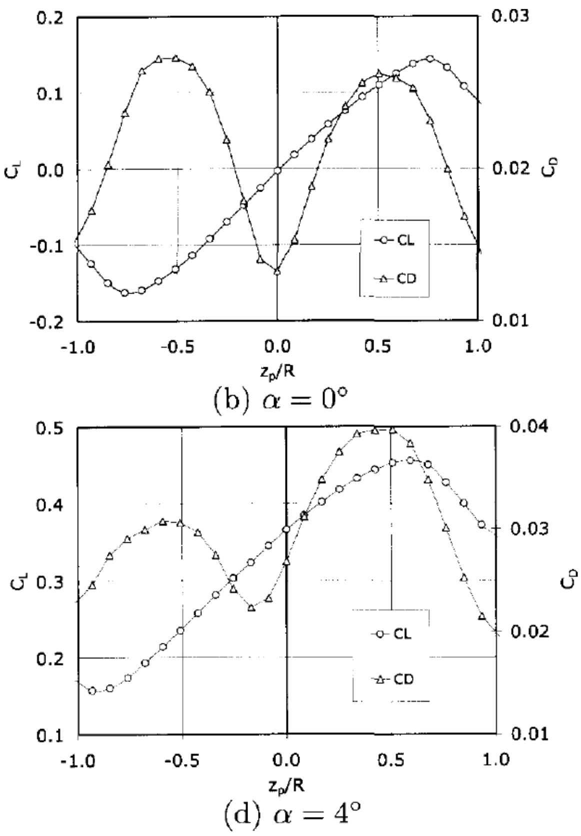

Figure 6.6: "Effect of propeller vertical position on the lift and drag coefficient of the APROPOS wing ... high thrust ($J = 0.433; T_c = 0.985$)" (Veldhuis [40])

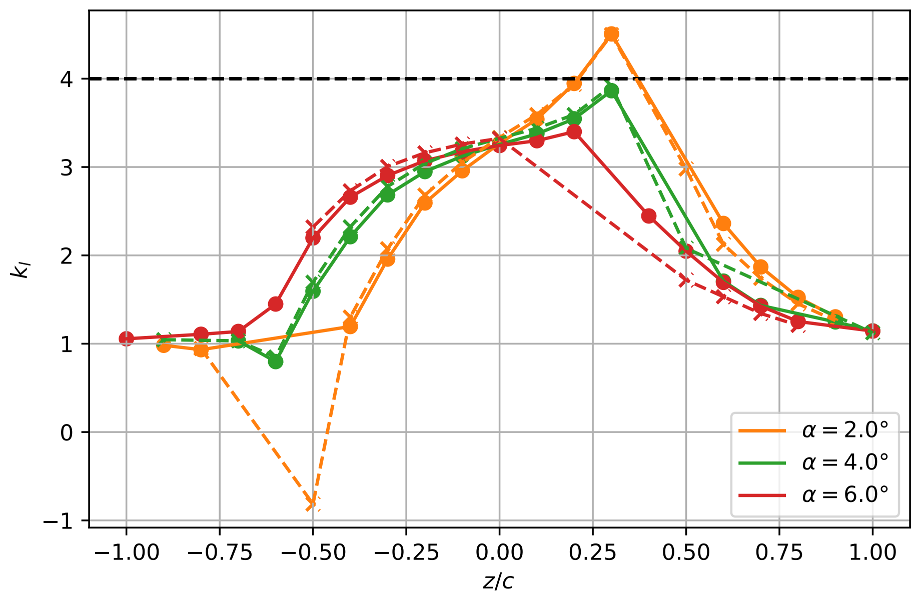

Figure 6.7: Effect of vertical propeller offset on the lift factor. NACA0012 $\alpha = 2°, M_\infty = 0.15, V_s/V_\infty = 2$. dashed lines: $Re = 2.51e6, n_{crit} = 3.0$

6.2.2. Pressure distributions

The pressure coefficients for the marked inviscid flow cases are shown in fig. 6.8. The value of maximum and minimum pressure exactly follow the dynamic pressure increase (factor 4) in case of the airfoil centered in the slipstream, however, the pressure distribution is not a perfect scaling, else a K_l of 4 would also be achieved here. The case producing highest lift, where the slipstream is just above the airfoil ($z/c = 0.4$), does not have the increase in stagnation point pressure. The decreased suction on the lower surface in the $z/c = 0.4$ case may be explained by the higher circulation. Details on the boundary layer development are included in chapter 7.

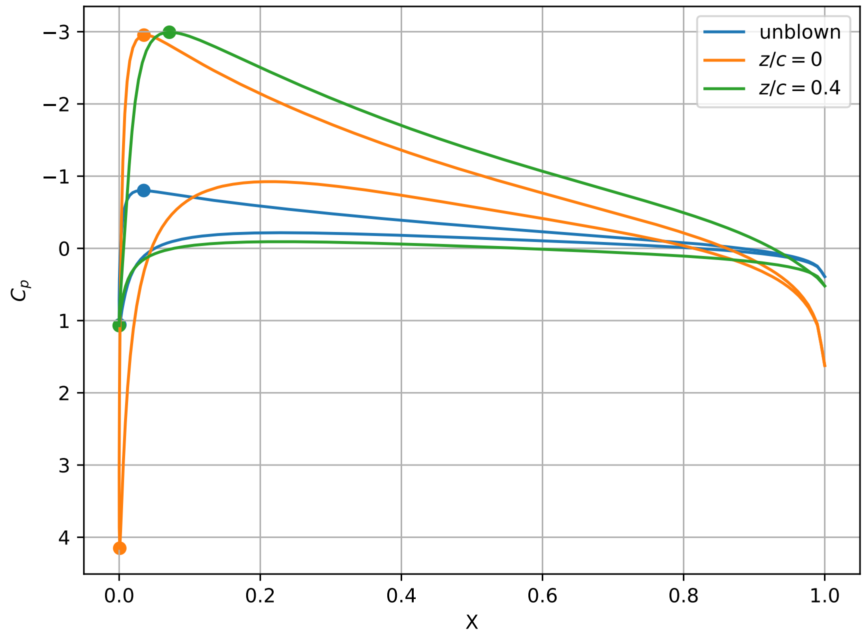

Figure 6.8: Pressure distributions around the NACA 0012 airfoil for different propeller positions. $\alpha = 2°$, $M_\infty = 0.15$, $V_s/V_\infty = 2$.

6.3. Slipstream contraction effects

This section investigates the contraction characteristics for an AD in MSES in a symmetrical setup. The effective lift augmentation may be predicted from the symmetrical slipstream development. The prediction through this lift augmentation is compared to a direct MSES simulation of an airfoil under angle of attack in the next section.

6.3.1. Symmetric contraction velocity development

The properties of the streamtube under contraction are compared to analytical models to determine both the impact of 3D assumptions and to determine how closely the match to the 2D model is. A contraction model may be used in cases where modeling contraction in MSES would not be desirable. The effect of non-axial development is also considered: this is useful knowledge in case the airfoil is close to the AD and not in the center of the slipstream.

Setup As already established in the domain study section 5.5 the free-contracting cases require far larger domains than the cases with fully developed slipstreams. For the high-speed case the domain size used is $[xin, xout, ytop, ybot] = [-15, 14, -7, 7]$ and for the low speed case $[xin, xout, ytop, ybot] = [-10, 7, -3.5, 3.5]$. A close-up of the resulting grid is shown in fig. 6.9.

ESDU85015b [39] shows that contraction takes place 2 diameters upstream and downstream. To enable proper comparison, the simulations are run with a uniform AD. A very thin wing (NACA 0001) is included to be able to run the simulation, at 0 angle of attack. The new double exponential option is very helpful in obtaining sufficient resolution around the AD edges. J_{max} was set to 100 (split 50/50.) It was challenging to a obtain a sufficiently straight disk. A satisfactory result was obtained by increasing I_{max} to 200 in the left domain, and setting the X-Factor to 1.0.

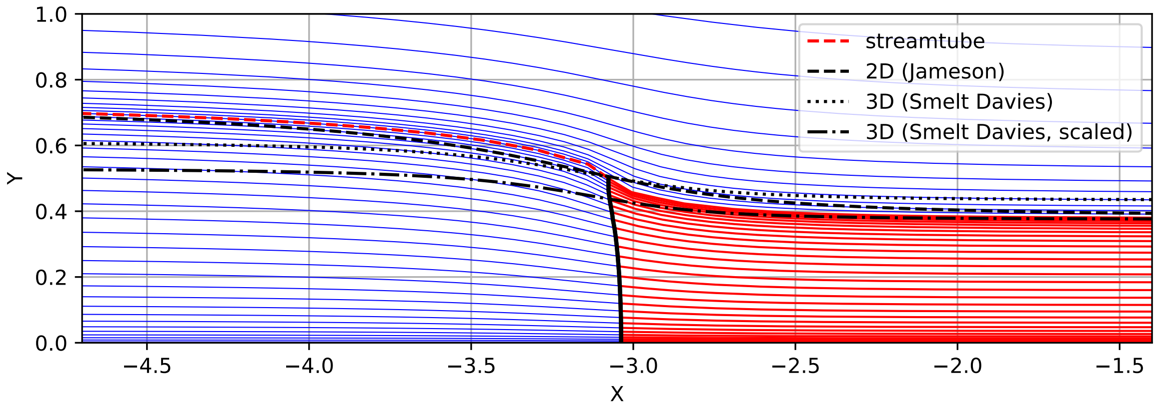

Figure 6.9: Slipstream showing contraction (NACA 0001 included). $V_s/V_\infty = 2.0, D/c = 1.0, \alpha = 0°, M_\infty = 0.15$

Symmetrical results In fig. 6.9, the resulting flowfield is shown. Wake contraction is clearly visible when putting the AD away from the left boundary of the domain. Far upstream and downstream there is a good match with the expected 2D results of Jameson. However, near the AD, contraction occurs much more sharply than expected from any other model. It is also interesting to compare with the 3D case, which, by definition, shows less contraction, as explained before. As the velocity downstream is of particular interest, it seems most logical to scale the actuator disk such that the slipstream height downstream be matched to the 3D case. The figure shows that downstream, the slipstream height becomes equivalent to a 3D problem with an AD of diameter $D/c = 0.866$ after about half a chord downstream, which seems to be the most accurate representation for practical propeller offsets of $x/c > d/2$.

In fig. 6.10 the angle of attack variation due to contraction is shown, for the radial postion of $0.5r$. This shows that the angle of attack variation is highly significant close to the propeller, but is reduced to $\alpha = 2$ at about 1 radius behind the actuator disk. This shows that the effect is limited provided that the airfoil is not too close to the actuator disk or the edges of the slipstream.

In fig. 6.11 eq. (3.2) is tested against velocity development in MSES. It is confirmed that contraction occurs much quicker than in the analytical model and the observed velocity lies around 10% of V_∞ higher than the model of Jameson just aft of the actuator disk. Remarkably, eq. (3.1b) shows a very good match with the MSES data downstream despite describing a 3D phenomenon, note once more that the scaled variant describes a slightly smaller AD of size $D/c = 0.866$. Note also the disturbance due to the presence of the NACA0001 airfoil between x=0 and x=1. The velocity near the inlet is slightly higher than expected from the downstream condition: this may be due to the boundary condition near the inlet, or the presence of the airfoil.

In fig. 6.12 the velocities at various horizontal stations are shown. It can be seen that near the edges of the AD the velocity is non-axial (i.e. tilted inward) but this effect vanishes very quickly. A velocity profile 1 diameter further away is of particular interest: there is already 95% velocity recovery but a 10% velocity deficit just outside of the wake.

The influence of the actuator disk on the inlet is noticeable as well: at the center there is a velocity increase of 6%. A small velocity deficit of approximately 98% recovery is retained past the airfoil and increases slightly towards the exit: Both these observations may have to do with the boundary conditions in the aforementioned section. The farfield streamlines are free to move: the (standard) infinite-flow farfield boundary condition is used as for all other MSES runs.

In conclusion It seems that for the symmetrical flow-case considered, MSES can give a reliable estimate of mean slipstream velocity and height development, also pertaining to a 3D provided that the AD is scaled: However, this is only applicable from about 1 diameter downstream, the exact accuracy cannot be assessed due to the influence of the airfoil and far-field boundary conditions. It is expected that this velocity development could give an indication for β, provided that the effect of finite slipstream height is also considered. It is again recommended to use 2D CFD validation material.

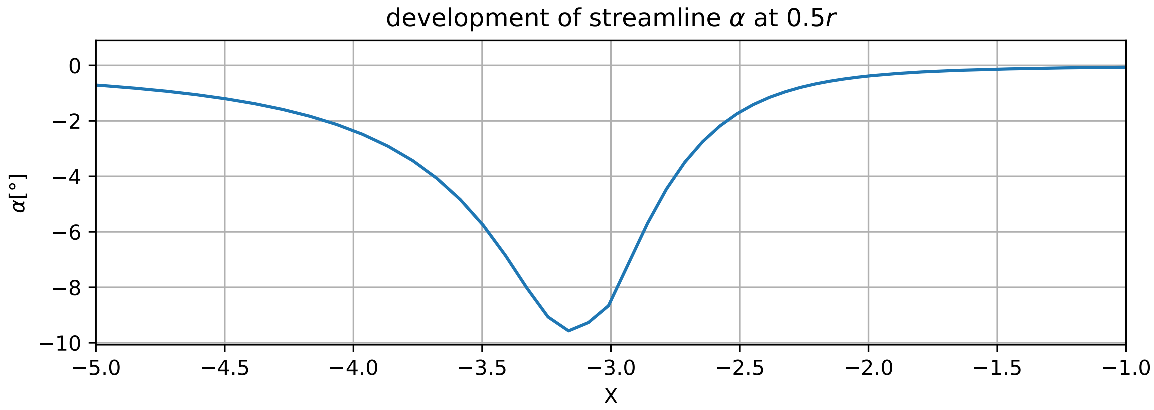

Figure 6.10: Angle of attack development due to contraction at 0.5r (NACA 0001 included). $V_s/V_\infty = 2.0, D/c = 1.0, \alpha = 0°, M_\infty = 0.15$

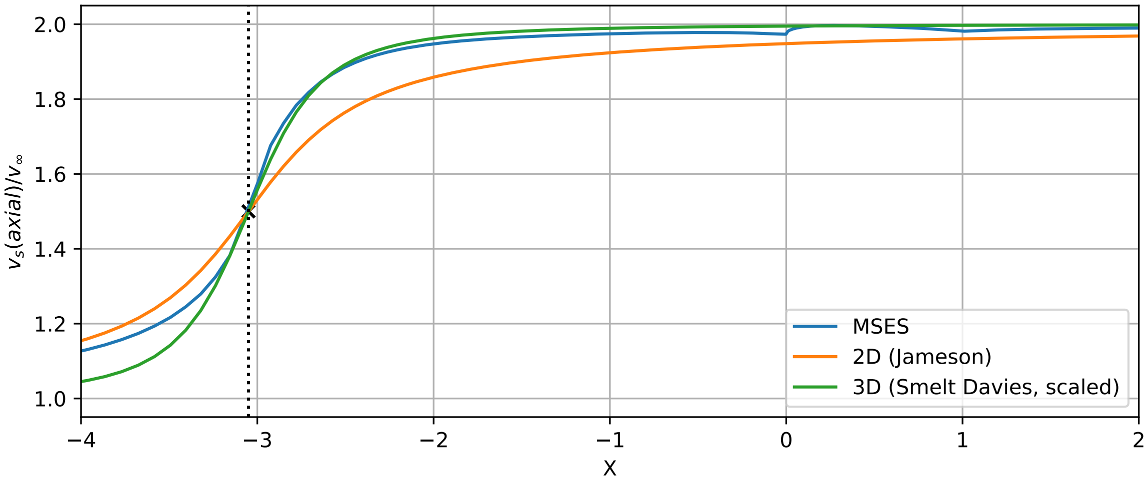

Figure 6.11: Mean axial slipstream velocity (NACA 0001 included). $V_s/V_\infty = 2.0, D/c = 1.0, \alpha = 0°, M_\infty = 0.15$

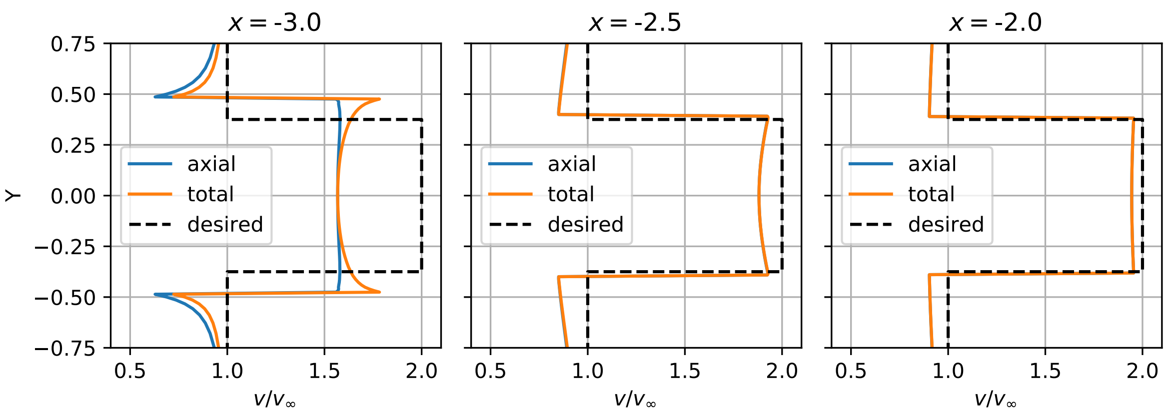

Figure 6.12: Velocity development in detail. $V_s/V_\infty = 2.0, D/c = 1.0, \alpha = 0°, M_\infty = 0.15$

6.3.2. Development of dynamic pressure & anticipated lift augmentation

The dynamic pressure increase in the slipstream may be obtained similarly to the velocities in the previous subsection. Simulations are also performed for a velocity ratio of $V_s/V_\infty = 1.5$ to allow for comparison. One may characterize the lift augmentation by an "effective" dynamic pressure increase. The relationship between dynamic pressure in the slipstream and lift augmentation is not as straightforward as it may seem, the considerations are as follows:

- **Offset** To determine the dynamic pressure increase with offset a representative chordwise location should be selected for probing the velocity increase as the slipstream may still be contracting in the region of the airfoil. It is assumed most appropriate to consider that the dynamic pressure increase is perceived at $0.25c$ rather than at the nose.
- **Height effect** More correct would be to include the effective velocity increase β into account when determining the equivalent slipstream q_{eff} to consider the effect of the limited slipstream height. The anticipated rise in q may be determined using the β factor as shown in eq. (6.5). For the case under consideration, it may be determined from fig. 6.4 that for a developed slipstream height of 0.833, $\beta = 0.75$ would be an appropriate guess, without further regard for vertical slipstream displacement in the domain. It was actually observed that $\beta = 0.78$, and subsequently updated.
- **Vertical displacement/blowing** As seen in section 5.5.3 the effect is small, but not negligible.
- **Velocity deficit outside of the wake** This is neglected: the extent is limited and not easily quantifiable: this would lead to a slight decrease in lift.

$$\frac{q_{eff}}{q_\infty} = \left(\frac{V_\infty + \beta \Delta V}{V_\infty}\right)^2 \tag{6.5}$$

The results of including β to arrive at the effective dynamic pressure increase is plotted in fig. 6.13. This is roughly equal to the lift increase that may be expected as will be included in the next section. To this end, the survey points with the different coordinates used later are indicated as well. Note that these results do not consider the effect of the velocity deficit directly outside of the wake. The development of the dynamic pressure due to axial velocity over the height of the slipstream (i.e. dynamic pressure profile) is also of interest and is considered next.

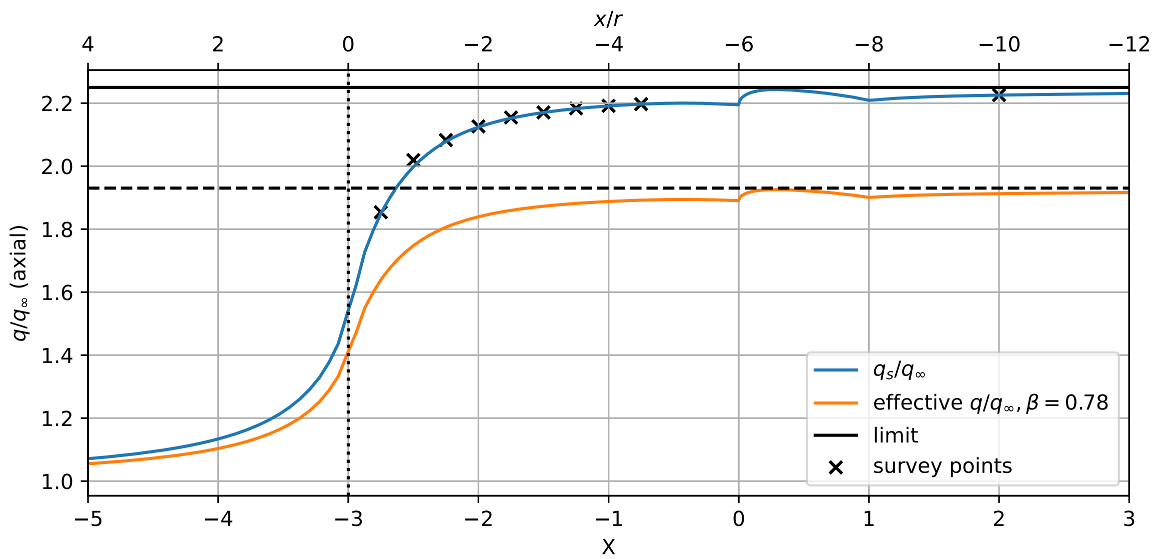

Figure 6.13: Mean dynamic pressure (NACA0001 included). $V_s/V_\infty = 1.5, D/c = 1.0, \alpha = 0°, M_\infty = 0.15$

The dynamic pressure development is very similar for different pressure ratios, as seen in fig. 6.14. Note that these are scaled for different contraction and magnitude. The axial Δq profile for $v_s/v_\infty = 2.0$ is smoother on the inboard side of the slipstream boundary than for $v_s/v_\infty = 1.5$ at $x = -3.0$. It seems that the final dynamic pressure is approached more slowly for the low speed case.

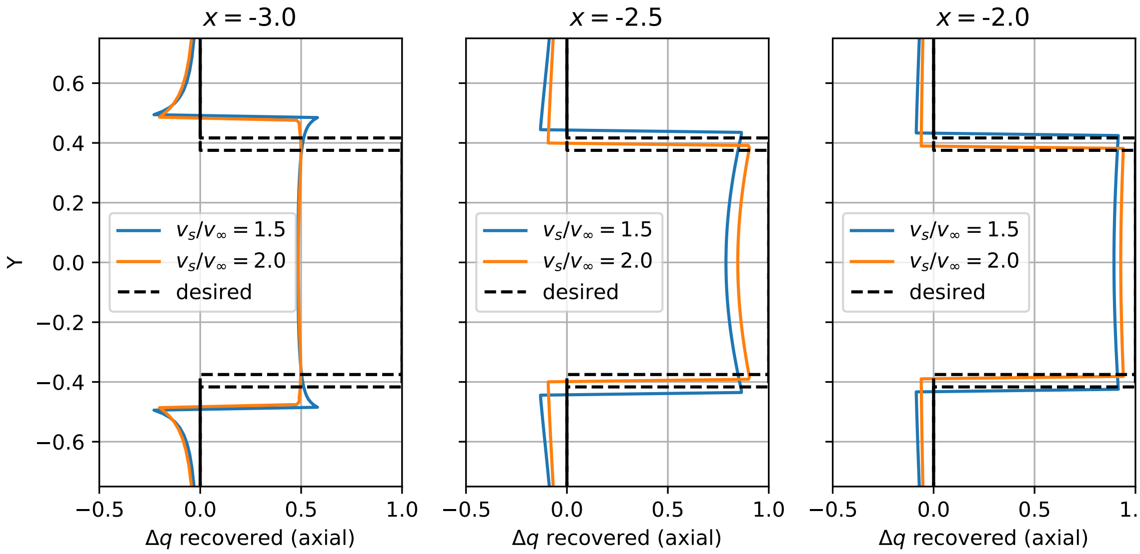

Figure 6.14: Dynamic pressure development in detail for $V_s/V_\infty = 1.5$ and $V_s/V_\infty = 2.0$. $D/c = 1.0, \alpha = 0°, M_\infty = 0.15$

The lack of velocity right outside of the slipstream is plotted in fig. 6.15. The contribution of the velocity (just) outside the streamtubes depends on the operating point of the airfoil/AD and no procedure is found to exist to determine how much impact this velocity deficit may have. The total q component around the AD edges is slightly larger than the axial component as the streamlines locally have a significant inward slope.

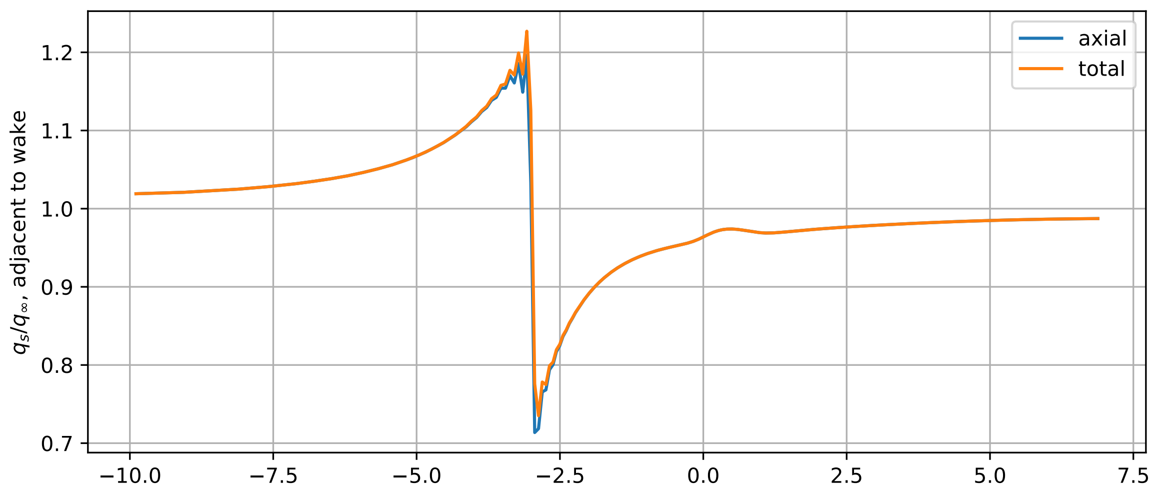

Figure 6.15: Dynamic pressure deficit just outside the slipstream (NACA0001 included). $V_s/V_\infty = 1.5, D/c = 1.0, \alpha = 0°, M_\infty = 0.15$

6.4. Effect of horizontal offset on lift

This section compares the effect of horizontal offset on lift in MSES simulations (which are 2D) to 3D VLM results to see how these relate. The MSES results of a lifting airfoil are also compared to those obtained by adding an unblown airfoil and compensating for the "effective dynamic pressure" as suggested by section 6.3.2. This may demonstrate that under certain conditions a free contraction case may be approached by combining the results of a simulation with a fully developed slipstream with a contraction model.

6.4.1. Comparison to Veldhuis & symmetrical results

This time, the airfoil is placed under angle of attack to produce an asymmetrical flowfield. The standard case is tested of a NACA0012 airfoil with a propeller $D/c = 1.0$. The number of inlet points is set to 100, and the streamlines are split 40/30 between the top and bottom domain. The free-stream angle of attack is varied from 0° to 5 °, at a velocity ratio of $V_s/V_\infty = 1.5$, at $M_\infty = 0.15$. Note that this is lower than the low-speed case of Veldhuis ($v = 75m/s$)[40], but it allows for better comparison with previous results. For all simulations, the domain size is set to $[xin, xout, ytop, ybot] = [-7, 7, -5, 5]$. A close-up of the grids is shown in fig. 6.16 & fig. 6.17. The resulting velocity fields are shown in fig. 6.18 & fig. 6.19.

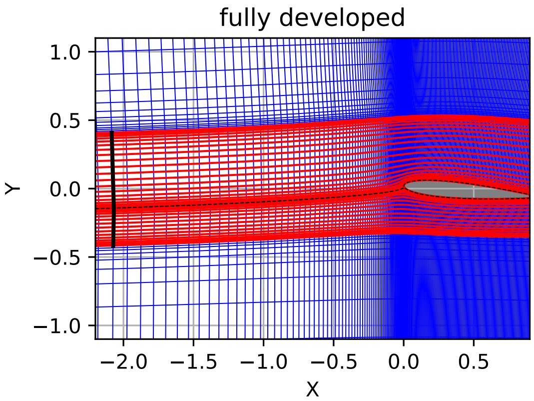

Figure 6.16: NACA0012 streamline grid with fully developed slipstream. $V_s/V_\infty = 1.5$, at $M_\infty = 0.15, \alpha = 5°$

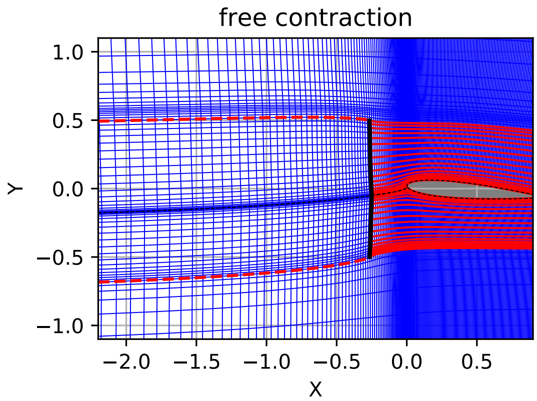

Figure 6.17: NACA0012 streamline grid for $x/r = -0.5$. $V_s/V_\infty = 1.5$, at $M_\infty = 0.15, \alpha = 5°$

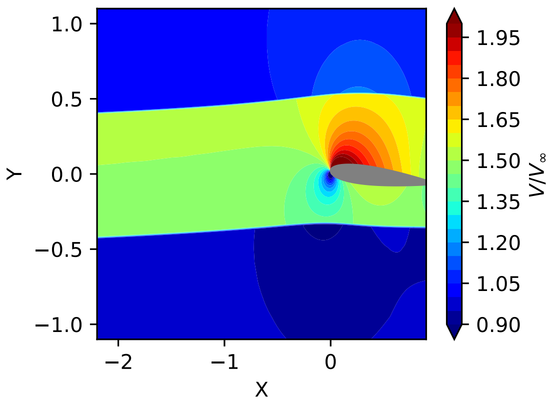

Figure 6.18: NACA0012 velocity field with fully developed slipstream. $V_s/V_\infty = 1.5$, at $M_\infty = 0.15, \alpha = 5°$

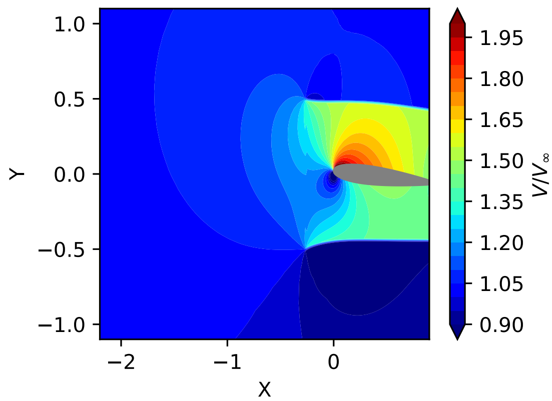

Figure 6.19: NACA0012 velocity field for $x/r = -0.5$. $V_s/V_\infty = 1.5$, at $M_\infty = 0.15, \alpha = 5°$

Comparison to Veldhuis: Veldhuis [40] presented the effects of horizontal offset as shown in fig. 6.20 this is the VLM result for a Fokker-50 like configuration. The results are standard at the results where the propeller is 1 diameter (2 radii) ahead of the wing/airfoil. Note that the results of Veldhuis indicate little difference between the low-speed and high-speed case, though the velocity fields are different. Similarly, the results seem fairly insensitive to the angle of attack in the current investigation, as seen in fig. 6.21. The latter shows less asymptotic behavior than the model of Veldhuis, though his model captures more (3D) effects. Actually, the effect of horizontal offset seems to be very limited: most results are within 10% of the fully contracted value. The limited effect of horizontal offset is noted in real life experiments such as ESDU88031 which mentions no specific provisions for propeller offset as long as it lies within 0.2 and 0.7 x_p/D.[29]

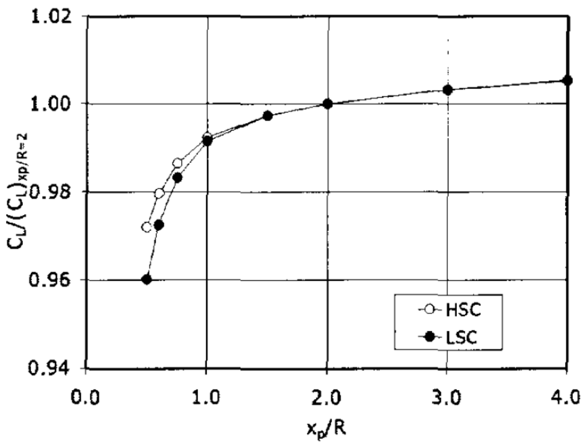

Figure 6.20: “Effect of propeller streamwise position on the wing of model 1 for the low speed case (LSC) and the high-speed case (HSC)” (Veldhuis [40])

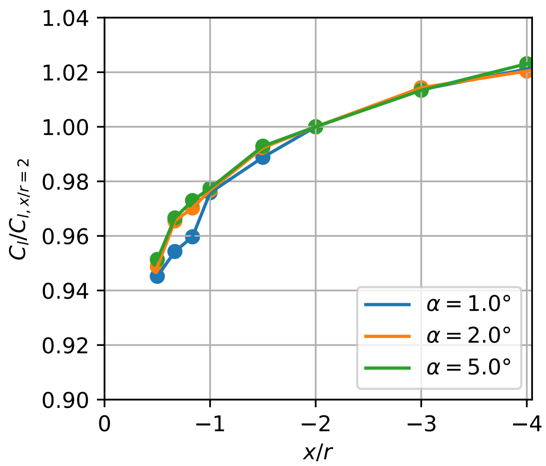

Figure 6.21: NACA0012 results for varying AD offset. $V_s/V_\infty = 1.5$, at $M_\infty = 0.15$

Comparison to q-development and pre-contracted results The results can be approximated by combining the contraction in a symmetrical case (or a model, for that matter), and the effective β factor due to slipstream height. Note that, as established in section 5.5.3, this β also depends on the correct horizontal position due to the upper surface blowing effect of upwash. With the current domain size, it is most appropriate to take the red line in fig. 5.32 as also indicated by the control point (labeled “baseline value”).

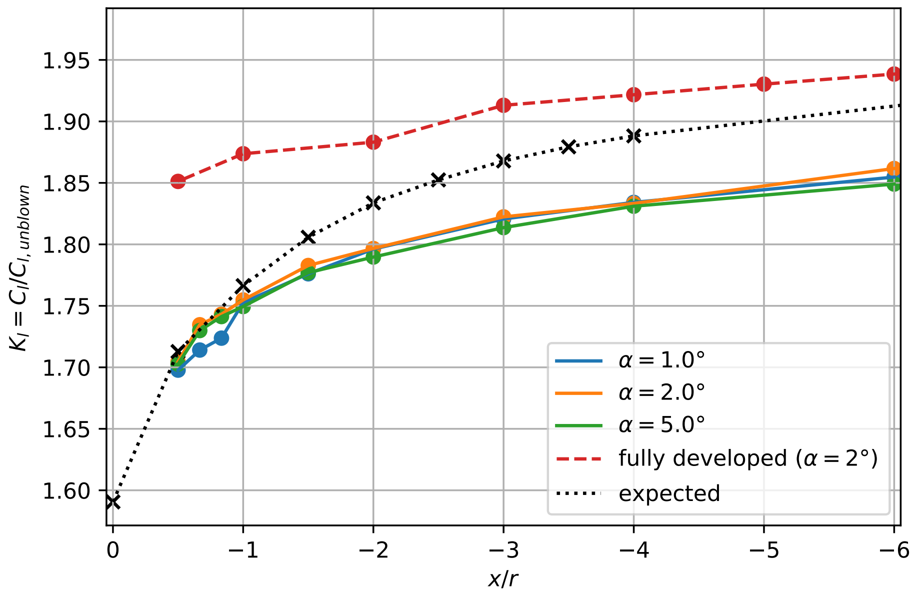

Figure 6.22: NACA0012 results for varying AD offset. $V_s/V_\infty = 1.5$, at $M_\infty = 0.15$

In fig. 6.22 this results in the top (dashed) line. Note that the slope of this line should also depend on α, $\alpha = 2$ is shown here. Combining both the effect of β and the total pressure development from section 6.3.2

yields the black dotted line. Note that one may argue that the lift is generated at the quarter-chord point, and hence, one should take $q_{eff,0.25c}$, which shifted the line left.

The velocity recovery outside of the slipstream, as plotted in fig. 6.15 is not considered in the determination of the k_l and hence leads to an under-prediction of lift. Mach effects were also not considered, and could lead to small deviations also. Still, the result is a rather accurate match.

Judging from the lack of difference between angle of attack, and the relative match with the dynamic pressure increase, it may be concluded that the effect of horizontal offset is mainly a dynamic pressure effect.

6.4.2. Comparison to CFD results of Patterson

Patterson [27] generated a very extensive set of 2D inviscid CFD simulations using NASA's OVERFLOW solver to quantify the lift increase in terms of β (see also section 6.1.2), and determine a surrogate model for β. As the propeller was modeled as an actuator disk, and the flow was compressible, the simulations are more complex than that of Nederlof. As the actuator disk was modeled as a jump in static pressure, changes in temperature and density were allowed to occur. Over-prediction of β was attributed to these effects: Many test points produced β's larger than 1, which is the theoretical maximum for a slipstream of infinite height. No correction was made for Mach number effects, though the simulations were run at a moderate Mach number of 0.2, with slipstream Mach numbers of up to 0.45. Despite noting the effect of slipstream displacement on β, the impact of changing vertical positions of slipstreams was not tested. In summary, Patterson evaluated the impact of the following parameters on β:

- Horizontal offset (x/c)
- Angle of attack (α)
- AD height (D/c)
- Slipstream velocity ratio (V_s/V_∞)

The simulations are repeated in MSES: An example setup for two cases is shown in fig. 6.23 and fig. 6.24, with the velocities in fig. 6.25 and fig. 6.26. The velocity ratio tested is $V_s/V_\infty = 1.5$ at Mach 0.2. The domain sizes are $[xmin, xmax, ybot, ytop] = [-12, 12, -6, 6]$ and $[xmin, xmax, ybot, ytop] = [-20, 18, -12, 12]$ for $D/c > 2.0$. This is considered suitable for $V_s/V_\infty = 1.5$, see also section 5.5.

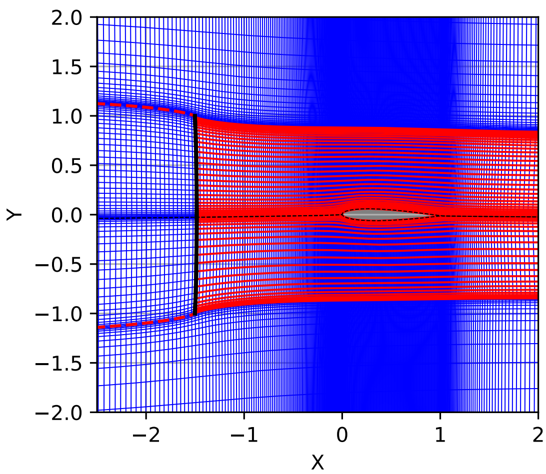

Figure 6.23: Setup of Patterson experiment for $D/c = 2.0$. NACA0012, $\alpha = 1°$, $V_s/V_\infty = 1.5$, $M_\infty = 0.2$

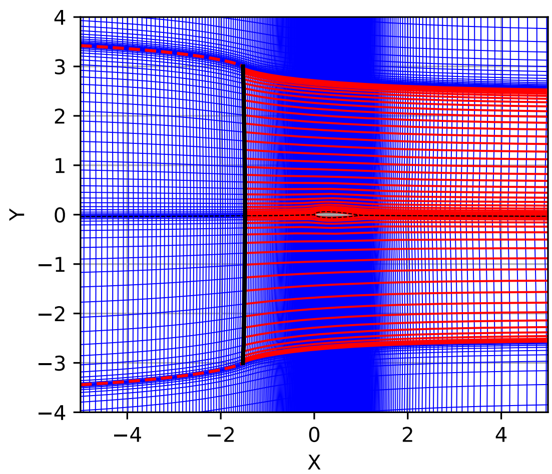

Figure 6.24: Setup of Patterson experiment for $D/c = 6.0$. NACA0012, $\alpha = 1°$, $V_s/V_\infty = 1.5$, $M_\infty = 0.2$

One would expect β to increase for horizontal offset x/c due to the increased slipstream development towards the anticipated velocity increase. One would generally also expect β to be increasing with AD height D/c. However, this would only keep increasing if the slipstream were to be fully contracted, which takes more distance for taller slipstreams. Due to the combined effect of slipstream contraction (velocity recovery) and slipstream height, the highest β at a small x/c may be obtained with smaller D/c values; the peak should hence shift to the right at larger x/c. Note also that the upper surface blowing effect is negligible for most of the offsets and D/c values considered here.

The results are compared against those of Patterson in fig. 6.27[27]. Note that the results of the MSES instigation lie significantly lower than the results of Patterson, but the general trends and scaling between the

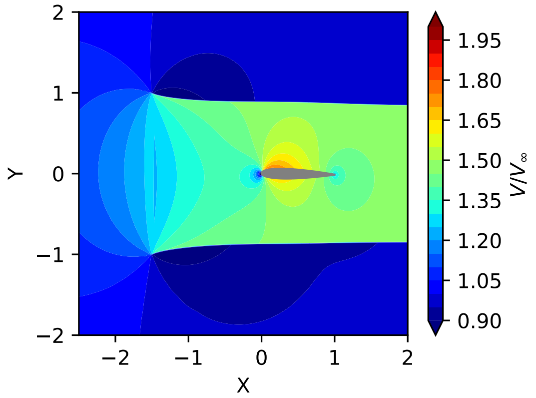

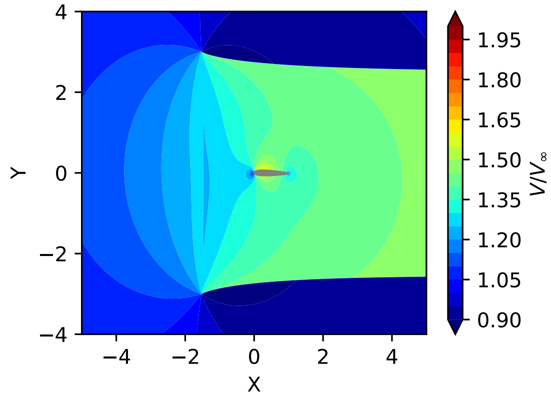

Figure 6.25: Velocity field of Patterson experiment for $D/c = 2.0$. NACA0012, $\alpha = 1°$, $V_s/V_\infty = 1.5$, $M_\infty = 0.2$

Figure 6.26: Velocity field of Patterson experiment for $D/c = 6.0$. NACA0012, $\alpha = 1°$, $V_s/V_\infty = 1.5$, $M_\infty = 0.2$

different offsets are similar. The velocity recovery in MSES showed at least $V_s/V_\infty = 1.489$ across all cases. The dip in some of the MSES results at $D/c = 5$ was not expected. It should be noted that the curvature of the quasi-normal line may lead to some inaccuracies with larger D/c values, but this does not seem to be the cause of the inconsistency at $D/c = 5, x/c = 1.0\&1.5$. The cause for these dips could not be found. Finally, the effect that small offsets benefit from smaller slipstreams is confirmed: the maxima indeed shift right with larger x/c.

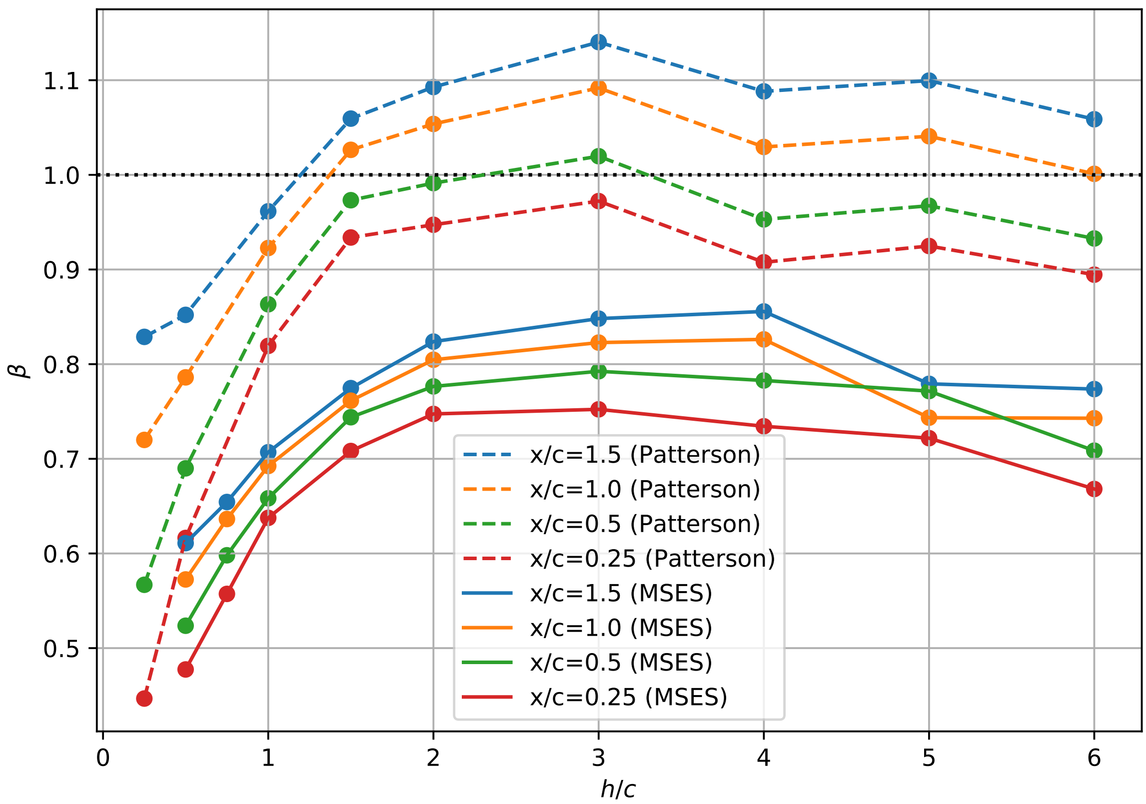

Figure 6.27: Effect of AD height and offset on β. Comparison to Patterson [27] NACA0012, $\alpha = 1°$, $V_s/V_\infty = 1.5$, $M_\infty = 0.2$

It is highly unusual that $\beta = 1$ was frequently exceeded in the CFD results of Patterson, this did not occur in MSES. Potential causes are listed below, but either the CFD simulations and/or MSES may still have some unresolved error:

- **Compressibility effects:** Assuming Prandtl Glauert's correction, one would expect an over-estimation of no more than 4.8% for a slipstream Mach number of 0.3. With $\beta = 1.15$, Patterson estimates the lift 10% above the theoretical limit for the case at hand.

- **Upper surface blowing:** Due to upwash of the airfoil, the slipstream can be redirected to the suction side of the airfoil and enhance lift as discussed section 6.1.2. However the extent of this effect should be very limited at the low angle-of-attack and large slipstream heights which produced the highest β values. This is supported by the dissertation of Patterson [27] which shows that the solution is independent of α for D/c ratios of 1.0 and above.

- **Influence on actuator disk or slipstream development:** Another theory is that the close vicinity of the airfoil somehow influences the development of the slipstream to produce higher circulation in the CFD investigation. This theory could not be tested.

It was found that for higher angles of attack the large domain sizes would sometimes converge on highly unusual and distorted results: e.g. a large negative local angle of attack at the wing: hence the results should always be interpreted with some caution.

6.5. Intermediate conclusions

General suitability of the method

- The results show that a potential flow solver can be used to analyze the lifting performance of an airfoil under a developed, uniform slipstream successfully under inviscid conditions. This was verified with CFD data to be highly accurate for a uniform slipstream, under low-lift conditions.

- The current method proved to be able to capture asymmetrical effects of vertical offset on the lift, contrary to mirrored images. Therefore, it is expected that the current method will be also be able to capture the asymmetrical effects that may be stronger with the addition of deflected flaps.

- The trend for vertical and horizontal offset are of similar nature as the APROPOS experiments.

- A remarkable and somewhat unexpected result is that the average axial velocity development in 3D is similar to that in 2D, in particular downstream of the AD. It could however not be guaranteed that the exact velocity variation throughout the wake (and adjacent to it) is entirely representative. Positioning grid refinements for the high lift cases under free contraction proved near impossible with the current methods.

Disadvantages of a freely-contracting slipstream

- **Difference 2D-3D** No match to a slipstream model could be found that accurately describes the contraction near the AD. This is due tot the fact that a strip cannot capture sideways contraction associated with a 3D actuator disk. Even though a scaled 3D approximation provided satisfactory results from around half a diameter behind the AD, the influence of the flow ahead of this flow on the airfoil is uncertain. As is the flowfield just outside of the slipstream, which should show a velocity deficit that slowly disappears.

- **Poor match with CFD validation data from Patterson[27]** Contrary to the pre-developed slipstream which matched well with the CFD validation data of Nederlof [28], the match with Patterson was poor.

- **Numerical instability and unsuitable BC's** Some results were obtained where the solution would crash or converge on a point where the slipstream was deflected by an un-physical amount leading to an extremely deformed grid. The inlet boundary condition which enforces parallel streamlines limits the accuracy of small grids, and may lead to inaccuracies on the larger grids.

(In)accuracies associated with a pre-contracted slipstream

- The slipstream does not shrink: it should shrink by 25% with a mean slipstream velocity ratio of 2.0. Having a fully developed slipstream may be a valid approximation from 1 to 2 diameters downstream of the actuator disk.
- The velocity deficit outside the wake is not captured, most likely leading to a (small) over-estimate of the lift, this may also be compensated for by slipstream models
- The influence of the airfoil on this contraction may not be properly resolved, the extent of this effect could not be determined.
- The lack of velocity deficit ahead of the airfoil may also lead to an over-estimate of the lift. The extent of this effect could also not be determined.

For the reasons above, and the fact that refinements can not reliably be added in high lift cases with free contraction, it is decided to use a pre-contracted disk for the following simulations. It is presumed that an inviscid slipstream model, or a symmetric simulation, would provide similar results than relying on contraction in MSES. This is beyond the scope of this thesis. Besides, utilizing a slipstream that has contracted fully will allow to better investigate the effect of high lift devices in isolation (in single interaction mode) by removing variables associated with the contraction process.

7

Viscous-inviscid results under non-uniform slipstream

An interesting intermediate step before assessing flaps is to consider an airfoil, but this time, with a non-uniform slipstream with the BL model enabled. The slipstream profile to be used is the mildly varying velocity profile. This is more realistic than the cases considered earlier, and will allow, for the first time, to consider effects on boundary layer development.

Setup: The parameters and constraints of the following experiments are identical to those described in section 9.1, also to be used later for the blown flaps. Note that the number of side points was set to the standard 141, as the airfoil is not operating near $C_{l,max}$. An example grid, used with a high slipstream position, is shown in fig. 7.1. The mildly varying slipstream with $h/c = 0.866$ is used, as introduced in section 5.2. It is interesting to see the effect of upper surface blowing on the boundary layer by comparing it to an unblown baseline, and the unblown case producing the same lift as a selected point with asymmetric blowing.The airfoil is the same symmetric airfoil also considered in part I of this report: the NACA0012. For easier comparison, the boundary layers are tripped at the nose.

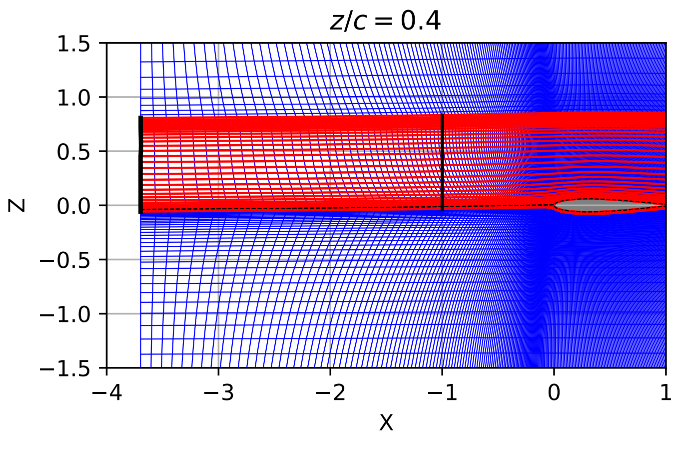

Figure 7.1: NACA0012 example grid. $M = 0.15, Re = 2.51e6, n_{crit} = 3.0, \alpha = 0°$

7.1. NACA 0012 under 0 angle of attack

The results the symmetrical sweep in terms of lift coefficient are shown in fig. 7.2. As expected for this case, the results are fully symmetrical about $z/c = 0$ apart from the failure to converge at $z/c = -0.7$. As in the inviscid case with uniform inflow, the highest lift is obtained with the majority of the slipstream touching the upper surface of the airfoil only.

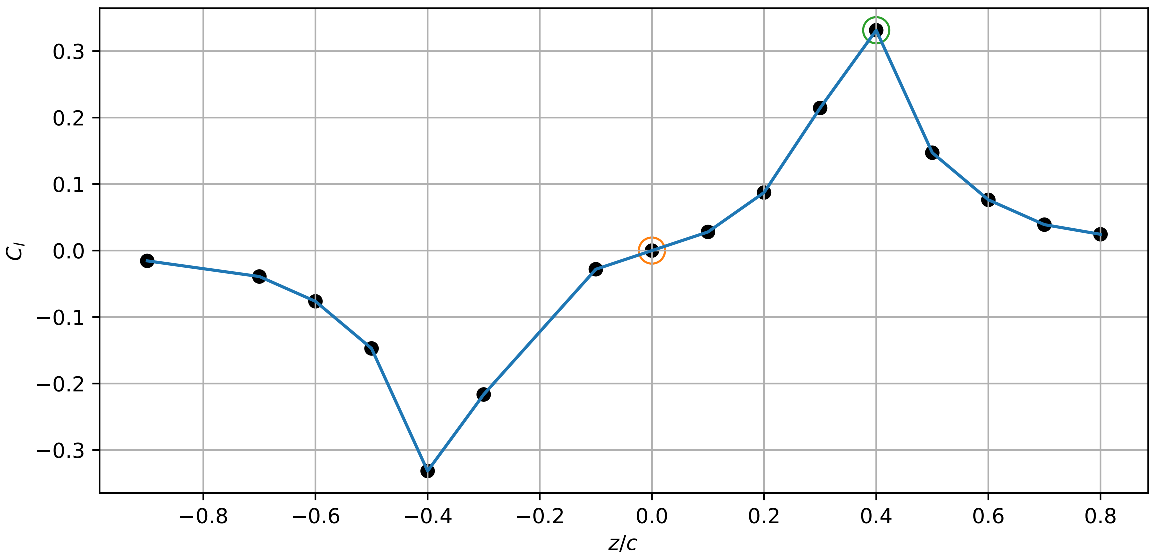

Figure 7.2: Variation of lift contributions with varying propeller z/c. NACA0012. $M = 0.15, Re = 2.51e6, n_{crit} = 3.0, \alpha = 0°$

The two positions highlighted in fig. 7.3 show that the velocity increase on either side of the airfoil depends largely on the momentum in its vicinity. The extent of the airfoil's influence can clearly be seen to extend throughout the height of the slipstream, and also below it. Also notice how the lower momentum in the center of the slipstream is still clearly visible. The lower slipstream position provides a far smaller lift increase than the higher position as the bottom side of the airfoil also experiences a substantial velocity increase, and hence drop in pressure. This demands a closer look at the pressure distributions.

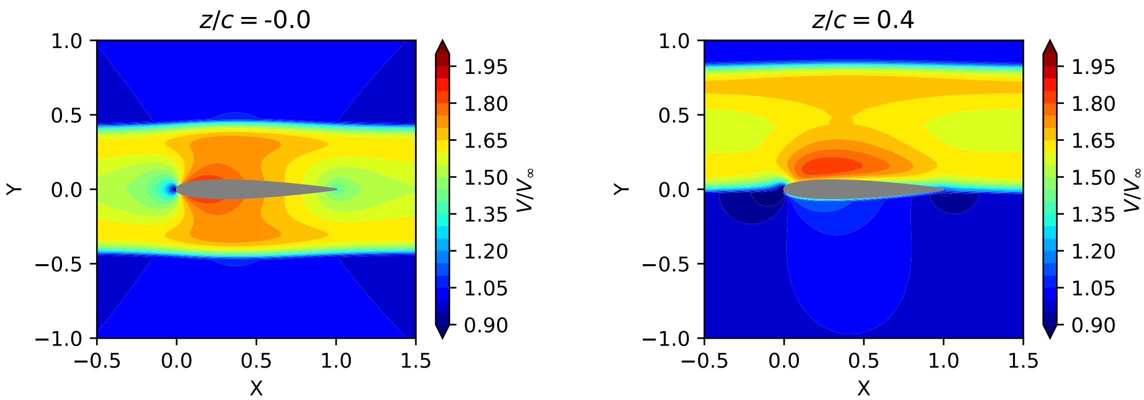

Figure 7.3: Velocity fields for the marked vertical propeller positions. NACA0012. $M = 0.15, Re = 2.51e6, n_{crit} = 3.0, \alpha = 0°$

Supplementing the velocity increase in fig. 7.3, the static pressure field can also be considered for both cases, as shown in fig. 7.4. The pressure distributions for both highlighted propeller positions are shown in fig. 7.5. Comparing both cases, it can be seen that the lower position, where the airfoil is more immersed in the slipstream, shows higher stagnation pressures, but less difference in suction between the upper and lower surface. Thus, the higher slipstream position leads to higher lift with lower stagnation pressures: the streamlines around the airfoil are in a low-momentum part near the boundary of the slipstream. The effect on the boundary layer is considered in section 7.3.

The stagnation pressures scale with the dynamic pressure of the dividing streamlines around the airfoil: this is indicated by the crosses in fig. 7.5. These may also be called stagnation streamlines. This also illustrates that, when considering the boundary layer, values such as the pressure gradient may need to be scaled as the energy in the boundary layer is different for each case.

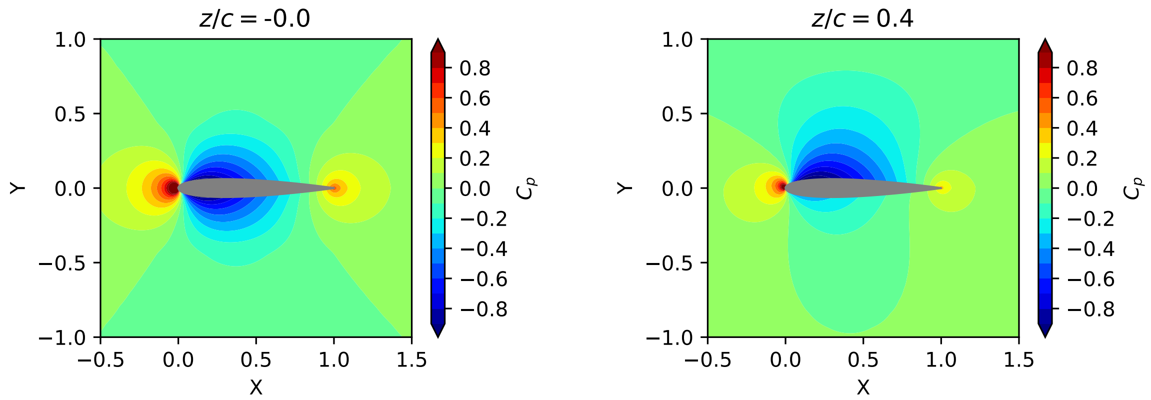

Figure 7.4: Pressure fields for the marked vertical propeller positions. NACA0012. $M = 0.15, Re = 2.51e6, n_{crit} = 3.0, \alpha = 0°$

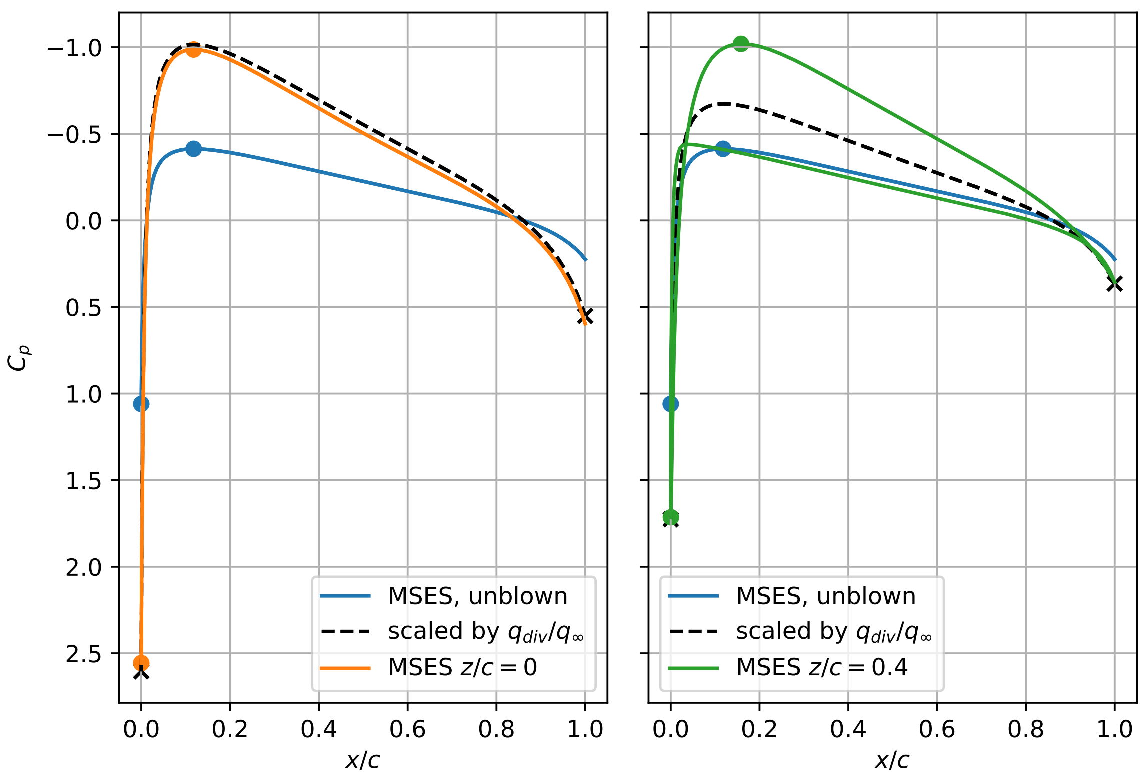

Figure 7.5: Pressure distributions for varying z/c. NACA0012. $M = 0.15, Re = 2.51e6, n_{crit} = 3.0, \alpha = 0°$

The boundary layer of the fully immersed case ($z/c = 0$ has slightly smaller displacement thickness (δ^*) than the baseline case due to the relatively high u_e in relation to the pressure variation. More information on boundary layer developments is shown in the next section.

7.2. Pressure distributions under lifting conditions

Before looking at the boundary layer results, it is first interesting to compare the pressure distributions. The fields are shown in fig. 7.6: the left airfoil is unblown and placed at 3° angle of attack, whilst the blown airfoil on the right produces the same lift at 0° due to upper surface blowing. Note how the right case shows larger areas of suction, less concentrated on the nose. Also note how the stagnation point on the right case has shifted upwards, rather than down and aft, as would normally be the case for lifting airfoils. The airfoil operates in the very edge of the slipstream, and a thin streamtube of high-momentum air passes on the underside of the airfoil as well, which would dissipate in real-life conditions.

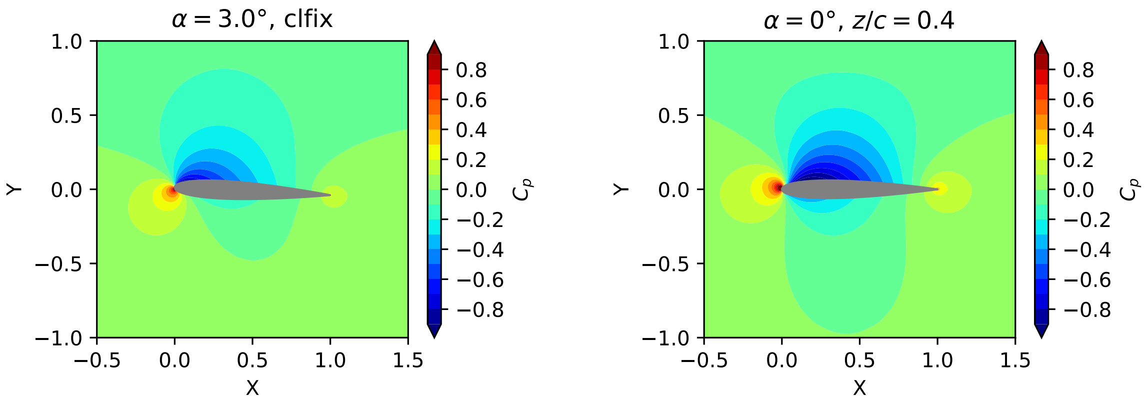

Figure 7.6: Pressure fields at $C_l = 0.33$, at $\alpha = 3°$ (unblown, clfix) and $\alpha = 0°$ (blown) NACA0012. $M = 0.15, Re = 2.51e6, n_{crit} = 3.0$

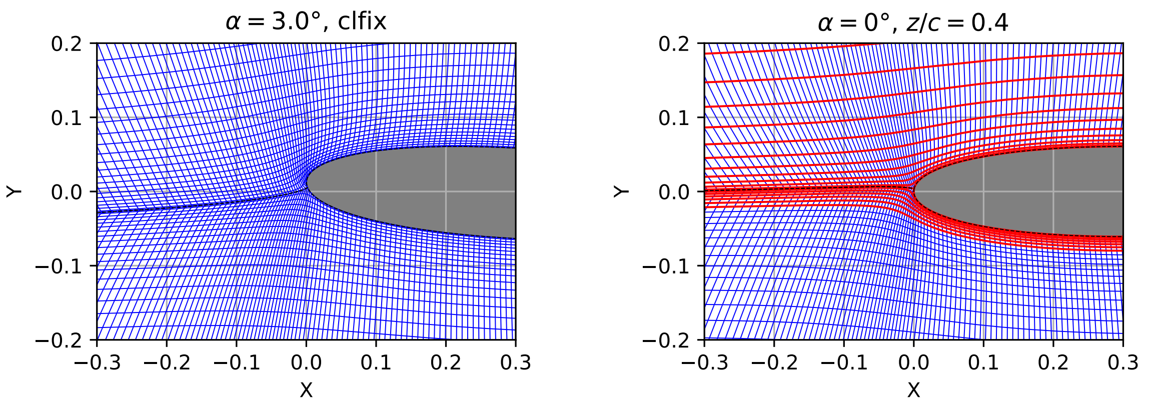

Figure 7.7: Nose streamline grids at $C_l = 0.33$, at $\alpha = 3°$ (unblown, clfix) and $\alpha = 0°$ (blown) NACA0012. $M = 0.15, Re = 2.51e6, n_{crit} = 3.0$

The pressure distributions shown in fig. 7.8 show a 'classical' airfoil pressure distribution on the left, and again the airfoil with upper surface blowing on the right. Note how the blown airfoil shows a pressure distribution more similar to a 'scaled' version of the unblown value at 0°. It is also interesting how the bottom surface suction peak and upper surface suction peak shifted clock-wise on the airfoil surface, as did the stagnation point, as shown in fig. 7.7.

The canonical pressure distributions in fig. 7.9 lead to similar conclusions. The suction peak is located more aft on the blown airfoil, and is more gradual. In terms of adverse pressures towards the trailing edge, the gradients for the lifting cases are similar, and both are sharper than the baseline case, though the unblown ($clfix$) case experiences a larger adverse pressure increase overall, which may lead to unfavorable boundary layer growth.

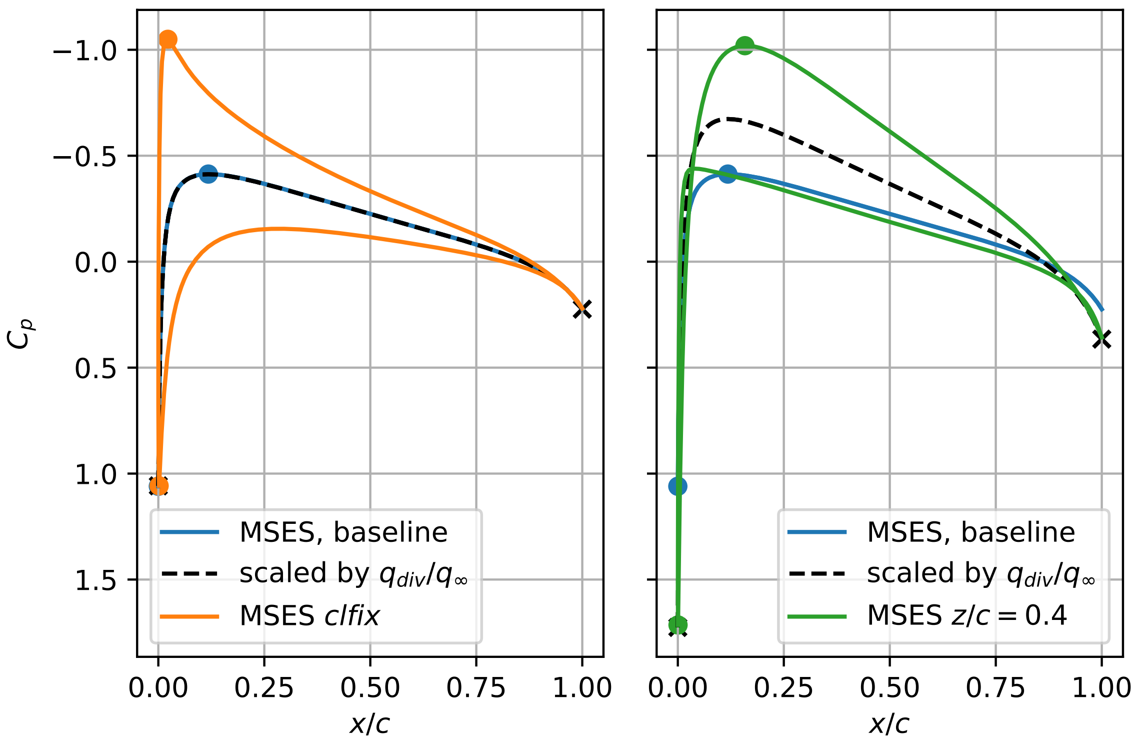

Figure 7.8: Pressure distributions for the selected cases. NACA0012. $M = 0.15, Re = 2.51e6, n_{crit} = 3.0$

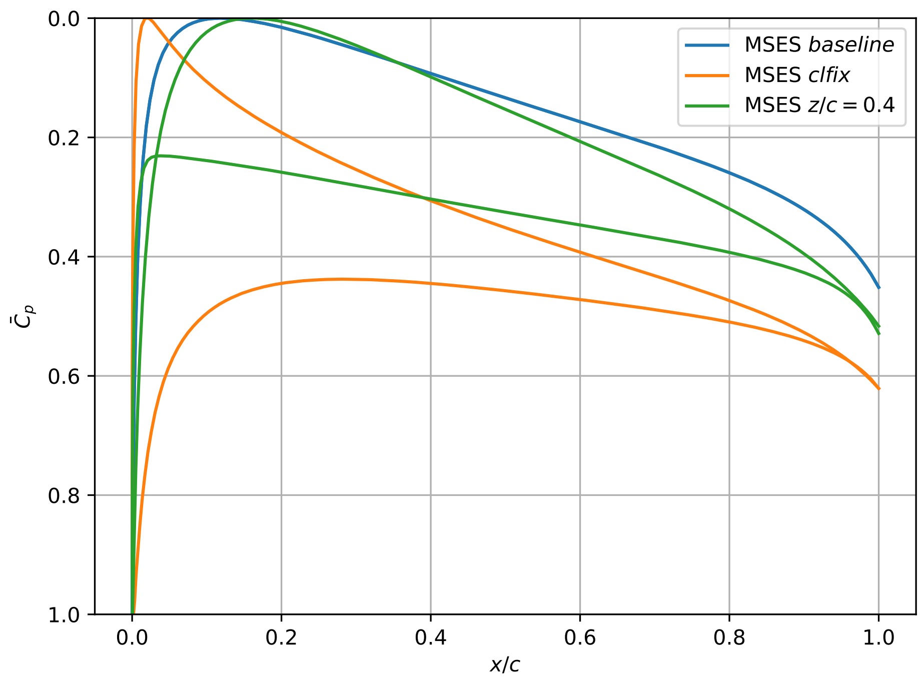

Figure 7.9: Canonical pressure distributions for the selected cases. NACA0012. $M = 0.15, Re = 2.51e6, n_{crit} = 3.0$

7.3. BL effects in lifting conditions

The boundary layer growth expected from the canonical pressures is confirmed by fig. 7.10. The adverse pressures are a precursor to BL growth: the $clfix$ case shows larger BL growth due to the pressures at the nose. The $z/c = 0.4$ case shows increasing BL growth near the trailing edge due to the higher pressure recovery than the baseline. How the BL is influenced by the different velocity field around the boudary layer may be examined by looking at the terms used by the BL model in MSES itself.

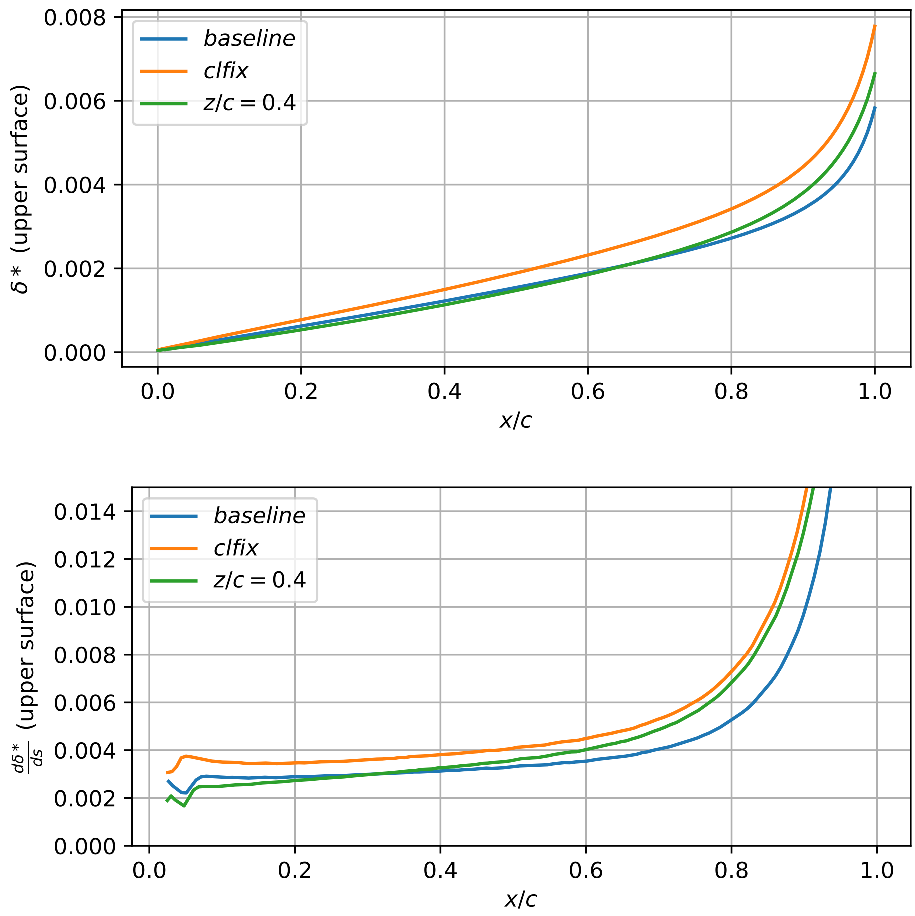

Figure 7.10: Boundary layer displacement thickness growth. NACA0012. $M = 0.15, Re = 2.51e6, n_{crit} = 3.0$

As outlined in section 4.3 and section 2.3.1, the BL is treated by a two-equation model. The integral momentum equation may be most interesting as an increasing momentum deficit is related closely to the boundary layer growth. This equation may also be split into two terms: one based on skin friction, and another with the collected velocity and BL history terms. The equation is repeated in eq. (7.1)

$$\frac{d\theta}{d\xi} = \frac{C_f}{2} - \frac{2\theta + \delta^*}{u_e}\frac{du_e}{d\xi} \tag{7.1}$$

Before using the simplified equations, it should be noted that the compressibility terms are indeed negligible: The external Mach reaches $M = 0.22$ for the lifting cases. It is also worth mentioning that the development of H is similar across the cases considered.

In fig. 7.11, the contribution of the terms is plotted. Interestingly, although skin friction itself is higher, it should be noted that the skin-friction coefficient (based on u_e) actually slightly decreases for the lifting cases, and the history/velocity terms are more dominant towards the solution. The case for $z/c = 0.4$ retains its advantage some distance past the pressure peak. The velocity terms of the equation are shown in fig. 7.12, which, in fact, is similar to the LHS of Gartshore's criterion as shown in section 2.3.3. This again confirms that the blown case is favorable around the nose region, but loses the advantage towards the trailing edge.

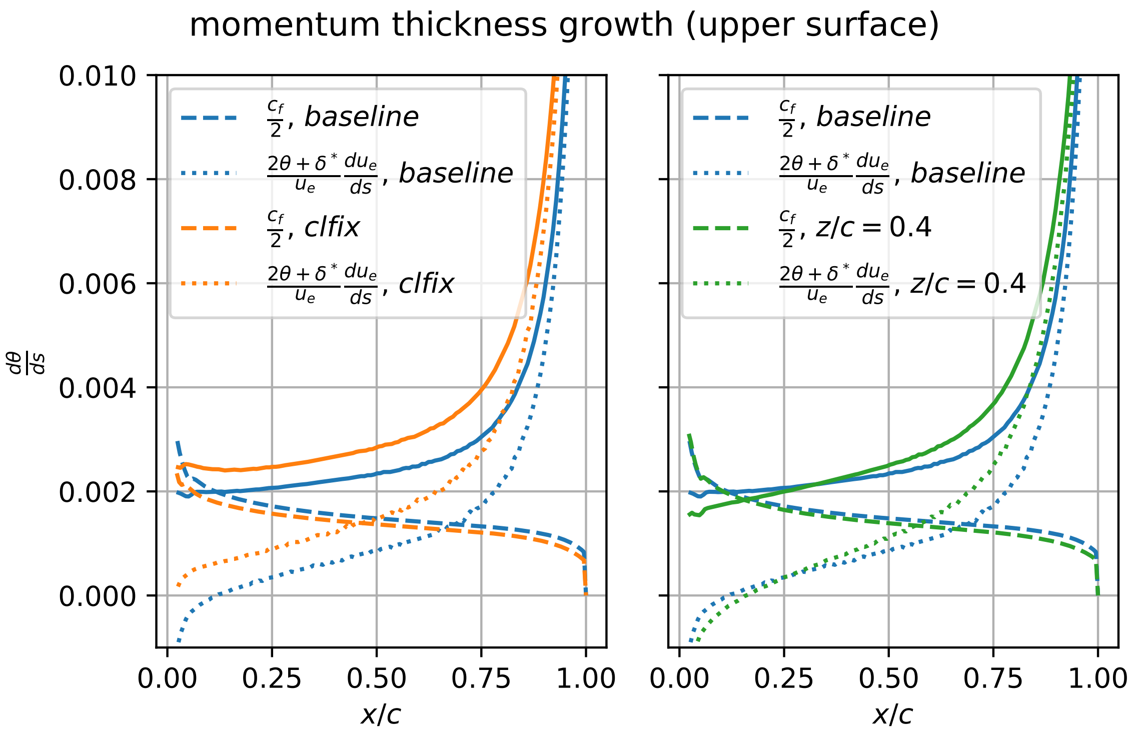

Figure 7.11: Integral momentum contributions for the selected cases. NACA0012. $M = 0.15, Re = 2.51e6, n_{crit} = 3.0$

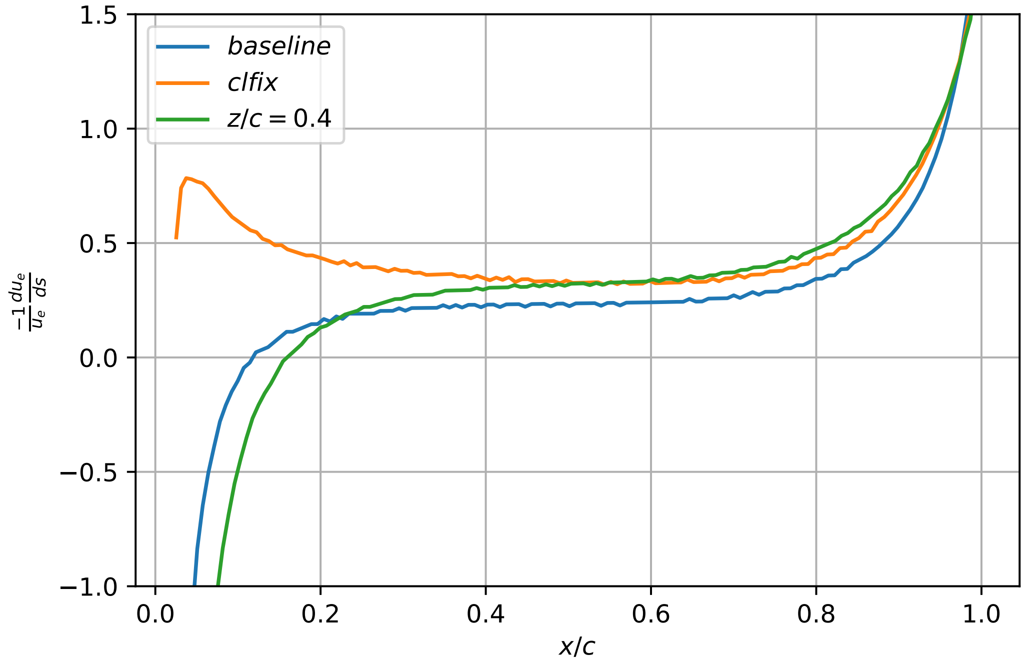

Figure 7.12: Integral momentum velocity term for the selected cases. NACA0012. $M = 0.15, Re = 2.51e6, n_{crit} = 3.0$

III
Multi-element airfoil

8
Flap setup & validation

This chapter aims to introduce the flap system used in the following experiments (NLR7301 with a fixed, 20° flap deflection). The flap and grid are extensively validated in this chapter, using the same conditions as the experiment. Some improvements to the grid and domain had to be made to enable proper evaluation of flaps. The refinement is now positioned by determining the upwash from a run on a lower-fidelity grid with single exponential spacing. This is no longer relying on a fudge-factor and hence more accuracy is guaranteed over the large range of lift coefficients to be examined, provided that the pre-run converges. This is described more elaborately in section 5.4.

8.1. NLR7301 with flap

Selection and properties: A flapped airfoil with a gap is required for assessing the influence of the velocity profile on a multi-element system. A suggested starting point is the NLR7301 configuration with flap: This was tested by van Dam [62], and also in MSc. Theses at TU Delft: Van Craenenbroeck [18] researched wake-bursting and Dolle [81] performed research into the separation behavior on TE flaps. A convenient property of this modified (early) supercritical airfoil is that there is the lack of an airfoil cove, which will definitely aid in MSES convergence. The coordinates of the original wind-tunnel experiment and a modified airfoil are conveniently included in the report of Dolle. For reference, a quick comparison to Dolle's numerical results are also possible.

The original wind-tunnel experiment conducted by the National Aerospace Laboratory (NLR) is well-documented by Van den Berg [82], and the data is deemed suitable for comparison with CFD data according to the AGARD Fluid Dynamics Panel [83]. Pressure measurements are available for angles of attack of 6.0°, 10.1° and 13.1°. Upon verifying the translation of some of the coordinates of the flap by Dolle it turned out that Dolle tested the case with a gap of 2.6%c. Van den Berg [82] also noted that for the larger gap no mixing of wing wake and flap boundary layer takes place. This is helpful as MSES is less reliable with confluence wakes which could lead to over-estimation of lift, at least in the original version, as hypothesized by Drela [32]. Laminar separation and transition takes place near the leading edge, and, according to van den Berg [82] its effect is is only very local. This is good to know as these bubbles can burst, which may not be predicted by MSES as shown by Veldhuis.[31]

Shape:

> "The basic airfoil section is an early supercritical section: NLR 7301. The wing upper surface up to the trailing edge at 94.36% chord and the wing lower surface up to 60 % chord coincide exactly with this profile. The shape of the wing shroud, between 60 % chord and the trailing edge, was designed on the basis of preliminary wind-tunnel test in such a way that nowhere flow separations occur." (Van den Berg [82])

Hence, the configuration was not necessarily optimized for high-lift conditions, it was only tested at $\delta_f = 20°$. The geometry of the airfoil with flap is shown in fig. 8.1. Note that the flap cannot be fully retracted into the cove, and it has a slight negative inclination to its chord line.

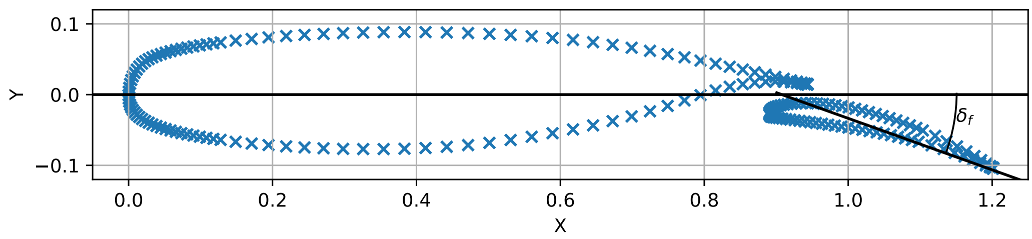

Figure 8.1: Coordinates of the NLR7301 airfoil with $\delta_f = 20°$

Stall:

> "The results suggest that the stall, which occurs between $\alpha = 14.1°$ and 15.1°, is due to boundary layer separation on the rear of the wing. Once a separation region is present at the wing trailing edge, it is unlikely to be a small separation region in view of the large positive pressure gradients above the flap. With a separation region extending beyond the flap, the flap lift will be small and consequently an abrupt lift loss is to be expected, in agreement with the lift curve ... " (Van den Berg [82])

The stalling behavior is somewhat ambiguous and not supported by measurements at a stalled angle. The large separation above the flap seems to be indicative as a "wake burst", which may be captured by MSES.

8.2. Lift polars

The lift polar allows to compare the MSES simulation with the experiment at all angles of attack. Besides, creating a polar also allows to check the accuracy of the solution, i.e. this should run smoothly.One concern regarding accuracy is whether the leading edge bubble is properly resolved as the Reynolds number lies between 1 and 3 million as suggested by Drela [24]. Though the bubble only has a very local effect on the flow according to van den Berg [82]. It is decided to use MPOLAR to create a viscous polar with the various settings. The reason MPOLAR can now be used is that no slipstream is present in this test and thus no refinement step needs to be undertaken. If small angle of attack changes are used, the solution process is much faster and more robust than starting simulations from scratch. The handling of non-converged points by domain splitting is also very helpful in proceeding after a non-converged point. However, mathematical errors can still cause an MPOLAR crash which requires re-starting at a slightly different α. The rationale behind considering a low turbulence amplification factor $n_{crit} = 3$ is explained in section 8.3. The domain size is $[xmin, xmax, ybot, ytop] = [-3.7, 5.5, -5.5, 6.4]$, this is rather large as it is also used for the blown experiments, see also section 9.1.

Initially, the simulations were run at $\alpha = 0°$ and 7° going up to 7° and 14°, respectively. However, this caused discontinuities in the solution near $C_{L,max}$ as in fig. D.1. It is suspected that the LE bubble is not properly resolved as this can lead to the "ragged" lift/drag polar curve as noted by the manual, which was observed as shown in fig. D.2.

Two methods to improve the resolution of the solution were tried: first is to increase the number of side points from 141 to 201. This did not significantly improve the results, yet increased lift somewhat. Another, more effective measure proved to obtain a grid (MSET and MSES solution) more nearer the maximum lift region. The results indicated in fig. 8.2 were obtained with a grid for $\alpha = 12°$. The results at maximum lift are smooth but required numerous restarts due to errors at certain points. The results going down 12 to 7.5° are smooth. This highlights the importance of opting for the right strategy when setting up a grid in MSET, as the blowing increases the lift, although in a different way than an increase in α. Some slight scalloping was noticed near $\alpha = 7°$ for the grid generated at 0°, but there is little discontinuity between the two grids. It is found that both MSES solutions, regardless of n_{crit}, consistently over-estimate the lift coefficient by 0.05, which increasingly lessens the relative deviation with increasing α.

The results with $n_{crit} = 3$ are presented in tabulated form in table 8.1, including the moment coefficients. The moment coefficients are consistently over-estimated by a greater amount. Note that the last entry is a separate start with a dedicated MSET grid, whereas the other data is generated with the polar, running upwards from 0° and 7° angle of attack.

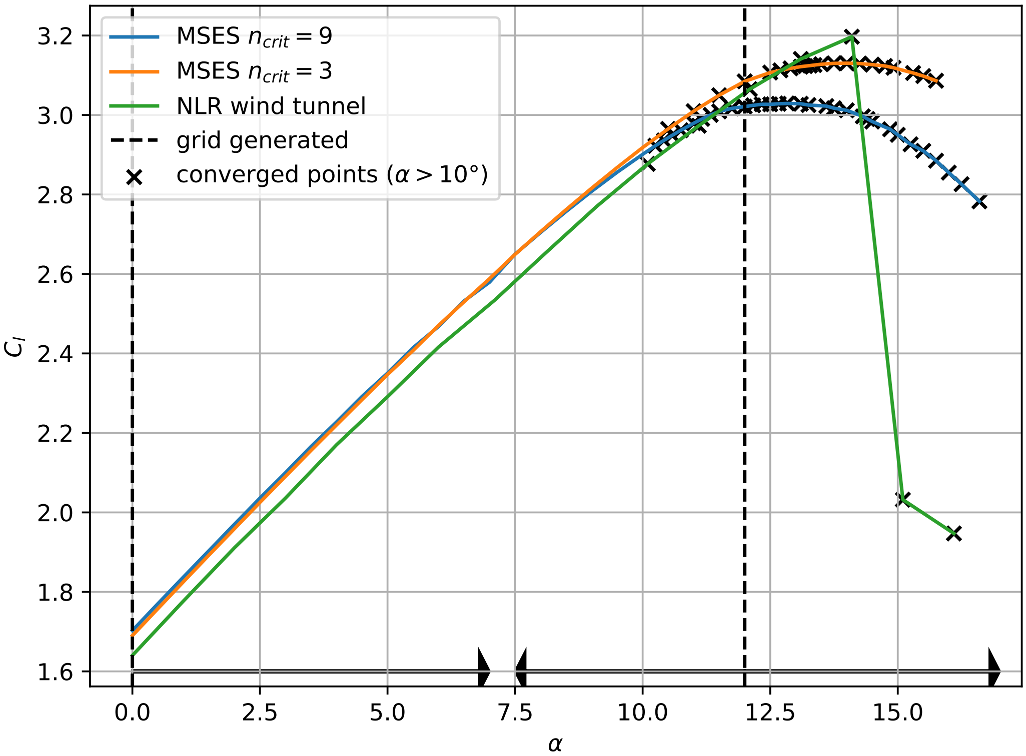

Figure 8.2: Lift polars of the NLR7301 with $\delta_f = 20°$ at various turbulence settings. $M = 0.185$

Table 8.1: Comparison of MSES data with experimental values. NLR7301 with $\delta_f = 20°$. $M = 0.185$, $Re = 2.51e6$, $n_{crit} = 3.0$.

α	C_l, experiment	C_l, MSES	deviation [%]	C_m, experiment	C_m, MSES	deviation [%]
0.0	1.64	1.69	3.0	-0.457	-0.474	3.8
6.0	2.42	2.47	2.1	-0.471	-0.489	3.8
10.1*	2.88	2.927	1.6	-0.463	-0.478	3.3
13.1	3.141	3.122	-0.6	-0.44	-0.438	-0.4
6.0**	2.42	2.474	2.2	-0.471	-0.49	3.9

**note: MSES result linearly interpolated between adjacent converged points*
***note: separate MSES simulation with MSET grid generated at $\alpha = 6°$.*

8.3. Bubble resolution & turbulent amplification selection

This section compares the properties of various grids near the LE bubble, all at an elevated number of airfoil side points of $N_{side} = 201$. Improper resolve of the bubble provides results with discontinuities, which would be detrimental to determining, for instance, a lift gradient. The most appropriate n_{crit} factor is also determined.

Grids used for the lift polar: The angle of attack at which the grid has an impact on the spacing over the entire airfoil. Too low resolution may lead to insufficient resolution near any laminar bubble. This particular configuration experiences a small bubble of high intensity on the upper surface near the LE, hence the grid requires extra attention.

Comparing fig. 8.3 with fig. 8.4 it can be seen that the latter has higher resolution near the LE. This is caused by the fact that the spacing is specified at the stagnation point, and the spacing distribution is generated according to the curvature. As the stagnation point at 12° lies in a lower-curvature region, the leading edge gets subsequent refinement. This is favorable for resolving the leading edge bubble at high lift conditions. This should also be considered later when adding the slipstream. Another effect is that a distribution associated with a certain curvature is “dragged” onto the bubble location leading to a different distribution with angle of attack, also.

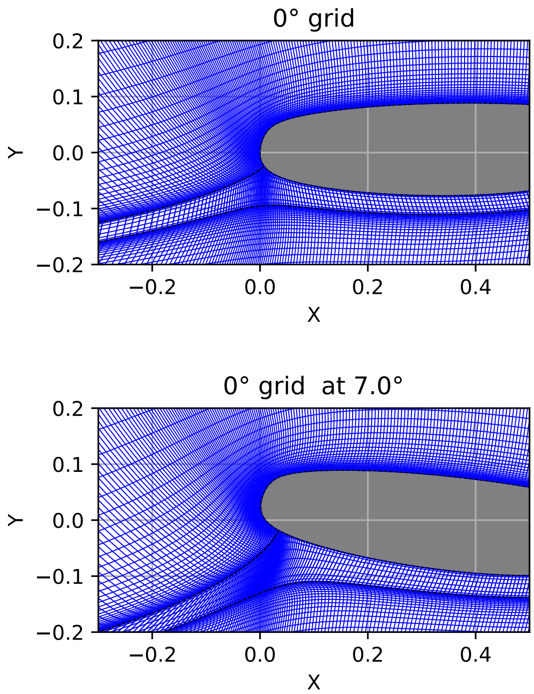

Figure 8.3: Grid in nose region. NLR7301 with $\delta_f = 20°$.

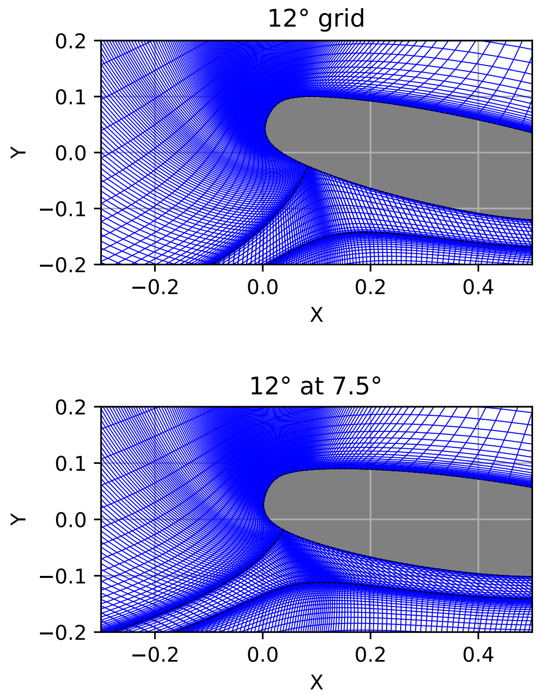

Figure 8.4: Grid in nose region. NLR7301 with $\delta_f = 20°$.

Characterizing sufficient bubble resolution: Noting that the accuracy of the solution depends on both the angle of attack at which the grid is generated, and the deviation in angle of attack, it is important to establish the correct spacing and the applicable angle of attack range in which accuracy can be guaranteed. As there is no angle of attack difference as such for the blown cases, it is more appropriate to look at the stagnation point shift.

Conveniently, the x-coordinate of the transition region remains fairly constant according to Van den Berg [82]: The laminar separation and turbulent reattachment line are between $x/c = 0.024$ to $x/c = 0.040$ for the examined angles ($\alpha = 6°, 10.1°, 13.1°$). With $n_{crit} = 3.0$, this region is smaller: ending at around $x/c = 0.035$.

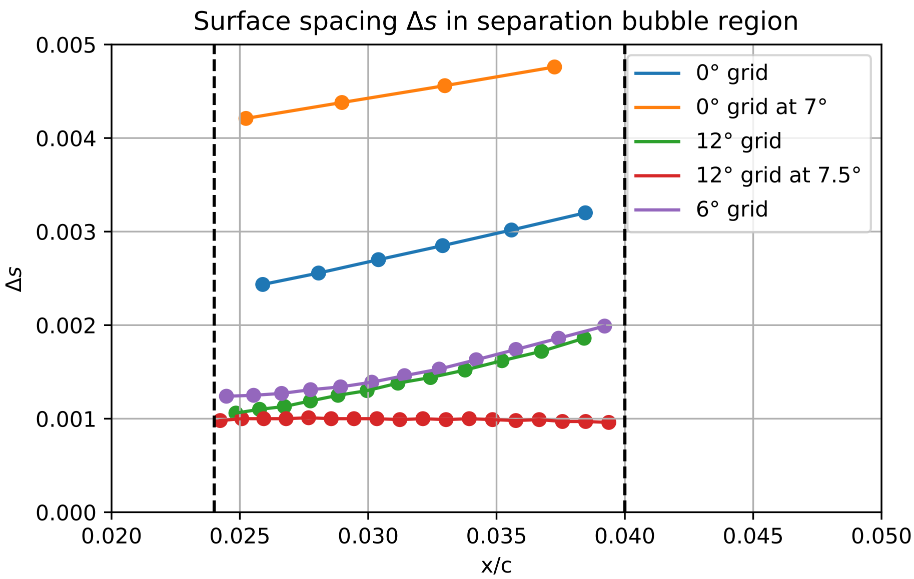

Figure 8.5: Resolution with various grids. NLR7301 with $\delta_f = 20°$.

The resolution in the stagnation point region is compared in fig. 8.5. Δs is the spacing between boundary layer nodes, with a lower value indicating a higher resolution. A rearward stagnation point shift of approximately $\Delta S_0 = 0.005$ is achievable whilst maintaining the same spacing as the 12° case. As 6° angle of attack is the point of interest, it is good to confirm that the standard grid generated at 6° shows excellent resolution in the bubble region. The grid is shown in fig. 8.6.

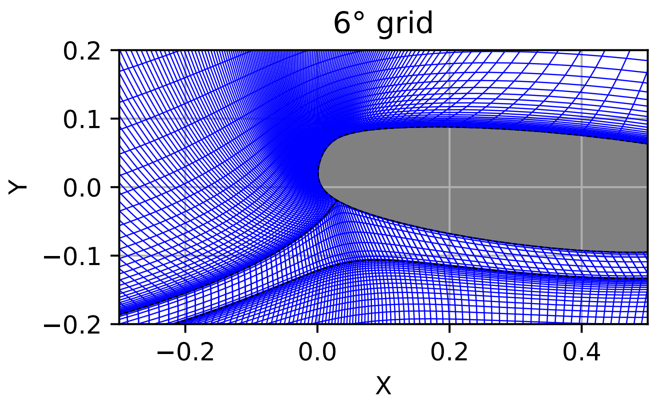

Figure 8.6: Grid in nose region. NLR7301 with $\delta_f = 20°$.

If, in other cases, the resolution near the leading edge is uncertain, it may be investigated by producing a polar as done for the unblown case. The spacing around the LE may be modified by either specifying a different spacing on the stagnation point, or by specifying a refinement region. Both these approaches would require iterations.

Selecting an appropriate turbulence amplification factor The turbulence amplification factor n_{crit} is lowered by means of experiment to consider the effect of the increased turbulence that may be associated in a propeller slipstream. The suggestion of Alba [42] of using $n_{crit} = 3.0$ rather than 9.0 is considered here. Coincidentally, the case with $n_{crit} = 3.0$ agrees much better than $n_{crit} = 9.0$ with the experimental data near maximum lift. This could indicate higher turbulence values in the wind tunnel or other effects such as a rougher wing surface or another type of transition being applicable. The BL properties discussed later in this section will help determine the appropriate n_{crit} value. It is suspected that lowered n_{crit} leads to earlier transition and better mixing of the flow, thus postponing the stall.

Both cases show significant wake growth that may become a wake-burst as shown in fig. 8.7 and fig. 8.8, with the maximum displacement thickness of the upper surface wake indicated. The case with lowered n_{crit} has less wake growth, explaining the higher lift. Although this wake growth leads to loss of lift, it is not as sudden as in the experiment.

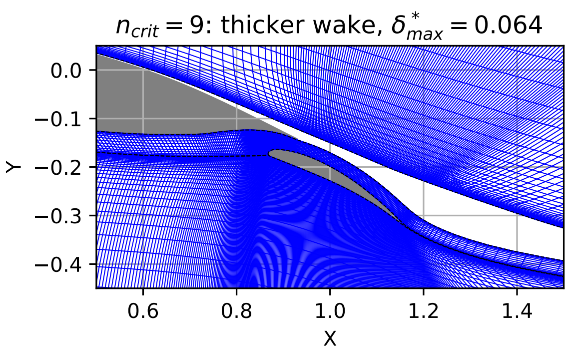

Figure 8.7: Flowfield with significant wake growth. NLR7301 with $\delta_f = 20°$. $M = 0.185, Re = 2.51e6, n_{crit} = 9.0, \alpha = 13.1°$

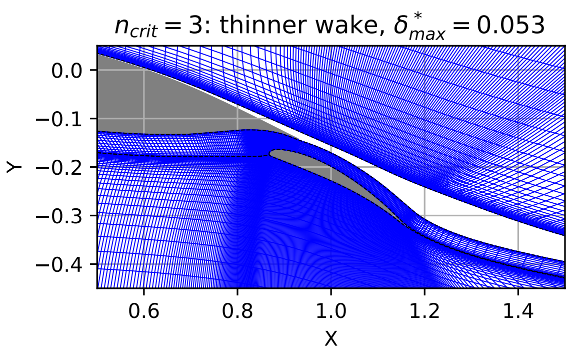

Figure 8.8: Flowfield with significant wake growth. NLR7301 with $\delta_f = 20°$. $M = 0.185, Re = 2.51e6, n_{crit} = 3.0, \alpha = 13.1°$

The Boundary layer plots in appendix C help in establishing the correct n_{crit} and accuracy of the MSES BL model. The report by Van den Berg [82] provides information on the observed flow characteristics and some data points on the BL data. The following conclusions may be drawn:

- The start and end of the LE separation bubble agrees well with the test report for $n_{crit} = 9$ whereas it is underestimated by $n_{crit} = 3$.
- The transition region of the test report effectively lies in-between the MSES transition locations established with $n_{crit} = 3$ and $n_{crit} = 9$.
- No separation on the lower surface should be present as the airfoil was redesigned for this (as reported by van den Berg [82]) but this does occur with $n_{crit} = 9$.
- The displacement thickness on the upper surface shows a slightly better match with $n_{crit} = 9$ except for the TE of the main element. The change in displacement thickness is almost negligible here and thus more prone to measurement inaccuracies.
- The displacement thickness and shape factor on the lower surface match far better with $n_{crit} = 3$.

As the influence of the LE bubble has little influence on this setup (as noted by Van den Berg [82]) and the lower surface gets far better resolved with $n_{crit} = 3$ it is decided that $n_{crit} = 3$ is more appropriate. Besides, as established before, this also matches the maximum lift more closely.

8.4. Pressure distributions

Moderate and high α: The pressure distributions require further investigation. It should be noted that the coordinates on the x-coordinates of the leading edges needed to be interpolated as instead their y-coordinates were included. Along the entire flap the y-coordinates also needed to be determined to allow for rotation to the XZ coordinate frame (aligned with the main elementl).

The pressure distribution for $\alpha = 6°$ is shown in fig. 8.9. Note that lift was overestimated by 2.1%: it is not entirely clear where this arose but the leading edge suggests some over-estimation.

The pressure distribution for $\alpha = 6°$ is shown in fig. 8.9. Note that lift was underestimated by 0.6%: in this case the suction on the aft of the main element and of the flap element are lower. There may still be a small over-estimate of the LE suction peak.

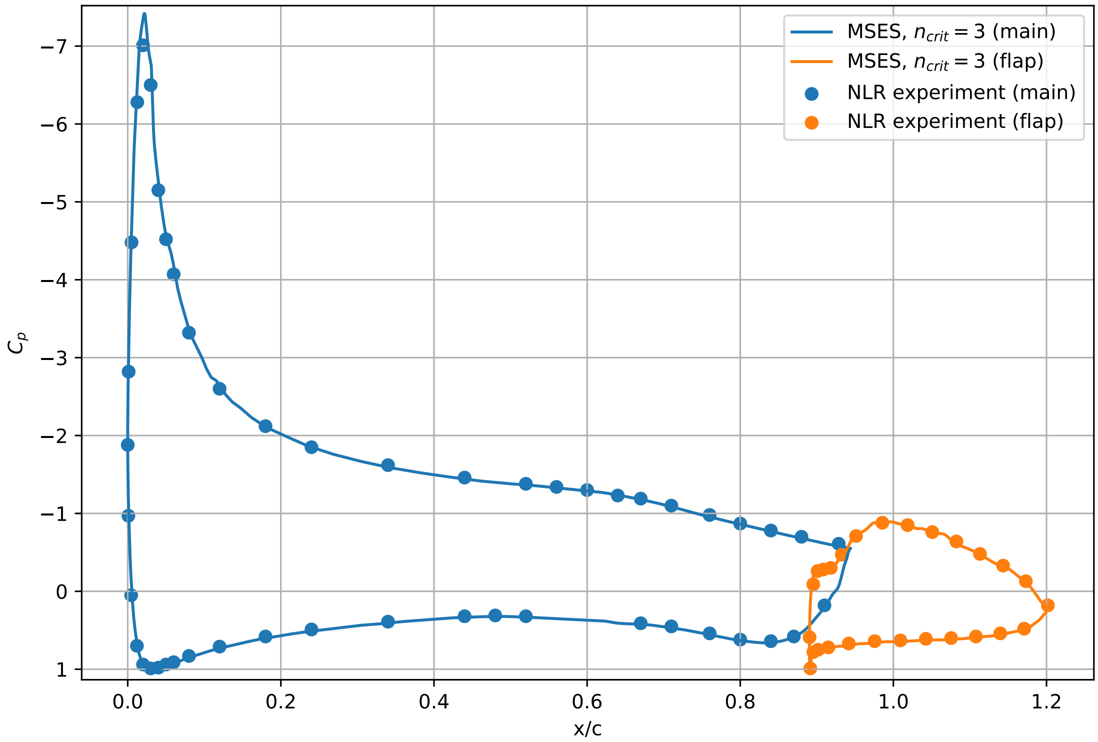

Figure 8.9: Pressure distribution comparison for the NLR7301 with $\delta_f = 20°$. $M = 0.185, Re = 2.51e6, n_{crit} = 3.0, \alpha = 6.0°$

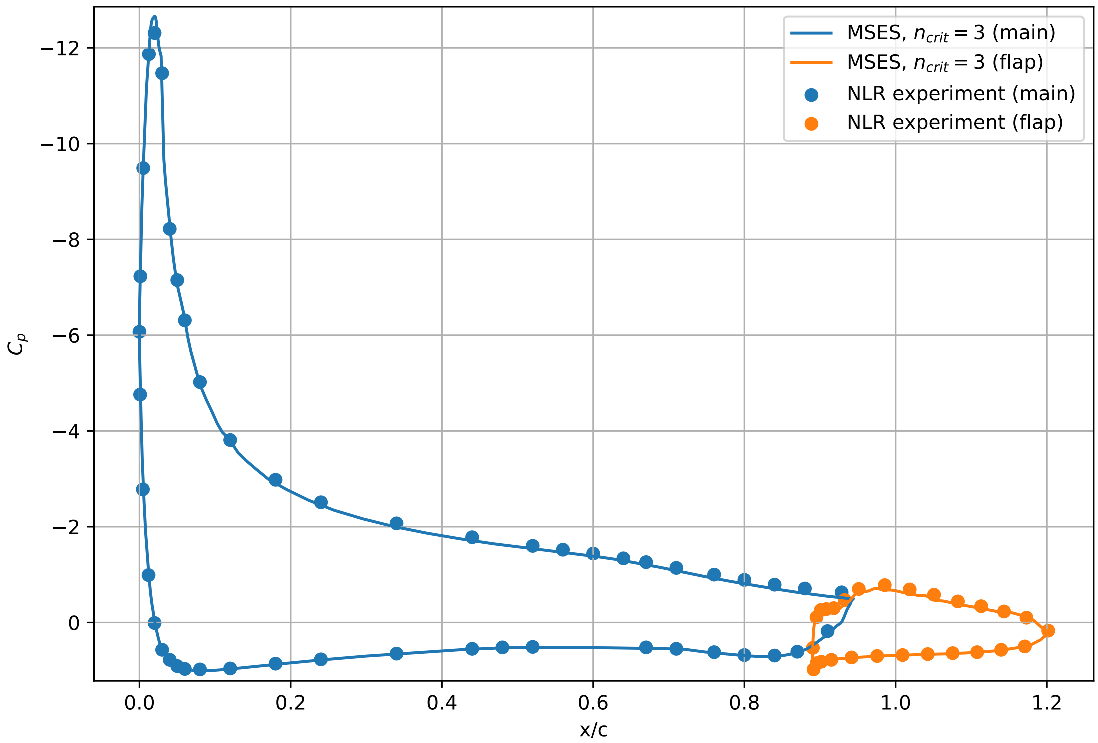

Figure 8.10: Pressure distribution comparison for the NLR7301 with $\delta_f = 20°$. $M = 0.185, Re = 2.51e6, n_{crit} = 3.0, \alpha = 13.1°$

9

Wing/flap performance

This chapter seeks to dive into increasing detail to look at the effects of having the multi-element airfoil submerged in a slipstream. The mildly-varying slipstream profile with $h/c = 0.866$ is used throughout most of this chapter, but some attention is also given to the more complex case with the hub-discontinuity, the strongly-varying slipstream. All simulations are run with the viscous boundary layer model on and off.

9.1. Setup with slipstream

The e^n transition model is used with $n_{crit} = 3.0$ as established before in section 8.3. The simulations are mostly run at the Reynolds number of the NLR experiment to allow for some comparison. For easier comparison between results, the main element BL is tripped at the nose (suction side) and 10% chord (pressure side). This combination also aids in convergence.

The AD is placed on the inlet, and the slipstream ("propeller") is constrained at $x/c = -1.0$. Iterative gridding is required for these high-lift, viscous cases, as explained more elaborately in section 5.4. A representative grid is shown in fig. 9.1. The standard domain is scaled up assuming a design c_l of 5 instead of 1.5 resulting in $[xmin, xmax, ybot, ytop] = [-3.7, 5.5, -5.5, 6.4]$. The selected angle of attack is $\alpha = 6°$ as this already shows wake-bursting at some propeller positions with reasonable convergence.

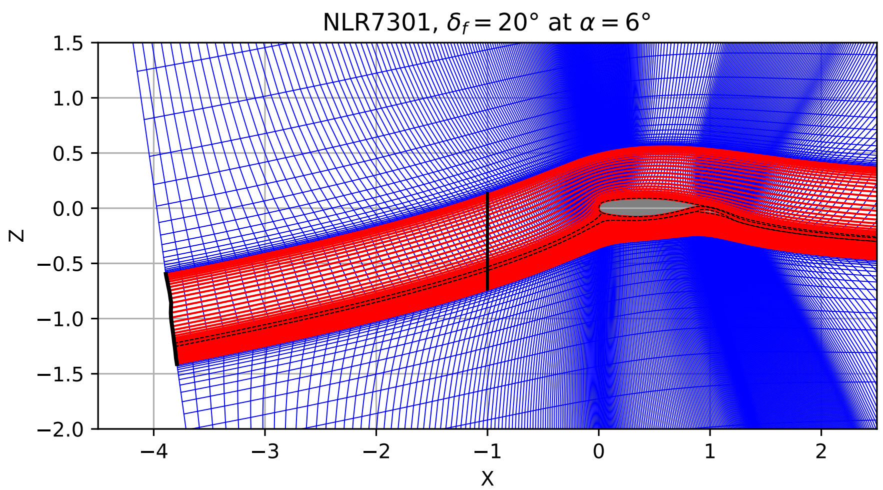

Figure 9.1: NLR7301 with $\delta_f = 20°$. $z/c = -0.3$, $h/c = 0.866$ $M = 0.185$, $Re = 2.51e6$, $n_{crit} = 9.0$, $\alpha = 6.0°$

High subsonic Mach numbers are generally observed near the nose for this particular case, the flap region generally showed lower Mach, most likely as this is only a two-element airfoil. With the high streamline density near the leading edge care should be taken that no shock-waves interfere with the BL. The boundary condition for Momentum/Entropy conservation option (ISMOM) is changed from 3 to 4, which relies on an automatic shock finder as outlined in the manual by Drela.[24]

9.2. Lifting contributions

The original lift coefficients of the flap system are shown in table 9.1. Recall the definition of K_l as in eq. (9.1): This may be used to normalize the lift increase of each airfoil element, better illustrating the relative change in lift with respect to the unblown baseline. With the lift values of table 9.1, the k_l graph in fig. 9.2 implicitly shows the lift coefficients: with a maximum $k_l = 2.24$, $C_l = 5.46$ is reached.

Table 9.1: Unblown lift values

	Combination	Main element	Flap
C_l	2.43	2.09	0.34

$$K_l = \frac{C_{l,blown}}{C_{l,unblown}} \tag{9.1}$$

The positions marked with a red circle are shown in fig. 9.3. It is noticed that the lift force on the flap is more sensitive to changes in vertical position than the main element as both a higher and a lower k_l is reached. Another observation is that the flap element apparently obtains more benefit from lower propeller positions. At high slipstream positions, the slipstream boosts the main element lift but the slipstream is not effectively deflected by the flap. Although the flap element appears to have a low 'weight' associated with it, the main element lift also depends significantly on the flap lift coefficient due to mutual interference, though this figure provides insufficient information to quantify the interference effects.

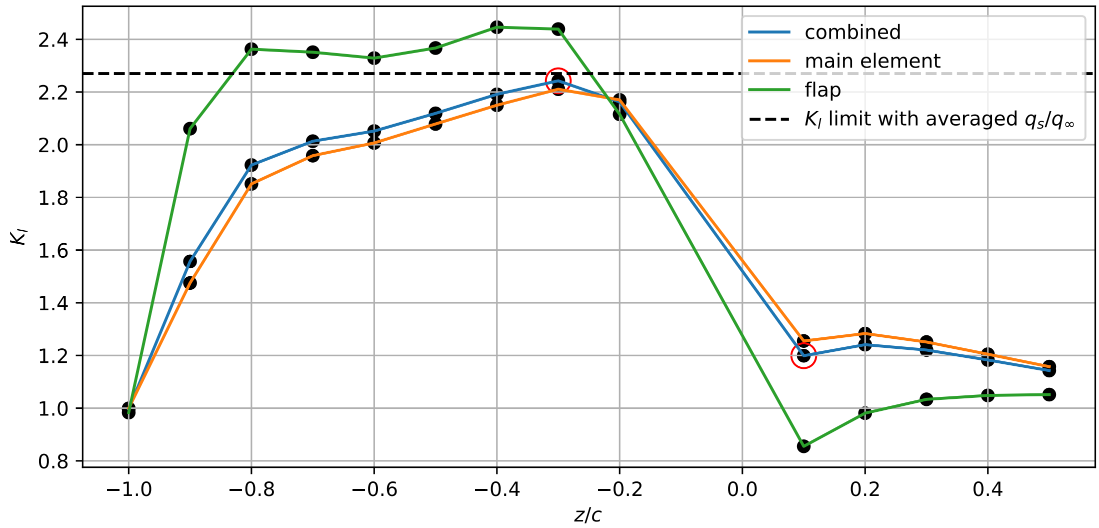

Figure 9.2: Variation of lift contributions with varying propeller z/c. NLR7301 with $\delta_f = 20°$. $M = 0.15, Re = 2.51e6, n_{crit} = 3.0, \alpha = 6.0°$

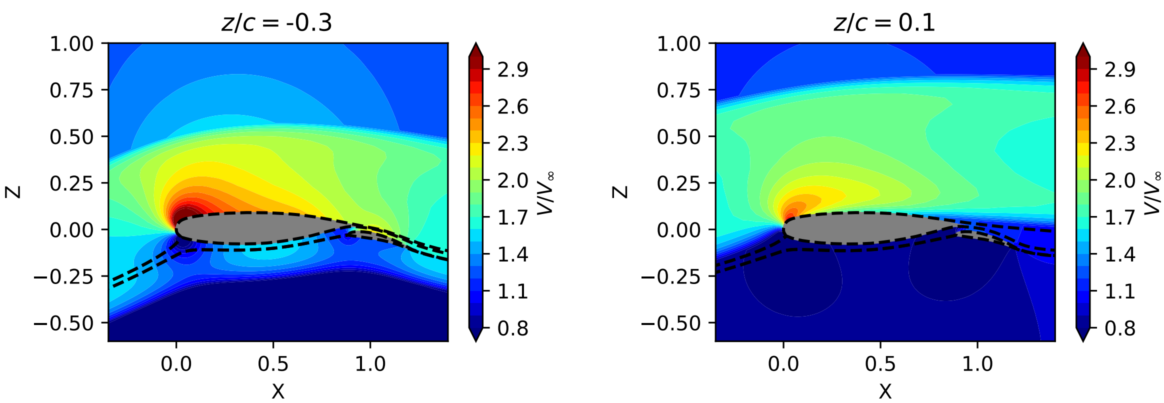

Figure 9.3: Velocity field for the marked vertical propeller positions. NLR7301 with $\delta_f = 20°$. $M = 0.15, Re = 2.51e6, n_{crit} = 3.0, \alpha = 6.0°$

Remarkably, a lift increase close to the theoretical limit based on the dynamic pressure may be reached: this would imply a β value of close to 1, despite the limited slipstream height of $h/c = 0.833$. This would also occur at the uncambered NACA0012 at small angle of attack, seen in section 6.2.1. This is suspected to occur due to the upper surface blowing effect, with both its inviscid effect of increased suction and the viscous effect of decreased boundary layer growth. These effects are further examined in this chapter.

9.3. Pressure distributions

Pressure coefficient for selected cases : The pressure coefficients for the selected points of high and low lift augmentation are shown in fig. 9.4.

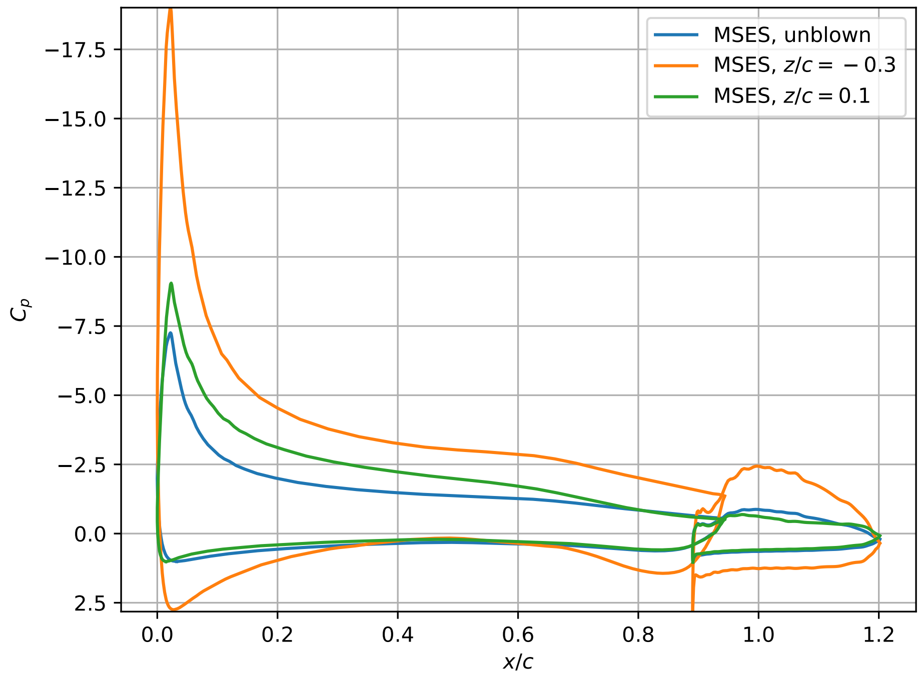

Figure 9.4: Pressure distributions for varying z/c. NLR7301 with $\delta_f = 20°$. $M = 0.15$, $Re = 2.51e6$, $n_{crit} = 3.0$, $\alpha = 6.0°$

The lower position (orange) greatly improves circulation on both elements. The aftward shift of the suction peak that was observed in section 7.2 is not observed here. The sharper nose of the NLR7301 airfoil compared to the NACA0012 and the fact that these experiments are at much higher lifting conditions may both explain the lack of this shift.

The high slipstream position (green) is only beneficial for improved upper surface suction, but actually deteriorates the lifting performance of the flap which could be interpreted as stalling. The slipstream, passing just above the airfoil combination, only positively affects the upper surface nose region by increasing suction.

The flap element shows no significant suction and hence produces much less lift: wake bursting is induced by the higher momentum air above the boundary layer which in itself contains less momentum. This wake bursting is also illustrated by fig. 9.5 indicating the boundary layer edge (the adjacent nodes got traced here). The influence of boundary layer behavior, pressure, and wake-bursting will be further explored in the next section.

9.4. Boundary layer growth & wake burst

The loss of lift associated with the $z/c = 0.1$ case is not explained by classical separation: there is no separation on the flap. The main phenomena leading to loss of lift is the main element boundary layer and wake growth (onset of bursting). It seems that the **'dumping effect'** and **'Off-the- surface Pressure Recovery'** is improved if the airfoil/flap combination is immersed in higher-velocity air. One may also express this effect as limited **'viscous decambering'** but as this would imply wake growth from the flap element this may not be an accurate description of the observed effects.

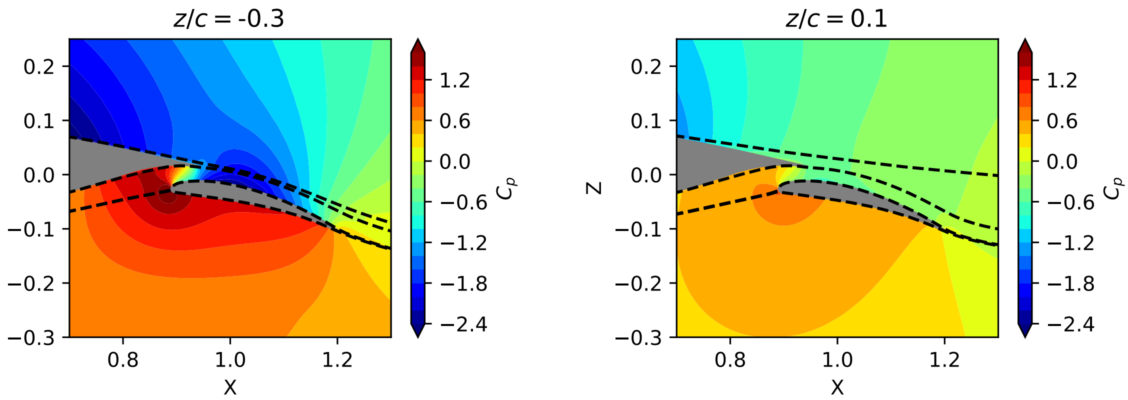

Figure 9.5: Pressure field for the marked vertical propeller positions. NLR7301 with $\delta_f = 20°$. $M = 0.15, Re = 2.51e6, n_{crit} = 3.0, \alpha = 6.0°$

The onset of wake burst is partly determined by the displacement thickness, which already grows on the main element surface. This is shown in fig. 9.6. It is confirmed that the slipstream can both increase and decrease boundary layer growth on the main element. Also note how the boundary layer from the lower surface in the wake is similar in shape to the main element displacement thickness, but smaller. It should be noted that both wake bursting and the immersion in the slipstream decrease the BL growth on the flap: The former through lowering suction and adverse pressure, and the latter through having more momentum near the flap than the surrounding air. The flap BL effect on lift is limited, as the wake bursting phenomenon is far more dominant.

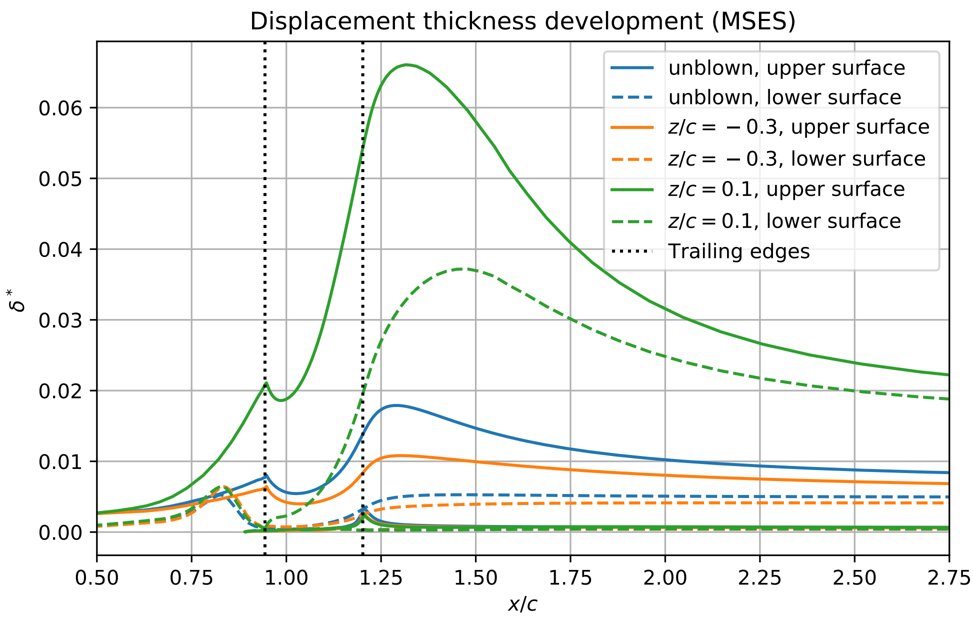

Figure 9.6: Displacement thickness for varying z/c. NLR7301 with $\delta_f = 20°$. $M = 0.15, Re = 2.51e6, n_{crit} = 3.0, \alpha = 6.0°$

Interestingly, fig. 9.7 illustrates that the bursting case of $z/c = 0.1$ shows a second pressure increase after the flap TE. This could be a precursor to wake growth. Closer comparison of the two figures reveals that, for 2 cases, the suction induced by the nose of the trailing element decreases the displacement thickness due to the higher velocities. This is however not the full story: there is no negative $d\bar{C}_p/dx$ for the 'green' case due to decreased circulation on the flap. δ^* is decreasing whilst θ is still increasing; the approach of considering $d\bar{C}_p/dx$ for growth of δ^* fails to consider the decrease in shape factor H due to the increased velocity around the flap nose. This actually develops favorably as proven by fig. 9.11.

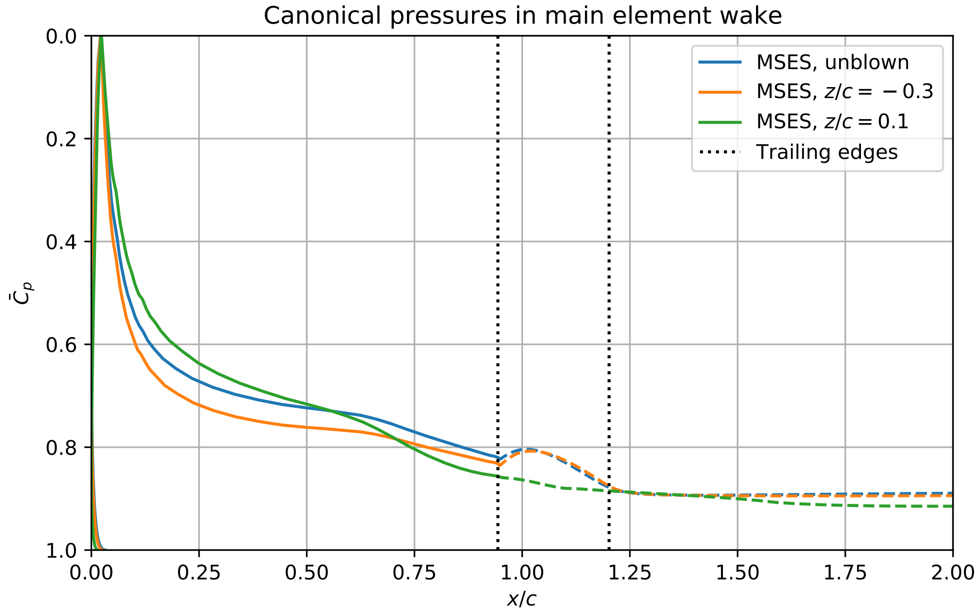

Figure 9.7: Canonical pressure distributions for varying z/c. NLR7301 with $\delta_f = 20°$. $M = 0.15, Re = 2.51e6, n_{crit} = 3.0, \alpha = 6.0°$

Gartshores criterion As explained in section 2.3.3, the Gartshore criterion eq. (2.4)[37] can predict wake growth. The requirement that boundary layers and wakes are not merged is satisfied by the NLR configuration with 2.6% gap, as noted by van den Berg [82]. As wake bursting can occur quite suddenly it will be interesting to see how the Gartshore criterion develops with different propeller positioning. The results for the Gartshore criterion are shown in fig. 9.8 and fig. 9.9. Note that the displacement thickness δ^* of the total wake is taken: the boundary layer of the pressure side of the airfoil contributes significantly to the thickness of the wake. Note that ds (or $d\xi$) is used rather than dx as the wake also travels significantly in the y direction.

For $z/c = -0.3$ and the baseline case (similar, not shown here), the criterion predicts the area of wake growth quite accurately. With a Mach number of around 0.35 above the flap, the assumption of negligible M_e^2 is acceptable. The criterion does not predict the case of for $z/c = 0.1$ however: the extent downstream of the flap gets grossly over-predicted and the magnitude is no longer related to the actual growth. As Van Craenenbroeck [18] concluded: the criterion may only be suitable for determining the presence of wake growth directly over the flap, and does not indicate the severity of it. Indeed, it seems like Gartshore criterion does not properly relate the development of δ^* and θ in the way MSES does, especially with a burst wake.

Driver and Mateer thresholds The thresholds suggested by Van Craenenbroeck [18] following the work of Driver and Mateer [38] are now considered, as introduced in section 2.3.3. As can be seen in fig. 9.10, the region of "wake burst onset" is indeed reached by the wake-bursting case of $z/c = 0.1$. Contrary to the Gartshore criterion, this threshold provides information on the onset of wake burst before the trailing edge of the flap without the discontinuity of the Gartshore criterion. This may be more easily measured in experiments. More importantly, the Driver-Mateer threshold may provide more insight in the severity of a wake-burst. Both these findings would require more investigation by considering different flap configurations in validated experiments. The Driver and Mateer thresholds may be a reliable indicator for the amount of lift loss due to wake bursting to be expected, or at which (higher) deflection angle this wake bursting would occur.

Shape factor The shape factor is an indication of flow reversal and may thus be used as an indication for wake burst. As shown in fig. 9.11, H shows higher peaks for the cases with more wake growth and subsequent bursting. As mentioned previously, $H > 4$ is indicative of separation, i.e. flow reversal, for turbulent flows. The "Driver and Mateer thresholds " appear slightly more sensitive than the H criterion: this is in-line with the observation that wake bursting may also occur with the flow being on the brink of separation, without any actual reversal.

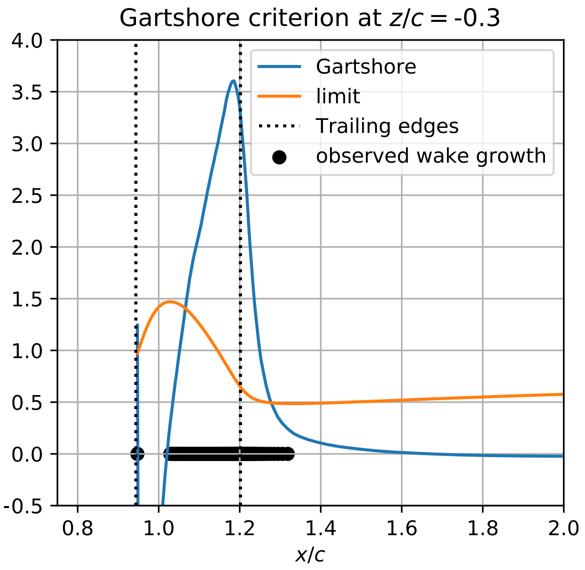

Figure 9.8: Gartshore criterion, position of highest lift, $z/c = -0.1$. NLR7301 with $\delta_f = 20°$. $M = 0.15, Re = 2.51e6, n_{crit} = 3.0, \alpha = 6.0°$

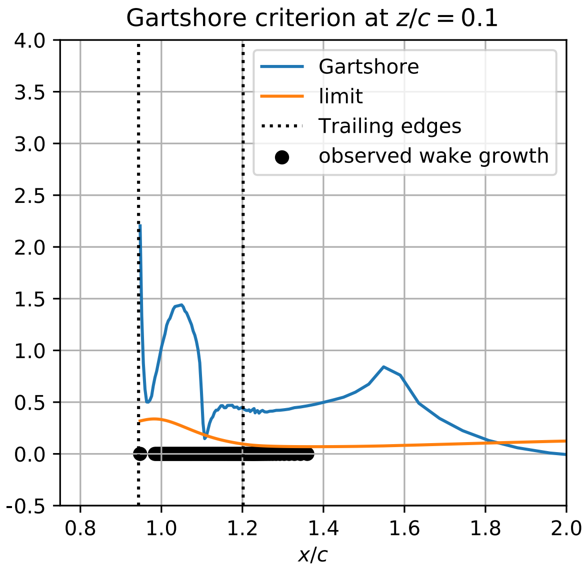

Figure 9.9: Gartshore criterion, position of lowest lift, $z/c = 0.3$. NLR7301 with $\delta_f = 20°$. $M = 0.15, Re = 2.51e6, n_{crit} = 3.0, \alpha = 6.0°$

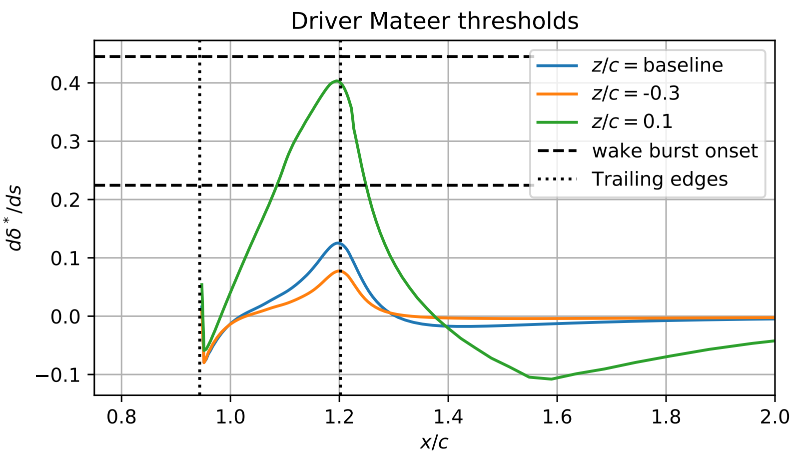

Figure 9.10: Driver and Mateer wake growth thresholds. z/c. NLR7301 with $\delta_f = 20°$. $M = 0.15, Re = 2.51e6, n_{crit} = 3.0, \alpha = 6.0°$

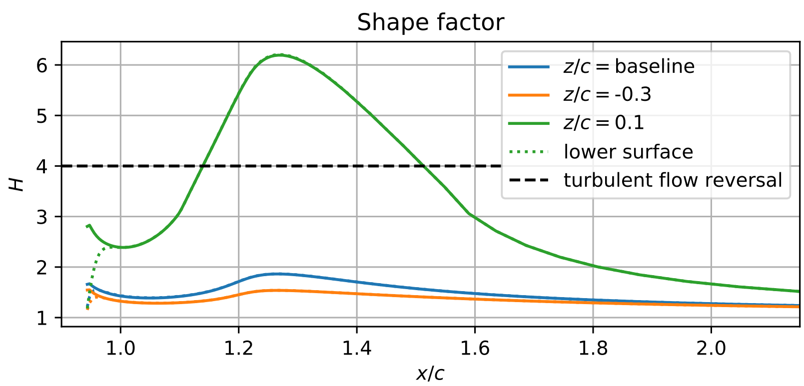

Figure 9.11: Development of the shape factor H for varying z/c. NLR7301 with $\delta_f = 20°$. $M = 0.15, Re = 2.51e6, n_{crit} = 3.0, \alpha = 6.0°$

9.5. Hub discontinuity

The slipstream with a strongly varying flow-field is also tested with a height of $h/c = 1.0$, the discontinuity in velocity at the hub increases the complexity of the flowfield. As there are two distinct peaks in slipstream velocity above and below the hub, this also impacts the results as such. As the slipstream (or any flow outside the boundary layer) is treated as inviscid, there is no mixing of the slipstream or any dissipation of the sharp velocity increase. Due to the relative scaling of the setup, this results in two distinct peaks of the lifting contribution as can be seen in the results in fig. 9.12 and fig. 9.13.

A notable difference between the two figures is that the flap lift contribution has a higher amplitude for the viscous case. This points to the preceding findings that the wake growth and bursting behavior can both be aggravated and improved by the propeller positioning.

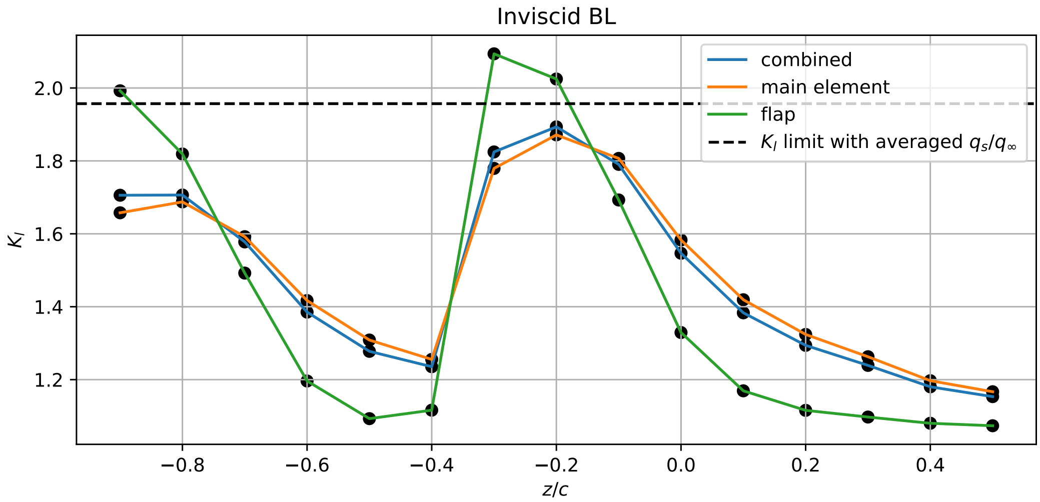

Figure 9.12: Variation of lift factor per element with varying propeller z/c. NLR7301 with $\delta_f = 20°$. $M = 0.15, inviscid, \alpha = 6.0°$

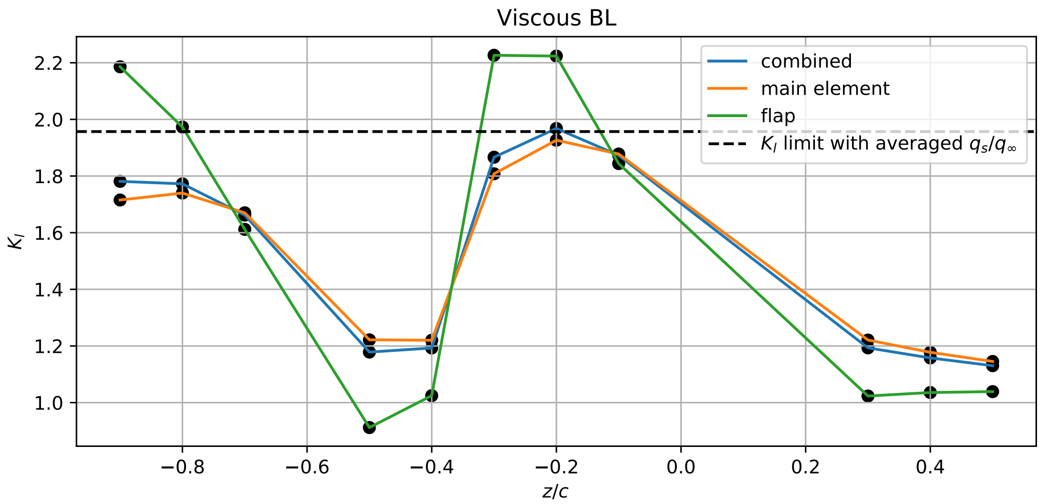

Figure 9.13: Variation of lift factor contribution per element with varying propeller z/c. NLR7301 with $\delta_f = 20°$. $M = 0.15, Re = 2.51e6, n_{crit} = 9.0, \alpha = 6.0°$

9.6. Intermediate conclusions & recommendations

Conclusions It seems that the current modification of MSES can handle non-uniform slipstream profiles on flaps reasonably well. Cases with a largely non-uniform flow-field, combined with the viscous formulation prove most difficult: about half the attempts converge. The station behind the propeller at $y = 0.5r$ was considered extensively, at which the velocity field shows a mild variation over the slipstream height.

- Highest lift is reached with the bulk of the slipstream momentum flowing over the top of the wing, similarly to the uniform AD cases considered with a single airfoil.
- With too high slipstream positions, wake bursting may be incurred, leading to a loss of lift. If the high-velocity core of the slipstream is (just) above the airfoil, the circulation on the main element increases due to the higher momentum flow above the upper surface. The boundary layer, however, has less momentum and is more prone to wake growth. The mutual interference effects with the flap that become negatively affected are the **Off-the-surface pressure recovery** and the **Dumping effect**. With the wake-burst, the circulation on the flap is decreased due to the lack of pressure recovery above the flap. This decreases the aforementioned effects, leading to earlier pressure recovery and more wake growth on the main element. For this particular case the lift values on the flap are more sensitive to vertical propeller positions and shifted by 0.1c with respect to the main element due to the aforementioned reasons.
- Intermediate slipstream positions placing the airfoil in high-momentum flow can suppress wake bursting. There is more momentum close to the airfoil and at the boundary layer which leads to less boundary layer growth. β values of 1.0 may be reached by means of upper surface blowing and separation suppression. As this configuration is driven by both suction on the upper surface and pressure on the lower, there is less of a strong preference for the elevated positions than for the single airfoil case. This causes a slipstream with a mildly varying velocity profile to have a large range of vertical positions with near-constant lift augmentation. Increased turbulence and Re in propeller slipstreams may improve maximum lift due to less boundary layer growth.
- Considering the velocity deficit at the propeller hub whilst neglecting the hub or propeller nacelle creates a greatly non-uniform flowfield, and two distinct lift peaks with a large drop in lift if the airfoil is in the center of the slipstream, between the two induced velocity peaks. These results should be interpreted with extra caution: viscous effects in the slipstream may even out the large velocity discontinuity that was modeled here, and it does not consider propeller hub and nacelle shape.

It is recommended to:

- Launch a 2D CFD or wind-tunnel exercise to validate the results. No suitable validation material was found. Boundary layer data would be of great interest, as would be the interaction with the wake.
- Consider the effect of viscosity on the wake itself: again this may be a 2D CFD computation. This is expected to smooth-out the large gradients in the velocity field and hence also smooth the results. For a 3D simulation there would also be a lateral component and variation of the flow.
- Consider the effects of the leading edge bubble: this was triggered in this study to remove its influence. The impact of blade passage on the boundary layer may impact results, especially near separation/wake bursting.

10

Parameter study: optimal gap, overlap & slipstream position with flap deflection

This chapter aims to provide insight on the effect of geometry in terms of gap, overlap and slipstream position on lifting performance. The goal is to optimize the design to delay viscous lift losses thus improving high-lift performance. The main limiting factors to maximum lift are wake confluence and wake bursting.

10.1. Setup

Two important design metrics for slotted flap systems are the overhang (or, overlap) and the gap. It is decided to stick to the variation of gap and overlap as their effects across changing angle of attack is more clear than the effect of specifying a hinge point and/or Fowler motion. The gap and overlap definition are illustrated in fig. 10.1: the gap is defined as the shortest distance from the TE up to the flap upper surface, and the overlap is defined positive as shown. As noted before, the NLR setup was not necessarily optimized for high-lift conditions, and only tested with a single overlap value of 5.3%c, and two gap values at 1.3%c and 2.6%c. The starting value of overlap is 2.6%c as the smaller overlap exhibits wake merging (i.e. confluence) as reported by Van den Berg.[82]

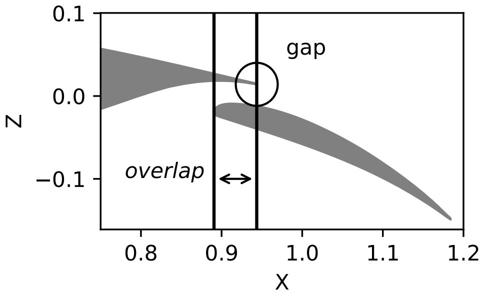

Figure 10.1: Gap and overlap definition. NLR7301 airfoil with $\delta_f = 30°$

The NLR7301-flap combination is again tested at $\alpha = 6°$. The flap angles are varied from $\delta_f = 10°$ up to $\delta_f = 40°$. Note that the NLR flap has a slightly negative inclination with respect to its coordinate frame as shown in fig. 8.1. Care should be taken when interpreting results due to changing vertical slipstream position as this impacts the lift. The slipstream is now constrained close to the airfoil at $x/c = -0.5$ which is still representative for DEP applications as shown in fig. 10.2 and fig. 10.3. There is still significant slipstream deflection, but the goal is to be able to produce lift polars without major discontinuities in lift. This configuration also improves convergence. The slipstream profile that is used is again the mildly varying velocity profile presented in section 5.2, with $h/c = 0.866$. It should be stressed that the results of this study are highly case-specific: a different distribution of velocity in the slipstream, different (average) speed increase, or a different geometrical set-up may produce different results.

The viscosity settings are identical to those in earlier experiments: $Re = 2.51e6$, $n_{crit} = 3.0$ and the boundary layer gets tripped at the main element nose (upper side) and 10% of the main element lower side. The flap upper and lower side are left free to transition towards the trailing edge. The domains are selected to be appropriate to lift values beyond the highest anticipated C_l: for the unblown case it is sized for $C_{l,max} = 5.0$ and the blown case is sized for $C_{l,max} = 10.0$, resulting in a domain size of $[xin, xout, ybot, ytop] = [-3.7, 5.5, -5.5, 6.4]$ & $[-5.2, 7.7, -7.7, 9.0]$, respectively.

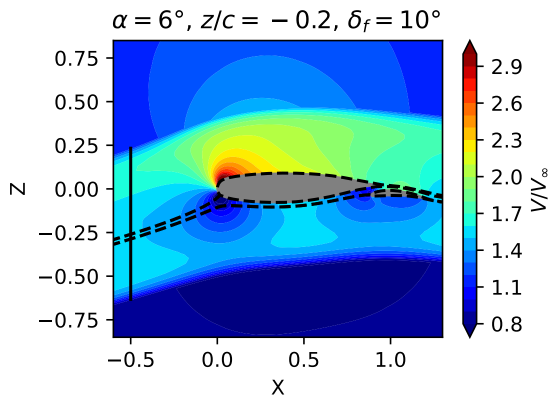

Figure 10.2: Velocity field. NLR7301 with $\delta_f = 10°$. $h/c = 0.866$, $M = 0.15$, $Re = 2.51e6$, $\alpha = 6.0°$

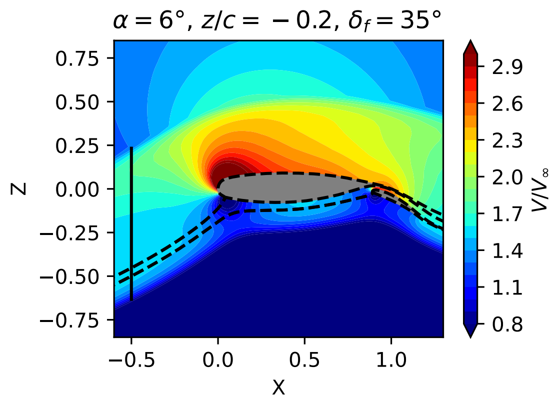

Figure 10.3: Velocity field. NLR7301 with $\delta_f = 35°$. $h/c = 0.866$, $M = 0.15$, $Re = 2.51e6$, $\alpha = 6.0°$

10.2. Baseline results

The lift polars for the baseline unblown and blown airfoil are compared in fig. 10.4 and fig. 10.5, note that the lift has more than doubled and thus the c_l axis are different. At $\alpha = 6°$, $C_{l,max}$ occurs at around $\delta_f = 37.5°$ for both the unblown and blown case. The results clearly indicate that the external blowing postpones the viscous de-cambering (or even wake-burst) of the system, leading to lift values closer to the inviscid result. A small kink in the viscous results can be noticed around $\delta_f = 27.5°$, this is due to the flap upper surface transition point moving forward significantly due to higher loading. Due to the changing vertical position of the slipstream due to upwash, the inviscid polar in fig. 10.5 deviates more from a straight line than the unblown case.

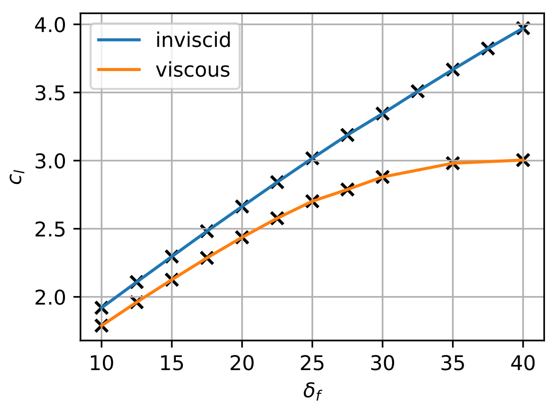

Figure 10.4: Unblown lift polar. NLR7301 with varying δ_f. $M = 0.15$, $Re = 2.51e6$, $\alpha = 6.0°$

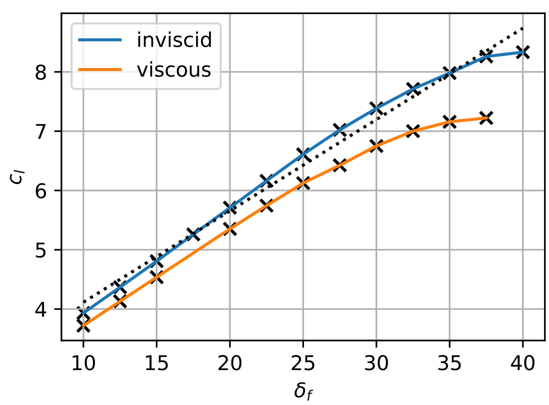

Figure 10.5: Blown lift polar. NLR7301 with varying δ_f. $M = 0.15$, $Re = 2.51e6$, $\alpha = 6.0°$

The results for lift factor K_l in fig. 10.6 show that the relative lift increase due to blowing increases with δ_f, moreso for the viscous than the inviscid results. The inviscid results only show the effect of slipstream deflection (which peaks earlier due to the higher lift and deflection). The viscous lift augmentation can reach a higher lift augmentation relative to the unblown case due to the favorable effect that blowing has on decreasing the growth of the boundary layer and supressing wake-bursting behavior.

The results for δC_l are shown in fig. 10.7. At first sight, this appears compatible with slipstream momentum theory (see section 3.2): which state that the lift increase is proportional to $mV_R sin(\alpha_s + \theta)$. Note that, as with the other results, these observations may only be valid for this particular setup; this particular $z/c = -0.2$ seems to be quite near the optimum.

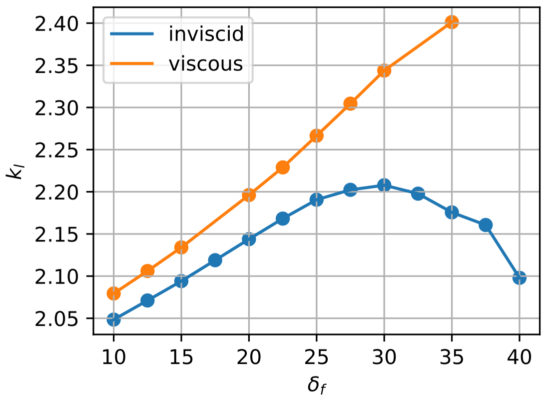

Figure 10.6: Lift ratio K_l due to blowing. NLR7301 with varying δ_f. $M = 0.15, Re = 2.51e6, \alpha = 6.0°$

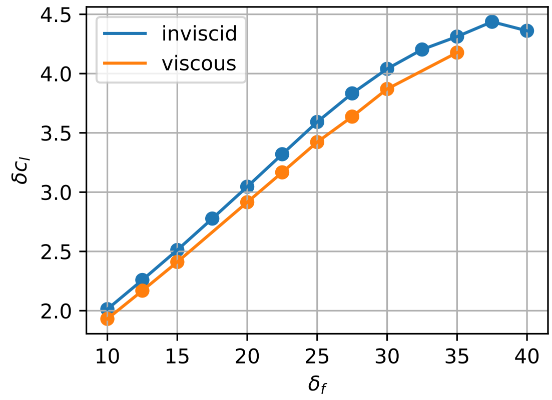

Figure 10.7: Lift increment due to blowing. NLR7301 with varying δ_f. $M = 0.15, Re = 2.51e6, \alpha = 6.0°$

10.3. Design space exploration

This section explores both the unblown and the blown design space for two deflections. Surface plots can simultaneously provide insight into the sensitivity to gap and overlap. An optimal gap/overlap combination for one deflection angle may not be the optimal for another one. Thus, this is compared across different flap deflection angles, whilst keeping the airfoil at 6° angle of attack. For both the blown and unblown design space the variables are included in table 10.1 and include the baseline of 2.6%c gap and 5.3%c overlap.

Table 10.1: Design space exploration variables

gap [%c]	1.8	2.2	2.6	3.0	3.4		
overlap [%c]	-0.7	0.3	1.3	2.3	3.3	4.3	5.3

Unblown design space It is decided to compare the baseline $\delta_f = 20°$ (as used throughout chapter 8 and chapter 9) and a more high-lift condition with $\delta_f = 27.5°$. Higher angles would not always converge. Comparing the results in fig. 10.8 and fig. 10.9, the following conclusions may be drawn:

- The optimal overlap is slightly lower for high flap-deflection, at 1.0%c instead of 1.5%c. See section 10.4.3 for more explanation on the effect of overlap.
- The optimum has small sensitivity to gap size for $\delta_f = 20°$ but small gaps are desirable for $\delta_f = 27.5°$. However, as discussed in section 10.4.2, MSES may over-estimate the results for small gaps.
- At higher lifting conditions, the C_l becomes relatively more sensitive to the design.

Blown results Under blowing the effect of slipstream position also needs to be considered. The vertical positions are varied from $z/c = -0.5$ to $z/c = -0.1$. At $z/c = -0.5$, most of the slipstream passes underneath the airfoil which, as established previously, is less ideal than the airfoil being in the lower half of the slipstream. For $z/c = -0.1$, almost the entire slipstream passes over the multi-element airfoil at $\delta_f = 35°$. Any higher may cause wake-bursting behavior as observed before. The results most relevant for high lifting performance (at $z/c = -0.2\& -0.3$) are shown in fig. 10.10 through fig. 10.13. The following conclusions may be drawn:

- Slightly smaller overlap than for the unblown case is desired for $\delta_f = 20°$. Similarly to the unblown case, optimal overlap is slightly lower for high flap-deflection, at around 1.0%c vs 2.0%c.
- Similarly to the unblown case, the optimum has limited sensitivity to gap size for $\delta_f = 20°$, with large gaps being slightly more preferable. For larger deflections on the other hand, the preference shift to smaller gap sizes of 2.6%c or less.
- Similarly to the unblown case, at higher lifting conditions, the C_l becomes relatively more sensitive to the design.

Finally, it is intresting to note that for the optimal gap, the lift scales approximately with the total chord length of the airfoil combination between the optimal overlap and the largest overlap (5.3%c).

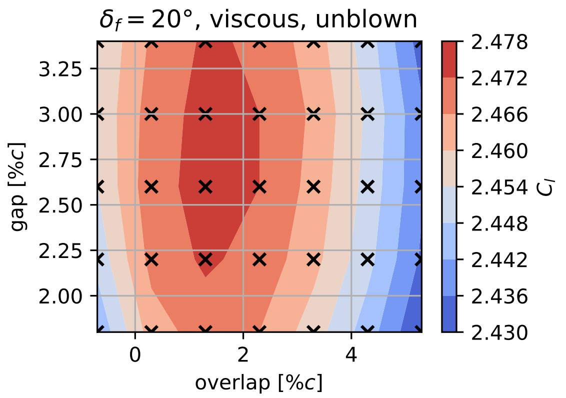

Figure 10.8: NLR7301 with $\delta_f = 20°$. $M = 0.15, Re = 2.51e6, \alpha = 6.0°$

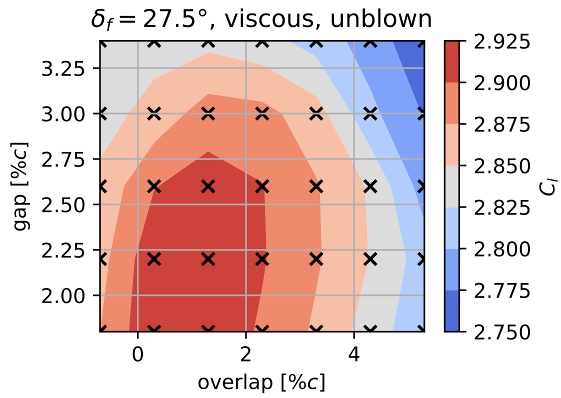

Figure 10.9: NLR7301 with $\delta_f = 27.5°$. $M = 0.15, Re = 2.51e6, \alpha = 6.0°$

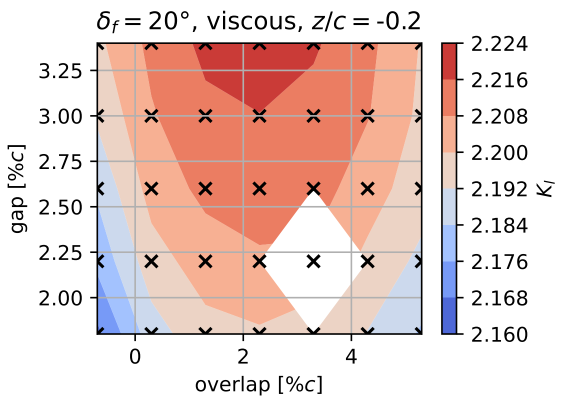

Figure 10.10: NLR7301 with $\delta_f = 20°$. $M = 0.15, Re = 2.51e6, \alpha = 6.0°$

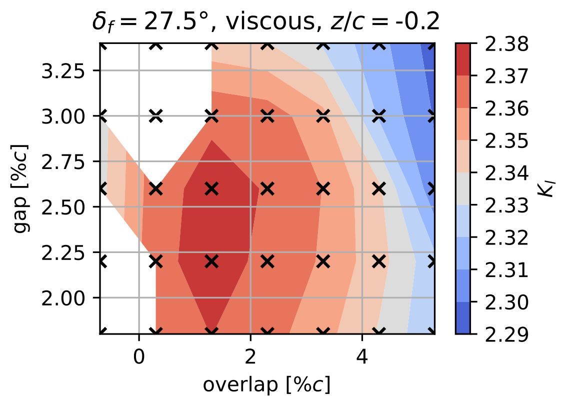

Figure 10.11: NLR7301 with $\delta_f = 27.5°$. $M = 0.15, Re = 2.51e6, \alpha = 6.0°$

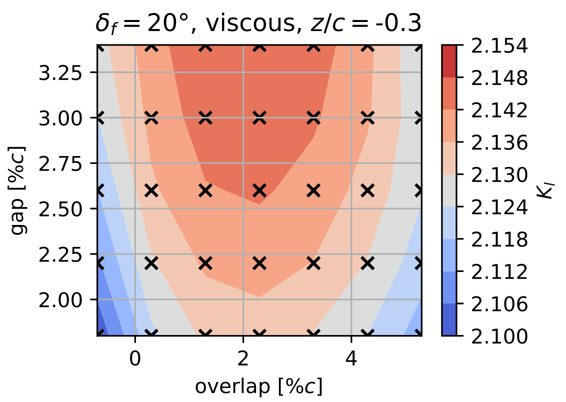

Figure 10.12: NLR7301 with $\delta_f = 20°$. $M = 0.15, Re = 2.51e6, \alpha = 6.0°$

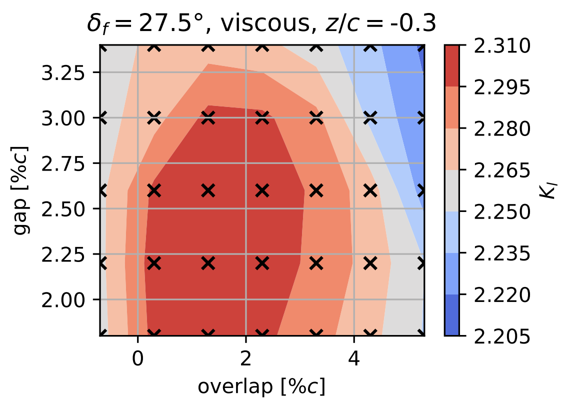

Figure 10.13: NLR7301 with $\delta_f = 27.5°$. $M = 0.15, Re = 2.51e6, \alpha = 6.0°$

10.4. Optimal designs

The design is now optimized for $\delta_f = 27.5°$ using the aforementioned contour plots by selecting the optimal gap, overlap and z/c value. For the blown case, the slipstream position is slightly lowered from $z/c = -0.2$ to $z/c = -0.25$ which delays the lift decrease due to slipstream position to higher deflection angles. It should be stressed again that the results are highly case-specific.

10.4.1. Optimized lift polars

Though the optimum gap would be in the order of 2.2%c, a gap size of 2.6%c is used to ensure a conservative design w.r.t. wake confluence, see also section 10.4.2. An overlap of about 1.0%c seems optimal for both the blown and unblown design. Hence, interestingly, the favorable effect of blowing occurs at very similar -if not identical- gap and overlap.

The resulting lift polars are shown in fig. 10.14 and fig. 10.15, note that the c_l axes are different as c_l's for the blown case are more than double that of the unblown case. For the unblown case the lift increase for the optimized design (with smaller overlap) gradually increases with δ_f. The lift increase for the blown case becomes most profound at high lift conditions: this is due to the fact that the slipstream got lowered ever so slightly to $z/c = -0.25$, which is favorable for high-lift conditions where most of the slipstream moves above airfoil without incurring separation. This does not positively impact the blown low-lift condition where the slipstream position is below the optimum. Though too few points converged to draw conclusions about the actual stalling behavior of both. However, at high δ_f there seems to be less leveling off of c_l for the blown case. The different wake-bursting behavior near maximum lift is discussed in section 10.4.3.

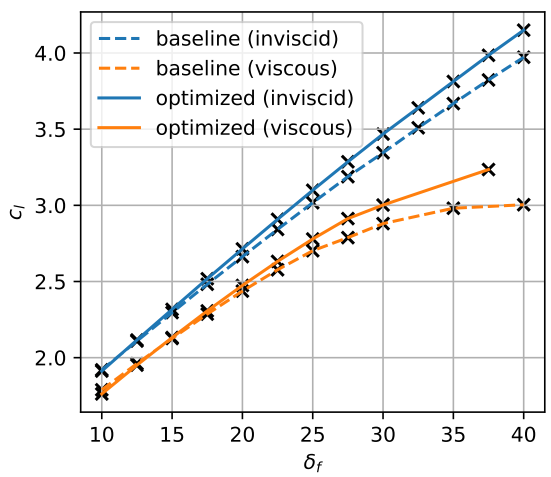

Figure 10.14: Optimized unblown lift polar. NLR7301 with varying $\delta_f, gap = 2.6\%c, overlap = 1.0\%c$. $M = 0.15, Re = 2.51e6, \alpha = 6.0°$

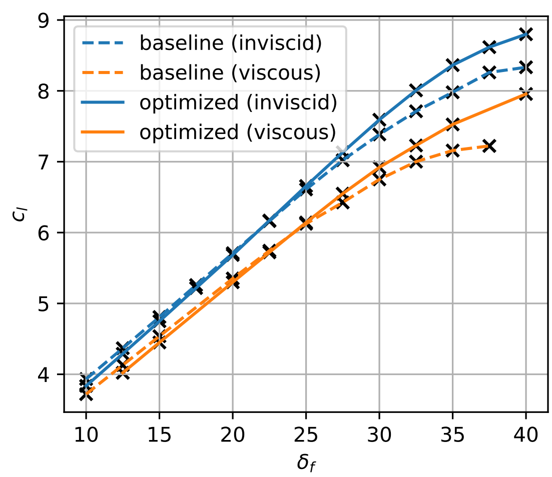

Figure 10.15: Optimized blown lift polar. NLR7301 with varying $\delta_f, gap = 2.6\%c, overlap = 1.0\%c$. $M = 0.15, Re = 2.51e6, \alpha = 6.0°$

Finally, it should be noted that the K_l and δC_l curves are similar to those in fig. 10.6 and fig. 10.7. Too few points converged for the unblown design to draw different conclusions, hence the new plots are not presented here. The inviscid K_l peaks 5° later, most likely due to the slightly lowered slipstream, which raises the point where the airfoil-flap system is in the optimal position.

10.4.2. Gap size & wake confluence

As noted in the preceding section, a lower limit on the gap size is imposed by the wake confluence effect. The ability of MSES to model lift decrease due to wake confluence does not appear to be implemented, hence, this important effect should be investigated further.

Wake confluence decreases lift for smaller gap sizes as the main element wake and flap boundary layer merge which leads to lower momentum in the boundary layer. The resulting lift decrease is illustrated by fig. 10.16. Below the optimum, wake confluence limits the lift. On the contrary, gap sizes larger than the optimum may decrease beneficial mutual interaction effects, which may be both inviscid and viscous in nature. Van Dam attributes lift loss mainly to viscous effects: “The lift loss at larger gap sizes is mostly the result of the boundary-layer development along the main element and the flap.” (Van Dam [52])

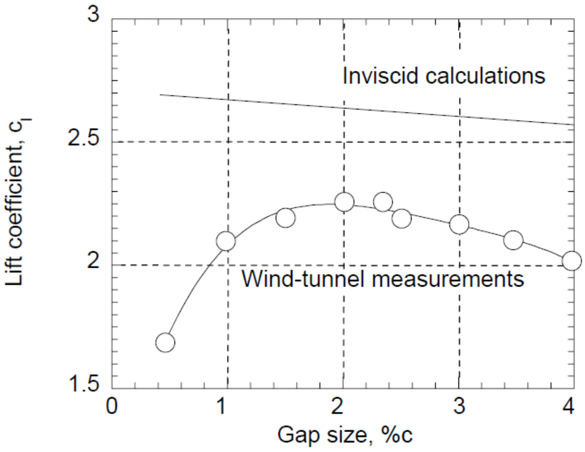

Figure 10.16: 'Effect of flap gap on lift coefficient on a two-element airfoil at $\alpha = 0°$, $Re = 3.7$ million, $M_\infty = 0.2$ (van Dam [52], originally from Brune and McMasters [84].)

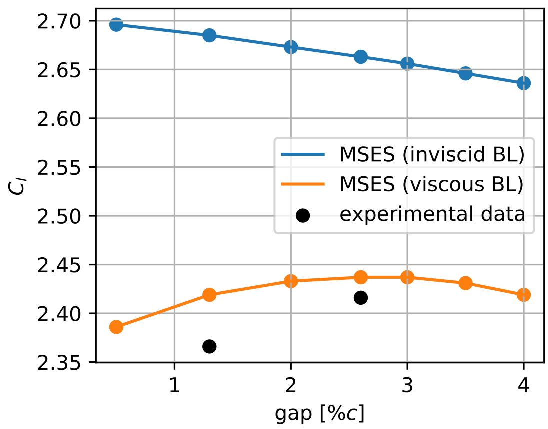

Figure 10.17: Lift coefficient for varying gap size. NLR7301 with $\delta_f = 20°$. $M = 0.15, Re = 2.51e6, \alpha = 6.0°$

It is interesting to see the effect of gap size on wake confluence for the flap system at hand. This is shown in fig. 10.17. For comparison, the wind-tunnel results (Van den Berg [82]) at $\alpha = 6°$ show that lift is lower with the smaller gap size, at which mixing (i.e. confluence) occurs. This is also seen from the velocity profiles in the test report: between the two deficits the velocity falls short of the potential value for the smaller gap. Unfortunately, velocity profiles from MSES could not easily be reconstructed for analyzing this behavior. Although a confluence model never appears to have been included in MSES, the results do show some lift decrease at the lower gap sizes. However, especially for the smallest gaps the lift decrease is not nearly as much as expected, hence the results should be approached with great caution. The decreasing trend for the inviscid analysis is also discernible in MSES.

10.4.3. Overlap & delayed wake-bursting

The impact of the overlap on the high-lift performance is explained in this section. The flow-field of the optimized design is also presented, as on the cover of this report.

The suction peak on the flap nose has the potential to provide a favorable pressure gradient for the boundary layer coming off the main element. In the original design, this property may not be fully utilized. The subsequent pressure increase over the aft part of the flap could prove more challenging towards wake bursting, but this is not necessarily dominant.

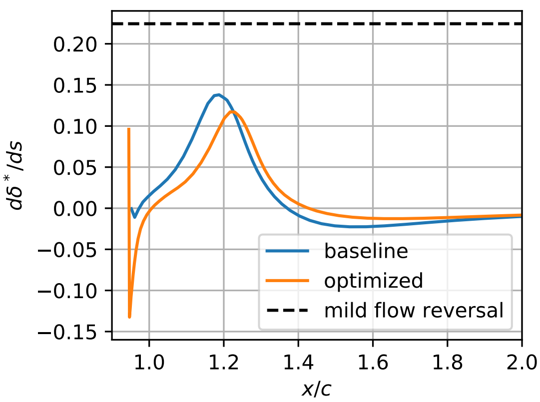

Figure 10.18: Driver and Mateer criterion: wake growth for optimized NLR7301 with $\delta_f = 35°$. $M = 0.15, Re = 2.51e6, \alpha = 6.0°$

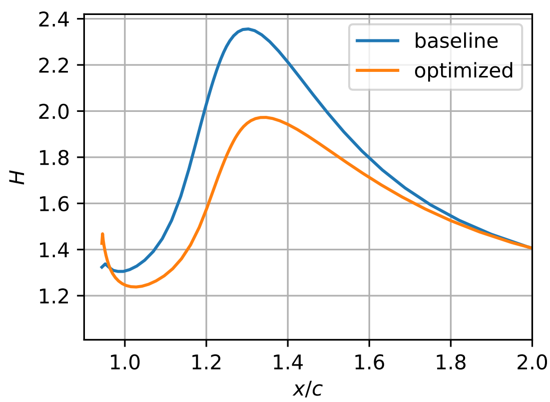

Figure 10.19: Shape factor development for optimized NLR7301 with $\delta_f = 35°$. $M = 0.15, Re = 2.51e6, \alpha = 6.0°$

For the blown case, and improvement in the Driver and Mateer criterion is seen in fig. 10.18. A smaller overlap leads to shrinkage of δ^* and, subsequently, delayed wake growth at a smaller magnitude. The shape factor is also lowered throughout the wake, as shown in fig. 10.19. It should be noted that other factors, such as the boundary layer (i.e. de-cambering) on the flap may also play a role: this may be the next limiting factor to lift, and relieve the adverse pressure gradient in the wake. For the unblown results there is also an improvement: at $\delta_f = 37.5°$ the Driver and Mateer wake-growth criterion peaks at 0.40 and the shape factor value peaks around 5.5. For the non-optimized case, these values would occur at 2.5° lower flap deflection.

The optimized configuration is presented at high-lift conditions in fig. 10.20 and fig. 10.21. The velocity increase over the leading part of the flap indeed favorably impacts the boundary layer leading to delayed the wake-bursting, and hence improving maximum lift.

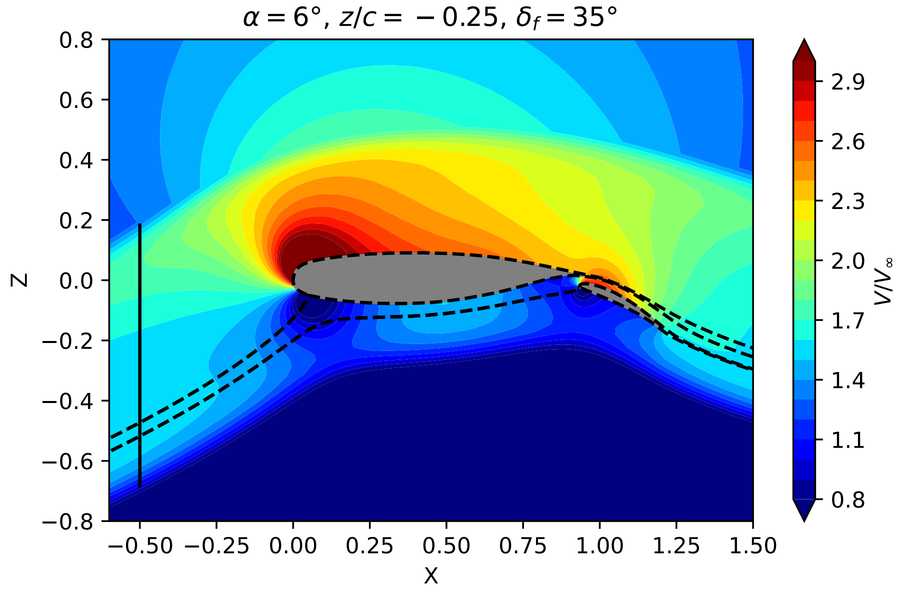

Figure 10.20: Optimized airfoil/slipstream configuration. NLR7301 with $\delta_f = 35°, gap = 2.6\%c, overlap = 1.0\%c$. $M = 0.15, Re = 2.51e6, \alpha = 6.0°$

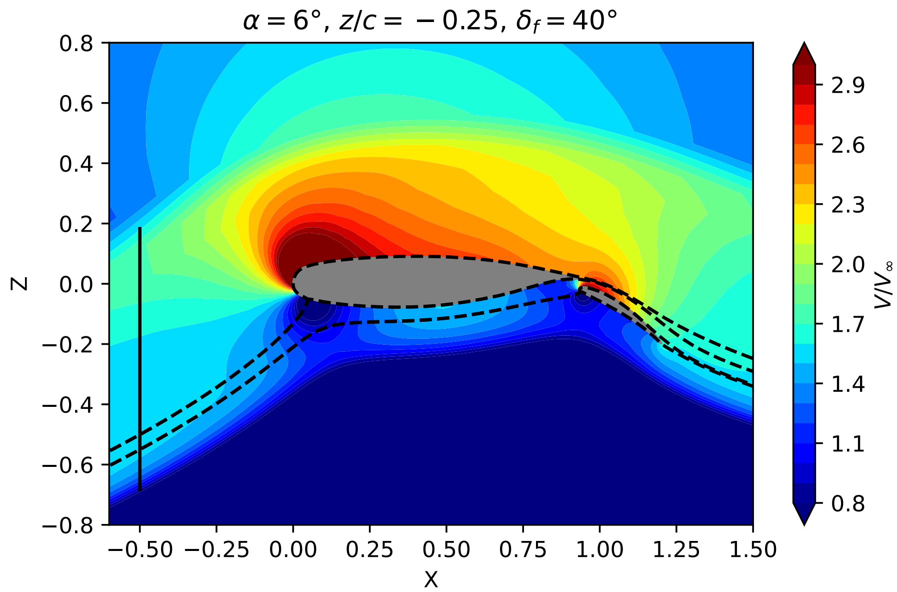

Figure 10.21: Optimized airfoil/slipstream configuration. NLR7301 with $\delta_f = 40°, gap = 2.6\%c, overlap = 1.0\%c$. $M = 0.15, Re = 2.51e6, \alpha = 6.0°$

11

Conclusions & Recommendations

11.1. Conclusions

There is renewed interest in using propellers to augment lift by means of blowing flaps, by technologies such as distributed electric propulsion (DEP). To this end, new and fast analysis tools are required to evaluate the design space of such systems. There has been limited CFD experience into this topic and also few experiments with DEP type configurations. Inviscid methods such as VLM, lifting line, or the Weissinger method prove promising. They have been successfully applied to the (unblown) high-lift problem and or to propeller blown wings in cruise. Combining the two has seen limited success as airfoils with high-lift devices have much higher effective camber and lift augmentation than cruise airfoils. Adoption of a 2D method with viscous-inviscid coupling could provide 2D 'tuning' of such inviscid methods to account for viscous effects. Some models for limited slipstream height in 2D exist but these do not consider asymmetrical effects such as upper surface blowing. They may also not be able to accurately model the deflection of a slipstream around a flapped airfoil. MSES is selected as the starting point, as it is already used extensively, and available within TU-Delft.

MSES is modified to evaluate the impact of limited slipstream height on the lift of multi-element high-lift devices in 2D. MSES provides a good starting point as its formulation of the steady-state Euler equations uses conservation of mass flow and total enthalpy (or, equivalently, total density) along streamlines. This allows to impose a jump in total enthalpy or pressure which, due to the inviscid nature of the Euler simulation, will result in the desired velocity increase. This velocity increase can follow any profile such as the "doughnut slice" obtained from an axial propeller flowfield. This can be both prescribed at the inlet or at any other desired location within the domain, yielding a 2D actuator disk. There are however also limitations to this method: Actuator disk inclination has no effect and hence a "propeller" under angle of attack cannot be modeled.

For a fully developed slipstream, i.e. where the total velocity increase is already present at the inlet, the MSES results match the CFD study by Robert Nederlof [28]. Adding refinements near the edges of the slipstream where a large velocity gradient is present improves the spread of the MSES simulation results to $+/-1\%$ or even less for larger slipstream height ratios. As the refinements are added in the initial grid generator MSET, it is necessary to obtain an estimate of the upwash and contraction of the slipstream beforehand: for low lift cases a fudge-factor may suffice but for high-lift conditions an iteration is required. This is a potential weak spot of the simulation. Further validation material is required for use with flaps and viscosity enabled: this could be either a wind-tunnel test or higher-fidelity CFD simulations.

A free-contraction AD is also considered: The contraction in MSES seems to follow the model of Smelt and Davies fairly closely, and the trends with vertical offset correspond to those expected. However, the MSES results provide much lower lift than those of the CFD simulations of Patterson [27]. Whether the issue lies with the results of Patterson or the MSES results is up for debate as Patterson would consistently obtain lift augmentation exceeding the theoretical maximum. It proves to be difficult to obtain the upwash and slipstream shrinkage to allow for sufficiently accurate placement of the streamlines, especially for high-lift cases where the dividing streamlines would curve significantly. Hence, it is decided that the free-contraction case has too much uncertainty: a correction factor to account for under-developed slipstreams may provide a reasonably accurate approximation.

Vertical placement of the slipstream has an important effect on lift that is already noticed for a single-element airfoil. For a NACA0012 with the boundary layer model enabled and a realistic propeller slipstream profile, $C_l = 0.33$ is easily attained, similar to placing an unblown airfoil at $\alpha = 3.0°$. This yields an "s"-shaped lift graph when plotted against slipstream vertical position: this was also observed in 3D with the APROPOS wind-tunnel experiment by Veldhuis [40]. A high position will cause upper surface blowing. Peculiarly, the stagnation point shifts upward and the pressure suction peak moves further aft.

Upper surface blowing of the NACA0012 results in a lower boundary layer displacement thickness than the unblown NACA0012 under angle of attack. From an analysis of the 2-equation boundary layer model it is found that the effect of velocity development is more dominant than that of skin friction. The more favorable pressure distribution of the blown case is responsible for improvement with respect to the case under angle of attack. The effects of viscosity should be interpreted with caution, especially if the lift augmentation is directly influenced by the large velocity increase near the edges of the slipstream. In reality, viscous effects in the slipstream may furher "smooth out" the velocity distribution. The effect of increased turbulence and the impingement of propeller wakes on the airfoil may also not be fully captured by simply expediting transition with triggering the boundary layer or setting a lower n_{crit}.

The lifting performance is also tested with a slotted high lift system: the NLR7301 with flap. This was first tested without blowing: It seems that MSES can closely approximate the lift curve up to $C_{l,max}$ with $n_{crit} = 3$ but the wake bursting occurs less sudden than on the wind-tunnel model. Care should be taken when initializing the grid: At these conditions, the airfoil has a bubble on the leading edge which can otherwise cause irregular results near $C_{l,max}$. Therefore, the boundary layer is tripped for the simulations with a slipstream.

It turns out that, as expected from the single airfoil, the slipstream can boost the lifting performance of the airfoil-flap combination significantly provided that it is correctly positioned. A major conclusion is that **the slipstream is able to both suppress and aggravate wake-bursting depending on the position.** This causes a relatively high lift variation on the flap lift between the slipstream positions. If the main element and flap are in a high-velocity part of the slipstream this has a favorable impact on the development of the boundary layer: the adverse pressure gradient can more easily be overcome. If too much of the slipstream momentum passes above the airfoil combination, it may actually decrease lift and incur a wake-burst. This is both due to the upper surface receiving less momentum which is detrimental for the BL development and the mutual interaction with the flap which obtains lower circulation. This decreases the "dumping effect" and "off-the surface pressure recovery". Furthermore, it is found that the criterion of Gartshore may not be able to predict the severity of a wake-burst, and that the criterion for wake growth (from the research of Driver and Mateer) or simply the shape factor, may be more reliable indicators.

Finally, a parameter study into the optimal gap, overlap, and slipstream position is undertaken to establish the effect on the lift with various flap settings on the flapped NLR7301 configuration. The blown cases show later viscous de-cambering and wake-bursting than the unblown reference. The optimal design seems identical between the blown and unblown situation. Optimal gap size depends on the lifting condition: high lift calls for a lower overlap, but the associated wake confluence effects do not seem to be properly considered by MSES. Wake bursting may be effectively delayed by shrinking the overlap to allow for the favorable effect of the LE suction of the flap on the wake coming of the main element. This study further demonstrates the capability of the modified MSES version as a blown flap redesign tool.

The set of research questions may be answered as follows: A coupled viscous/inviscid solver can be used to predict the 2D airfoil lifting behavior under influence of a propeller/slipstream. This can be effectively approached with a streamline discretized solver by introducing a jump in total pressure or total enthalpy. This is demonstrated successfully by modifying MSES. The limitations of this method are that AD inclination and 3D effects could are not included. Cases with free-contraction (i.e. where the slipstream is not fully developed) are also difficult to resolve, mainly due to issues with properly refining the grid. Another limitation is the fact that viscosity outside of the airfoil boundary layer is not considered, and this may influence development of the slipstream. Finally, it is confirmed using this code that the presence of a slipstream may improve maximum lift by means of upper surface blowing. There are also favorable effects on the boundary layer if the wing is immersed in a high-momentum part of the slipstream: this may lead to slower boundary layer growth and delay wake-bursting to higher angles of attack.

Hence, the code developed in this Thesis may be used to assess the performance of a 2D or wide slipstream. It may also be used to provide insight into the performance of 3D configurations or "tune" an inviscid solution with 2D data.

11.2. Recommendations

The recommendations can be divided into multiple areas: namely in the areas of validation, viscosity, incorporation of propeller effects, and the overall implementation and boundary conditions.

Validation It proved rather difficult to find suitable validation material to exactly match the assumptions made in MSES. It is recommended to perform both (RANS) CFD and wind-tunnel experiments to test not only the inviscid simulation but also if the viscous boundary layer model still holds, and what the impact of neglecting the effect of viscosity on the slipstream velocity profile is. Hence it is recommended to:

- Perform wind-tunnel tests: To limit 3D effects a near 2D wind-tunnel test could be performed where the flap would span the entire test section. A rectangular slipstream with a velocity profile constant along the span would be the ideal situation. This could be produced by flow-retarding screens, blowing slots/divergent ducts, or by propellers with some overlap. This can be used to check the limitations of the assumptions with respect to contraction and viscous effects, and also to evaluate all results such as slipstream position and other design variables. Care should be taken when correcting for wall effects as there can be a high degree of slipstream deflection.

- Perform (RANS) CFD experiments: More Euler computations can be used to further test non-uniform velocity profiles, airfoils with (slotted) high-lift devices, and also to explain the discrepancy with the material of Patterson. Viscous simulations can provide further insight into the limitations of the current method, be it on contraction, the boundary layer model on the airfoil, or viscocity within the rest of the slipstream. This may also be used to determine the extent of these assumptions and point in directions of potential mitigation of these shortcomings.

Viscous effects As mentioned before, there are multiple areas where viscous phenomena are not incorporated or simplified. Hence it is recommended to:

- Consider what the most appropriate transition settings are, considering that propellers cause unsteady effects. Care should be taken when assessing the flapped NLR7301 near maximum lift due to the small laminar bubble on the nose.

- Consider the limitations of the fact that the slipstream itself is simulated as an Euler flow, and potentially provide mitigation or a model. If viscosity between adjacent streamlines would be implemented the simulation would step closer to the realm of CFD.

- A way of modeling or detecting wake confluence and avoiding the associated gap sizes should be implemented.

- It should be investigated how the development of the shape factor in the wake can be used to predict and assess the severity of a wake-burst.

Propeller & 3D effects Besides the limitations with respect to viscosity and unsteadiness, there are more limitations associated with the AD assumption in this thesis. It is recommended to investigate these. Some of these include:

- Angle-of-attack effects of the actuator disk could not be modeled in the current formulation. The velocity increment does not alter the direction of the slipstream, which will need at least a correction under real-life cases.

- Mutual interaction effects cannot be modeled: Propellers under incidence will perform different to those in uniform-inflow. To implement two-way interaction, the velocity field resulting from MSES could be transferred to a simulation that can handle these effects.

- General 3D effects are of course not modeled by this method, and should be handled by an overarching simulation model.

Implementation, boundary conditions Finally the reliability of the current grid refinement procedure could be improved upon: relying on an iteration increases the risk of inaccuracies, and these may not always be spotted during, an automated optimization process. There is also a need to devise a procedure that can effectively provide the refined grid for assessing a free-contracting slipstream under high-lift conditions. A different implementation, i.e. where the mass flow distribution can be changed during the solution process, may provide a solution. The boundary conditions of straight inflow and classic far-field representation may not be best suited for free-contraction either: they require a much larger grid. The reason why exit size matters as much in these cases is not yet fully understood and also requires further investigation.

Bibliography

[1] C. E. Hange. Short field take-off and landing performance as an enabling technology for a greener, more efficient airspace system, 2009.

[2] R. Radespiel, W. Heinze, and L. Bertsch. *High-Lift Research for Future Transport Aircraft*. DLR, 2017.

[3] D. Agrawal, F. Asad, B. M. Berk, T. Long, J. Lubin, C. Courtin, M. Drela, R. Hansman, and J. L. Thomas. Wind tunnel testing of a blown flap wing. In *AIAA Aviation 2019 Forum*. AIAA, 2019.

[4] P. P. van Zelst. Literature study: Propeller-wing-flap interaction modeling, 2020.

[5] F. D. Harris. *Introduction to autogyros, helicopters, and other V/STOL aircraft*. National Aeronautics and Space Administration, Ames Research Center, Moffett Field, Calif., 2011.

[6] C. A. Holzhauser, R. C. Innis, and H. C. Quigley. A flight investigation of the performance, handling qualities, and operational characteristics of a deflected slipstream STOL transport airplane having four interconnected propellers. Technical Report NASA-TN-D-2231, NASA Ames Research Center, 1964.

[7] R. E. Kuhn. Semiempirical procedure for estimating lift and drag characteristics of propeller-wing-flap configurations for vertical-and short-take-off-and-landing airplanes. Technical Report MEMO 1-16-59L, NASA, 1959.

[8] J. K. Viken, S. Viken, K. A. Deere, and M. Carter. Design of the cruise and flap airfoil for the X-57 Maxwell distributed electric propulsion aircraft. In *35th AIAA Applied Aerodynamics Conference*. 2017.

[9] J. Murray and J. Lechniak. The LEAPTech experiment, approach, results, recommendations, 2016.

[10] G. J. J. Ruijgrok. *Elements of airplane performance*. Delft Academic Press (VSSD), Delft, 2nd edition, 2009.

[11] NASA. X-57 maxwell, 2019.

[12] A. Gnadt, S. Isaacs, R. Price, M. Dethy, and C. Chappelle. Hybrid turbo-electric STOL aircraft for urban air mobility. In *AIAA Scitech 2019 Forum*. AIAA, 2019.

[13] J. H. Diekmann. Flight mechanical challenges of STOL aircraft using active high lift. *Journal of Aircraft*, 56(5):1753–1764, 2019.

[14] B. W. McCormick. *Aerodynamics of V/STOL flight*. Academic Press, New York, 1967.

[15] B. Norton. *STOL Progenitors : the Technology Path to a Large STOL Aircraft and the C-17A*. American Institute of Aeronautics and Astronautics, Reston, 2002.

[16] N. Beck, R. Radespiel, C. Lenfers, J. Friedrichs, and A. Rezaeian. Aerodynamic effects of propeller slipstream on a wing with circulation control. *Journal of Aircraft*, 52(5):1422–1436, 2015.

[17] M. Burnazzi and R. Radespiel. Synergies between suction and blowing for active high-lift flaps. *CEAS Aeronautical Journal*, 6, 2015.

[18] J. Van Craenenbroeck. *Boundary layer suction configurations with minimal pump requirements for multi-element airfoils*. Msc. thesis, Delft University of Technology, 2016.

[19] H. L. Turner and F. J. Drinkwater III. Some flight characteristics of a deflected slipstream V/STOL aircraft. Technical Report TN-D-1891, NASA, 1963.

[20] Jane's by IHS Markit. All the world's aircraft: In service, 2019.

[21] Jane's by IHS Markit. All the world's aircraft: Development & production, 2019.

[22] J. D. Anderson Jr. *Fundamentals of Aerodynamics*. Mc Graw Hill, 5th edition, 2011.

[23] J. C. Duensing, J. A. Housman, D. Maldonado, J. C. Jensen, C. C. Kiris, and S. Y. Yoo. Computational simulations of electric propulsion aircraft: the X-57 Maxwell, 2019.

[24] M. Drela. *A User's Guide to MSES 3.05*. MIT Department of Aeronautics and Astronautics, 2007.

[25] N. K. Borer, M. D. Moore, and A. Turnbull. Tradespace exploration of distributed propulsors for advanced on-demand mobility concepts. In *14th AIAA Aviation Technology, Integration, and Operations Conference*. 2014.

[26] M. D. Patterson, M. J. Daskilewicz, and B. German. Simplified aerodynamics models to predict the effects of upstream propellers on wing lift. In *53rd AIAA Aerospace Sciences Meeting*. AIAA, 2015.

[27] M. D. Patterson. *Conceptual Design of High-Lift Propeller Systems for Small Electric Aircraft*. PhD thesis, Georgia Insitute of Technology, 2016.

[28] R. Nederlof. *Improved modeling of propeller-wing interactions with a lifting-line approach*. Msc. thesis, Delft University of Technology, 2020.

[29] ESDU. ESDU88031(e) lift and longitudinal forces on propeller/nacelle/wing/flap systems. Technical report, IHS Markit, 1988/2015.

[30] A. M. O. Smith. High-lift aerodynamics. *Journal of Aircraft*, 12(6):501–530, 1975.

[31] L. L. M. Veldhuis. Aircraft aerodynamics primer, 2014.

[32] M. Drela. Newton solution of coupled viscous/inviscid multielement airfoil flows. In *21st Fluid Dynamics, Plasma Dynamics and Lasers Conference*. AIAA, 1990.

[33] L. Murillo and J. McMasters. A method for predicting low-speed aerodynamic characteristics of transport aircraft. In *Applied Aerodynamics Conference*. 1983.

[34] J. Katz. Large-scale vortex-lattice model for the locally separated flow over wings. In *14th Fluid and Plasma Dynamics Conference*. 1981.

[35] J. Katz and A. Plotkin. *Low-Speed Aerodynamics*. Cambridge Aerospace Series. Cambridge University Press, Cambridge, 2nd edition, 2001.

[36] B. W. Pomeroy, J. M. Diebold, P. J. Ansell, and M. S. Selig. Study of burst wakes in a multi-element airfoil flowfield. *AIAA Journal*, 52(4):821–831, 2014.

[37] I. Gartshore. Predictions of the blowing required to suppress separation from high-lift aerofoils. In *Meeting on the Prospects for Improvement in Efficiency of Flight*. 1970.

[38] D. M. Driver and G. G. Mateer. Wake flow in adverse pressure gradient. *International Journal of Heat and Fluid Flow*, 23(5):564–571, 2002.

[39] ESDU. ESDU85015(b) introduction to installation effects on thrust and drag for propeller-driven aircraft. Technical report, IHS Markit, 1985/2006.

[40] L. L. M. Veldhuis. *Propeller Wing Aerodynamic Interference*. PhD thesis, Delft University of Technology, 2005.

[41] F. M. Catalano. On the effects of an installed propeller slipstream on wing aerodynamic characteristics. *Acta Polytechnica*, 44(No. 3/2004), 2004.

[42] C. Alba. *A Surrogate-Based Multi-Disciplinary Design Optimization Framework Exploiting Wing-Propeller Interaction*. Msc. thesis, Delft University of Technology, 2017.

[43] R. Smelt and H. Davies. *Estimation of increase in lift due to slipstream*. Aeronautical Research Committee, London, 1937.

[44] T. Burton. *Wind energy : handbook*. J. Wiley, Chichester; New York, 2001.

[45] A. Jameson. Analysis of wing slipstream flow interaction. Technical Report NASA-CR-1632, Grumman Aerospace Corp., Bethpage, NY, United States, 1970.

[46] D. A. Spence and S. B. Gates. The lift coefficient of a thin, jet-flapped wing. *Proceedings of the Royal Society of London. Series A. Mathematical and Physical Sciences*, 238(1212):46–68, 1956.

[47] E. C. Maskell, D. A. Spence, and S. B. Gates. A theory of the jet flap in three dimensions. *Proceedings of the Royal Society of London. Series A. Mathematical and Physical Sciences*, 251(1266):407–425, 1959.

[48] C. Courtin, M. J. Burton, A. Yu, P. Butler, P. D. Vascik, and R. J. Hansman. Feasibility study of short takeoff and landing urban air mobility vehicles using geometric programming. In *2018 Aviation Technology, Integration, and Operations Conference*. AIAA, 2018.

[49] J. Roskam. *Airplane design. Pt. 6. Preliminary calculation of aerodynamic, thrust and power characteristics.* Roskam Aviation and Engineering, Ottawa, Kansas, 1987.

[50] B. R. Williams. Viscous-inviscid interaction schemes for external aerodynamics. *Sadhana*, 16(2):101–140, 1991.

[51] E. Obert. *Aerodynamic Design of Transport Aircraft*. IOS Press, 2009.

[52] C. P. van Dam. The aerodynamic design of multi-element high-lift systems for transport airplanes. *Progress in Aerospace Sciences*, 38(2):101–144, 2002.

[53] J. C. Le Balleur and M. Néron. A viscous-inviscid solver for high-lift incompressible flows over multi-element airfoils at deep separation conditions. Technical Report AGARD-CP-515, 1993.

[54] L. Ting and C. H. Liu. Thin airfoil in nonuniform parallel streams. *Journal of Aircraft*, 6(2):173–175, 1969.

[55] B. F. R. Ewald (Editor). Wind tunnel wall correction. Technical Report AGARD-AG-336, 1998.

[56] R. K. Prabhu. *Studies on the Interference of Wings and Propeller Slipstreams*. PhD thesis, Old Dominion University, 1984.

[57] M. Yahyaoui. Generalized vortex lattice method for predicting characteristics of wings with flap and aileron deflection. *International Journal of Mechanical, Aerospace, Industrial, Mechatronic and Manufacturing Engineering*, 8(10), 2014.

[58] B. Bohari, Q. Borlon, P. B. Mendoza-Santos, A. Sgueglia, E. Benard, M. Bronz, and S. Defoort. Conceptual design of distributed propellers aircraft: Non-linear aerodynamic model verification of propeller-wing interaction in high-lifting configuration. In *2018 AIAA Aerospace Sciences Meeting*. AIAA, 2018.

[59] E. Moerland. *Development of an aeroelastic analysis tool for structural sizing of high-lift devices during preliminary design*. Msc. thesis, Delft University of Technology, 2011.

[60] B. Rajeswari and H. N. V. Dutt. Analysis of wing flap configurations by a nonplanar vortex lattice method. *Journal of Aircraft*, 25(2):97–98, 1988.

[61] B. Singh. *A Medium-Fidelity Method for Rapid Maximum Lift Estimation*. Msc. thesis, Delft University of Technology, 2017.

[62] C. P. van Dam, J. C. Vander Kam, and J. K. Paris. Design-oriented high-lift methodology for general aviation and civil transport aircraft. *Journal of Aircraft*, 38(6):1076–1084, 2001.

[63] J. Weissinger. The lift distribution of swept-back wings. Technical Report TM-1120, NASA Langley, 1947.

[64] W. F. Phillips and D. O. Snyder. Modern adaptation of prandtl's classic lifting-line theory. *Journal of Aircraft*, 37(4):662–670, 2000.

[65] J. Fischer. *Simulation & Analysis of the Aerodynamic Interactions between Distributed Propellers and Wings*. Msc. thesis, Delft University of Technology, 2017.

[66] K. Epema. *Wing Optimisation for Tractor Propeller Configurations: Validation and Application of Low-Order Numerical Models Adapted to Include Propeller-Induced Velocities*. Msc. thesis, Delft University of Technology, 2017.

[67] S. Rethorst. Aerodynamics of nonuniform flows as related to an airfoil extending through a circular jet. *Journal of the Aerospace Sciences*, 25(1):11–28, 1958.

[68] L. Muller, W. Heinze, D. Kozulovic, M. Hepperle, and R. Radespiel. Aerodynamic installation effects of an over-the-wing propeller on a high-lift configuration. *Journal of Aircraft*, 51(1):249–258, 2014.

[69] K. A. Deere, S. Viken, M. Carter, J. K. Viken, M. Wiese, and N. Farr. Computational analysis of powered lift augmentation for the LEAPTech distributed electric propulsion wing. In *35th AIAA Applied Aerodynamics Conference*. 2017.

[70] A. M. Stoll. Comparison of CFD and experimental results of the LEAPTech distributed electric propulsion blown wing. In *15th AIAA Aviation Technology, Integration, and Operations Conference*. 2015.

[71] M. Drela and M. B. Giles. Viscous-inviscid analysis of transonic and low reynolds number airfoils. *AIAA Journal*, 25(10):1347–1355, 1987.

[72] M. Drela. *Two-dimensional transonic aerodynamic design and analysis using the Euler equations*. Ph. d., Massachusetts Institute of Technology, 1986.

[73] M. Drela. XFOIL: An analysis and design system for low Reynolds number airfoils. In *Conference on Low Reynolds Number Airfoil Aerodynamics*, University of Notre Dame, 1989. MIT.

[74] D. Florjancic. *Improved Design of a High Lift System for General Aviation Aircraft*. Msc. thesis, Delft University of Technology, 2015.

[75] C. L. Rumsey and J. P. Slotnick. Overview and summary of the second AIAA high-lift prediction workshop. *Journal of Aircraft*, 52(4):1006–1025, 2015.

[76] M. Orlita. *Cruise Performance Optimization of the Airbus A320 through Flap Morphing*. Msc. thesis, Delft University of Technology, 2016.

[77] Kounenis C. *Wake Bursting Effects of a Drooped Spoiler Panel in a Wing-Flap Configuration*. Msc. thesis, Delft University of Technology, 2012.

[78] F. Johansson. Illustration of Newton's method., 2011.

[79] M. Drela. *MSES Domain Size Sensitivity Study*. MIT Department of Aeronautics and Astronautics, 1996.

[80] S. A. Chadha, B. W. Pomeroy, and M. S. Selig. Computational study of a lifting surface in propeller slipstreams. In *34th AIAA Applied Aerodynamics Conference*. 2016.

[81] T. J. A. Dolle. *Flap Performance Improvement by Surface Excitation*. Msc. thesis, Delft University of Technology, 2009.

[82] B. van den Berg. Boudary layer measurements on a two-dimensional wing with flap. Technical report, National Aerospace Laboratory NLR, 1979.

[83] AGARD Fluid Dynamics Panel. A selection of experimental test cases for the validation of CFD codes, volume 1. Technical Report AGARD-AR-303-VOL-1, 1994.

[84] G. W. Brune and J. H. McMasters. Computational aerodynamics applied to high-lift systems. In *Applied Computational Aerodynamics*, pages 389–433. 1989.

A

Modified MSES inputs & roadmap

In this appendix, the changes to the input/output files required for MSET and MSES are listed. These are handled automatically by the wrapper but could of course be adjusted by hand. As this will only refer to changes made, for the general syntax and meaning of the inputs not discussed here, one could either refer to the source code of MSES, or the manual by Drela [24]. Internal variables that were added are not discussed in this appendix. The roadmap with the points of interaction with Python is shown in fig. A.1 as originally found in the manual by Drela[24]. The plotting functionalities of MSES/MPLOT did not run on the current Windows 10 configuration, but most results could be printed or dumped using MPLOT, and subsequently be plotted using Python's Matplotlib library.

The following files of the source code have been modified:

init.f, MSES.INC, mset.f, iomses.f, STATE.INC, mplot.f

In order to allow the refinement of the grid at certain locations in MSET, parameters need to be passed. It is found most convenient to include them as an extra row in the $gridpar.xxx$ file:

[RFLOCT, RFLOCB, NTT, NBB, EDGEHT, EDGEHB, RDOWNT, RDOWNB]

- **RFLOCT, RFLOCB** Top and bottom grid refinement location on the MSET inlet plane. Different than the AD disk coordinates due to contraction and possibly upwash.
- **NTT, NBB** Number of streamlines above the top, and below the bottom refinement.
- **EDGEHT, EDGEHB** Height of the smallest refinement cells adjacent to the top and bottom refinement location in MSET.
- **RDOWNT, RDOWNB** Correction factor for upwash of the topmost and botmost element, as defined by the ratio printed by the modified MSET, and that observed in the flowfield resulting from a representative MSES solution.

In order to allow implementation of the actuator disk with varying position and velocity field, more parameters need to be passed to MSES via the $mses.xxx$ file. Descriptions are automatically added in MSES for most of the original inputs, and by the wrapper for the new inputs. Similarly to the manual by Drela [24], the list of variables as present in the Fortran source code is presented below, the last 3 rows contain the new variables:

...
[ISDELH XCDELH PTRHIN ETAH]
[ZBOT ZTOP XPROP PROPIN]<– new (see below)
[PRP1 PRP2 P3 P4 P5]<– new (see below)
[P6 P7 P8 P9 P10 P11]<– new (see below)

- **ISDELH** has similar function to original: ISDELH=0 now allows to specify an actuator disk at any region of interest on the domain: both in front of the airfoil or on the airfoil surface. ISDELH=1, 2... indicates an option to constrain the actuator disk to an airfoil side of choice numbered top to bottom with a maximum of 2 times the number of blades, as numbered originally. However, as a new feature the height of the AD as specified by the difference between ZBOT and ZTOP is retained. This is ideal for considering the maximum theoretical effect of upper or lower surface blowing.
- **XCDELH** Has similar meaning as before: it indicates where the velocity jump is imposed. However, it may now also be placed in front of the airfoil, and a velocity profile may be assigned elsewhere (see XPROP).
- **ZBOT, ZTOP, XPROP** The bottom, top, and horizontal coordinate of the desired propeller location. For a non-uniform flow-field, the velocity profile gets assigned tot the appropriate streamlines here, but it is introduced at XCDELH. This is specified in the airfoil centered coordinate frame.
- **PROPIN** Propeller incidence angle. This feature is disabled in the final version of MSES used due to lack of desired effect: the code is added to the init.f file, commented out.
- **PRP1... P5** The polynomial coefficients/weights for the velocity spline on the top half of the actuator disk/propeller. Note that PTRHIN is used as the constant for this fifth order polynomial. PRP1 through P5 are the coefficients for the 1st and 5th order terms, respectively, where the Z-coordinate is the base. If these values are 0 a constant velocity will be imposed. Reason for calling PRP1 and PRP2 as such is that the variables P1 and P2 were already in use.
- **P6...P11** Polynomial coefficients/weights for the bottom domain. P6 now represent the constant for the lower domain and should be equal to PRP1 in the uniform flow-case.

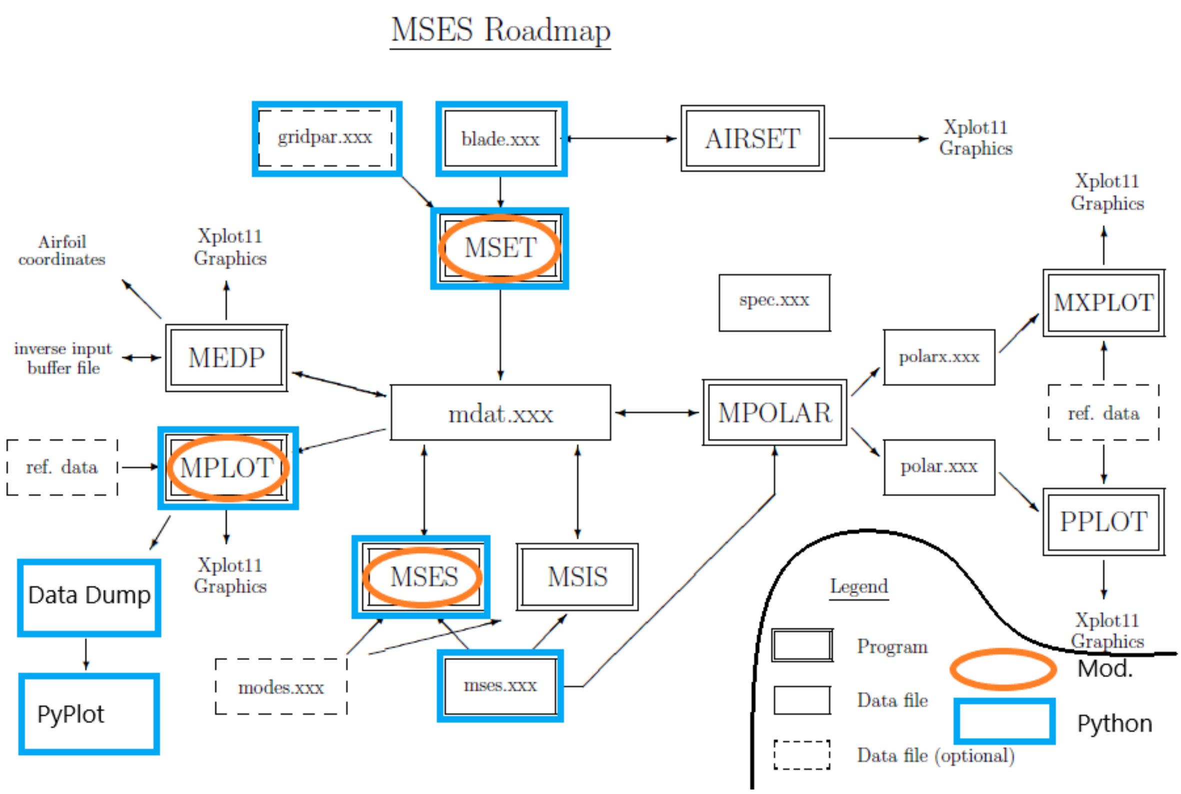

Figure A.1: Modifications to the MSES software. Roadmap courtesy of Drela [24].

B

Domain sensitivity study data

The domain sensitivity study could not all be compared in the dedicated sections (section 5.5.2 & section 5.5.3), therefore, the simulation inputs and the result in terms of recovered exit dynamic pressure are included here.

Table B.1: Domain study parameters for the smaller AD ($h/c = 1.0$).

I	X_ad	XIN	XOUT	YBOT	YTOP	QR
0	-4.0	-5.0	3.5	-3.5	3.5	2.230
1	-4.0	-5.0	5.0	-3.5	3.5	2.243
2	-4.0	-5.0	7.0	-3.5	3.5	2.247
3	-4.0	-10.0	3.5	-3.5	3.5	2.201
4	-4.0	-10.0	5.0	-3.5	3.5	2.231
5	-4.0	-10.0	7.0	-3.5	3.5	2.241
6	-2.0	-5.0	3.5	-3.5	3.5	2.208
7	-2.0	-5.0	5.0	-3.5	3.5	2.230
8	-2.0	-5.0	7.0	-3.5	3.5	2.239
9	-2.0	-10.0	3.5	-3.5	3.5	2.201
10	-2.0	-10.0	5.0	-3.5	3.5	2.228
11	-2.0	-10.0	7.0	-3.5	3.5	2.237
12	-2.0	-10.0	3.5	-5.0	5.0	2.184
13	-2.0	-10.0	5.0	-5.0	5.0	2.223
14	-2.0	-10.0	7.0	-5.0	5.0	2.235
15	-4.0	-20.0	6.0	-12.0	12.0	2.047
16	-4.0	-20.0	12.0	-12.0	12.0	2.212
17	-4.0	-20.0	18.0	-12.0	12.0	2.229

Table B.2: Domain study parameters for the large AD ($h/c = 4.0$).

I	X_ad	XIN	XOUT	YBOT	YTOP	QR
0	-8.0	-10.0	6.0	-3.5	3.5	2.245
1	-8.0	-10.0	12.0	-3.5	3.5	2.249
2	-8.0	-10.0	18.0	-3.5	3.5	2.250
3	-8.0	-20.0	6.0	-3.5	3.5	2.242
4	-8.0	-20.0	12.0	-3.5	3.5	2.248
5	-8.0	-20.0	18.0	-3.5	3.5	2.249
6	-4.0	-10.0	6.0	-3.5	3.5	2.218
7	-4.0	-10.0	12.0	-3.5	3.5	2.239
8	-4.0	-10.0	18.0	-3.5	3.5	2.242
9	-4.0	-20.0	6.0	-3.5	3.5	2.217
10	-4.0	-20.0	12.0	-3.5	3.5	2.239
11	-4.0	-20.0	18.0	-3.5	3.5	2.242
12	-4.0	-20.0	6.0	-6.0	6.0	2.145
13	-4.0	-20.0	12.0	-6.0	6.0	2.223
14	-4.0	-20.0	18.0	-6.0	6.0	2.234
15	-4.0	-20.0	6.0	-12.0	12.0	2.047
16	-4.0	-20.0	12.0	-12.0	12.0	2.212
17	-4.0	-20.0	18.0	-12.0	12.0	2.229

Table B.3: Domain study for the pre-contracted cases.

I	X_ad	XCON	XIN	XOUT	YBOT	YTOP	CL
0	-5.02	-5.02	-5.0	3.5	-3.5	3.5	0.4794
1	-4.52	-4.52	-4.5	3.5	-3.5	3.5	0.4776
2	-4.02	-4.02	-4.0	3.5	-3.5	3.5	0.4759
3	-3.52	-3.52	-3.5	3.5	-3.5	3.5	0.4742
4	-3.02	-3.02	-3.0	3.5	-3.5	3.5	0.4725
5	-2.52	-2.52	-2.5	3.5	-3.5	3.5	0.4710
6	-2.02	-2.02	-2.0	3.5	-3.5	3.5	0.4698
7	-5.02	-5.02	-5.0	5.0	-5.0	5.0	0.4813
8	-4.52	-4.52	-4.5	5.0	-5.0	5.0	0.4793
9	-4.02	-4.02	-4.0	5.0	-5.0	5.0	0.4774
10	-3.52	-3.52	-3.5	5.0	-5.0	5.0	0.4756
11	-3.02	-3.02	-3.0	5.0	-5.0	5.0	0.4738
12	-2.52	-2.52	-2.5	5.0	-5.0	5.0	0.4720
13	-2.02	-2.02	-2.0	5.0	-5.0	5.0	0.4702
14	-5.02	-5.00	-5.0	3.5	-3.5	3.5	0.4793
15	-5.02	-4.50	-5.0	3.5	-3.5	3.5	0.4772
16	-5.02	-4.00	-5.0	3.5	-3.5	3.5	0.4751
17	-5.02	-3.50	-5.0	3.5	-3.5	3.5	0.4730
18	-5.02	-3.00	-5.0	3.5	-3.5	3.5	0.4709
19	-5.02	-2.50	-5.0	3.5	-3.5	3.5	0.4688
20	-5.02	-2.00	-5.0	3.5	-3.5	3.5	0.4666
21	-5.02	-1.50	-5.0	3.5	-3.5	3.5	0.4645
22	-5.02	-1.00	-5.0	3.5	-3.5	3.5	0.4624
23	-5.02	-0.50	-5.0	3.5	-3.5	3.5	0.4555
24	-5.02	-0.25	-5.0	3.5	-3.5	3.5	0.4503
25	-5.02	-5.00	-5.0	5.0	-5.0	5.0	0.4812
26	-5.02	-4.50	-5.0	5.0	-5.0	5.0	0.4791
27	-5.02	-4.00	-5.0	5.0	-5.0	5.0	0.4770
28	-5.02	-3.50	-5.0	5.0	-5.0	5.0	0.4749
29	-5.02	-3.00	-5.0	5.0	-5.0	5.0	0.4728
30	-5.02	-2.50	-5.0	5.0	-5.0	5.0	0.4708
31	-5.02	-2.00	-5.0	5.0	-5.0	5.0	0.4687
32	-5.02	-1.50	-5.0	5.0	-5.0	5.0	0.4666
33	-5.02	-1.00	-5.0	5.0	-5.0	5.0	0.4593
34	-5.02	-0.50	-5.0	5.0	-5.0	5.0	0.4570
35	-5.02	-0.25	-5.0	5.0	-5.0	5.0	0.4515

C

Boundary Layer development

The displacement thickness Several conclusions can be drawn from the displacement thickness as presented in fig. C.1. On the upper surface of the main airfoil, the displacement thickness is very slightly decreased by the lower n_{crit}, which is favorable for postponing separation. Contrary to that, it is larger on the flap upper surface trailing edge. As expected, the lower n_{crit} expedites transition and leads to smaller laminar separation bubbles before transition and re-attachment. The reason this leads to higher displacement thickness on the bottom surface around $0.8c$ is not clear.

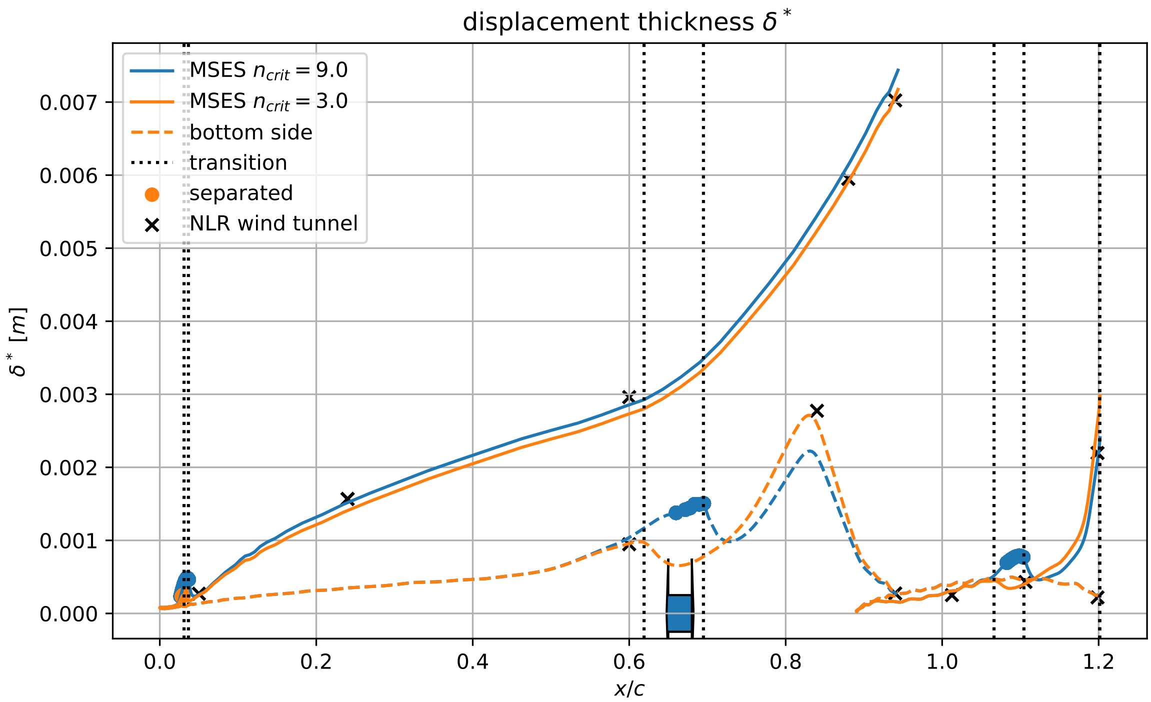

Figure C.1: Displacement thickness of the NLR7301 with flap at various turbulence settings. $\alpha = 6°$, $M = 0.15$
note: Arrow indicates lower surface transition region

The shape factor It can be seen from the results in fig. C.2 that the lower n_{crit} causes lower H and less flow reversal due to earlier transition. The slightly larger H value on the flap TE associated with the lower n_{crit} could lead to earlier TE separation.

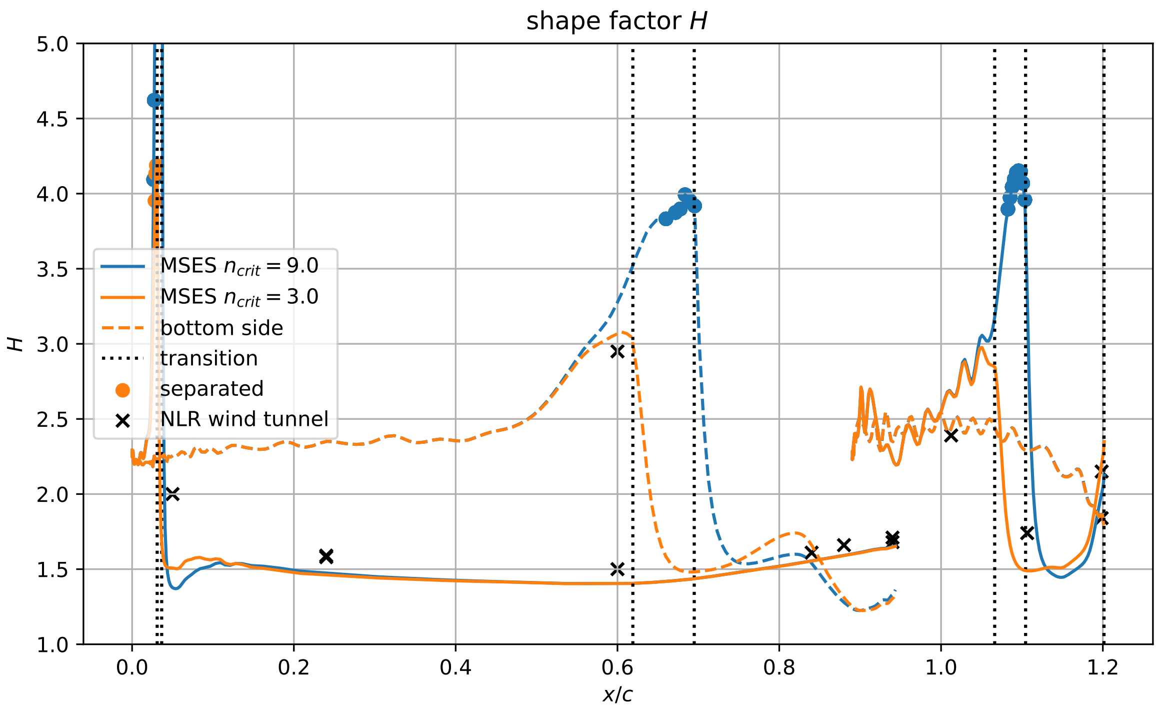

Figure C.2: Shape factor of the NLR7301 with flap at various turbulence settings. $\alpha = 6°, M = 0.15$

D

Scalloped polar results

The scalloping of the results near CL_{max} with the grid generated at 7° in fig. D.1 becomes more pronounced in the L/D polar shown in fig. D.2. Note that the MSES simulations were run at slightly lower Mach number which has little impact on the solution. For comparison, the improved L/D polar results with more LE bubble accuracy are shown in fig. D.3.

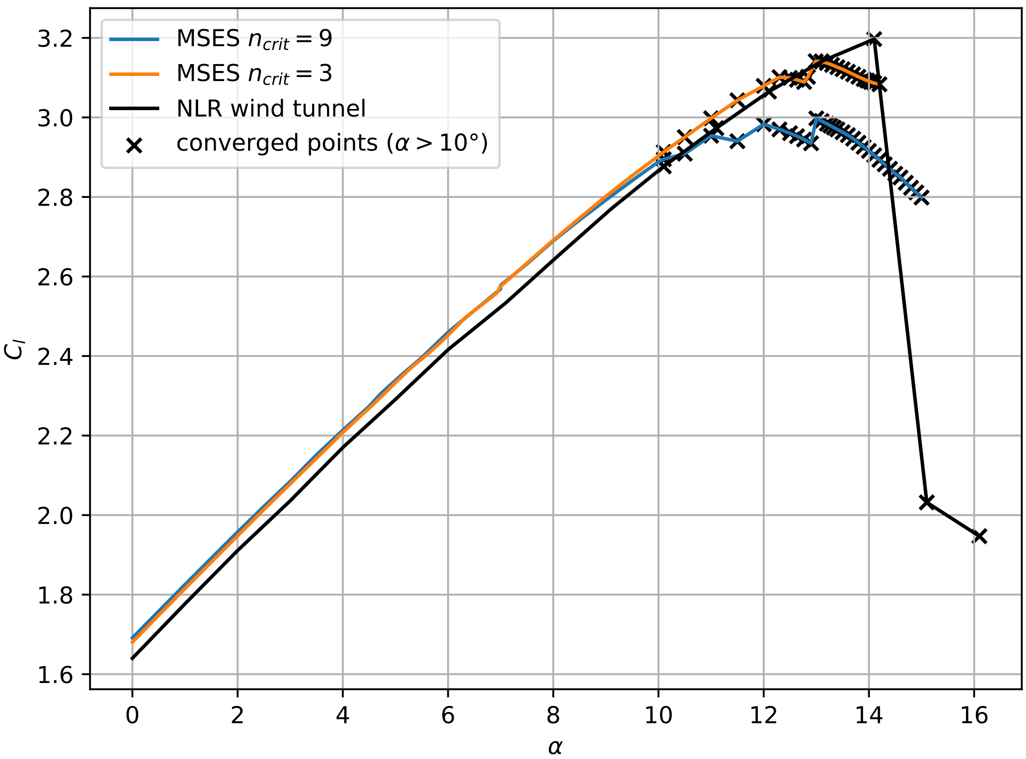

Figure D.1: ‘Scalloped’ lift polars of the NLR7301 with $\delta_f = 20°$ at various turbulence settings.$M = 0.15(MSES), M = 0.185(experiment)$

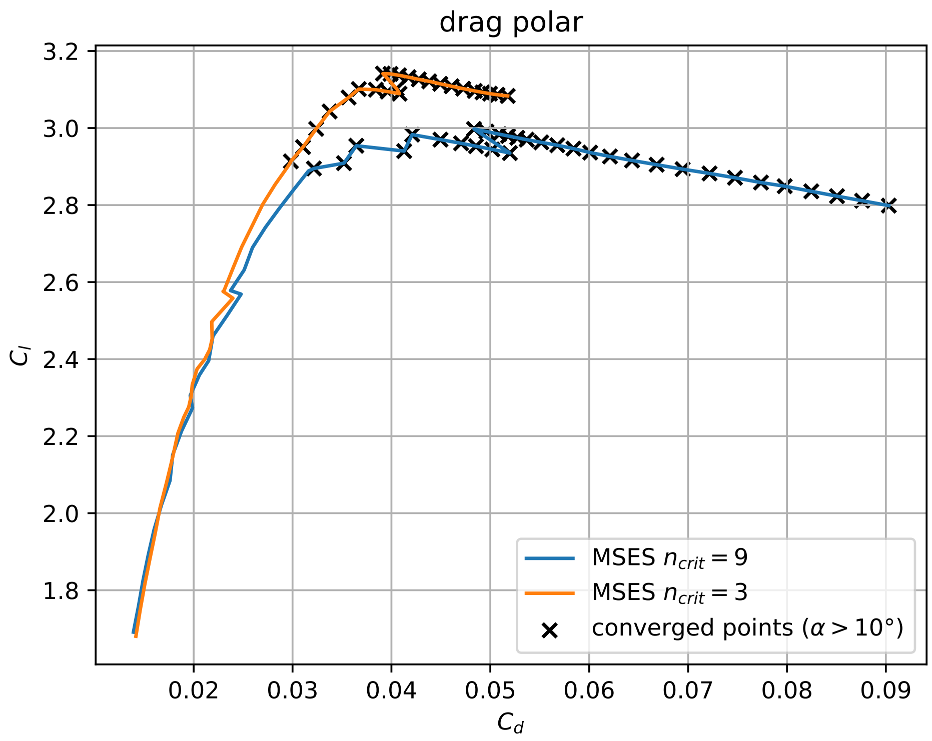

Figure D.2: 'Scalloped' lift-drag polar of the NLR7301 with δ_f = 20° at various turbulence settings.$M = 0.15(MSES), M = 0.185(experiment)$

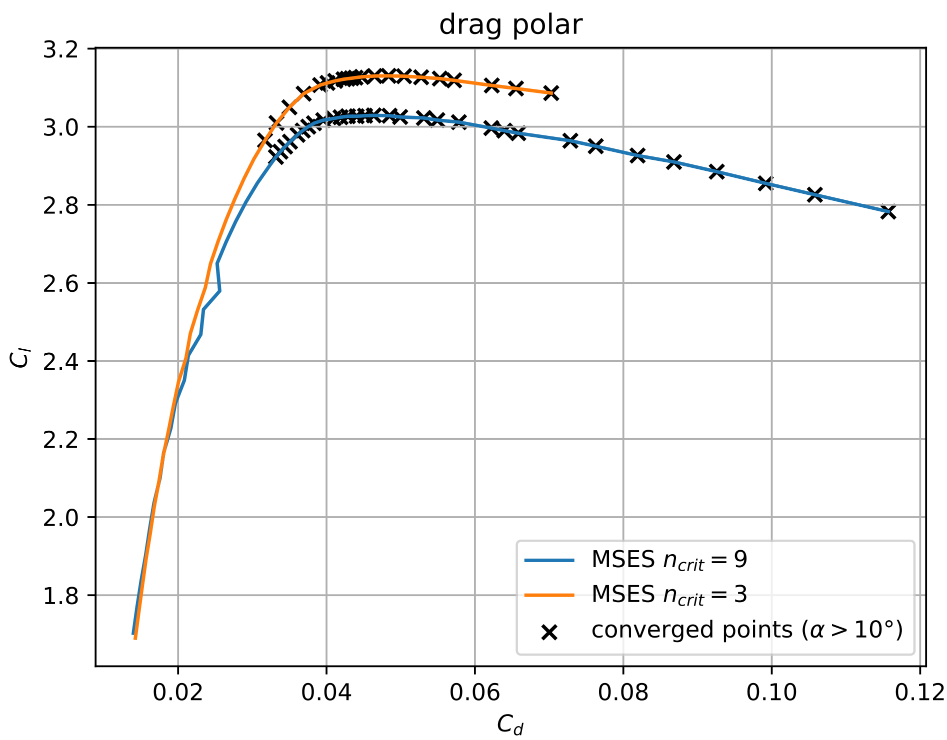

Figure D.3: Improved lift-drag polar of the NLR7301 with δ_f = 20° at various turbulence settings.$M = 0.185(MSES), M = 0.185(experiment)$